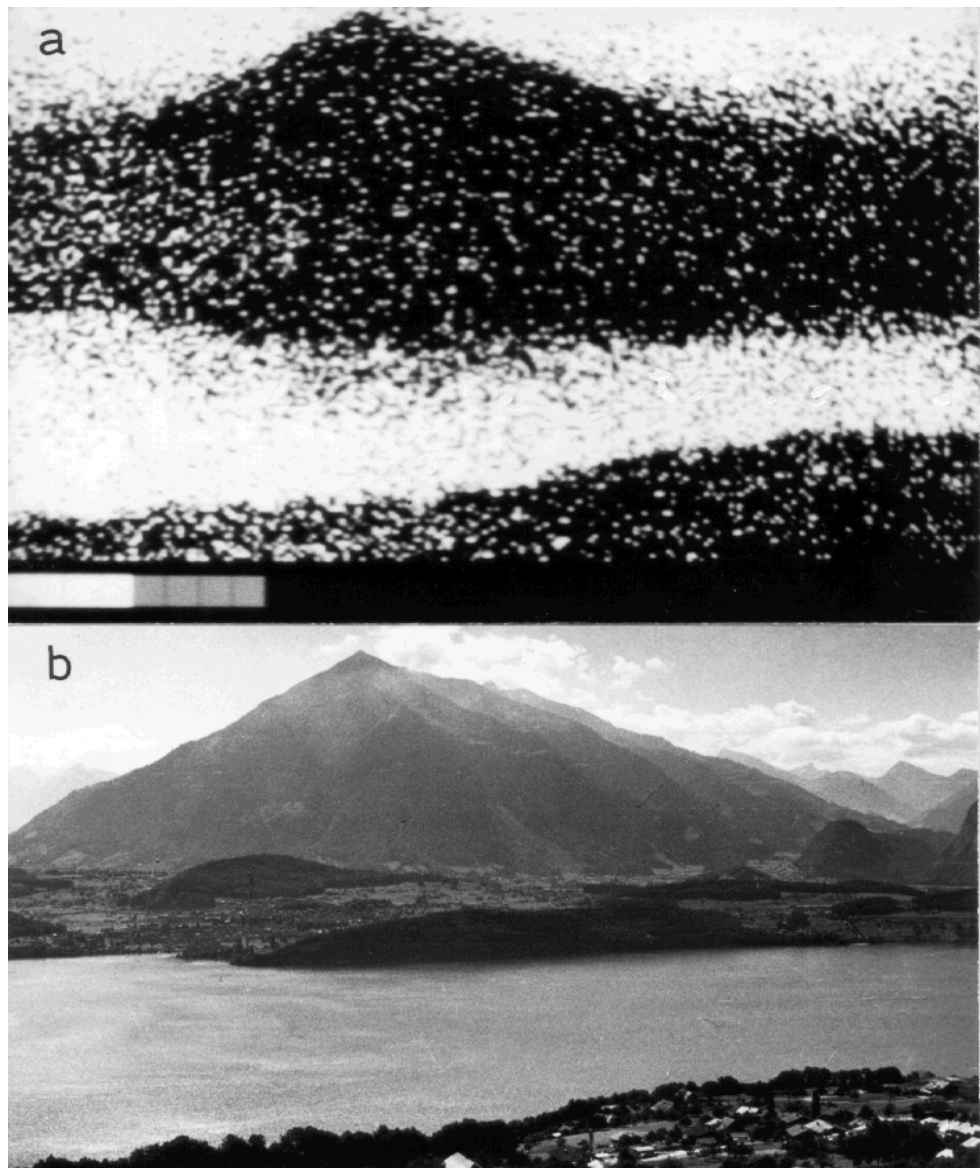


COST 712: Final Report of Project 1

# Radiative Transfer Models For Microwave Radiometry





# Radiative Transfer Models For Microwave Radiometry

**COST — European cooperation in the field of scientific and technical research**

Meteorology

**COST Action 712: *Application of Microwave Radiometry to Atmospheric Research and Monitoring***

**Final Report of Project 1: *Development of Radiative Transfer Models***

ISBN 92-828-9842-3

Edited by Christian Matzler, Bern, Switzerland, February 2000

*Cover picture:* Observed radiative transfer at *Lake of Thun* with the town of *Spiez* and the conical mountain *Niesen* as seen from NE (a) with an early microwave radiometer at a wavelength of 3 mm, and (b) in visible light, from G. Schaeerer and E. Schanda, *Deteriorating effects on 3 mm wave passive imagery*, Proc. 9<sup>th</sup> Symp. Rem. Sens. Env., Ann Arbor, Michigan, pp.1593-1602 (1974), see also E. Schanda, *Passive microwave sensing* in Schanda (ed.), *Remote Sensing for Environmental Sciences*, Springer Ecological Studies 18, pp. 187-256 (1976).

## Contents

Introduction .....	5
1 Objectives of COST Action 712 and of its Project 1 .....	5
2 Short history of Project 1 .....	5
3 Working Group Meeting in Spiez .....	6
4 Purpose of this report .....	7
5 Outlook .....	7
6 Acknowledgments .....	8
References .....	8
Spectroscopy and microwave radiative transfer in the clear atmosphere .....	9
1 Progress since April 1997 .....	9
2 Recommended models: Accuracy and state of validation .....	14
3 Recommendations for future development of models .....	17
4 Availability of databases and models .....	18
References .....	20
BEAM: a fast line-by-line model for atmospheric transmission in the millimeter and submillimeter range .....	31
1 Introduction .....	31
2 Components of BEAM .....	31
3 Future work .....	32
References .....	33
Overview of RTTOV-5 .....	35
References .....	36
Clouds and precipitation .....	37
1 Introduction .....	37
2 Hydrometeors .....	38
3 Radiative transfer models .....	49
4 Future developments .....	59
5 Acknowledgements .....	60
References .....	60
A Permittivity models .....	66
B 3-D recursive solution for isotropically scattering media .....	69
C Model descriptions .....	70
Microwave emission from covered surfaces: zero-order versus multiple scattering .....	73
1 Introduction .....	73
2 Zero-order scattering model (Kirdashev et al. 1979) .....	73
3 Multiple-scattering model in two-stream approach (MEMLS_ simplified) .....	74
4 Comparison .....	75
5 Effects of lateral inhomogeneity .....	78
6 Conclusions .....	79
References .....	80
Relief effects for passive microwave remote sensing .....	81
1 Introduction .....	81
2 Flat horizon .....	81
3 Terrain with tilted surfaces .....	83
4 The example of southern Norway .....	86
5 Conclusions .....	88
References .....	88
Microwave emission from soil and vegetation .....	89

1	Introduction.....	89
2	Microwave emission from vegetation .....	89
3	Microwave emission from soil.....	91
4	Selection of emission models.....	93
5	Conclusions and recommendations.....	99
	References.....	100
	Development of microwave emission models of snowpacks .....	105
1	Passive microwave remote sensing of snow .....	105
2	Modeling efforts for seasonal snow and ice sheets.....	106
3	Recommended microwave emission models for snowpacks .....	112
	References.....	114
	Fast models for land surface emissivity .....	117
1	Why develop a fast model?.....	117
2	Empirical models .....	117
3	A semi-empirical model.....	118
4	Advantages and disadvantages.....	118
5	Fitting model parameters.....	119
6	Future refinements to the semi-empirical fast emissivity model .....	126
	References .....	126
	Ocean surface emissivity modelling.....	129
1	Short overview of the sea surface emissivity modelling.....	129
2	The models to be proposed .....	132
3	Model comparison.....	136
4	A fast ocean emissivity model .....	141
5	Concluding remarks .....	146
	References .....	146
	Emissivity modelling of sea ice and lake ice.....	149
1	In-situ measurements.....	149
2	Microwave emissivity models of lake and sea ice .....	153
3	Recommendations and further improvements.....	161
	References .....	161
	Appendix A: Surface emissivity data from microwave experiments of the University of Bern.....	163
	References .....	163
	Instrument characteristics .....	164
	Test sites, objects and data.....	165
	Appendix B: Surface emissivity data from PORTOS-Avignon experiment.....	171
	References .....	171
	Appendix C: Members and Addresses .....	173
	COST 712, Project 1 Members .....	173
	Other.....	174

# Introduction

## 1 Objectives of COST Action 712 and of its Project 1

As described in the Memorandum of Understanding [1] the aims of COST Action 712 *Application of Microwave Radiometry to Atmospheric Research and Monitoring* are to improve the application of microwave radiometry to the understanding and monitoring of the hydrological cycle, and tropospheric-stratospheric exchange. This includes research to understand and to model the atmospheric processes involved in these phenomena. These objectives can be achieved through developments in the following areas:

1. improved models of the interaction of microwave radiation with the Earth's atmosphere and surface,
2. improved retrieval, analysis and assimilation techniques, through which atmospheric and surface parameters are estimated from the data,
3. verification and validation studies, through which the accuracy and characteristics of the data analysis techniques may be assessed,
4. improved measurement facilities and techniques, including ground-based, aircraft-borne and space-based systems.

The COST action supports the above activities through sharing of information on state-of-the-art methods and facilities, and through exchange of data and software where appropriate.

Area 1 is addressed here as the topic of Project 1 *Development of Radiative Transfer Models*. Its focus is the development of improved physical models, fast physical and semi-empirical models and the improvement of critical elements in radiative transfer (e.g. microwave dielectric properties of water, ice, soil, vegetation and of various mixtures). The models include resonant and continuum absorption and refraction by the clear atmosphere, microwave emission and scattering by water and ice clouds, precipitation, microwave emission of the earth's surface over land and sea, considering rough-surface scattering, surface covers with volume scattering, and relief effects, an example of which is given in the cover figure. While absorption and refraction are governed by the dielectric properties of the media involved, reflection and scattering are also sensitive to the heterogeneity, shape and geometrical arrangement of individual elements.

## 2 Short history of Project 1

This report is the result of the progress achieved in Project 1 (for members, see Appendix to this report) of COST Action 712 since the first workshop in April 1997 held at EUMETSAT in Darmstadt, Germany. The work was done along the lines of recommendations presented in the first report [2], based on the discussions in Darmstadt and on subsequent reviews made by project members and by additional experts.

Project 1 was divided into three subgroups dedicated to (1) clear atmosphere, (2) clouds and precipitation and (3) surface emissivity. The group interacted mainly via email. In summer 1998 it was decided to compile the progress in a final report to be available to the other projects before the end of Action 712. Discussions on the results took place during and after the Project 1 Meeting at Hotel Bellevue, Spiez, Switzerland on January 21-22, 1999.

### **3 Working Group Meeting in Spiez**

#### **Agenda and main conclusions**

##### **Subgroup 1, "Spectroscopy and Radiative Transfer of the Clear Atmosphere"**

(Coordination: Phil Rosenkranz and Agnes Bauer)

1.1 Nicole Jacquinet-Husson: Status of the GEISA data base

1.2 Agnes Bauer: Review of recent experimental and theoretical studies in the spectroscopy of the clear atmosphere over the 100 to 1000 GHz range

1.3 Dietrich Feist: BEAM: a fast line-by-line model for atmospheric transmission in the mm and sub-mm range

1.4 Steve English: Fast radiative transfer model (RTTOV-5) in use at ECMWF and UKMO

1.5 Phil Rosenkranz: Review of recent literature on critical parameters

##### Main conclusions:

- Important progress was achieved, especially in the understanding of continuum absorption.
- Ambiguities, difficulties in line identification, incompleteness and missing information (e.g. errors) are handicaps in current databases. Efforts continue to improve the situation, e.g. for the spectral bands of SOPRANO and MASTER.

##### **Subgroup 2 "Radiative Transfer of Clouds and Precipitation"**

(Coordination: Harald Czekala and Peter Bauer)

2.1 Peter Bauer: Introduction

2.2 Harald Czekala: Microwave radiative transfer with multiple scattering by non-spherical particles (fully polarimetric, scattering data base under construction)

2.3 Peter Bauer: Aspects of forward radiative transfer modeling in precipitating clouds for improved rainfall retrievals (3-d effects)

2.4 Dave Jones: Forward modelling of microwave brightness temperatures from numerical weather prediction model fields (an adaptation of Kummerow's plane-parallel Eddington approximation code)

##### Main conclusions:

- Ongoing research in all fields makes it difficult to recommend specific radiative transfer models.
- The proper selection of hydrometeor profiles (and thus of cloud physics) has largest effect on brightness temperatures.
- 3-D effects are noticeable, if neglected they lead to underestimates of rain rates.

##### **Subgroup 3 "Modeling microwave emission of the surface"**

(Coordination: Laurence Eymard and Christian Mätzler)

3.1 Klaus-Peter Johnsen: Sea-ice emissivity

3.2 Laurence Eymard: Overview of ocean emissivity modeling

3.3 Steve English: FASTEM a fast ocean emission model

3.4 Piotr Sobieski: Two-scale model

3.5 Laurence Eymard: Comparison of 2-scale and geometric-optics model

3.6 Tim Hewison: FASTEM – landpart

3.7 Christian Mätzler: Relief effects

3.8 Andre Chanzy: Microwave emission models of bare soil and vegetation

3.9 Martti Hallikainen: HUT snow emissivity model

3.10 Christian Mätzler: Microwave emission model of layered snowpacks

##### Main conclusions:

- Significant progress was achieved, especially in assessing effects and errors in ocean emission.
- Physical and semi-empirical models were developed for sea ice, snow and vegetation on land. Model optimization, parameter determination and error assessment are ongoing.
- Empirical data bases can form the source of fast and simple models.
- Special effects result by the relief.



Participants at the Spiez Meeting, from left to right: A.Tassa, P.Sobiesky, D.Jones, Z.Dunkel, K.P.Johnsen, L.Eymard, T.Hewison, A.Chanzy, M.Hallikainen, D.Pick, P.van de Griend, S.English, A.Bauer, P.Rosenkranz, H.Czekala, P.Bauer.

#### ***List of Participants:***

Name	Country	Name	Country	Name	Country
Agnes Bauer	F	Laurence Eymard	F	Dave Jones	UK
Peter Bauer	D	Dietrich Feist	CH	Niklaus Kämpfer	CH
Stefan Bühler	D	Adriaan van de Griend	NL	Christian Mätzler	CH
Andre Chanzy	F	Martti Hallikainen	FI	David Pick	UK
Harald Czekala	D	Tim Hewison	UK	Phil Rosenkranz	USA
Zoltan Dunkel	COST	Nicole Jacquinet-Husson	F	Piotr Sobieski	BE
Stephen English	UK	Klaus-Peter Johnson	D	Alessandra Tassa	IT

#### ***4 Purpose of this report***

The purpose of this report is to make the results of Project 1 available to the other projects of Action 712, to the meteorological community and to the still wider community interested in remote sensing, climatology, hydrology and earth system sciences. The results consist of model assessments, model descriptions, data for validation, recommendations of which models should be used and where the development is heading to.

#### ***5 Outlook***

Since the beginning of microwave radiometry, radiative transfer and its related spectral data have been evolving and improving. The present report may be regarded as a milestone, but not as the goal of this process. The work has to continue. Recommendations for future studies as seen by the authors of this report are listed in the different chapters. As COST performs Actions for a limited period of time, Project 1 passes this task over to future initiatives in the development of microwave radiative transfer.



Spiez and Lake of Thun on Jan. 22 1999, view in direction East, next to Hotel Bellevue

## **6 Acknowledgments**

This report would not have been possible without the volunteering work of all authors of this report, members of Project 1, and reviewers of the report in earlier versions. Thanks go to Lorenz Martin who helped in the file translation and format adaptation process, to Dietrich Feist who traced reading, writing and printing problems, to David Pick, Andrej Hocevar and Zoltan Dunkel for advice in administrative tasks, to Tom Schmugge who acted as an external reviewer, and to Helene Mätzler for her loving support to the editor. The working-group meeting in Spiez was supported by the COST Office in Brussels and by the Swiss Federal Office of Education and Science, Contract No. C97.0027.

## **References**

- [1] Memorandum of Understanding for the Implementation of a European Concerted Research Action Designated as COST Action 712 "Microwave Radiometry", COST 281/95, Brussels (1995).
- [2] Mätzler C. (ed.) "Development of Radiative Transfer Models", COST Action 712, Report from Review Workshop 1, EUMETSAT, Darmstadt, Germany, April 8 to 10, 1997, Oct. (1997). Available from COST Office, Square de Meeus 8, 1/56, DG XII B.1, B-1040 Brussels, or from the editor.

# Spectroscopy and microwave radiative transfer in the clear atmosphere

Agnes Bauer, Nicole Jacquinet-Husson and Philip Rosenkranz

## 1 Progress since April 1997

This section reviews results obtained or published since the first Project 1 workshop, and thus supplements and brings up to date the report by Rosenkranz and Bauer (1997).

### 1.1 Line parameter databases

#### 1.1.1 HITRAN-96

The most recent edition of HITRAN on CD-ROM includes a new graphical user interface, HAWKS, for both UNIX and Windows operating systems. The database itself was last updated in 1996. The November 1998 issue of the Journal of Quantitative Spectroscopy and Radiative Transfer is devoted to the latest version of the HITRAN database. Rothman *et al.* (1998) give a detailed description of the improvements of this database. The main molecules and the main points of interest in view of atmospheric investigations in the microwave and millimeter-wave range are the following:

##### - H<sub>2</sub>O

Rotational transitions for HDO have been updated. A large uncertainty exists in the positions and strength of high J and K weaker rotational lines for the other isotopomers of H<sub>2</sub>O.

The data for the air-broadened and self-broadened halfwidths and the temperature dependence *n* of the air broadened halfwidth on HITRAN are a mixture of experimental and theoretical coefficients. The halfwidths are added to the database with an algorithm operating as follows: for a given spectral line, the algorithm first attempts to add measured halfwidths to the line. If no measurements are available, the algorithm defaults to the theoretical value for the halfwidths. If no theoretical value is available for the particular transition, the algorithm takes the scaled average halfwidth and adds that to the HITRAN line. A similar procedure is followed for the temperature dependence of the halfwidth.

##### - O<sub>2</sub>

The calculations of the energies and positions benefited from newer, more accurate Hamiltonian formalisms and constants. However, halfwidths listed for microwave lines are from an out-of-date reference. For the weak electric quadrupole transitions, a newer value of the quadrupole moment led to intensities a factor of 5.8 weaker; no lines of that type survived the intensity cut-off for the 1996 version.

##### - O<sub>3</sub>

The updates in the millimeter-wave range concern the 667 and 676 isotopomers.

##### - Indices of refraction

The 1996 HITRAN version contains a compilation of the indices of refraction of various atmospheric particles.

## - Line mixing

Line mixing is not currently addressed in HITRAN. Several researchers are developing schemes for including line mixing, but this would require significant radiative transfer code alterations.

## - Collision Induced Absorption

These parameters are not yet included in HITRAN.

### 1.1.2 GEISA-97

Since 1974, the ARA (Atmospheric Radiation Analysis) group at LMD (Laboratoire de Météorologie Dynamique du CNRS, France) has developed and maintained the GEISA (Gestion et Etude des Informations Spectroscopiques Atmosphériques: Management and Study of Atmospheric Spectroscopic Information) computer accessible database system (Chédin *et al*, 1982; Husson *et al*, 1992, 1994). This early effort implemented the line-by-line and layer-by-layer approach for forward radiative transfer modeling. This activity is of interest to research groups involved in direct and inverse radiative transfer studies (Jacquinet-Husson *et al*, 1998).

The 1997 version (Jacquinet-Husson *et al*, 1998, 1999) of the GEISA database (hereafter referred to as GEISA-97) contains line parameters for 42 molecules (96 isotopic species) with 1,346,266 entries between 0 and 22,656 cm<sup>-1</sup>. It has molecules of interest for both terrestrial and other planetary atmospheres (for example, C<sub>2</sub>H<sub>4</sub>, GeH<sub>4</sub>, C<sub>3</sub>H<sub>8</sub>, C<sub>2</sub>N<sub>2</sub>, C<sub>4</sub>H<sub>2</sub>, HC<sub>3</sub>N, H<sub>2</sub>S, HCOOH and C<sub>3</sub>H<sub>4</sub>, for the Giant Planets). GEISA-97 has been developed in close cooperation with the contributors of three spectroscopic databases, ATMOS-95 (Atmospheric Trace Molecule Spectroscopy) (Brown *et al*, 1996), HITRAN-96 (HIgh resolution TRANsmission) (Rothman *et al*, 1998) and TDS (Tomsk Dijon Spectroscopic project; Traitement des Données Spectroscopiques)/STDS (Spherical Top Data System) (Tyuterev *et al*, 1994; Wenger and Champion, 1998).

In addition to the individual lines spectroscopic data catalog, GEISA-97 also has a catalog of infrared cross-sections at different temperatures and pressures for 23 species (such as chlorofluorocarbons) with complex spectra that are too dense for discrete parameterization.

The detailed summary of the line parameters in GEISA-97 is provided in Table 1. The items listed for each molecular species, given in column 1, are: the identification code (ID codes defined for the GEISA management software in Chédin *et al*, 1986), the number of lines, the intensity average, the mean halfwidth at half maximum, the identification codes of its various isotopes, and for each isotope: the number of lines, the transitions minimum and maximum wavenumbers (in cm<sup>-1</sup>), and the lines intensities minimum and maximum values (in cm molecule<sup>-1</sup>), in columns 2 to 11, respectively. The GEISA database format and the procedure for obtaining it are described in Section 4.2.

The contents of the GEISA-97 and HITRAN-96 databases are compared in Table 2 where the molecular species cataloged in the line parameters portion of GEISA-97 and HITRAN-96 are given. The molecular species formula are listed in column 1 and their identification codes for database management in column 2, where GEISA-97 is referred to as G and HITRAN-96 as H. For each molecular species, the numbers of bands, isotopes and lines, are given in columns 3, 4 and 5, respectively, for both databases. The minimum and maximum spectral ranges (cm<sup>-1</sup>) corresponding to the GEISA-97 transitions are in columns 6 and 7, respectively.

### 1.1.3 MASTER-SOPRANO

Two instruments, MASTER (Millimeter wave Acquisition for Stratosphere / Troposphere Exchanges Research) and SOPRANO (Submillimeter Observation of Processes in the Atmosphere Noteworthy for Ozone), are planned by ESA for a possible limb sounding mission for the time frame 2000+. Measurements will be carried out for different species in appropriate altitude ranges and with adequate vertical resolution. A list of species to be studied, with their target lines, has been defined by ESA; it is given in Tables 3 and 4, together with the spectral ranges of the detectors.

There is a lack of knowledge concerning the spectra covered by these instruments, mainly because of an inadequacy or insufficiency of existing databases. The purpose of the study (Bauer *et al*, 1997) was the elaboration of a new database concerning the main lines of the recommended species. A general survey of the main existing databases covering millimeter and submillimeter wavelengths was performed, allowing a critical analysis of their qualities.

The ATMOS (Brown *et al*, 1987) , SAO (Chance *et al*, 1994), GEISA (Husson *et al*, 1994) , JPL (Pickett *et al*, 1998) and HITRAN (Rothman *et al*, 1998) databases were first considered. An initial retrieval error analysis, based on the optimal estimation method (Rodgers, 1990), was performed at IFE-Bremen by S. Buehler and K. Künzi in order to identify the crucial parameters to be taken into account in the new database (Bauer *et al*. 1997). The parameters involved in the error analysis calculations were:

agam : air broadening parameter  
sgam : self broadening parameter  
n : temperature exponent of agam  
n-self : temperature exponent of sgam

The analysis resulted in a list of priorities for the various species in the frame of the MASTER and SOPRANO instruments. The air broadening coefficients were determined to be the most important parameters; temperature dependences of air broadening parameters could be significant in some cases.

After this first analysis, the format of the new database was determined (see Section 4.3). It would include the best parameters of the JPL, HITRAN, GEISA and SAO databases and the latest available data from the literature. For the lines which were determined as priorities (target or interfering lines) new linewidth measurements, described in Section 1.2, were carried out in two laboratories when the corresponding data were missing or inaccurate in the existing databases.

The new database for the MASTER and SOPRANO instruments was then generated at LPPM-Paris Orsay by A.Perrin, using the best available line parameters (line positions, line intensities and line widths), including the new measured values. Also many other molecules, such as COF<sub>2</sub>, H<sub>2</sub>O<sub>2</sub>, HO<sub>2</sub>, OCS, H<sub>2</sub>CO, SO<sub>2</sub> and NO<sub>2</sub> have been included, either for a possible influence of their interfering lines on the target lines, or for their own interest as detectable species in the atmosphere. The content of this database is summarized in Table 5; its format and access information are given in Section 4.3. With the additional species, the new database includes revised data for more than 1700 lines belonging to the MASTER-SOPRANO ranges, extended to  $\pm 0.1$  GHz of each band, except for the SOPRANO A1 band where the strong O<sub>3</sub> line at 498.7 GHz has been taken into account and was also measured at DLR.

## 1.2 Laboratory measurements

### 1.2.1 Linewidth measurements

The measurements in the frame of the MASTER and SOPRANO instruments were carried out at LSH-Lille by J.M.Colmont and G.Wlodarczak and at DLR-Munich-Oberpfaffenhofen by G.Wagner and M.Birk, using very different procedures, depending on the equipment of each laboratory (Bauer et al. 1997).

For all DLR measurements (CO, O<sub>3</sub>, BrO, ClO), a Bruker IFS 120 HR Fourier-Transform Spectrometer was used, with suitable equipment for the submm range. Two absorption cells were used: a short glass cell and a White-type multireflection cell, specially designed for FIR measurements. In both cooled cells, the average gas temperature was retrieved from relative CO line strengths.

A spectrometer using millimeter wave techniques was used at LSH, using klystrons or carcinotrons as sources. A cooled cell was used for N<sub>2</sub>O, CO and O<sub>3</sub>, a heated cell for both H<sub>2</sub><sup>16</sup>O and H<sub>2</sub><sup>18</sup>O measurements. Some species (O<sub>3</sub>, BrO and ClO) were created in the laboratories and specific set-ups were needed .

Three distinct differences appear when comparing DLR and LSH measurements:

- a) The pressures were significantly larger for DLR (LSH -500  $\mu$ bar, DLR 10-300 mb).
- b) Self broadening did not need to be taken into account in the LSH procedure.
- c) LSH made about 20 measurements at a wide range of broadening gas pressures at each temperature for N<sub>2</sub> and O<sub>2</sub>. DLR made mostly two measurements at each temperature for air since the time required for a single measurement is substantially larger in the case of the FTS. The DLR measurements cover a 60000 times larger frequency range, allowing use of information from other transitions, e.g. for determination of particle density and temperature and of dependence of pressure broadening on quantum numbers.

Line broadening parameters  $\gamma_{air}$  and their temperature dependence parameters n were determined by DLR and LSH for the following species : N<sub>2</sub>O , CO, O<sub>3</sub>, H<sub>2</sub><sup>16</sup>O, H<sub>2</sub><sup>18</sup>O, BrO, ClO. Cross check measurements by both laboratories were carried out for two lines (CO and O<sub>3</sub>); the agreement between the measurements allowed an assessment of the accuracy of the measurements. Table 6 summarizes the results obtained for the various lines.

### 1.2.2 Water vapor continuum measurements

Radiative transfer models require a description of what is now known as the continuum of water vapor; the continuum absorption in far wings of lines and atmospheric windows is defined as the difference between observed absorption and what can be described by conventional line profiles, such as Van Vleck-Weisskopf.

Most of the experimental data have been obtained from field experiments, very few from laboratory studies. After laboratory absorption measurements in the near wing of the 183 GHz line, the LSH-Lille carried out systematic studies in the window at 239 GHz, for pure water vapor and an atmospheric mixture of water vapor with nitrogen. A continuum effect could be confirmed and its parameters quantitatively defined: absorption higher than that predicted by conventional lineshape models, stronger negative temperature dependence, non-negligible quadratic term in partial H<sub>2</sub>O pressure, and frequency dependence.

Among the possible explanations of this continuum, the inadequacy of impact lineshapes far from the center of lines gave rise to far wing theory, more easily derived in the IR range. The Ma and Tipping model (1990) is in good agreement with the LSH experiments in some cases (Bauer *et al.*, 1995).

Other explanations for the continuum have been proposed and are periodically put forward, such as a possible spectral contribution of dimers, aerosol clusters, weakly bound complexes, or collision induced absorption phenomena.

To get more insight into possible mechanisms, which could lead to a model able to reproduce all the dependences, LSH carried out further experiments at 239 GHz with other mixing partners: CO<sub>2</sub> (Bauer *et al.*, 1996), Ar (Bauer *et al.*, 1998), C<sub>2</sub>H<sub>4</sub>. Absorption by all these H<sub>2</sub>O-X mixtures presents a continuum effect, of various intensity. Other mixing gases are planned. A multipolar dependence, or the role of collision induced absorption may be involved. An explanation of the temperature dependence in the Lille experiments through weakly bound complexes has been proposed (Vigasin, 1998).

### 1.3 Water vapor continuum modeling

References will be made to versions of H.J. Liebe's Millimeter-wave Propagation Model (MPM). To help clarify the discussion, Table 7 lists the publication dates of major changes in MPM, which underwent numerous revisions during the years that Liebe was active.

A comparison and analysis of published measurements on water vapor (Rosenkranz, 1998a) has drawn the conclusion that the laboratory data are best represented by a combination of the foreign-broadened continuum component from MPM87 with the self-broadened component of the water continuum from MPM93. This conclusion is based on the model of binary interactions, by requiring the self-broadened component to be consistent between pure water vapor and mixtures of H<sub>2</sub>O with N<sub>2</sub>.

For the future, it will be desirable to go beyond the MPM formulation, with a continuum model that applies to both microwave and infrared spectral ranges. There are two reasons: First, applications are being extended into the submillimeter wavelengths. Second, if the microwave and infrared continua are the result of the same process (e.g. molecular collisions) then greater confidence can be placed in a model if it satisfactorily represents the entire frequency range of the modeled phenomenon. For example, there is a similarity between the center of the v<sub>2</sub> vibrational band of water vapor and the microwave part of the spectrum, which is the center of the pure rotational band when frequencies are understood in the sense of a two-sided Fourier transform (-∞ to +∞). The model described by Clough *et al* (1989) would fit these requirements, except that versions of the model up to 2.2 have been based on infrared measurements that now appear to include some erroneous data. Recent measurements of the v<sub>2</sub> band by Tobin *et al* (1996) have yielded new values near the band center, and an improved model is under development (Mlawer *et al.*, 1998).

### 1.4 Atmospheric transmittance measurements

Cruz-Pol *et al* (1998) measured downwelling brightness temperatures at nine frequencies between 20 and 32 GHz at two sites in California and Florida. They fitted a model to this data and derived values for four parameters related to the intensity and width of the 22-GHz line, the water continuum, and oxygen absorption. The same adjustments were applied to both self-broadening and foreign-broadening. Relative to MPM92, the best fit was obtained with a 6% increase in line intensity, 7% increase in line width, 4% increase in the water continuum, and 7% increase in oxygen. The latter two increases in parameter values were not statistically

significant, however. Since the atmospheric state was determined from radiosondes, these values are dependent on the accuracy of those soundings.

The higher line width found by Cruz-Pol *et al* (1998) may be within the uncertainty of laboratory determinations (see the discussion in Section 2.1), although their application of the same adjustment factor to both self- and foreign-broadened widths, which are very different for water vapor, raises questions of method. Their 6% increase in line intensity at 22 GHz is definitely inconsistent with calculations based on laboratory measurements of water's dipole moment. These calculations differ by at most  $\sim 1\%$  in different databases (HITRAN, JPL, GEISA). On the other hand, the measurement of humidity in the atmosphere to an accuracy of a few percent is a very difficult task; for example, see Revercomb *et al* (1998) and Lesht (1998). Hence there is a strong possibility that the discrepancy in intensity observed by Cruz-Pol *et al* is attributable to the *in situ* comparison measurements.

Serabyn *et al* (1998) have observed atmospheric emission spectra between 330 GHz and 1 THz with a Fourier-transform spectrometer on Mauna Kea, Hawaii (elevation 4.1 km). To date, only a preliminary analysis of the data has been published; it showed the presence of continuum absorption and somewhat lower residuals between measurements and calculations using a Van Vleck-Weisskopf line shape than using a kinetic line shape.

A new radiometer with eight channels in the 50-56 GHz band and eight channels in the  $118.75 \pm 4$  GHz band was operated on the NASA ER-2 by M.I.T. personnel in 1998. The instrument observes the atmosphere both below the aircraft and at zenith, through a pipe. Data from takeoffs and landings will be used to test atmospheric transmittance models.

### 1.5 Rapid transmittance algorithms

A rapid transmittance algorithm approximates the result of a line-by-line summation, but with significantly less computation. This is achieved by means of coefficients that are pre-computed, usually only for a specific instrument with defined channels and viewing geometry. Hence the two characteristics on which to evaluate this type of algorithm are accuracy with respect to the line-by-line model used, and speed. It appears that errors in approximation of transmittance are generally less than  $10^{-2}$ , and sometimes much less, which is small compared to the uncertainties in the line-by-line models. This is a desirable state of affairs, but it also means that the true accuracy of a transmittance calculation is limited by the line-by-line model. One might therefore expect computational speed to acquire relative importance, yet papers often do not attempt to quantify this characteristic of the rapid algorithms.

In addition to the references in McMillin (1997), three more recent papers have appeared on rapid algorithms for microwave instruments. The algorithm of Rosenkranz (1998b) computes opacity from fixed gases, water vapor, and cloud liquid water separately. Magnetic field perturbations to oxygen-line channels are included. Feist and Kämpfer (1998) developed a millimeter and submillimeter propagation model based on a merger of the JPL and HITRAN line databases with MPM93. It incorporates an automatic frequency selection algorithm to speed up computation. Saunders *et al* (1999) describe a combined infrared/microwave transmittance model which considers fixed gases, water vapor, and ozone.

## 2 Recommended models: Accuracy and state of validation

In the stratosphere, microwave lines of many molecular species are observable. The lines are narrow in comparison to their center frequencies. A Lorentz lineshape usually suffices unless

Doppler broadening is significant, which can be reliably calculated; then a Voigt lineshape may be appropriate. The Lorentz shape is a simple expression, and for the Voigt, accurate series expansions are available. Modeling of absorption is then largely concerned with values for line frequency, intensity, width and possibly shift, as discussed in Section 1. However, particular effects such as Zeeman splitting also need to be considered for a few gases.

At tropospheric pressures, lines from the minor constituents of the atmosphere are both broad and weak, consequently very difficult to detect against the background of the more abundant gases H<sub>2</sub>O, O<sub>2</sub>, and N<sub>2</sub>. Modeling of absorption by these three gases involves, in addition to the above-mentioned line parameters for H<sub>2</sub>O and O<sub>2</sub>, consideration of the water vapor continuum, oxygen line mixing, and collision-induced absorption by nitrogen. Models for these effects are evaluated below.

## 2.1 Absorption by water vapor

The development of absorption models is a continuing process, but at the time of writing, the water vapor model described by Rosenkranz (1998a) is recommended. However, for some specific applications it might be necessary to supplement it with lines in addition to the 16 which it includes. The laboratory data discussed there extend from 40 GHz to 239 GHz. Liebe (1987) discusses some atmospheric measurements at 430 GHz. In Rosenkranz (1998a), a comparison of calculations based on radiosondes, using the combined continuum model, with ground-based measurements of atmospheric microwave emission at 90 GHz showed reasonable agreement for precipitable water vapor up to 3 cm. Any error on the order of 5% or more would be noticeable with these data. (The radiosondes themselves may not be more accurate than this.) However, in the case of one tropical atmosphere with 4.5 cm of precipitable water vapor, measurements made from an aircraft were higher than the aforesaid model by the equivalent of ~10% in opacity at both 89 and 157 GHz. Although the laboratory measurements covered the range of water vapor densities found in tropical atmospheres, they show no evidence for any departure from the quadratic dependence of absorption on water density which is characteristic of binary interactions. Thus there appears to be an unresolved disagreement between the pictures presented by the laboratory and this one atmospheric profile. More tropical measurements would be useful to examine this problem.

Gamache *et al* (1994) surveyed and compared ~4000 published infrared and microwave measurements of water vapor line widths, broadened by various perturbing gases. They concluded that experimentalists frequently underestimate uncertainties in measurements, sometimes ignoring the possibility of systematic errors. They estimate that as a general rule, most H<sub>2</sub>O line widths are uncertain by 10-15% (2 standard deviations) for broadening by dry air components and 20-25% for self-broadening. Although this rather pessimistic conclusion may be justified as a general rule, they also identified lines, among them those at 22 and 380 GHz, for which the uncertainties were evaluated as less than 5%. Unfortunately the 183 GHz line is one for which there exists a wide deviation of experimental widths (see Figure 2 in Gamache *et al*, 1994). The value recommended here, from Bauer *et al* (1989), lies near the center of the range of measurements.

Although the water vapor line absorption and the continuum are generally treated separately in models, the derivation of the continuum is linked to a line absorption model. The continuum is really an empirical correction added to the line model to obtain agreement with some particular set of measurements. As a consequence of this re-fitting to data involved in derivation of the continuum, errors in the resulting model at window frequencies, where the continuum is dominant, result from the data used and the fitting procedure rather than from the line absorption model.

Uncertainties in line and continuum parameters affect calculated brightness temperatures in various ways, depending on frequency, atmospheric state, and conditions of observations. For example, an increase in a water line width by x percent will reduce its opacity at line center by x percent but increase the line's opacity in its far wings by x percent. The latter opacity may be smaller than the continuum contribution, however. Although the greatest sensitivity of upwelling brightness temperature to H<sub>2</sub>O opacity occurs in the semi-transparent parts of the spectrum and over an ocean surface, it is also true that for the water vapor sounding application, an error in opacity per unit of water translates into an equivalent and opposite error in inferred water vapor at the corresponding sounding altitude.

## 2.2 Absorption by oxygen

The most extensive set of measurements on the 50 to 70 GHz oxygen band at atmospheric pressures is that reported by Liebe *et al* (1992); any recommended model should be consistent with those measurements. There are therefore two possible choices among published line width and mixing parameters for O<sub>2</sub>: MPM92 (Liebe *et al*, 1992), or MPM93 (Liebe *et al*, 1993). The difference between them is that only the mixing coefficients in MPM92 were derived from the 1992 measurements; the widths were from earlier work by Liebe and co-workers using a different spectrometer which (unlike the later instrument) was designed for measurement of line widths, using low pressures at which the lines are resolved. In MPM93 the widths of all of the lines between 50 and 70 GHz were increased by 5% and their mixing coefficients were increased by 15%. (These two adjustments act in opposite directions on absorption at the higher pressures.) The result is a slightly better fit to the 1992 measurements. Unfortunately, an undesirable effect was also introduced, which is that O<sub>2</sub> absorption computed with the 1993 parameters becomes negative for some frequencies greater than 170 GHz (P. Rayer, private communication, 1995). Also, the 5% increase in widths is larger than the uncertainties reported by Liebe for his original width measurements. For these reasons, we recommend the line parameters in Liebe *et al* (1992).

Since the line mixing parameters in MPM92 are determined by adjustment to laboratory measurements, in general it provides an excellent fit to those measurements, which were estimated to have an accuracy of  $\pm 2\%$  rms for the higher rates of absorption. Systematic departures of the model from the measurements (by as much as 20% at 50 GHz) are visible in Figures 5 and 6 of Liebe *et al* (1992), but only at the highest pressure (1013 hPa) and lowest temperature (6C), consequently the highest density, measured. With the data in Liebe *et al* (1992) it was not possible to address the question of how well the model would extrapolate to temperatures lower than 6C and frequencies outside of 50-70 GHz. Ground-based measurements of sky brightness temperature at 31 and 90 GHz show a fairly constant bias which could be removed if MPM92 predicted ~20% more absorption by O<sub>2</sub> at those frequencies (e.g., see Rosenkranz, 1998a); however, this bias is opposite in sign to the apparent error at 50 GHz noted above. Measurements from an aircraft of downward-propagating brightness temperatures by Schwartz (1997) were consistent with MPM92 in the frequency range 52 to 55 GHz. Although these measurements were not precise enough to decide between MPM92 and MPM93, the result can be interpreted as validation of the temperature dependence within that band. Schwartz's measurements near 118 GHz, however, were best reproduced by increasing the width of that line in the middle and upper troposphere, which could be done by increasing its temperature dependence from T<sup>-0.8</sup> to T<sup>-0.97</sup> at constant pressure.

Width parameters of oxygen's 118-GHz and 425-GHz lines in MPM92 were based on the laboratory measurements by Setzer and Pickett (1977) and Pickett *et al* (1981). The temperature dependence of line width at 425 GHz is rather anomalous: T<sup>-0.2</sup> at constant pressure.

Further laboratory measurements on the submillimeter lines would be advisable prior to their use for remote sounding.

### 2.3 Collision-induced absorption by nitrogen

Models for the collision-induced absorption spectrum of N<sub>2</sub> have been created by Borysow and Frommhold (1986), Poll and Hunt (1981), and others. The model of Borysow and Frommhold, which is used in FASCODE, seems to be the most theoretically grounded and complete in range of temperature (50 to 300K) and frequency (0 to 10 THz). However, for frequencies  $\nu < 300$  GHz, an asymptotic expression of the form

$$C P^2 \nu^2 (300/T)^x$$

can also be used to compute absorption, where P is the total pressure of the dry-air components, and T is temperature in Kelvin. Values of the constants C and x obtained from data in various sources are compared below:

C (neper/km)(hPaGHz) <sup>-2</sup>	x	Reference
$6.5 \cdot 10^{-14}$	3.6	Borysow and Frommhold (1986)
$6.4 \cdot 10^{-14}$	3.55	Dagg <i>et al</i> (1975)
$1 \cdot 10^{-13}$	?	Occelli <i>et al</i> (1991)

## 3 Recommendations for future development of models

- 1) The frequency and temperature ranges of absorption models should be extended.
- 2) Further testing of models in varied atmospheric conditions, including tropical humidity regimes, is desirable. Satellite measurements may be helpful to validate spectroscopic parameters at 183 GHz. However, for all measurements in the atmosphere, it is essential to place emphasis on obtaining accurate *in-situ* data for comparison. Especially in the case of water vapor, this is a problem of non-negligible difficulty.
- 3) Line widths and temperature dependences in the submillimeter spectrum of oxygen (e.g. 425 GHz) need to be re-measured to provide a firm basis for atmospheric sounding. For the MASTER and SOPRANO bands, the following further line measurements are recommended:

MASTER	B	O <sub>3</sub> at 301813 MHz, N <sub>2</sub> O at 301442 MHz
	C	H <sub>2</sub> O at 321225 MHz
	D	HNO <sub>3</sub>
SOPRANO	A1	N <sub>2</sub> O, O <sub>3</sub>
	A2	CH <sub>3</sub> Cl, H <sub>2</sub> O
	B1	O <sub>3</sub>
	B2	HOCl, O <sub>3</sub>
	C	CH <sub>3</sub> Cl
	D	requirements need to be studied
	E	O <sub>3</sub> , NO
	F1	O <sub>3</sub> , NO
	F2	requirements need to be studied

- 4) Theoretical work should investigate the temperature and frequency dependence of the water-vapor continuum, both for pure vapor and for mixtures with various non-dipolar gases having a range of quadrupole moments.
- 5) Development of line pressure-broadening theory should be continued, with the goal of deriving all parameters in a spectroscopic database from theoretical calculations, with laboratory measurements of selected lines used for validation. The pressure-broadened parameters of greatest utility for atmospheric applications are: (i) halfwidths and shifts for dry air as a perturber (i.e., weighted sum of N<sub>2</sub> and O<sub>2</sub>); (ii) halfwidths and shifts for H<sub>2</sub>O as a perturber; (iii) line-mixing coefficients for the 50-70 GHz O<sub>2</sub> band, for both dry air and H<sub>2</sub>O as perturbers. Self-broadened halfwidths are unnecessary (for gases other than H<sub>2</sub>O).

## **4 Availability of databases and models**

### **4.1 HITRAN database**

Periodic archival database releases will be continued on a CD-ROM, up to now at 4-5 year intervals. But new validated data will be released via the web site of HITRAN as they become available. Information and addresses can be obtained from :

<http://www.HITRAN.com>

This website also provides a way of getting information from other databases linked to HITRAN.

### **4.2 GEISA database**

The current GEISA-97 database, and the former version GEISA-92 as well, are available, with their associated management software, freely from the ARA/LMD group workstations (IBM RISC 6000 or SUN) Web site:

<http://wwwара.polytechnique.fr>

<http://ara01.polytechnique.fr/registration>

It is possible to extract part of the database on line using the GEISA associated management software facilities, as described in Husson *et al* (1992) and Chédin *et al* (1986).

Added to this facility, the GEISA-97 file as a whole, with related description and general information files, are available from the following anonymous ftp site:

ara01.polytechnique.fr, subdirectories: pub/libgeisa

More complementary information and assistance will be provided upon request at the following e-mail address: [husson@ara01.polytechnique.fr](mailto:husson@ara01.polytechnique.fr).

The format fields for each transition are the same as in the previous editions and the fields are shown and defined in Table 8. The A-J fields are those used in the GEISA management associated software (Husson *et al*, 1992, 1994). A blank field corresponds to missing information.

### **4.3 MASTER-SOPRANO database**

This database is available through Internet access from LPPM (Paris-Orsay).

machine: 193.55.16.151

user: anonymous

password: any

```
cd pub  
cd ESA
```

Two subfiles are available: DATA (ASCII), DOCUMENT (binary)

The format of the MASTER-SOPRANO database is as follows:

---

MO (I2)	= molecule number
ISO (I1)	= isotope number (1 = most abundant, 2 = second, etc...)
* F (F13.4)	= frequency of transition in MHz
# ERRF(F8.4)	= estimated error in F in MHz
S (E10.3)	= intensity in $\text{cm}^{-1}/(\text{molecule.cm}^{-2})$ at 296 K
* AGAM (F5.2)	= air-broadened halfwidth (HWHM) in MHz/Torr at Tref
* SGAM (F5.2)	= self-broadened halfwidth (HWHM) in MHz/Torr at Tref
E (F10.4)	= lower state energy in wavenumbers ( $\text{cm}^{-1}$ )
N (F4.2)	= coefficient of temperature dependence of air-broadened halfwidth
# N_self (F4.2)	= coefficient of temperature dependence of self-broadened halfwidth
# Tref (F7.2)	= reference temperature for AGAM and SGAM
D (F8.6)	= shift of transition due to pressure (MHz/Torr)
V1 (I3)	= upper state global quanta index
V2 (I3)	= lower state global quanta index
Q1 (A9)	= upper state local quanta
Q2 (A9)	= lower state local quanta
IERS (I1)	= accuracy index for S
IERH (I1)	= accuracy index for AGAM
# IERN (I1)	= accuracy index for N

---

#### Comments

1. Format strings in brackets (e.g., '(I2)') are according to FORTRAN syntax.
2. Rows marked with an asterisk (\*) have different format or units from similar rows in HITRAN.
3. Rows marked with a (#) are not included in HITRAN.
4. The accuracy indices are defined as follows:

Index	0	1	2	3	4	5	6	7	8	9
Accuracy	200%	100%	50%	30%	20%	10%	5%	2%	1%	0.5%

A program written in FORTRAN accesses the line lists of all molecules and gives the list of lines by increasing frequency.

#### 4.4 JPL line database

The Jet Propulsion Laboratory's Submillimeter, Millimeter, and Microwave Spectral Line Catalogue (Pickett *et al*, 1998) is available at : <http://spec.jpl.nasa.gov>

#### 4.5 SAO line database

The line database of the Smithsonian Astrophysical Observatory is available at:

<http://firs-www.harvard.edu/www/sao92.html>

## 4.6 MIT transmittance models

Fortran routines are available by anonymous ftp at: mesa.mit.edu  
in the directories

phil/lbl\_rt (line-by-line absorption)

and phil/rapid\_rt (rapid transmittance).

The files readme.lbl and readme.rapid describe the contents of these directories.

## References

- Bauer, A., M. Godon, M. Kheddar, and J. M. Hartmann, Temperature and Perturber Dependences of Water Vapor Line-Broadening. Experiments at 183 GHz; Calculations Below 1000 GHz, *J. Quant. Spectrosc. Radiat. Transfer*, 41, pp. 49-54 (1989).
- Bauer, A., M.Godon, J.Carlier and Q.Ma, Water Vapor Absorption in the Atmospheric Window at 239 GHz, *J.Quant. Spectrosc. Radiat.Transfer*, 53, 411- 423 (1995).
- Bauer, A., M.Godon, J.Carlier and R.R.Gamache, Absorption of a H<sub>2</sub>O-CO<sub>2</sub> Mixture in the Atmospheric window at 239 GHz; H<sub>2</sub>O-CO<sub>2</sub> Linewidths and Continuum *J.Mol.Spectrosc.*,176, 45-57 (1996).
- Bauer, A., M.Birk, G.Wagner, J.M.Colmont, D.Priem, G.Wlodarczak, S.Buehler, A.von Engeln, K.Künzi, and A.Perrin, Study on a Spectroscopic database for millimeter and submillimeter wavelengths. ESA contract No 11581/95/NL/CN (1997).
- Bauer, A., M.Godon, J.Carlier and R.R.Gamache, Continuum in the Windows of the Water Vapor Spectrum Absorption of H<sub>2</sub>O-Ar at 239 GHz and linewidths calculations, *J.Quant. Spectrosc. Radiat.Transfer*, 59, 273-285 (1998).
- Borysow, A. and L. Frommhold, Collision-induced Rototranslational Absorption Spectra of N<sub>2</sub>-N<sub>2</sub> Pairs for Temperatures from 50 to 300 K, *Astrophys. J.*, 311, pp. 1043-1057 (1986).
- Brown, L. R., Gunson, M. R., Toth, R. A., Irion, F. W., Rinsland, C. P. and Goldman, A., Atmospheric trace molecule spectroscopy (ATMOS) linelist, *Applied Optics*, 35, 2828-2848 (1996).
- Brown, L.R., C.B. Farmer, and C.P. Rinsland R.A. Toth. *Applied Optics*, 26, 5154-5182 (1987).
- Chance, K., K.W.Jucks, D.G.Johnson, and W.A.Traub, *J. Quant. Spectrosc. Radiat. Transfer*, 52, 447-457 (1994).
- Chédin, A., Husson, N. and Scott, N. A., Une banque de données pour l'étude des phénomènes de transfert radiatif dans les atmosphères planétaires: la banque GEISA, *Bulletin d'Information du Centre de Données Stellaires (France)*, 22, 121-121 (1982).
- Chédin, A., Husson, N., Scott, N. A., Cohen-Hallaleh, I. and Berroir, A., The GEISA data bank 1984 version. Internal Note LMD, n° 127, February 1985, reviewed october 1986.
- Clough, S. A., F. X. Kneizys, and R. W. Davies, Line Shape and the Water Vapor Continuum, *Atmospheric Research*, 23, pp. 229-241 (1989).
- Cruz-Pol, S. L., C. S. Ruf, and S. J. Keihm, Improved 20- to 32-GHz atmospheric absorption model, *Radio Science*, 33, pp. 1319-1333 (1998).
- Dagg, I. R., G. E. Reesor, and J. L. Urbaniak, Collision Induced Absorption in N<sub>2</sub>, CO<sub>2</sub>, and H<sub>2</sub> at 2.3.cm<sup>-1</sup>, *Can. J. Phys.*, 53, pp. 1764-1776 (1975).
- Feist, D. G. and N. Kämpfer, BEAM: a fast versatile model for atmospheric absorption coefficients from 0-1000 GHz, in *Microwave Remote Sensing of the Atmosphere and Environment* (T. Hayasaka, D. L. Wu, Y.-Q. Jin and J. Jiang, ed.), Proceedings of SPIE, 3503, pp. 301-312, Beijing, China (1998).
- Gamache, R. R., J. M.Hartmann and L. Rosenmann, Collisional broadening of water vapor lines. I- A survey of experimental results, *J. Quant. Spectrosc. Radiat. Transfer*, 52, pp. 481-499 (1994).
- Husson, N., Bonnet, B., Scott, N.A. and Chédin, A., Management and study of spectroscopic informa-

- tion: the GEISA program. *J. Quant. Spectrosc. Radiative Transfer*, **48**, 509-518 (1992).
- Husson, N., Bonnet, B., Chédin, A., Scott, N. A., Chursin, A. A., Golovko, V. F. and Tyuterev, Vl. G., The GEISA data bank in 1993. A PC/AT compatible computers' new version. *J. Quantit. Spectrosc. Radiative Transfer*, **52**, 425-438 (1994).
- Jacquinet-Husson, N., Scott, N. A., Chédin, A., Bonnet, B., Barbe, A., Tyuterev, Vl. G., Champion, J. P., Winnewisser, M., Brown, L. R., Gamache, R., Golovko, V. F. and Chursin, A., The GEISA system in 1996: Toward an operational tool for the second generation vertical sounders radiance simulation. *J. Quant. Spectros. Radiative Transfer*, **59**, 511-527 (1998).
- Jacquinet-Husson, N., Arié, E., Ballard, J., Barbe, A., Bjoraker, G., Bonnet, B., Brown, L.R., Camy-Peyret, C., Champion, J.P., Chédin, Chursin, A.A., Clerbaux, C., Duxbury, G., Flaud, J.M., Fourrié, N., Fayt, A., Graner, G., Gamache, R., Goldman, A., Golovko, VI., Guelachvilli, G., Hartmann, J.M., Hilico, J.C., Hillman, J., Lefèvre, G., Lellouch, E., Mikhaïlenko, S.N., Naumenko, O.V., Nemtchinov, V., Newnham, D.A., Nikitin, A., Orphal, J., Perrin, A., Reuter, D.C., Rinsland, C.P., Rosenmann, L., Rothman, L.S., Scott, N.A., Selby, J., Sinitsa, L.N., Sirota, J.M., Smith, A.M., Smith, K.M., Tyuterev, Vl.G., Tipping, R.H., Urban, S., Varanasi, P., Weber, M., The 1997 spectroscopic GEISA databank. *J. Quant. Spectros. Radiative Transfer*, **62**, pp. 205-254 (1999).
- Lesht, B. M., Uncertainty in radiosonde measurements of temperature and relative humidity estimated from dual-sonde soundings made during the September 1996 ARM Water Vapor IOP. Proceedings of the 10th Symposium on Meteorological Observations and Instrumentation, pp. 80-83, Am. Meteorol. Soc, Phoenix, Arizona, January 11-16, 1998.
- Liebe, H. J., A Contribution to Modeling Atmospheric Millimeter-wave Properties, *Frequenz*, **41**, pp. 31-36 (1987)
- Liebe, H.J., P.W. Rosenkranz, and G.A. Hufford, Atmospheric 60-GHz Oxygen Spectrum: New Laboratory Measurements and Line Parameters, *J. Quant. Spectrosc. Radiat. Transfer*, **48(5/6)**, pp. 629-643 (1992).
- Liebe, H.J., G.A. Hufford, and M.G. Cotton, Propagation Modeling of Moist Air and Suspended Water/Ice Particles at Frequencies Below 1000 GHz. AGARD Conference Proc. 542, Atmospheric Propagation Effects through Natural and Man-Made Obscurants for Visible to MM-Wave Radiation, pp.3.1-3.10 (1993).
- Ma, Q., and R.H.Tipping, Water Vapor Continuum in the Millimeter Spectral Region, *J.Chem.Phys.***93**, 6127-6139 (1990).
- McMillin, L. M., Fast parametric models for the clear atmosphere, in *Development of Radiative Transfer Models* (C. Mätzler, ed.), pp. 23-25, October 1997.
- Mlawer, E. J., S. A. Clough, P. D. Brown, and D. C. Tobin, Collision-Induced Effects and the Water Vapor Continuum, Proc. 8th Atmos. Radiation Meas. (ARM) Sci. Team Meeting, Tucson, Arizona, March 23-27, [http://www.arm.gov/docs/documents/technical/conf\\_9803](http://www.arm.gov/docs/documents/technical/conf_9803) (1998).
- Occelli, R., H. Chaaban, J. M. Moynault, R. Coulon, and A. Balsamo, Submillimetric and Millimetric Collision-Induced Absorption Spectra in Compressed Gaseous Nitrogen Using Very Low-Frequency Optical Source, *Can. J. Phys.*, **69**, pp. 1264-1272 (1991).
- Pickett, H. M., E. A. Cohen and D. E. Brinza, Pressure Broadening of Oxygen and its Implications for Cosmic Background Measurements, *Astrophys. J.*, **248**, pp. L49-L51 (1981).
- Pickett, H. M., R. L. Poynter, E. A. Cohen, M. L. Delitsky, J.C. Pearson and H. S. P. Müller, Submillimeter, Millimeter, and Microwave Spectral Line Catalogue, *J. Quant. Spectros. Radiative Transfer*, **60**, 883-890 (1998).
- Poll, J. D., and J. L. Hunt, Analysis of the Far Infrared Spectrum of Gaseous N<sub>2</sub>, *Can. J. Phys.*, **59**, pp. 1448-1458 (1981).
- Revercomb, H. E., W. F. Feltz, R. O. Knuteson, D. C. Tobin, P. F. W. van Delst, and B. A. Whitney, Accomplishments of the Water Vapor IOPs: An Overview. Proceedings of the Eighth Atmospheric Radiation Measurement (ARM) Science Team Meeting, Tucson, Arizona, March 23-27, 1998. ([http://www.arm.gov/docs/documents/technical/conf\\_9803](http://www.arm.gov/docs/documents/technical/conf_9803))
- Rodgers, C.D., Characterization and error analysis of profiles retrieved from remote sounding measurements, *J.Geophys.Res.* **95 D**, pp. 5587-5595 (1990).
- Rosenkranz, P. W., and A. Bauer, Spectroscopic Databases and Transmittance Models for the Clear

- Atmosphere, in *Development of Radiative Transfer Models* (C. Mätzler, ed.), pp. 13-22, October 1997.
- Rosenkranz, P. W., Water vapor microwave continuum absorption: A comparison of measurements and models, *Radio Science*, **33**, pp. 919-928 (1998a). Correction, *Radio Science*, **34**, p. 1025 (1999).
- Rosenkranz, P. W., Improved rapid transmittance algorithm for microwave sounding channels, *1998 IEEE International Geoscience and Remote Sensing Symposium Proceedings*, pp.728-30 (1998b).
- Rothman, L. S., Rinsland, C. P., Goldman, A., Massie, S. T., Flaud, J.-M., Perrin, A., Dana, V., Mandin, J.-Y., Schroeder, J., Mc Cann, A., Gamache, R. R., Wattson, R. B., Yoshino, K., Chance, K., Jucks, K., Brown, L. R. and Varanasi, P., The HITRAN molecular spectroscopic database and HAWKS (HITRAN Atmospheric Workstation): 1996 edition. *J. Quant. Spectrosc. Radiative Transfer*, **60**, 665-710 (1998).
- Saunders, R., M. Matricardi, and P. Brunel, An Improved Fast Radiative Transfer Model for Assimilation of Satellite Radiance Observations, *Q. J. Roy. Meteor. Soc.* **125**, pp. 1407-1426 (1999).
- Schwartz, M. J., Observations and Modeling of Atmospheric Oxygen Millimeter-wave Transmittance. Ph.D. Thesis, Mass. Inst. of Tech. Dept. of Physics, Cambridge, MA (1997).
- Serabyn, E., E. W. Weisstein, D. C. Lis, and J. R. Pardo, Submillimeter Fourier-transform spectrometer measurements of atmospheric opacity above Mauna Kea, *Applied Optics*, **37**, pp. 2185-2198 (1998).
- Setzer, B. J. and H. M. Pickett, Pressure broadening measurements of the 118.750 GHz oxygen transition, *J. Chem. Phys.*, **67**, pp. 340-343 (1977).
- Tobin, D. C., L. L. Strow, W. J. Lafferty, and W. B. Olson, Experimental investigation of the self- and N<sub>2</sub>-broadened continuum within the v<sub>2</sub> band of water vapor, *Applied Optics*, **35**, pp. 4724-4734 (1996).
- Tyuterev, Vl.G., Babikov, Yu.L., Tashkun, S.A., Perevalov, V.I., Nikitin, A., Champion, J.P., Hilico, J.C., Loete, M., Pierre, C.L., Pierre, G. and Wenger, Ch., T.D.S. spectroscopic databank for spherical tops. *J. Quant. Spectrosc. Radiative Transfer*, **52**, 459-480 (1994).
- Vigasin, A.A., Temperature Effect on the Water Vapor Continua Absorption in Various Gas Phase Mixtures. International Conference on Water in the Gas Phase, Paris, June 1998.
- Wenger, C. and Champion, J.P., S.T.D.S. Spherical Top Data System. A software for the simulation of spherical top spectra. *J. Quant. Spectrosc. Radiative Transfer* **59**, 471-480 (1998).

Table 1: Content of GEISA-97 line catalog.

Mol.	ID	# Lines	Intensity average	Alpha average	Iso. ID	# Lines	F-Min (cm <sup>-1</sup> )	F-Max (cm <sup>-1</sup> )	Int-Min (cm molec <sup>-1</sup> )	Int-Max (cm molec <sup>-1</sup> )
H <sub>2</sub> O	1	50217	1.450E-21	0.069	161	30117	0.401	22656.465	1.010E-32	2.670E-18
					162	9799	0.007	5507.548	1.240E-32	2.700E-22
					171	3744	6.471	11150.790	1.490E-27	9.830E-22
					181	6357	6.785	13900.421	1.000E-27	5.390E-21
					182	200	1231.680	1607.611	1.000E-26	7.940E-26
CO <sub>2</sub>	2	62816	1.793E-21	0.071	626	27896	442.006	9648.007	0.000E+00 (\$)	3.520E-18
					636	9154	497.201	8104.666	0.000E+00 (\$)	3.570E-20
					628	13554	507.860	8132.007	1.390E-36	6.850E-21
					627	6625	554.909	6961.226	1.000E-27	1.280E-21
					638	2312	567.596	4946.384	3.700E-27	7.230E-23
					637	1584	584.754	3641.072	3.710E-27	1.360E-23
					828	1107	615.974	3669.609	1.760E-40	1.310E-23
					728	288	626.438	2358.226	3.870E-27	2.500E-24
					838	296	2115.685	2276.481	4.870E-42	1.760E-25
O <sub>3</sub>	3	281607	6.533E-23	0.069	666	167755	0.026	4060.783	4.060E-29	4.200E-20
					668	19147	0.921	1177.493	4.880E-28	7.760E-23
					686	7513	1.177	1145.690	7.500E-28	7.560E-23
					667	58254	0.289	820.380	5.340E-31	5.570E-25
					676	28938	0.213	822.795	1.490E-31	6.060E-25
N <sub>2</sub> O	4	26771	2.688E-21	0.075	446	19423	0.838	5131.249	4.000E-27	1.000E-18
					447	1004	542.242	3482.917	3.430E-26	4.150E-22
					448	2034	545.179	3463.967	1.230E-25	2.050E-21
					456	2128	5.028	3462.689	5.220E-26	3.670E-21
					546	2182	4.858	3473.528	4.720E-26	3.600E-21
CO	5	13515	7.545E-22	0.047	26	5908	3.530	8464.883	7.880E-78	4.460E-19
					27	748	3.714	6338.061	8.190E-40	1.600E-22
					28	770	3.629	6266.578	7.610E-39	8.320E-22
					36	4768	3.414	8180.219	3.610E-73	4.680E-21
					38	741	3.462	6123.294	2.580E-40	8.700E-24
					37	580	1807.871	6196.551	1.030E-36	1.680E-24
<u>CH<sub>4</sub></u>	6	66883	2.622E-22	0.052	211	56989	0.010	6184.492	4.060E-34	2.062E-19
					311	9894	0.032	6069.086	4.100E-34	2.329E-21
O <sub>2</sub>	7	6292	4.117E-26	0.044	66	1435	0.000	15927.806	0.000E+00 (\$)	8.833E-24
					67	4186	0.000	14536.515	1.147E-47	5.337E-26
					68	671	1.572	15851.213	1.186E-35	1.710E-26
NO	8	94738	4.989E-23	0.053	46	93360	0.000	9273.214	1.401E-85	6.211E-20
					48	679	1601.909	2038.846	4.190E-28	1.390E-22
					56	699	1609.585	2060.462	4.430E-28	2.550E-22
SO <sub>2</sub>	9	38853	1.065E-21	0.114	626	38566	0.017	4092.948	1.020E-28	6.090E-20
					646	287	2463.470	2496.088	9.740E-24	3.430E-23
NO <sub>2</sub>	10	100680	6.194E-22	0.067	646	100680	0.498	2938.381	4.240E-28	1.300E-19
					511	1090	0.375	5179.786	5.460E-29	1.990E-21
PH <sub>3</sub>	12	4635	6.457E-21	0.075	131	4635	17.805	2445.553	3.690E-28	2.930E-19
HNO <sub>3</sub>	13	171504	6.879E-22	0.105	146	171504	0.035	1769.982	3.490E-27	3.020E-20
OH	14	41786	1.048E-21	0.044	61	41631	0.005	19267.869	1.401E-85	3.458E-18
					62	90	0.010	1.824	2.090E-31	5.780E-29
					81	65	0.053	6.325	1.200E-30	1.200E-26
HF	15	107	6.772E-19	0.041	19	107	41.111	11535.570	1.100E-26	1.440E-17
HCl	16	533	3.189E-20	0.040	15	284	20.270	13457.841	1.090E-26	5.030E-19
					17	249	20.240	10994.721	1.010E-26	1.610E-19
HBr	17	576	1.072E-20	0.051	19	289	16.237	9758.564	1.000E-26	1.210E-19
					11	287	16.232	9757.189	1.010E-26	1.180E-19

Table 1. continued.

Mol.	ID	# Lines	Intensity average	Alpha average	Iso. ID	# Lines	F-Min (cm <sup>-1</sup> )	F-Max (cm <sup>-1</sup> )	Int-Min (cm molec <sup>-1</sup> )	Int-Max (cm molec <sup>-1</sup> )
HI	18	237	4.623E-21	0.050	17	237	12.509	8487.305	1.020E-26	1.540E-19
<u>ClO</u>	19	7230	1.605E-22	0.087	56 76	3599 3631	0.028 0.015	1207.639 1199.840	1.520E-29 5.090E-30	3.240E-21 1.030E-21
<u>OCS</u>	20	24922	4.251E-21	0.090	622 624 632 623 822 634	14500 4764 2403 1802 1096 357	0.406 0.396 0.404 509.007 0.381 1972.188	4118.004 4115.931 4012.468 4115.588 4041.565 2910.543	1.560E-25 6.400E-27 1.720E-27 1.010E-23 2.620E-28 1.010E-23	8.550E-20 4.720E-20 1.200E-20 8.430E-21 2.090E-21 5.240E-22
H <sub>2</sub> CO	21	2702	8.610E-21	0.120	126 128 136	1772 367 563	0.000 0.035 0.037	2998.527 47.486 75.745	1.020E-38 1.160E-30 2.020E-30	7.500E-20 1.110E-22 6.290E-22
<u>C<sub>2</sub>H<sub>6</sub></u>	22	14981	2.686E-22	0.101	226 236	8944 6037	765.027 725.603	3000.486 918.717	5.800E-27 1.320E-28	3.210E-20 1.770E-23
<u>CH<sub>3</sub>D</u>	23	11524	9.333E-25	0.060	212	11524	7.760	3146.460	5.570E-30	4.030E-22
<u>C<sub>2</sub>H<sub>2</sub></u>	24	1668	2.340E-20	0.061	211 231	1432 236	604.774 613.536	3358.285 3374.223	1.370E-27 3.820E-26	1.080E-18 1.580E-20
<u>C<sub>2</sub>H<sub>4</sub></u>	25	12978	1.411E-21	0.087	211 311	12967 281	701.203 2947.832	3242.172 3180.238	6.940E-26 5.060E-24	8.410E-20 1.620E-21
GeH <sub>4</sub>	26	824	4.978E-20	0.100	824	804	1937.371	2224.570	1.960E-22	3.680E-19
HCN	27	2575	1.205E-20	0.132	124 125 134	2275 115 185	2.956 2.870 2.880	18407.973 9671.953 9627.961	1.780E-28 5.110E-26 4.150E-26	7.100E-19 2.730E-21 8.290E-21
C <sub>3</sub> H <sub>8</sub>	28	9019	4.168E-23	0.080	221	9019	700.015	799.930	3.770E-24	4.310E-22
C <sub>2</sub> N <sub>2</sub>	29	2577	2.668E-21	0.080	224	2577	203.955	2181.690	6.590E-24	2.580E-20
C <sub>4</sub> H <sub>2</sub>	30	1405	3.445E-21	0.100	211	1405	190.588	654.425	2.650E-24	6.930E-20
HC <sub>3</sub> N	31	2027	2.693E-21	0.100	124	2027	474.293	690.860	6.360E-24	4.420E-20
HOCl	32	15565	2.295E-21	0.060	165 167	8057 7508	0.024 0.349	3799.249 3799.682	1.650E-27 7.220E-28	3.590E-20 1.140E-20
N <sub>2</sub>	33	117	5.729E-29	0.047	44	117	2001.711	2619.230	2.330E-34	3.410E-28
CH <sub>3</sub> Cl	34	9355	5.584E-22	0.085	215 217	5311 4044	679.050 674.143	3172.927 3161.830	1.250E-25 4.190E-26	1.130E-20 3.540E-21
<u>H<sub>2</sub>O<sub>2</sub></u>	35	100781	5.090E-22	0.107	166	100781	0.043	1499.487	5.090E-29	5.610E-20
<u>H<sub>2</sub>S</u>	36	20788	2.992E-22	0.136	121 131 141	12330 3564 4894	2.985 5.601 5.615	4256.547 4098.234 4171.176	1.450E-26 2.020E-26 2.020E-26	1.360E-19 5.990E-21 1.080E-21
HCOO <sub>H</sub>	37	3388	5.186E-21	0.400	261	3388	1060.962	1161.251	2.140E-22	2.840E-20
COF <sub>2</sub>	38	54866	2.178E-21	0.084	269	54866	725.005	1981.273	4.740E-24	3.830E-20
SF <sub>6</sub>	39	11520	4.551E-21	0.050	236	11520	940.425	952.238	2.160E-22	1.500E-20
C <sub>3</sub> H <sub>4</sub>	40	3390	4.277E-22	(*)	341	3390	290.274	359.995	2.020E-23	3.180E-21
<u>HO<sub>2</sub></u>	41	26963	9.907E-22	0.088	166	26963	0.055	3675.819	3.550E-27	2.900E-20
CIONO <sub>2</sub>	42	32199	1.093E-22	0.140	564 764	21988 10211	763.641 765.212	797.741 790.805	1.250E-24 6.340E-25	3.850E-22 1.260E-22
TOTAL LINES IN GEISA 1997: 1,346,266										

Underlined molecules are new or updated for GEISA-97

(\*) missing value set to 0.000

(§) minimum intensity value corresponding to extremely weak line

Table 2: Summary of the molecular species catalogued in the line parameter portion of GEISA-97 and HITRAN-96

Mol.	Mol ID G	Mol ID H	# of bands G	# of bands H	# of isot. G	# of isot. H	# Lines G	# Lines H	F-Min (cm <sup>-1</sup> )	F-Max (cm <sup>-1</sup> )
H <sub>2</sub> O	1	1	139	137	5	4	50217	49444	0.401	22656.465
CO <sub>2</sub>	2	2	626	589	9	8	62816	60802	442.006	9648.007
<u>O<sub>3</sub></u>	3	3	108	106	5	5	281607	275133	0.026	4060.783
<u>N<sub>2</sub>O</u>	4	4	163	162	5	5	26771	26174	0.838	5131.249
CO	5	5	104	47	6	6	13515	4477	3.414	8464.883
<u>CH<sub>4</sub></u>	6	6	55	42	2	3	66883	40958	0.010	6184.492
O <sub>2</sub>	7	7	18	18	3	3	6292	6292	0.000	15927.806
NO	8	8	293	50	3	3	94738	15331	0.000	9273.214
<u>SO<sub>2</sub></u>	9	9	9	9	2	2	38853	38853	0.017	4092.948
<u>NO<sub>2</sub></u>	10	10	11	11	1	1	100680	100680	0.498	2938.381
<u>NH<sub>3</sub></u>	11	11	34	34	2	2	11152	11152	0.215	5294.501
<u>PH<sub>3</sub></u>	12	28	5	2	1	1	4635	2886	17.805	2445.553
<u>HNO<sub>3</sub></u>	13	12	12	13	1	1	171504	165426	0.035	1769.982
<u>OH</u>	14	13	221	103	3	3	41786	8676	0.005	19267.869
HF	15	14	6	6	1	1	107	107	41.111	11535.570
HCl	16	15	17	17	2	2	533	533	20.240	13457.841
HBr	17	16	16	16	2	2	576	576	16.232	9758.564
HI	18	17	9	9	1	1	237	237	12.509	8487.305
<u>ClO</u>	19	18	12	12	2	2	7230	7230	0.028	1207.639
<u>OCS</u>	20	19	151	7	6	4	24922	858	0.381	4118.004
H <sub>2</sub> CO	21	20	10	10	3	3	2702	2702	0.000	2998.5274
<u>C<sub>2</sub>H<sub>6</sub></u>	22	27	3	2	2	1	14981	4749	725.603	3000.486
<u>CH<sub>3</sub>D</u> (\$)	23		9	(*)	1	(*)	11524	7074	7.760	3146.460
<u>C<sub>2</sub>H<sub>2</sub></u>	24	26	10	10	2	2	1668	1668	604.774	3358.285
<u>C<sub>2</sub>H<sub>4</sub></u>	25	(*)	11	(*)	2	(*)	12978	(*)	701.203	3242.172
GeH <sub>4</sub>	26	(*)	1	(*)	1	(*)	824	(*)	1937.371	2224.570
HCN	27	23	41	8	3	2	2575	772	2.870	18407.973
C <sub>3</sub> H <sub>8</sub>	28	(*)	1	(*)	1	(*)	9019	(*)	700.015	799.930
C <sub>2</sub> N <sub>2</sub>	29	(*)	29	(*)	1	(*)	2577	(*)	203.955	2181.690
C <sub>4</sub> H <sub>2</sub>	30	(*)	30	(*)	1	(*)	1405	(*)	190.588	654.425
HC <sub>3</sub> N	31	(*)	31	(*)	1	(*)	2027	(*)	474.293	690.860
HOCl	32	21	6	6	2	2	15565	15565	0.024	3799.682
N <sub>2</sub>	33	22	1	1	1	1	117	120	2001.711	2619.230
CH <sub>3</sub> Cl	34	24	8	8	2	2	9355	9355	679.050	3172.927
<u>H<sub>2</sub>O<sub>2</sub></u>	35	25	2	2	1	1	100781	5444	0.043	1499.487
<u>H<sub>2</sub>S</u>	36	31	30	11	3	3	20788	7151	2.985	4256.547
HCOOH	37	32	7	7	1	1	3388	3388	1060.962	1161.251
COF <sub>2</sub>	38	29	7	7	1	1	54866	54866	725.005	1981.273
SF <sub>6</sub>	39	30	1	1	1	1	11520	11520	940.425	952.238
C <sub>3</sub> H <sub>4</sub>	40	(*)	1	(*)	1	(*)	3390	(*)	290.274	359.995
<u>HO<sub>2</sub></u>	41	33	4	4	1	1	26963	26963	0.055	3675.819
ClONO <sub>2</sub>	42	35	3	3	2	2	32199	32199	763.641	797.741
Total			2255	1470	96	82	1346266	999361		

Underlined molecules are new or updated for GEISA-97

(§) Individual molecule in GEISA ; isotope of CH<sub>4</sub> in HITRAN

(\*) Molecule not included in HITRAN

*Table 3:* MASTER instrument characteristics.

Band	Wavenumber range [GHz]	Species to be retrieved	Other species
A	199-207	N <sub>2</sub> O, H <sub>2</sub> <sup>18</sup> O	O <sub>3</sub>
B	296-306	<sup>18</sup> OO, O <sub>3</sub> , N <sub>2</sub> O	O <sub>3</sub>
C	318-326	H <sub>2</sub> O	O <sub>3</sub>
D	342-348	CO, HNO <sub>3</sub>	O <sub>3</sub>

*Table 4 :* SOPRANO instrument characteristics.

Band	Wavenumber range [GHz]	Species to be retrieved	Other species
A1	499.4-503.5	BrO, ClO, O <sub>3</sub>	N <sub>2</sub> O
A2	503.5-505.0	CH <sub>3</sub> Cl	O <sub>3</sub>
B1	624.5-626.6	H <sup>35</sup> Cl, H <sup>37</sup> Cl	O <sub>3</sub>
B2	628.2-628.7	HOCl	<sup>18</sup> OO
C	635.5-637.5	CH <sub>3</sub> Cl	O <sub>3</sub>
D	730.5-732.0	<sup>18</sup> OO	O <sub>3</sub>
E	851.3-852.8	NO	O <sub>3</sub>
F1	951.6-953.1	NO	O <sub>3</sub>
F2	953.9-955.4	<sup>18</sup> OO	O <sub>3</sub>

Table 5: Description of the MASTER-SOPRANO database.

molecule	isotope	molecular and isotopic code	file	number of lines
<b>H<sub>2</sub>O</b>	1 16 1	1 1	fih2o.1	6
	1 18 1	1 2	fih2o.2	5
	1 17 1	1 3	fih2o.3	2
	1 16 2	1 4	fih2o.4	3
<b>O<sub>3</sub></b>	16 16 16	3 1	fio3.1	278
	16 16 18	3 2	fio3.2	95
	16 18 16	3 3	fio3.3	41
	16 16 17	3 4	fio3.4	434
	16 17 16	3 5	fio3.5	439
<b>N<sub>2</sub>O</b>	14 14 16	4 1	fin2o.1	25
	14 15 16	4 2	fin2o.2	3
<b>CO</b>	12 16	5 1	fico.1	2
<b><sup>18</sup>O<sup>16</sup>O</b>	18 16	7 2	fio2.2	4
<b>NO</b>	14 16	8 1	fino.1	24
<b>HNO<sub>3</sub></b>	1 14 16	12 1	fhno3.0	1528
	1 14 16	12 1	fhno3.6	952
	1 14 16	12 1	fhno3.7	1056
	1 14 16	12 1	fhno3.8	895
	1 14 16	12 1	fhno3.9	1840
<b>HCl</b>	1 35	15 1	fihcl.1	3
	1 37	15 2	fihcl.2	3
<b>ClO</b>	35 16	18 1	ficlo.1	72
	37 16	18 2	ficlo.2	68
<b>HOCl</b>	1 16 35	21 1	fihocl.1	153
	1 16 37	21 2	fihocl.2	218
<b>CH<sub>3</sub>Cl</b>	12 1 35	24 1	fich3cl.1	448
	12 1 37	24 2	fich3cl.2	205
<b>BrO</b>	79 16	33 1	fibro.1	54
	81 16	33 2	fibro.2	74
<b>COF<sub>2</sub></b>	12 16 22	29 1	ficof2.1	851
<b>NO<sub>2</sub></b>	14 16	10 1	fino2.1	137
<b>HO<sub>2</sub></b>	1 16	35 1	fiho2.1	134
<b>SO<sub>2</sub></b>	32 16	9 1	fiso2.1	122
<b>H<sub>2</sub>O<sub>2</sub></b>	1 16	25 1	fih2o2.1	222
<b>H<sub>2</sub>CO</b>	1 12 16	20 1	fih2co.1	2
<b>OCS</b>	16 12 32	19 1	fiocs.1	3

Total number of lines 10401

Caption:

- Molecule: identification of the molecule
- Isotope: isotopic species
- Molecular and isotopic code used for MASTER-SOPRANO
- File: name of the file in the MASTER-SOPRANO database
- Number of lines: number of lines in each file

*Table 6:* Summary of DLR and LSH measurements. Line broadening parameters are given in MHz/Torr, at 296 K.

Instrument	Species	Line frequency (GHz)	$\gamma_{\text{air}}$ (MHz/Torr)	$n_{\text{air}}$
MASTER A	N <sub>2</sub> O	201.0	3.256 (12)	0.79 (3)
	H <sub>2</sub> <sup>18</sup> O	203.4	3.824 (26)	0.90 (4)
C	H <sub>2</sub> O	325.2	3.674 (24)	0.64 (9)
D	CO	345.2	2.713 (64)	0.773 (80)
SOPRANO A1	O <sub>3</sub>	498.7	2.859 (11)	0.740 (24)
		500.4	2.798 (57)	0.876 (80)
		501.8	2.785 (28)	0.784 (62)
	<sup>79</sup> BrO	499.0	3.54 (28)	0.45 (18)
	<sup>35</sup> ClO	501.3	3.23 (13)	0.689 (61)

*Table 7:* Evolution of the H<sub>2</sub>O continuum and O<sub>2</sub> line parameters in Liebe's Millimeter-wave Propagation Model.

Year	H <sub>2</sub> O continuum	O <sub>2</sub> parameters
1977	3	1
1978	0	1
1981	0	2
1984	1	0
1987	1	0
1989	0	2
1992	0	1
1993	3	2

Key

0: no change

1: new measurements by Liebe and co-workers

2: revised analysis of earlier measurements by Liebe and co-workers

3: based on measurements by others

*Table 8:* Fields of the format for each transition in the GEISA database.

Fortran Format Descriptor	F10.6	D10.3	F5.3	F10.3	A36	F4.2	I4	I3	A3	I2	I1	E10.3	F5.4	F8.6	I3	I6	160 characters
C % Format Descriptor	10.6f	10.3e	5.3f	10.3f	.36s	4.2f	4i	3i	.3s	2i	1i	10.3e	5.4f	8.6f	3i	6i	
Fortran Variable Type <sup>1</sup>	R*4	R*8	R*4	R*4	C*36	R*4	I*4	I*4	C*4	I*4	I*4	R*4	R*4	I*4	I*4	I*4	100 bytes
C Variable Type <sup>2</sup>	F	D	F	D	C[36]	F	I	I	C[4]	I	I	F	F	I	I		
Byte internal Storage <sup>3</sup>	4	8	4	4	36	4	4	4	4	4	4	4	4	4	4	4	
Field Name <sup>4,5</sup>	A	B	C	D	E	F	G	I	J	K	L	M	N	O	P	Q	16 fields

(1) The *R, I, C* symbols are abbreviations for the conventional *Real, Integer* and *Character* Fortran type declarators.

(2) The *F, D, I, C* symbols are abbreviations for the standard *float, double, integer* and *char C* type declarators.

(3) Real type values (Fortran *R\** or C *F, D*) are stored in *IEEE* format.

(4) Character strings (*E* and *J* fields) are blank right justified (no ending null character).

The *A-J* fields are those used in the GEISA software:

(A) Wavenumber (cm-1) of the line associated with the vibro-rotational transition.

(B) Intensity of the line (cm molecule<sup>-1</sup> at 296K).

(C) Lorentzian collision halfwidth (cm<sup>-1</sup> atm<sup>-1</sup> at 296K).

(D) Energy of the lower transition level (cm<sup>-1</sup>).

(E) Transition quantum identifications for the lower and upper levels of the transition, as the following:

    TR1     upper state vibrational identification,

    TR2     lower state vibrational identification,

    RN1     upper state rotational identification,

    RN2     lower state rotational identification.

Blank fields (spaces) at this place match missing information.

(F) Temperature dependence coefficient *n* of the halfwidth. Its value is set to zero if *n* is not available.

(G) Identification code for isotope.

(I) Identification code for molecule.

(J) Internal GEISA code for data identification.

(K) Molecule number.

(L) Isotope number (1=most abundant, 2=second, etc.).

(M) Transition probability (debye).

(N) Self-broadened halfwidth (HWHM) (cm<sup>-1</sup> atm<sup>-1</sup> at 296K).

(O) Air-broadened pressure shift of line transition (cm<sup>-1</sup> atm<sup>-1</sup>).

(P) Accuracy indices for frequency, intensity and halfwidth.

(Q) Indices for look-up of references for frequency, intensity and halfwidth.



# **BEAM: a fast line-by-line model for atmospheric transmission in the millimeter and submillimeter range**

D. G. Feist and N. Kämpfer

## **1 Introduction**

While there are general models like MODTRAN[3] available for the IR and UV/Visible, microwave models are usually very specialized. The BErnese Atmospheric Model, BEAM, was therefore developed as a general-purpose model for the simulation of microwave propagation in the atmosphere. BEAM can be used for nearly all microwave radiative transfer problems from the troposphere to the mesosphere. At the Institute of Applied Physics in Bern, BEAM is used as the core of our operational retrieval models as well as for the simulation of measurement campaigns and future instruments.

## **2 Components of BEAM**

### **General remarks**

BEAM is supposed to be a general-purpose model for millimeter and submillimeter wave propagation. The main design parameters were speed and flexibility. Therefore, the code was written as a modular C-library that can easily be accessed with other applications. Our experience is that well written C-programs run faster and are easier to port to other systems than programs in most other languages. So far, BEAM runs on at least five different platforms and operating systems without any changes to the source code.

In order to be as flexible as possible, all memory allocations in BEAM are done dynamically. There are no hidden maximum sizes for any data structure except for the available memory of the machine or limitations of the operating system. This was another reason to write the program in C.

### **Spectral line database**

There are several spectral line databases available for the millimeter and submillimeter range. The most widely used are probably GEISA [10], HITRAN [9], and the JPL spectral line catalog [8]. We focussed our attention to [8] and [9]. Both catalogs have their advantages and disadvantages. Neither of them is sufficient on its own for atmospheric modeling in the millimeter and submillimeter range. The JPL catalog, for example, does not contain information on line broadening. This information is contained in HITRAN. On the other hand, HITRAN is rather aimed at the infrared and UV/visible range and covers considerably fewer lines than the JPL catalog in the millimeter and submillimeter range. Most of the molecules and isotopes in the JPL catalog are actually missing in HITRAN. It is also our opinion that the information in the JPL catalog is in general more accurate than the same information in HITRAN.

To solve these problems, BEAM provides its own spectral line database BEAMCAT as well as the software to generate it [1]. This database is a compilation of information from the JPL catalog and HITRAN. The general principle is to take spectral line information from the JPL catalog and supplement it with line broadening parameters from HITRAN. If a transition in the JPL catalog does not exist in HITRAN, either because just the transition or the isotope itself is missing in HITRAN, reasonable default values can be supplied by the user. Transitions that exist in HITRAN but not in the JPL catalog can also be merged into BEAMCAT, however, this feature is still experimental.

The identification of spectral lines in the two catalogs cannot be done by frequency because the catalog values differ largely for many transitions. Instead, the transitions have to be identified by their quantum numbers. This is a complex and hideous task because the quantum number formats in both catalogs are very different and neither format is well documented. Quantum number information is also often incomplete on both catalogs. The BEAMCAT software uses several identification tactics that are able to identify practically all spectral lines in JPL and HITRAN below 10000 GHz (the frequency limit of the JPL catalog). The software can be used to merge updated versions of both catalogs as soon as they become available.

### **Line-by-line code**

The line-by-line module of BEAM reads the line entries from the BEAMCAT database to calculate the absorption coefficients. All the routines are numerically optimized and use one of the fastest algorithms for the calculation of the line shape function [4]. Filters are available to select sets of species. It is also possible to select all lines in a frequency range that contribute more than a user-defined minimum brightness temperature. In this case, a simplified radiative transfer has to be used which might not be appropriate for complex radiative transfer problems.

The routines are designed to handle large frequency grids with many thousands of lines at high speed. Size and resolution of the frequency grid are completely user-defined, no limits are imposed by the program. An automatic frequency selection algorithm allows to perform the calculations on a much smaller frequency grid that can later be interpolated to the original resolution. The reduced frequency grid speeds up the calculations by a factor of 10-200 with a typical accuracy of better than 0.1% compared to the full resolution. Further details are described in [2].

### **Water vapor and dry-air continuum**

BEAM contains the widely used MPM model by H. J. Liebe [6, 7]. We converted the FORTRAN code for MPM-93, which is available on the author's FTP site at <ftp://ntia.its.bldrdoc.gov/pub>, into C and implemented it into BEAM. The different modules of MPM-93 for O<sub>2</sub>, H<sub>2</sub>O, and N<sub>2</sub> continuum can be selected individually in addition to the line-by-line code. Only the gas phase modules of MPM-93 were implemented in BEAM.

MPM has its own hard-coded spectral line database for H<sub>2</sub>O and O<sub>2</sub>. These lines are known to the automatic frequency selection algorithm of BEAM. This way the numerical improvements of BEAM can also be utilized in calculations with MPM. However, when MPM is activated, the frequency range of BEAM is limited to below 1 THz because of the way the H<sub>2</sub>O continuum is implemented in MPM-93.

## **3 Future work**

There are several things that remain to be improved in BEAM:

- large parts of the documentation are still missing. The code itself is well documented but many comments are in German.
- other continuum models besides MPM should be implemented
- an even better frequency reduction algorithm has been proposed recently by Kuntz [5]. This algorithm also works well with unevenly-spaced frequency grids
- a website for BEAM is under construction at <http://www.cx.unibe.ch/~feist/BEAM/>

- future versions of BEAMCAT should be able to use information from other spectral line databases besides JPL and HITRAN, e.g. GEISA

## References

- 1** D. G. Feist. BEAMCAT 1.0: A spectral line database for millimeter and submillimeter wave propagation in the earth's atmosphere. Technical Report 99-1, Institute of Applied Physics, Sidlerstr. 5, 3012 Bern, Switzerland, March 1999.
- 2** D. G. Feist and N. Kämpfer. BEAM: a fast versatile model for atmospheric absorption coefficients from 0-1000 GHz. In Tadahiro Hayasaka, Dong Liang Wu, Ya-Qiu Jin, and Jing shan Jiang, editors, *Microwave Remote Sensing of the Atmosphere and Environment*, volume 3503 of *Proceedings of SPIE*, pp. 301-312, Beijing, China, SPIE - The International Society for Optical Engineering (1998).
- 3** F. X. Kneizys, L. W. Abreu, G. P. Anderson, J. H. Chetwynd, E. P. Shettle, A. Berk, L. S. Bernstein, D. C. Robertson, P. Acharya, L. S. Rothman, J. E. A. Selby, W. O. Gallery, and S. A. Clough. The MODTRAN 2/3 report and LOWTRAN 7 model. Technical report, Ontar Corporation, 9 Village Way, North Andover, MA 01845, U.S.A., January (1996).
- 4** M. Kuntz. A new implementation of the Humlicek algorithm for the calculation of the Voigt profile function. *J. Quant. Spectrosc. Radiat. Transfer*, 57(6), pp. 819-824 (1997).
- 5** Martin Kuntz. Efficient line-by-line calculation of absorption coefficients. *J. Quant. Spectrosc. Radiat. Transfer*, Vol. 63, pp. 97-114 (1999).
- 6** Hans J. Liebe. An updated model for millimeter wave propagation in moist air. *Radio Sci.*, 20(5):1069-1089, September-October (1985).
- 7** Hans J. Liebe. MPM - an atmospheric millimeter-wave propagation model. *Interntl. J. Infrared & Millimeter Waves*, 10(6), pp. 631-650 (1989).
- 8** H. M. Pickett, R. L. Poynter, E. A. Cohen, M. L. Delitsky, J. C. Pearson, and H. S. P. Müller. Submillimeter, millimeter, and microwave spectral line catalog. *J. Quant. Spectrosc. Radiat. Transfer*, 60(5), pp. 883-890 (1998).
- 9** L. S. Rothman, C. P. Rinsland, A. Goldman, S. T. Massie, D. P. Edwards, J.-M. Flaud, A. Perrin, C. Camy-Peyret, V. Dana, J.-Y. Mandin, J. Schroeder, A. McCann, R. R. Gamache, B. B. Wattson, K. Yoshino, K. V. Chance, K. W. Jucks, L. R. Brown, V. Nemtchinov, and P. Varanasi. The HITRAN molecular spectroscopic database and HAWKS (HITRAN Atmospheric Workstation): 1996 edition. *J. Quant. Spectrosc. Radiat. Transfer*, 60(5), pp. 665-710 (1998).
- 10** Jacquinet-Husson, N., Arié, E., Ballard, J., Barbe, A., Bjoraker, G., Bonnet, B., Brown, L.R., Camy-Peyret, C., Champion, J.P., Chédin, Chursin, A.A., Clerbaux, C., Duxbury, G., Flaud, J.M., Fourrié, N., Fayt, A., Graner, G., Gamache, R., Goldman, A., Golovko, Vl., Guelachvilli, G., Hartmann, J.M., Hilico, J.C., Hillman, J., Lefèvre, G., Lellouch, E., Mikhaïlenko, S.N., Naumenko, O.V., Nemtchinov, V., Newnham, D.A., Nikitin, A., Orphal, J., Perrin, A., Reuter, D.C., Rinsland, C.P., Rosenmann, L., Rothman, L.S., Scott, N.A., Selby, J., Sinitsa, L.N., Sirota, J.M., Smith, A.M., Smith, K.M., Tyuterev, Vl.G., Tipping, R.H., Urban, S., Varanasi, P., Weber, M., The 1997 spectroscopic GEISA databank. *J. Quant. Spectros. Radiative Transfer*, 62, pp. 205-254 (1999).



## Overview of RTTOV-5

Steve English

RTTOV is a radiative transfer model for very rapid computation of top of atmosphere radiances for a range of operational spaceborne radiometers (McMillin, 1997). It is mainly the result of collaboration between the European Centre for Medium Range Weather Forecasts, the UK Meteorological Office and Météo France. The latest version, RTTOV-5, was released in 1999 and has been developed with the following features:

- It is written in FORTRAN-77 for ease of portability
- It is based on the TOVS fast radiative transfer (RT) model RTTOV (Eyre, 1991), using the same basic structure of the code as far as possible and rules for TL, AD and K routines. The new model is described by Saunders et al. (1999).
- It extends the water vapour profile to 0.1hPa and now includes ozone in the profile vector.
- It potentially supports all satellite IR and microwave passive radiance observations (e.g. ATOVS, SSM/I, METEOSAT imager, GOES IR sounder etc.) with the same code but using different RT coefficient files. Currently only ATOVS (NOAA-11 through 15) and METEOSAT 5-7 have RT files.
- It allows surface emissivity to be input for each channel now and includes the FASTEM sea surface microwave emissivity model using surface wind speed and SST as input (see COST712 report section on "FASTEM").
- It has a more flexible user interface to permit input of new variables (e.g. profiles of liquid water, and more surface and cloud parameters) and to allow easy future extension to other input variables (e.g. profiles of ice water, precipitation, etc.). The number of levels can also be changed (43 is the current default) for those users who wish to generate their own RT coefficients.

The changes are made through an include file to parameter statements (cparam.h). - It applies a check on the input profile variables to make sure they are within the limits of which the fast model can compute realistic transmittances. If they are outside the limits but still physically reasonable a calculation will still be performed but flagged. If the profile is not physically reasonable RTTOV will return with an error flag set and no radiances computed. - A single documented ASCII RT coefficient file is used as input for each satellite type. This facilitates export of the code and makes it clear what values are used.

- It outputs intermediate products of the RT calculations in addition to simulated radiances and brightness temperatures (e.g. transmittance profiles).

Distribution of RTTOV is managed by the European Centre for Medium Range Weather Forecasts free of charge subject to completion of a registration form. To request RTTOV-5 you should send an email to [data.services@ecmwf.int](mailto:data.services@ecmwf.int). They will then send a form to fill in. There are 2 options one to get the code on floppy disk suitable for PCs and second to get the code by FTP as a unix compressed file for unix workstations.

## **References**

- Eyre J.R.: "A fast radiative transfer model for satellite sounding systems", ECMWF Tech. Memo. 176 (1991).
- McMillin L.M. "Fast Parametric Models for the Clear Atmosphere", in Mätzler C. (ed.) "Development of radiative transfer models", COST Action 712, Report from Review Workshop 1, EUMETSAT, Darmstadt, Germany, April 8 to 10, 1997, Oct. (1997).
- Saunders R.W., M. Matricardi and P. Brunel: "An improved fast radiative transfer model for assimilation of satellite radiance observations", Q. J. Royal Meteorol. Soc., Vol. 125, pp. 1407-1426 (1999).

# Clouds and Precipitation

Harald Czekala and Peter Bauer

David Jones, Frank Marzano, Alessandra Tassa, Laura Roberti, Stephen Englisch,  
Pedro Baptista, Alberto Mugnai and Clemens Simmer

The subgroup 2 of Project 1 reviews the progress in microwave modeling of clouds and precipitation in this chapter.

## 1 *Introduction*

The simulation of microwave radiative transfer in clouds and precipitation requires a great deal of effort covering the following aspects:

- The proper definition of the lower boundary condition, i.e., surface emissivity of various surfaces such as ocean water, land surfaces including soil and vegetation, as well as snowcover.
- The knowledge of atmospheric background absorption in the desired frequency range.
- The description of the optical properties of individual hydrometeors as a function of their type, composition, and shape as well as of the corresponding particle size distributions.
- Information on the distribution of the hydrometeors in space. This is also determined by the regarded cloud dimensions.
- The applicable and/or appropriate radiative transfer model type.
- In case of the intention to simulate spaceborne sensor signatures, the inclusion of antenna imaging specifications.

Fig. 1 gives an overview of the logical flow and the elements of the radiative transfer problem, here, in order to generate a database for further use in inversion schemes. Apart from aiming at highest possible accuracy, the maintenance of computational efficiency implies limitations to some of the above components. For example the use of full three-dimensional models (e.g., Monte-Carlo type) is very time consuming which may be inappropriate in case large data volumes are to be analyzed. The higher degree of model sophistication usually goes with a general increase of model variable numbers. Thus model upgrading may be inhibited by the lack of additional information on how to properly determine the model parameters, even when generalization is required. Thus the following model descriptions aim at generalized models keeping the intention of accuracy and feasibility in mind.

When discussing the accuracy of the different models one should keep in mind the specific purpose for which these models so far have been developed. Practical applications (retrieval) will focus on the large scale effects (as seen in microwave satellite imagery) and always will be constrained by the limited computational resources. Calculations for ground based observations and investigations of fundamental effects require high accuracy calculations. While all available radiative transfer models are subject to further improvement, there does not exist a recommended model which includes all the latest developments of the different scientific groups. The reason for this may be the diversity and complexity of both, the desired applications and the radiative transfer techniques which have to be combined.

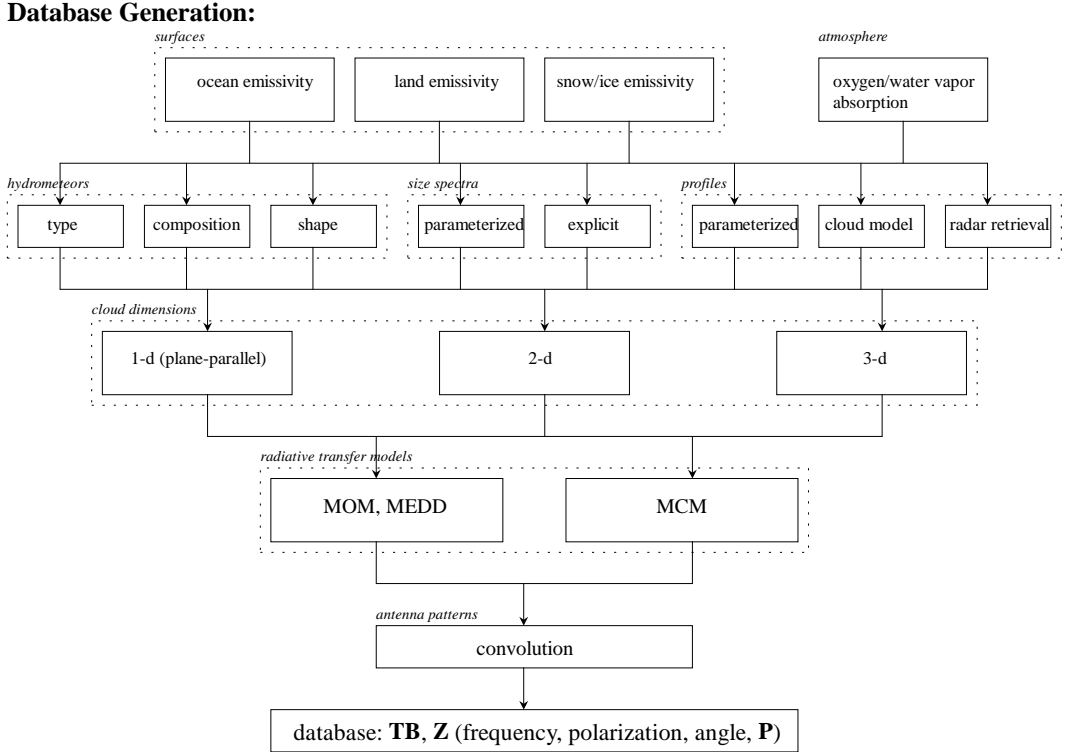


Figure 1: *Components of radiative transfer simulations in clouds.*

## 2 Hydrometeors

When calculating microwave radiative transfer for passive remote sensing of atmospheric water and ice, the radiative transfer models (RTM) have to account for multiple scattering by hydrometeors. Most types of hydrometeors, such as raindrops and nearly all ice particles, do not have a spherical geometry and therefore need single scattering models (SSM) which compute the scattering of electromagnetic waves by particles of nonspherical shape. Such models provide an approximative solution of Maxwell's equations for the specified particle geometry. From these single scattering models we are able to calculate extinction, emission, and scattering parameters for radiative transfer calculations. Single scattering results heavily depend on the the shape and refractive index of the particle under consideration.

### 2.1 Treatment of liquid (nonspherical) hydrometeors

Only small liquid hydrometeors (like cloud droplets) may be treated by means of Lorenz-Mie theory when single scattering calculations have to be performed. Such particles are on the one hand very small compared to wavelength, on the other hand they meet the requirements of spherical shape. Raindrops are highly nonspherical (Pruppacher and Pitter, 1971; Chuang and Beard, 1990) and therefore need other single scattering methods than Mie theory.

The development of SSM for nonspherical particles has significantly improved. One of the commonly used methods is the discrete dipole approximation (DDA, Draine and Flatau 1994). This technique offers a nearly free choice of particle shape and works well for ice particles, but

collapses when applied to microwaves and water drops. The reason can be found in the large refractive index when considering liquid phase instead of ice. So up to now only *Extended Boundary Condition Method* (EBCM) algorithms have been used for raindrops with spheroid shape and DDA for ice particles of more complex geometry.

In order to minimize computation time a database system can be developed to store the results of single scattering calculations (extinction matrix, scattering matrix and absorption vector). By simply presenting the specific parameters (e.g. size, shape, frequency, refractive index, phase etc.) scattering data may be retrieved exactly from this database, or added to the database, or even interpolated from the closest values stored in the database.

### 2.1.1 Single scattering models

To compute the interaction parameters (extinction, absorption, scattering) of nonspherical particles with sizes in the same order of magnitude of the wavelength under consideration there exists a variety of models. Upon definition of input parameters for shape, size, frequency, refractive index and the set of directions  $(\theta, \phi; \theta', \phi')$  the SSM compute the amplitude scattering function (ASF):

$$\begin{pmatrix} E_{vs}(\theta, \phi) \\ E_{hs}(\theta, \phi) \end{pmatrix} = \begin{pmatrix} f_{vv}(\theta, \phi; \theta', \phi') & f_{vh}(\theta, \phi; \theta', \phi') \\ f_{hv}(\theta, \phi; \theta', \phi') & f_{hh}(\theta, \phi; \theta', \phi') \end{pmatrix} \times \begin{pmatrix} E_{vi}(\theta', \phi') \\ E_{hi}(\theta', \phi') \end{pmatrix}. \quad (1)$$

From the ASF, which links the incident polarized plane wave  $(E_{vi}, E_{hi})$  to the scattered wave  $(E_{vs}, E_{hs})$ , we are able to compute the interaction parameters according to Tsang et al. (1985). The extinction matrix  $\bar{\bar{\sigma}}_e(\theta, \phi)$  is computed from the forward scattering amplitudes using the optical theorem.

Four angles are necessary for the scattering phase matrix  $\bar{\bar{\mathbf{P}}}(\theta, \phi; \theta', \phi')$ . The absorption coefficient in the case of non-spherical particles is no longer a single number but becomes a vector that varies with the direction of incidence. By integrating over  $\phi'$  and averaging over  $\phi$  the azimuthal dependency is cancelled out for one-dimensional plane parallel radiative transfer applications. The above equations describe scattering by a single particle of a certain size. In order to calculate the radiation interaction parameters of a specific atmospheric layer the single scattering quantities have to be integrated over particle size distributions.

#### Extended Boundary Condition Method (EBCM) T-matrix code

A computer code (FORTRAN-77) based on to the extended boundary condition method has been developed by Michael Mishchenko (NASA Goddard Institute for Space Studies) and freely available via the internet (<http://www.giss.nasa.gov/~crmim/>). The code is known to be the fastest for rotationally symmetric nonspherical particles, but unfortunately it is limited to particles with an additional mirror symmetry to the plane of rotation.

The code is available in four different versions, by allowing for the choice between fixed or random orientation of the particles on the one hand, and double and extended precision encoding on the other hand. Unfortunately, most compilers cannot handle extended precision variables. The model can easily be encoded as a subroutine which takes the drop specification as input and computes the T-Matrix. Once this is done, a second subroutine may be called to calculate the ASF for a specified set of angles  $(\theta, \phi; \theta', \phi')$  without redoing the T-matrix calculation again.

#### DMF code

The Discretized Mie Formalism, developed by Tom Rother and Karsten Schmidt at DLR Neustrelitz (Rother and Schmidt, 1996; Rother, 1998), has also been used to calculate the ASF. The

main advantage of this method is the possibility to define more general particle shapes: Rotational symmetric particles with a boundary surface  $r = r(\theta)$  (with the condition that  $r(\theta)$  has a unique solution) may be chosen. So this method is able to handle rotational symmetric objects with star-shaped cross sections.

However, there are some drawbacks when using this code: First of all, it is not available to public users. Secondly, establishing a software connection between a calling RTM and the SSM may result in several problems, thus recoding of some parts of the DMF code can be necessary. This task can only be done in close cooperation with the developers of the code, so the DMF cannot be used as a "black-box" code.

Finally, the code is very slow. Although the estimation of the T-matrix takes a comparable amount of time (compared to the EBCM code by Mishchenko), the final calls for the computation of the ASF are considerably slower (approximately by a factor 50 to 100). One simplified atmospheric profile with 5 layers of rain and ice particles takes, calculated for 6 frequencies, took several weeks on two DEC-Alpha workstations with 333 MHz.

### Scattering database

In order to use nonspherical scattering calculations for applications of the RTM the results of the single scattering calculations are stored and may be called from a database whenever used. The time used for searching, locating and loading the scattering data belonging to a certain set of parameters (specifying the scattering calculation) from disk is comparable to the computation time for simple Mie scattering calculations. This database technique prevents re-calculation of nonspherical scattering calculations, which are 3 to 5 orders of magnitude more time consuming.

The scattering database is encoded as a source code package that builds up a library (by executing a Makefile) that may be linked to a RTM. All the user needs to know is the set of interface routines to the database which are provided in FORTRAN-77 and C language (for the C version an additional header file is available).

The interface routines allow to create, open or close the database for scattering data with a given angular resolution. Once such a database is opened, the users may search for a specified target, read a target (from the database) or write a target (to the database). If a target is non-existing during a write attempt, the target is added to the database. If a target is non-existing during a read attempt, the reaction depends on the access mode: If the database is searched with "interpolating-access", the result for the scattering properties is calculated by linear interpolation between the nearest neighbors of the existing data.

The data saved on hard disk can not be ordered arbitrarily due to the amount of disk space used: The file size will be in the range of several Gigabytes, which prevents re-ordering of the file after adding new data. Instead the information about the different scattering calculations is stored in a tree-structure, which is saved to an additional information file and must be completely held in the main memory while working with the database.

For real applications the computer memory requirements will quickly grow to several hundreds of Megabytes. This will be no fundamental problem since most computers used for the application of nonspherical scattering RTM will be able to handle such requests.

The database library is not fully tested up to now and is therefore not distributed. After detailed checks the software will be made available to the community via internet. For information and requests on this topic please contact Harald Czekala (address available from page 9 of this report).

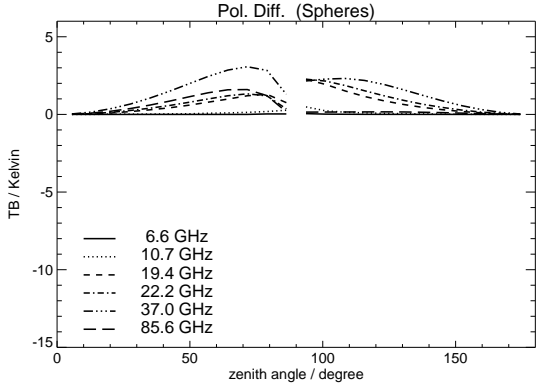


Figure 2: *Polarization difference for spherical drops and a constant rain rate of 10 mm/h. Zero angle denotes the direction of vertically upwelling radiation, 180 degree is the direction of downwelling radiation. At the horizontal viewing direction(90 degree) the 1D-model is undefined.*

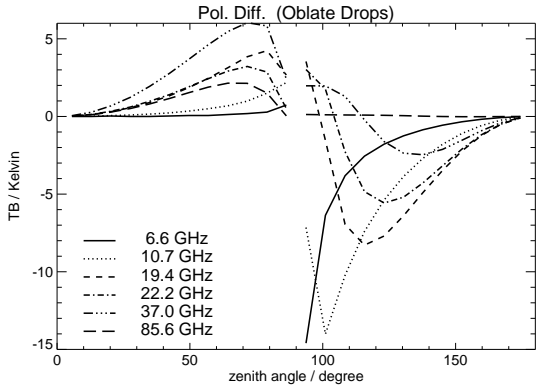


Figure 3: *Polarization difference for spheroid raindrops. The shape is approximated by volume equivalent spheroids with size-dependent aspect ratio, all other settings as in Fig. 2.*

### 2.1.2 Example of results

Radiative transfer calculations taking into account the nonsphericity of raindrops and ice particles for multiple scattering have been performed recently (Czekala and Simmer 1998a, 1998b, 1998c, Czekala 1998, Czekala et al. 1998, 1999). Since the results show a complex dependence on frequency, viewing angle, rain rate and surface conditions, the discussion of these results will not be given in this report. A detailed comparison of spherical and nonspherical scattering particles and the resulting implications for remote sensing of precipitation can be found in the literature referenced above.

For illustration purposes we will only give an example of polarization differences (vertically polarized intensity minus horizontally polarized intensity) resulting from spherical raindrops (Fig. 2) and nonspherical oblate raindrops (Fig. 3). The nonspherical particles are chosen to be spheroids with their axis of rotational symmetry aligned to the vertical. A 2 km thick rain layer above ground level is assumed with a fixed rain rate of 10 mm/h. The cloud reaches from 300 to 3000 meters height.

While spheres produce positive polarization differences at all directions of propagation, the

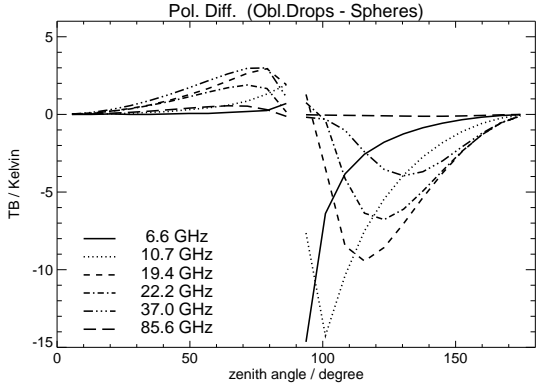


Figure 4: *Difference of polarization differences for spheroid minus spherical raindrops.*

results obtained with spheroids show significant changes: At upward directions the radiation emerging from the atmosphere shows, in general, larger polarization difference, whereas the downwelling radiation exhibits negative polarization difference. This behaviour is strongly affected by frequency, optical thickness, viewing angle and many other parameters. The resulting differences when using spheroids instead of spheres (Fig. 4) show that the shape of raindrops is a parameter which should not be neglected in state-of-the-art radiative transfer models.

## 2.2 Frozen hydrometeors

A brief inspection of aircraft 2D images of frozen hydrometeors shows a tremendous degree of variability in their structure. They often display non-spherical symmetry and, especially in the case of snow and aggregates, their shape may not be generally approximated as simple functions of their size. Also, cross-polar radar observations above the melting layer demonstrate that snow and aggregate hydrometeors may exhibit a range of "canting" angles as they fall. Frozen hydrometeors therefore present a challenge not only in choosing an adequate single particle extinction approach but also in the selection of the radiative transfer model itself. It is for these reasons that the simplifying assumption of spherical particles is often made.

In the generation of databases for retrieval schemes or in the validation of numerical weather prediction (NWP) models against satellite microwave observations, it is usually appropriate for the radiative transfer model to adopt the same assumptions of frozen hydrometeor PSDs and size-density relationships as in the "parent" atmospheric model. While this is obviously the preferred approach, Schols et al. (1999) demonstrate that the NWP model must explicitly represent the different frozen hydrometeor species (specifically snow/aggregates and graupel/hail) which are observed by the measuring system for a meaningful comparison with observations to be made. Lower resolution operational NWP models which rely on parameterisations for convective processes and only explicitly represent large scale precipitation processes may either make no inherent assumption about ice density or may use a single ice species with a decreasing density with size (e.g. Wilson and Ballard, 1999). The sensitivity of the forward modelled brightness temperatures to the oversimplistic description of the ice microphysics in the NWP (and hence radiative transfer) models must be borne in mind when microwave observations are used to infer NWP performance or generate retrieval databases.

Cloud resolving models (CRMs) and high-resolution non-hydrostatic mesoscale models which

are capable of representing convective processes explicitly, generally include representations of multiple ice species. These may be broadly classified as graupel (density constant, between 0.3 and 0.6 gcm<sup>-3</sup>), snow/aggregates (density variable or at a constant value less than 0.1 gcm<sup>-3</sup>) and cloud ice (density constant, between 0.1 and 0.6 gcm<sup>-3</sup>), although further partitioning of the ice species (e.g. higher density hail) is occurring as models become more advanced (Ferrier (1994)).

A wide range of PSDs are employed in the literature ranging from monodisperse sizes (for cloud ice only), through exponential descriptions such as Marshall-Palmer (1948) and Sekhon-Srivastava (1970) to the more flexible gamma distributions (e.g. Swann 1998). Whichever PSD is chosen, one must be aware of the potential effects of truncating the PSD at a given maximum size when calculating the extinction properties of a volume of atmosphere. Ice mass lying outside the evaluated range of radii is usually redistributed back into the considered range of particle radii. The impact that this has on the extinction properties of a volume of atmosphere is very much dependent on the assumed PSD and density for a given species and the microwave frequency.

The large choice of PSDs, densities and truncation limits produces differing multifrequency brightness temperature signatures with significant consequences for retrievals using database techniques (Panegrossi et al (1998)). There is therefore a continuing requirement for the study of these effects in order to attempt to reproduce realistic multifrequency brightness temperature signals from advanced atmospheric models. In support of this, well-instrumented aircraft, radar and radiometer campaigns to validate the assumptions made within the radiative transfer models must also be carried out.

Jones and Thomason (1995) describe an airborne experiment where 2D cloud and precipitation images of frozen hydrometeors were reduced to spectra of *equivalent cross-sectional area spheres* (Moss and Johnson, 1994) for the calculation of volume extinction parameters at 89 and 157 GHz. A size-density relationship for the equivalent sphere distribution was obtained which convincingly predicted S-band radar reflectivity factor Z values and gave ice water content (IWC) values which were consistent with those calculated from the 2D probes using the species classification technique of Cunningham (1978) at a range of environmental temperatures from -3 to -35°C . This relationship was:

$$\rho(r) = (0.92 - \rho_{\text{inf}}) \exp(-Ar^2) + \rho_{\text{inf}} \quad (2)$$

where  $\rho(r)$  is the effective homogenous density of the equivalent cross-sectional area sphere of radius  $r$  mm,  $A = 25$  and  $\rho_{\text{inf}} = 0.045$  gcm<sup>-3</sup>. (The ability of this parameterisation to produce both realistic IWC values *and* radar Z values suggests the effective particle density is represented well across the entire size spectrum, as these quantities gain most of their contribution from the smaller and larger particle sizes, respectively.)

By applying the density parameterisation to each measured equivalent sphere PSD, it was possible to simultaneously calculate the IWC and Z values in addition to the extinction parameters required for 1D radiative transfer. Maxwell-Garnett ice matrices with spherical air inclusions (and also simple ice/air averages) were used to modify the ice refractive index; the Mie code of Wiscombe (1980) was used to calculate the extinction coefficient, single scattering albedo and asymmetry factor. These extinction parameters were then integrated over all measured equivalent sphere PSDs and then approximated by simple analytical functions of IWC or Z. This was best achieved by grouping the PSDs into a number of environmental temperature "bins" so that the predominance of smaller hydrometeors at higher altitudes were reflected in the extinction parameterisations. Vertical slices of radar reflectivity data could then be converted into

extinction parameter profiles which could be used to forward model *downwelling* microwave TBs which were compared to observations from the Microwave Airborne Radiometer Scanning System (MARSS, English et al. 1994) as the aircraft flew along a radar radial. Such an approach may seem inflexible as the extinction parameterisations must be re-evaluated for new frequencies and alternative refractive index models and are therefore not immediately applicable to simulations of multi-frequency top-of-atmosphere brightness temperatures from NWP or cloud-resolving models. However it made the validation experiment independent from potentially inconsistent PSD assumptions and so the validation exercise could be considered to be more directed at testing the validity of the equivalent sphere approach combined with the refractive index modification model.

The MARSS radiometer measured in both upward and downward directions. The validation was performed against down-welling brightness temperatures using cold space as a uniform background. The up-welling MARSS brightness temperatures were used to define the lower boundary condition in the radiative transfer model (Jones 1995), removing the need to model the atmosphere below the aircraft as well as reducing the impact of calibration biases in the measurements. Such an approach is recommended for future measurement missions.

An important lesson learned from this experiment was that the presence of supercooled cloud liquid water places significant uncertainty on such a validation exercise. S-band radar reflectivities values above the melting layer are typically in the range 0 to 25 dBZ, compared to a typical ensemble of cloud water droplets with a liquid water content of  $0.1 \text{ g m}^{-3}$  which has a reflectivity of less than -20 dBZ (Sauvageot and Omar, 1987) rendering it "invisible" to the radar. Cloud liquid water (CLW) absorption at SSM/I and AMSU frequencies is proportional to the total liquid water content and is much more pronounced than at S-band due to the increase in the imaginary part of the refractive index of water with frequency. Therefore CLW could not be neglected in the forward model during validation and it was necessary to parameterise the liquid water fraction (defined as the fraction of total water condensate mass that is liquid) as a function of temperature using additional aircraft microphysics measurements. Future measurement campaigns should exploit a wider range of (lower) microwave frequencies to help constrain the liquid water column.

The results indicated that insufficient extinction at the higher MARSS frequency was produced by the ice hydrometeor extinction parameterisation. While this may be in part due to the deficiencies of the liquid water fraction parameterisation and uncertainties in the permittivity of supercooled water at these higher frequencies (Lipton et al. (1999)), a tentative conclusion is that the description of snow and aggregates as a collection of lower refractive index homogeneous spheres may not necessarily be a good one at smaller wavelengths. (Note that Jones (1995) and Jones and Thomason (1995) employed an erroneous coding of Maxwell-Garnet effective permittivity).

Many more well-instrumented measurement campaigns in both mid-latitude and tropical environments (such as the TRMM validation experiments — <http://trmm.gsfc.nasa.gov>) are required for validation of both the atmospheric and the radiative transfer models.

## 2.3 Inhomogeneous melting particles

The modelling of melting particle properties depends on the meltwater fraction as a function of fall distance below the zero degree isotherm as well as the particle permittivity as a function of the approach chosen for the mixing of the permittivity contributions by air, ice, and water. The first is generally simulated regarding the particle's heat budget in an environment of changing

temperature and moisture along its descent (Rutledge and Hobbs, 1983; Mitra et al., 1990). Details of the latter are given in the next section and the appendix.

### 2.3.1 Permittivity models

Generally, the effective permittivity of an inhomogeneous particle is calculated as a function of the individual contributions by water, ice, and air. Historically, depending on the assumed microstructure of the particle, either a distinction of a host material (matrix) and an inclusion material is made or both components are treated similarly and form an aggregate-type composite. The most widely used formulation of the first type follows the Maxwell-Garnett approach (Maxwell-Garnett, 1904; MG) while the second type was developed by Bruggeman (1935; BR). Bohren and Battan (1982) updated MG for elliptical inclusions. Principally, these models do not adjust the effective permittivity to frequency or spatial structure, i.e., size and distribution of the inclusions in the matrix, but rather apply to the small grain limit where the structure dimension is well below the wavelength.

Mainly from radar backscattering modeling, new approaches appeared to better represent the observations at higher frequencies and for various particle types and melting stages. For a spatially homogeneous ice-water mixture, i.e., water pockets randomly distributed in the particle volume, Meneghini and Liou (1996) developed an analytical function to better represent the complex particle permittivity at a frequency of 7.7 GHz and at intermediate melting stages employing an error function. The application of this model (here called ML96) to other frequencies may not seem justified, but the effective permittivity calculation is driven by the weights obtained from the error function which are closely tied to the permittivity of snow at early melting stages and water at late stages which imply a frequency dependence themselves. Recently, Meneghini et al. (1998) (ML98) improved the numerical accuracy of the calculations by employing a continuous multiple components particle approach with parameterizations which allow its efficient application to frequencies between 10 and 95 GHz. This model is based on the assumption that the properties of the constituents are homogeneous, isotropic and linearly superimposed.

Another approach is represented by the assumption that inhomogeneous particles can be constructed from concentric shells of material with different dielectric properties. The most common example is a water-coated ice sphere which may be a sufficient approximation for melting hailstones or graupel with high densities. In case of snow, more complicated compositions of each layer are required which may be again provided by application of MG to each component. Shivala and Lindell (1989) developed the theoretical background for various permittivity profiles through inhomogeneous particles. This allowed the more sophisticated treatment of continuous permittivity changes in radial direction. Thus density and permittivity discontinuities as assumed by the a shell model represent a simplification of this approach which seems justified due to the lack of information on density and composition variation as a function of particle radius and melting stage.

For purposes of radar reflectivity modeling in the melting layer Fabry and Szyrmer (1998), here called FS98, implemented a two-shell model which was also used in the framework of a microphysical melting model by Szyrmer and Zawadski (1999). In this model, the core consists of ice inclusions in a water matrix which serves again as a matrix for air inclusions. The latter are considered as bubbles in a comparably solid environment. The outer shell is treated as ice inclusions in a water matrix which represent inclusions in an air matrix thus indicating the rather loose connection of individual ice crystals so that air can not be trapped between them.

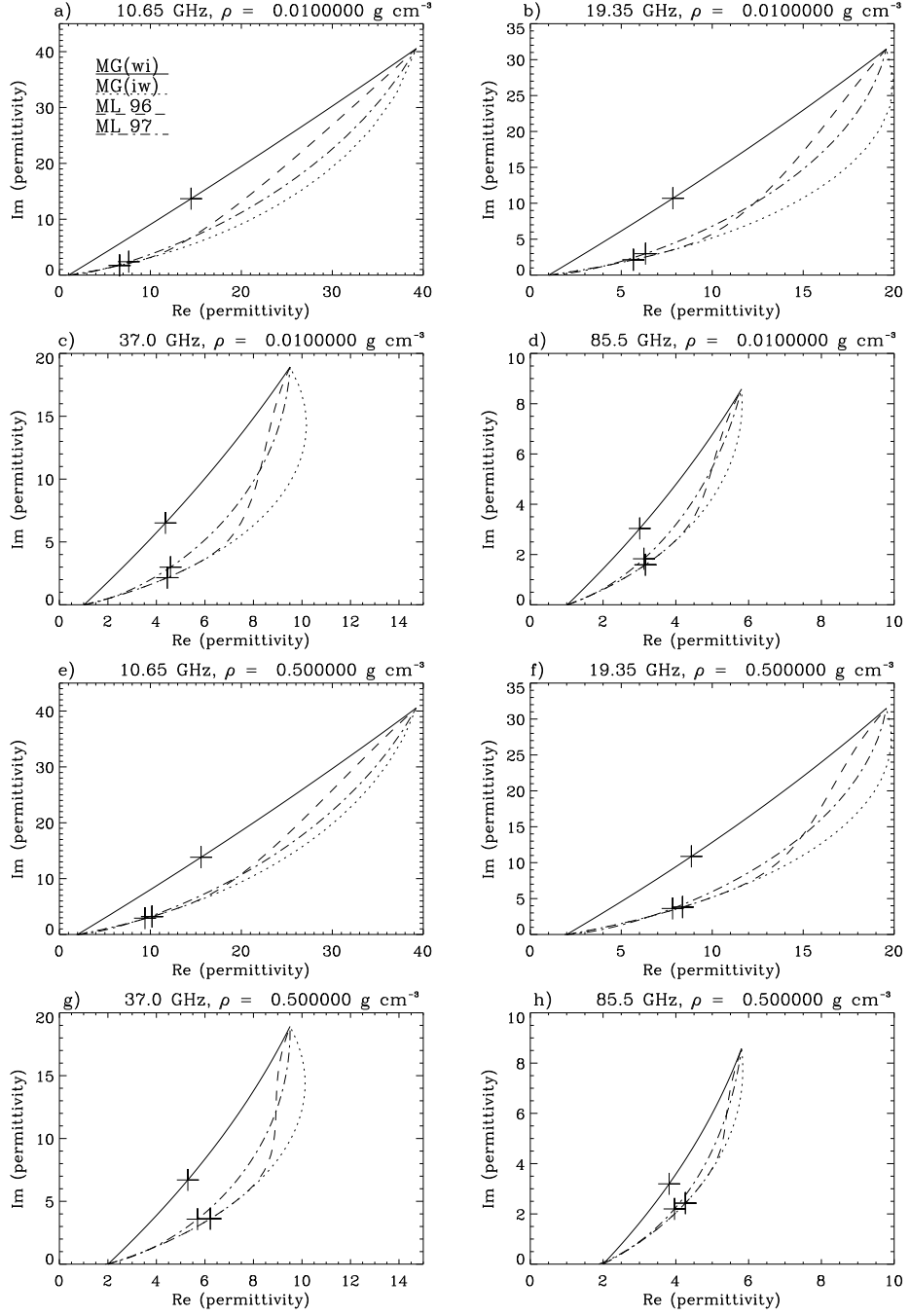


Figure 5: Complex dielectric permittivity for melted water volume fractions between 0 and 1 for a spherical snow particle with density  $0.05 \text{ g/cm}^3$  at 10.7 GHz (a), 19.4 GHz (b), 37.0 GHz (c), and 85.5 GHz (d); (e) - (h) like (a) - (d) for particle density of  $0.25 \text{ g/cm}^3$ . Symbols mark meltwater fraction of 50%.

The permittivities of each layer are then calculated by application of MG.

### 2.3.2 Model intercomparison

Fig. 5 shows model results for the real and imaginary parts of the dielectric permittivity at four frequencies vs. the water volume fraction assuming initial snow densities of  $0.05 \text{ g/cm}^3$  (a-d) and  $0.25 \text{ g/cm}^3$  (e-h), respectively. Here, the FS98 model was implemented assuming that the effective permittivities of core and coat could be again combined by applying the MG formula for spherical inclusions.

The MG - configurations show the dominance of the respective contribution from the material chosen as the matrix which seems unrealistic when applied to cloud particles at least at those melting stages where (1) melting begins and a water matrix was assumed or (2) melting is almost complete and an ice matrix was assumed.

ML96 is mainly driven by those parameters determining the error function impact which is obvious from the relatively drastic switch between states close to  $MG_{iw}$  or  $MG_{wi}$ . The crosses indicate the permittivities at a meltwater mass fraction of 50%. From this indication it becomes obvious that ML96 is identical to  $MG_{iw}$  well beyond a 50% ice mass fraction at all frequencies and initial particle densities. Thus, as for  $MG_{iw}$ , a weak radiative effect of melting particles can be expected for this model unless particle concentrations would become very high. Even though the permittivities reach values close to those of  $MG_{wi}$  at later stages, the particles are almost completely melted thus too small to produce much emission. Summarizing, the strongest effect of ML96 can be expected at low frequencies and very low particle densities (big particles), while in other cases the influence on particle emission will be weak. As mentioned above, the very limited validity of ML96 at higher frequencies requires a careful interpretation.

ML98 can be regarded as close to the average of  $MG_{iw}$  and  $MG_{wi}$ . Since neither  $MG_{iw}$  nor  $MG_{wi}$  show a strong density dependence for a fixed particle size, ML98 will be comparably insensitive to particle density as well. The shell-model (FS98) shows an important difference to the others at early melting stages: the imaginary part of the permittivity is higher than computed from any other model except  $MG_{wi}$  while for larger water fractions a weaker effect than ML98 is produced. This will result in a stronger increase of bright band reflectivity and emission right below the freezing level followed by a stronger decrease further below once meltwater fractions exceeds 40-50%. Thus a sharper peak will be generated.

### 2.3.3 Scattering calculations

Fig. 6 show the results from calculations employing the FS-model for a rainrate of 1 mm/h below the melting layer. The most important feature with respect to microwave emission is the relative change of volume extinction. Maximum effects are a factor of 3 difference between the extinction of the rain spectrum and that in the bright band which causes an increase of total optical depth without changing the rainrate. The single scattering albedo shows a sharp drop below the freezing level due to the increasing liquid fraction in the particles as does the asymmetry parameter. The bright band is well represented in the radar reflectivity with an increase by 13 dB.

Bauer et al. (1998) and Bauer et al. (1999) investigated the effect of the inclusion of melting layer microphysics on apparent brightness temperatures at the frequencies of the SSM/I and TMI. A large dependence of signatures on the implemented permittivity model was observed which was connected to the assumed particle spectrum before melting. Thus a range of almost negligible effects for a graupel spectrum and effects of 50 K for a snow spectrum and large snow particles were simulated. Reducing the number of free parameters by founding the simulations on spectral cloud model outputs prescribing size distributions and size-dependent densities pro-

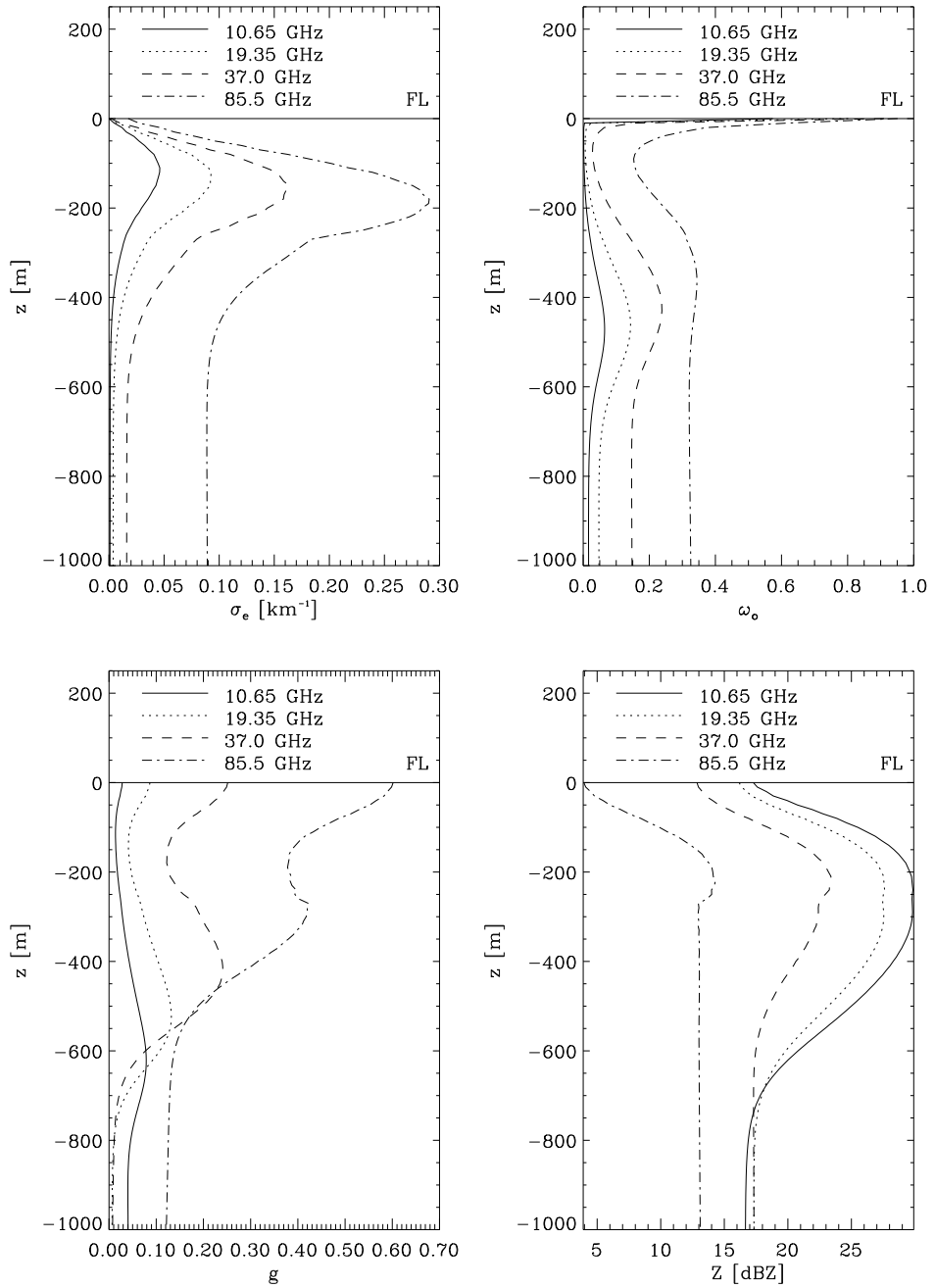


Figure 6: Volume extinction coefficient (a), single scattering albedo (b), asymmetry parameter (c), and radar reflectivity (d) in the melting layer and at four frequencies assuming a rainrate of 1 mm/h using the model of Fabry and Szyrmer (1998).

duced local effects of about 10 - 15 K for the ML-permittivity models and 30 K for MG (water matrix). These brightness temperature changes can be interpreted in terms of surface rainrates, i.e., the deviation of retrieved rainrate from a retrieval neglecting melting layers which may reach the amount of the retrieved rainrate itself.

### **3 Radiative transfer models**

In the case of radiative transfer modeling in rainclouds the contributions from hydrometeors will dominate the total radiation intensity which leads directly to the questions of polarization (mainly when non-spherical particles are present) and dimensionality (since clouds show strong horizontal and vertical inhomogeneities). Plane parallel approximations to radiative transfer are strictly valid only in the limit of the absorption mean free path of photons being significantly shorter than the horizontal inhomogeneities of the medium. For clouds and precipitation not only scattering becomes an important factor in the radiative transfer process, but also the discrete nature of clouds is responsible for much larger inhomogeneities. Furthermore, recent advances in dynamical cloud modeling (Tao et al., 1987; Tripoli, 1992) have made available a great deal of fine scale cloud hydrometeor information together with cloud structure during its evolution. Such information can now be used to study the effects of arbitrary horizontal distribution.

In general, the plane parallel assumption suffers from two types of problems that must be analyzed separately. The first is physical, the second is geometric. The main physical problem is that the radiation is "trapped" in each subcloud considered as an infinite layer. At low frequencies the low radiation emitted inside the cloud is not allowed to exit the sides of the cloud and, consequently, in terms of brightness temperatures the plane parallel results are slightly warmer when emission processes dominate. At high frequencies, when there is scattering in the higher layers, the average brightness temperature is lower for the same reasons.

The geometry problems arise because plane parallel radiative transfer cannot deal with inhomogeneities in horizontal direction which leads to a geometric shift in the cloud radiometric footprint with respect to the real cloud position. This problem is partly overcome by adjusting the columns of the plane parallel model to the viewing direction along the slant path (Roberti et al., 1994; Bauer et al., 1998), however, more information on the accuracy of this approximation is needed when very intense precipitative events are involved. The nature and extent of the problem was demonstrated by several researchers using simple box-type cloud models (Weinman and Davies, 1978; Kummerow and Weinman, 1988; Haferman et al., 1993; Petty et al., 1994; Roberti et al., 1994; Liu et al., 1996).

#### **3.1 Model intercomparison**

In particular the satellite rainfall retrieval community is aware of the problem of the accuracy of models used for building retrieval databases. For the purpose of uncertainty estimation of radiative transfer modeling vs. retrieval errors, an intercomparison of available models applied to various plane parallel cloud profiles, surface conditions, and observation angles has been carried out (Smith et al., 1998). The cloud profiles covered several liquid water and ice distributions from cloud model simulations for which pre-calculated optical parameters were provided. Fig. 7 shows the four cases (rows) and the corresponding extinction coefficients, single scattering albedos, and asymmetry parameters at 4 frequencies (columns). Cases 1 to 4 represent low

water and low ice contents, low water and high ice contents, high water and low ice contents, high water and high ice contents, respectively. The corresponding surface rainrates are 0.94, 0.34, 9.46, and 90.23 mm/h. The simulations were carried out for five frequencies (10.7, 19.35, 22.235, 37.0, 85.5 GHz), over two surface types (ocean with constant emissivity of 0.4 and land with constant emissivity of 0.85), and at two zenith angles (0 and 53 degrees). The participating models were:

1. CSU-1: two-stream Eddington approximation, Fresnel surface reflection (F. Evans, Colorado State University),
2. CSU-2: see CSU-1 with delta scaling (F. Evans, Colorado State University),
3. FSU-1: two-stream Sobolev solution, Fresnel surface reflection (E. Smith, Florida State University),
4. FSU-2: see FSU-1 with Lambertian surface reflection (E. Smith, Florida State University),
5. IFA: discrete-ordinate solution, Lambertian surface reflection (F. Marzano, University dell'Aquila),
6. NASA-1: two-stream Eddington approximation, Fresnel surface reflection (C. Kummerow, NASA GSFC),
7. NASA-2: Monte Carlo model, Fresnel surface reflection (C. Kummerow, NASA GSFC),
8. DLR-1: two-stream Eddington approximation, Fresnel surface reflection (P. Bauer, DLR),
9. DLR-2: Matrix Operator model, Fresnel surface reflection (P. Bauer, DLR).

Examples of the results are given in Figs. 8 and 9 for an ocean surface at different zenith angles. Two features appear as a result of the treatment of surface reflection and scattering by hydrometeors. Those models (number 4 and 5) which use the assumption of Lambertian surface reflection disagree with the others by several degrees (up to 20 K at 19.35 and 37 GHz for nadir incidence). This effect is reduced for higher surface emissivities (not shown here) and higher atmospheric opacities. Secondly, those models which are multistream solutions of the radiative transfer equation and the Monte Carlo model (number 5, 7 and 9) principally provide a more exact treatment of multiple scattering which becomes evident at large ice contents (cases 2 and 4) at 85.5 GHz, and 53 degrees zenith angle. The delta scaling seems to be more efficient at lower zenith angles and can partially compensate for the lack of accuracy implied by the Eddington approximation. From these intercomparisons it may be suggested to either use multi-stream models with an accurate treatment for low surface emissivities (other than Lambertian) or to use two-stream Eddington approximation type models including delta scaling.

### 3.2 Applicability of radiative transfer theory

Natural media, characterized by random discrete scatterers (particles), may be classified with respect to: i) dielectric constant or permittivity; ii) particle concentration, i.e. fraction of volume occupied; iii) mutual position, i.e. statistical correlations. Media are defined as tenuous if the particle permittivity is slightly different from that of the background medium, non tenuous

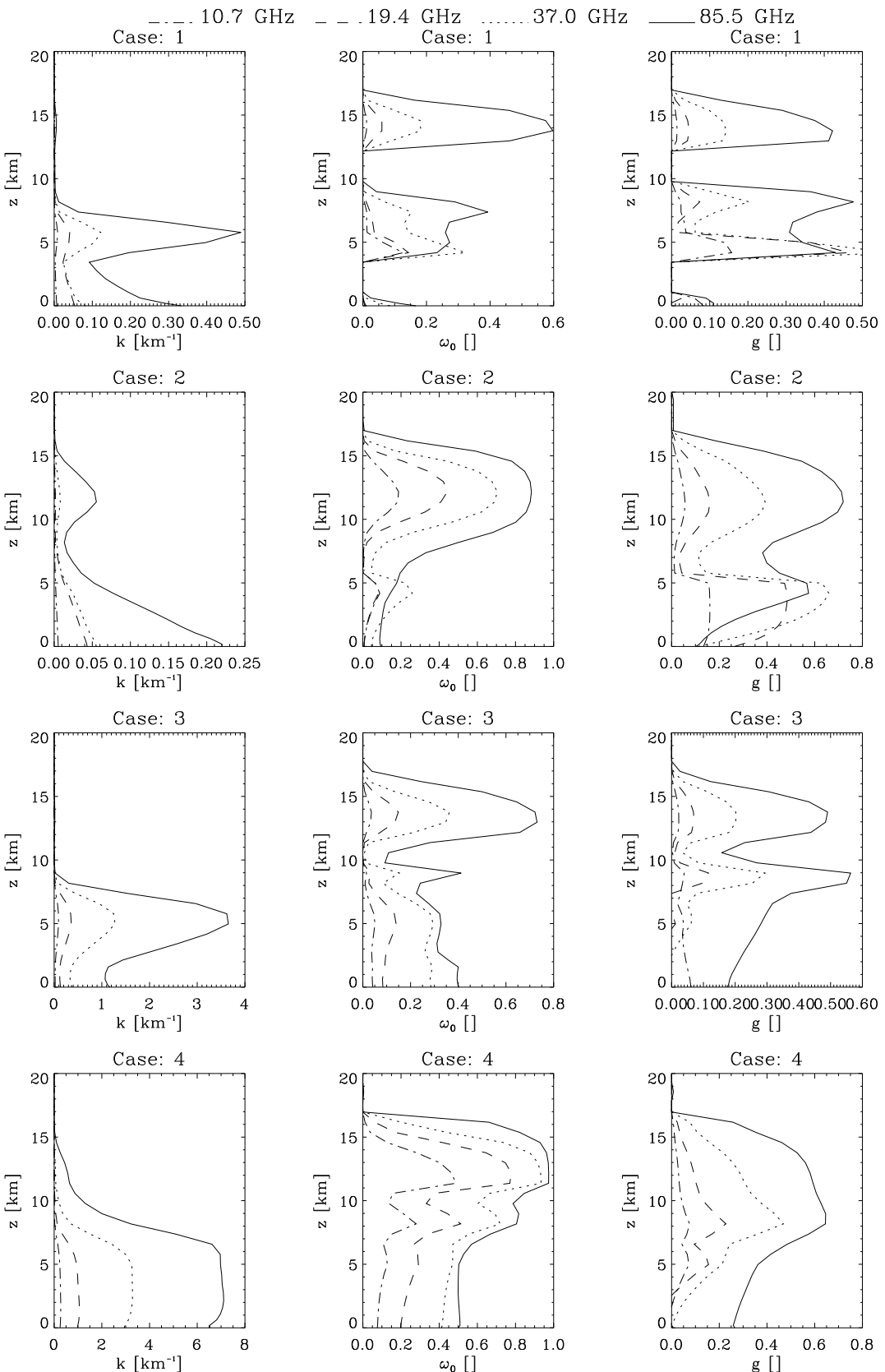


Figure 7: Profiles of optical parameters for four cases (rows) and the corresponding extinction coefficients  $k$ , single scattering albedos  $\omega_0$ , and asymmetry parameters  $g$  at 4 frequencies (columns).

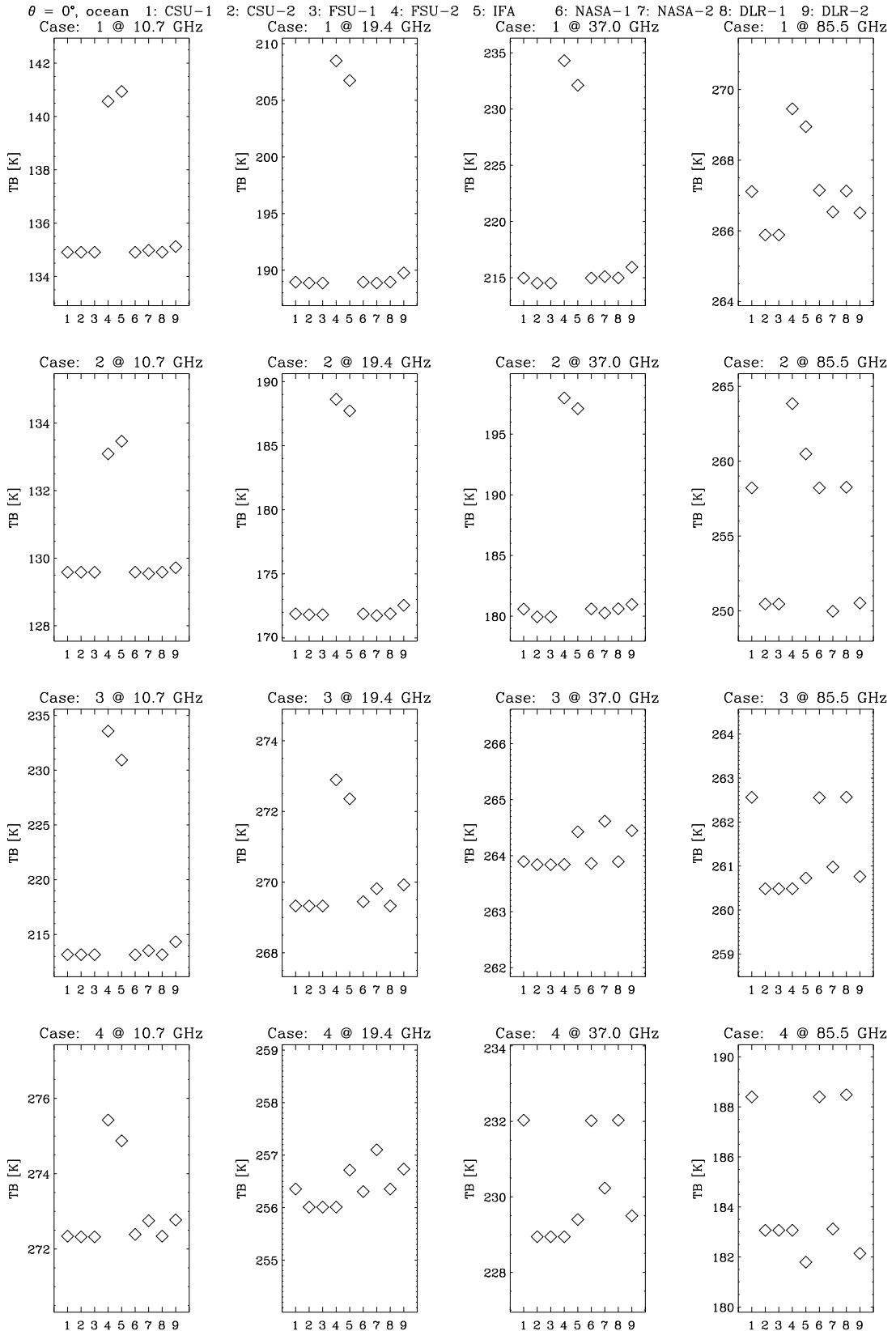


Figure 8: Brightness temperatures at vertical incidence for four cases (rows) at four frequencies (columns) over a surface with constant emissivity of 0.4 versus model number given in the text.

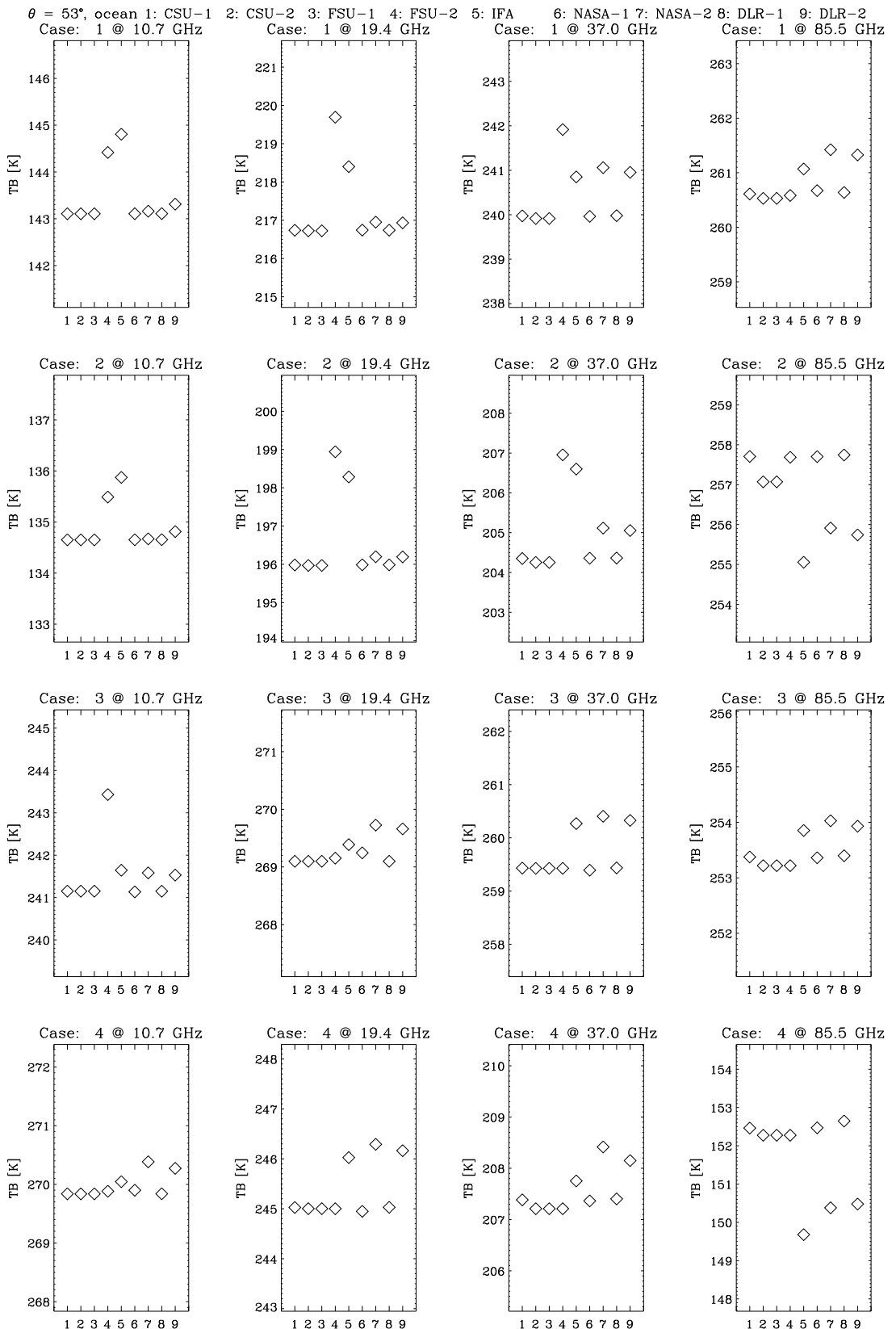


Figure 9: Same as Fig. 8 for a zenith angle of 53 degrees.

vice versa. A dense medium is characterized by an appreciable fractional volume occupied by random particles, while it is called non-dense if the opposite holds (Tsang et al., 1985). Many natural media are dense non-tenuous media, like dry snow (mixture of ice in air with ice volume fraction  $\in [10\%, 40\%]$ ) or wet snow (where also water is present with water volume fraction  $\in [0\%, 10\%]$ ). On the other hand, both non-precipitating and precipitating clouds with water and iced hydrometeors can be considered as non-dense non-tenuous media.

From a propagation point of view, in a tenuous non-dense medium the effective propagation constant of a coherent wave will be quite similar to that of the background medium and the particle position is basically independent from each other so that correlation among particle positions can be neglected. The same applies to non-tenuous non-dense media. Space-time time correlations among particles become important when considering dense media both tenuous and non-tenuous. The basic assumption in both single-scattering theory (SST) and radiative transfer theory (RTT) is the assumption of independent (incoherent) scattering. The physical applicability of this hypothesis is related to the fact that: i) if the particles are supposed to be randomly distributed within the volume, there is no coherent phase relationships between the fields scattered by the individual particles (i.e., particle positions are uncorrelated); ii) if the concentration is small enough, the shadowing of one particle by another may be ignored (i.e., far-fields approximation can be used). The previous assumptions leads to the conclusion that scattered Stokes vectors of each individual particle can be summed up to compute ensemble averages so that volume extinction rate and phase matrix are simply calculated as integrals weighted by the given size distribution.

Let us consider some examples relative to atmospheric clouds by analyzing two typical particle size distributions (PSD).

1. The Modified-Gamma (MG) PSD for droplets of non-precipitating clouds like stratus and cumulus mediocris, and cumulus congestus (Chylek et al., 1992): They exhibit a mode radius of 10, 15, and 20 microns with a liquid water content of 0.25, 0.50, and  $0.80 \text{ g/m}^3$ , respectively (Ulaby et al., vol. I, pp. 306-308, 1982). If the integration over the PSD is extended from 0 to infinity (i.e., overestimating the cloud mass density), then the obtained volume fractions are  $0.25 \cdot 10^{-6}$ ,  $0.50 \cdot 10^{-6}$ , and  $0.80 \cdot 10^{-6}$ , respectively.
2. The Marshall-Palmer PSD for raindrops of precipitating clouds (nimbostratus and cumulonimbus), which can be considered a particular case of MG-PSD (Marshall and Palmer, 1948): Again, by integrating over the PSD from 0 to infinity, for rainfall rates of 10 mm/h (moderate rain) and 100 mm/h (heavy rain), the volume fractions are equal to  $6.28 \cdot 10^{-6}$  and  $4.22 \cdot 10^{-5}$ , respectively.

The above volume fractions are much smaller than 0.05, which would be at the limit of the RTT applicability. It is concluded that atmospheric clouds and precipitation can be considered as non-tenuous and non-dense media, and conventional RTT is applicable for any cloud condition and for current microwave observations.

### 3.3 1-D polarized radiative transfer

Polarization of microwave radiation is a well known feature in the remote sensing applications. While the most obvious effect of precipitation is the depression of polarization induced by the Fresnel surface of the ocean, rain and hail particles tend to produce polarization by scattering and emission. Since the interaction parameters for the different components of the Stokes vector

are not the same and coupling between the components is done by the scattering process, the need of polarized radiative transfer models is obvious.

The first (and simplest) radiative transfer models were one-dimensional approximations of the radiative transfer equation. There exists a variety of different implementations with specific simplifications. The Eddington-approximation (Weinman and Davies, 1978) uses a simplified scattering mechanism and no polarization. A widely used adaption of this code is the Kummerow model (Kummerow, 1993), which is still an unpolarized model.

Other models take into account the polarized radiation by means of the full Stokes vector, but interaction parameters (extinction, absorption) are only scalar and the amplitude scattering function is diagonal (Bauer und Schluessel, 1993; Simmer, 1994). This approximation is only correct in the limit of very small or perfectly spherical particles. Nonspherical particles require an extinction matrix, scattering phase matrix and emission vector with angular dependent values. The practical problems when considering nonspherical particles within radiative transfer calculations are manifold:

- Modification of the radiative transfer scheme to full angular dependence.
- The four component radiative transfer in case of 3D-models (transmission integrals can no longer be defined because of the coupling of all four components).
- Selection of single scattering models (SSM).
- Combination of RTM and SSM, which may be difficult due to
  - different computer codes,
  - different coordinate systems,
  - different unit systems (SI, CGS, . . . ),
  - unknown coefficients (normalization or other) applied to the absolute values,
  - the large amount of data,
  - computing time,
  - legal matters (copyright, publication, etc.).
- Testing of numerical results with known models.
- Validation of numerical results with measurements.
- Optimization of algorithms to obtain a tool for practical applications rather than only theoretical case studies.

We have modified the 1D-RTM by Simmer (1994) to nonspherical scattering (Czekala and Simmer, 1998; Czekala, 1998). In addition to Rayleigh phase functions and Lorenz-Mie theory for scattering by perfect spheres we have connected two SSM that are able to calculate single scattering by certain nonspherical particle shapes to the RTM. Both models, the Extended Boundary Condition Method (EBCM) T-matrix code from Mishchenko (Mishchenko et al., 1996) and the Discretized Mie Formalism by Rother and Schmidt (1997), have been compared and perfect agreement was found.

Other RTM that take into account the nonspherical geometry of hydrometeors exist (Haferman et al. 1995, Evans and Stephens 1995a, 1995b, Evans et al. 1998; Hornbostel and Schroth

1995). Most models focus on either ice particle scattering (Evans and Stephens), or use random orientation for the oblate raindrops (Haferman et al. 1995). For a detailed discussion of radiative transfer modeling efforts (both, 3D and nonspherical scattering) we recommend the review chapter by Haferman (1999).

### 3.3.1 Implications on radiative transfer

The most common representation of polarized light is the Stokes vector  $\bar{\mathbf{I}} = (I_v, I_h, U, V)$ , which contains four elements that unambiguously define the polarization state by means of intensities. It is defined from the electric field components of a polarized wave,  $E_l$  and  $E_r$ , in the following manner:

$$\bar{\mathbf{I}} = \begin{pmatrix} I_v \\ I_h \\ U \\ V \end{pmatrix} = \begin{pmatrix} |E_v|^2 \\ |E_h|^2 \\ 2 \operatorname{Re}(E_v E_h^*) \\ 2 \operatorname{Im}(E_v E_h^*) \end{pmatrix}. \quad (3)$$

When switching from spherical scattering particles to nonspherical particles that do not have random orientation in space, the (one-dimensional) radiative transfer equation

$$\cos \theta \frac{d\bar{\mathbf{I}}(z, \theta)}{dz} = -\sigma_e(z) \bar{\mathbf{I}}(z, \theta) + \sigma_a(z) B(T(z)) + \int_0^\pi \bar{\mathbf{P}}(z, \theta, \theta') \bar{\mathbf{I}}(z, \theta') \sin \theta' d\theta' \quad (4)$$

is modified to the vector radiative transfer equation (VRTE) with angular dependence of the interaction parameters

$$\cos \theta \frac{d\bar{\mathbf{I}}(z, \theta)}{dz} = -\bar{\sigma}_e(z, \theta) \bar{\mathbf{I}}(z, \theta) + \bar{\sigma}_a(z, \theta) B(T(z)) + \int_0^\pi \bar{\mathbf{P}}(z, \theta; \theta') \bar{\mathbf{I}}(z, \theta') \sin \theta' d\theta', \quad (5)$$

where  $\bar{\mathbf{I}}$  denotes the Stokes vector for polarized light,  $z$  the vertical position,  $\theta$  the zenith angle of propagation direction,  $T(z)$  the temperature at height  $z$ ,  $B(T)$  the temperature dependent emission according to Planck's law, and  $\theta'$  the direction of incoming radiation that is scattered into the direction of propagation  $\theta$ . The scalar coefficients  $\sigma_e$  and  $\sigma_a$  for extinction and absorption change to an extinction matrix and absorption vector, respectively, which depend on the direction of propagation.

In case of one-dimensional radiative transfer the first two components of the Stokes vector (1) are not connected to the last two components, leading to a two component equation. The  $(2 \times 2)$  extinction matrix is diagonal. This is important for the solution scheme with the successive order of scattering (SOS) method: The atmosphere is divided into sublayers that are small enough to assume only one single scattering process within the layer. With this assumption the source function is iteratively computed until a consistent solution is obtained. The SOS scheme computes transmission of the radiation intensity within each layer analytically with the exponential function. This is only possible because of the separation of variables within the Stokes vector.

For 3D-radiative transfer the extinction matrix is not in a diagonal form. Therefore the extinction of all four components of the Stokes vector is coupled. The definition of a transmission or optical thickness for single components of the Stokes vector is no longer possible and the discretization scheme along the optical path has to account for the transmission solution by very

small steps. If the steps are small enough, the change of intensity due to extinction is a linear function of the intensity itself and can be computed at each step.

Furthermore the 3D-solution needs to handle extinction and scattering matrices that depend on 5 coordinates (three for location and two for direction) and a scattering phase matrix that depends on 7 coordinates (three for location, two for direction of propagation, two for the direction of incoming radiation that is scattered into the direction of propagation). Mathematically this is a system of four coupled integro-differential equations in a 7-dimensional space with boundary conditions. The solution is a non-trivial serious computational problem due to the large amounts of data which has to be handled on the one hand and the enormous computing time requirements on the other hand.

### 3.3.2 Recommendations

The task of combining a RTM with a SSM for nonspherical particles causes many practical problems and is up to now still in progress. The way how to connect two models depends very much on the specific encodings. Results from recent calculations suggest that there may be significant effects on precipitation retrieval schemes induced by the nonspherical nature of the hydrometeors. However, there does not exist a complete model that can be suggested for practical applications.

## 3.4 3-D Monte Carlo models

An unpolarized 3-D Monte Carlo radiative transfer code has been developed (Roberti et al., 1994) which can take into account the horizontal inhomogeneities of the underlying surface, both in terms of emissivity and height. In this scheme the photons are started at the point at which the brightness temperature,  $TB$ , is to be computed, in the direction opposite to that in which they would physically propagate inside the medium. Each photon is then traced backward through the medium, following probability interaction laws, which are sampled by the selection of numbers from a quasi-random sequence. The interaction can be by scattering or absorption events. When the photon is absorbed, it is considered as being emitted at the point of absorption with the TB equal to the physical temperature of the medium in that point. This Monte Carlo code can account for atmospheric and surface emission and scattering, cosmic background radiation and for a digital terrain model. The Monte Carlo code has recently been extended to take into account non-spherical oriented particles (Roberti and Kummerow, 1999).

## 3.5 3-D recursive solution for isotropically scattering media

A recursive solution of the three-dimensional radiative transfer equation for a horizontally finite and vertically inhomogeneous scattering medium can be derived (Brussaard, 1985; Marzano et al., 1999). The appealing aspect of this solution is that it is simple and relatively fast with respect to more general 3-D solution algorithms, as those based on the Monte Carlo technique (Roberti et al., 1994). However, in the form briefly resumed here, it is limited by the assumption of isotropic multiple scattering and is suitable to be implemented only for canonical shapes of rain clouds (as cylindrical or cubic cells). This solution has found interesting applications for simulating ground-based radiometric observations in the 10-50 GHz band of cumuliform rain clouds along earth-satellite microwave links (Marzano et al., 1997).

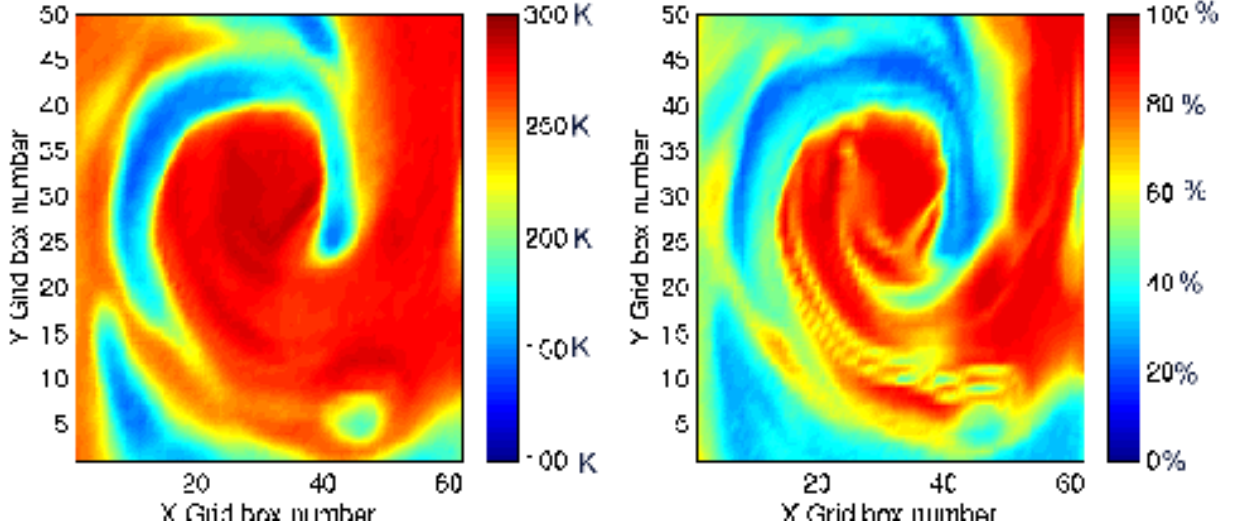


Figure 10: *Comparison between 1D and 3D Radiative Transfer Models. The left panel shows a map of the vertically-polarized simulated brightness temperatures (at 85 GHz and at model resolution of 3.3 km) as obtained by a 3-D Monte Carlo model. The right panel shows, for each model grid point, what percentage of the upwelling brightness temperature is due to photons emitted inside the slanted column associated to that grid point. Contribution to local brightness temperature at 85.5 GHz by emission/scattering in double-inclined 1-D path approximation with respect to 3-D sources.*

Using the iterative method, the solution to radiative transfer is generally found through successive order of scattering approximations (Tsang et al., 1985). In this scheme the zeroth order solution represents the case in which the multiple scattering is neglected. The n-th order solution is then obtained supposing the solution of order (n-1) as a source of the multiple scattering term in the radiative transfer equation, being a correspondence between the order of scattering and the multiple scattering paths. The rationale of the proposed method is to find a solution for the pseudo-source function by a recursive technique and then to use the integral form of the radiative transfer equation to calculate the observed brightness temperature.

The complete cloud model, described in Marzano et al. (1999), takes into account the presence of mixed- phase spherical hydrometeors and precipitating ice, so that its results are representative for convective storms observed from ground-based radiometers along Earth-satellite paths. The impact of different drop size distributions and variable raincell radii has been also evaluated. Simulation results have shown some typical effects due to the 3-D volume properties, like an absolute maximum of observed brightness temperatures with elevation scanning in case of intense precipitation and a relative sensitivity to azimuthal variations in antenna pointing. Comparisons between 3-D raincell and 1-D rain slab results have shown significant differences in simulated brightness temperature and path attenuation values. An equivalent slab height has been introduced in order to reduce these discrepancies so that 1-D simulations can be performed by correcting for the effect of finite horizontal extent of cumuliform storms.

### 3.6 Evaluation of 1-D models adjusted to 3-D geometries

The modification of 1-D models to 3-D cloud observation geometries refers to the reorganization of the 3-D cloud structure into slant paths along the downwelling and reflected as well

as upwelling radiance beams. A primary objective would be the intercomparison of polarized simulations of this model type with those from a 3-D model performed for realistic cloud structures. For this purpose 3-D cloud simulations provide a convenient data source. Bauer et al. (1998) found local differences below 3 K at frequencies below 40 GHz and maximum local errors of 8 K at 85.5 GHz comparing a modified Eddington model to a Monte Carlo model (Roberti et al., 1994). These simulations were carried out for a squall line cloud simulation over tropical oceans at the original cloud model spatial resolution. Once TMI or SSM/I antenna patterns were regarded, the differences between both models almost completely disappeared. A similar comparison for a hurricane simulation provided field - averaged differences in the range of the radiometer noise at all frequencies below 90 GHz for the brightness temperatures while only at 85.5 GHz the differences between the standard deviations of brightness temperatures showed amounts of  $\sim$ 5 K. At an average brightness temperature level this seems acceptable while in case of weighting functions (e.g., Mugnai et al., 1993) and regarding local conditions greater problems occur: Fig. 10 shows fractions of the brightness temperatures explained by scattering and emission sources along the double slant path in the modified 1-D model when compared to a Monte Carlo 3-D model. At those locations where local source distributions show the largest inhomogeneities (see left-hand panel in figure 10) and deviate most strongly from the specular radiance path geometry, the lowest fractions occur: between 20 paths while the rest is contributed from outside. Thus the answer to the question whether geometrically adjusted 1-D models can replace 3-D models depends on the purpose of the application, the investigated cloud systems, and the measurement frequency. In case of very strong gradients of scattering and emission sources and frequencies above say 50 GHz a 3-D treatment is therefore recommended.

## **4 Future developments**

The 1D polarized radiative transfer calculations including nonspherical particles performed at the University of Bonn are currently subject of validation experiments. First results seem to prove the major differences between spherical and oblate raindrop scattering for ground based measurements. The scattering database, which is crucial when calculating large amounts of atmospheric data with the RTM, is tested and will be released in the near future. With this tool we are able to do calculations for more realistic hydrometeor profiles as determined by cloud models or accurate measurements.

Since the 1D-approximation is not a good approach to most rainy conditions, the model will be extended to 3D-geometry. Further improvement can be reached by introducing tilted hydrometeors, so that preferred orientations of raindrops due to wind shear may be accounted for.

The validation of models of millimeter-wave ice extinction has shown to be difficult even with a very comprehensive set of supporting measurements. The greatest uncertainty is the contribution from supercooled liquid water due to the insensitivity of the radar to small water droplets in the presence of larger ice particles. A solution would be to employ a lower frequency upward-looking radiometer (e.g. at 21 and 37 GHz) to provide a constraint on the total liquid water column. More validation experiments at this wider range of frequencies are required with the measurements extending below the melting layer.

The parameterisation for ice density was very consistent with other observations and may therefore be effectively used in a radiative transfer model which assumes spherical particles for

frontal precipitation. However care should be taken if the input fields come from, for example, a numerical weather prediction model as such a parameterisation may be inconsistent with the microphysical description of that model.

From the simulations of the melting layer it became evident that – at least for radar — the largest uncertainties are related to the unknown particle spectra above the freezing level including the size-density relationship. This seems more crucial for snowflakes than for graupel since these tend to be larger and less dense thus creating bigger effects. Associated with that is the unknown distribution of meltwater in the particle during melting. Most permittivity models treat the particle in the same way throughout melting which does not reflect realistic conditions as observed in the few available experimental studies (e.g., Mitra et al., 1990). Thus a multiple stage model is required which can provide a more accurate description of particle composition (and maybe shape) associated with a flexible permittivity approach adjusted to the local conditions (Walden and Holt, 1999, pers. communication). For the benefit of improved hydrometeor retrievals, the next step has to be the implementation of these models into three-dimensional cloud models providing an estimate of the effects of melting particles at scales of airborne and spaceborne radiometers. This may require an update of cloud model microphysical parameterisations which mostly suppress a category of melting particles due to the coarse vertical resolution.

## 5 Acknowledgements

The work on scattering by nonspherical particles at the University of Bonn was supported (in parts) by the Deutsche Forschungsgemeinschaft under Si 606/1–1 and 606/1–2. We thank Michael Mishchenko for making available the EBCM code. Tom Rother and Karsten Schmidt agreed to the employment of their DMF code for parts of the study at Bonn, Stephan Havemann supplied lots of help while adapting the DMF to the radiative transfer code. Jeff Haferman is acknowledged for many helpful and encouraging discussions.

## References

- Bauer, P., Schluessel, P., 1993: Rainfall, total water, ice water, and water-vapour over sea from polarized microwave simulations and SSM/I data. *J. Geophys. Res.*, **98**, 20737-20759.
- Bauer, P., Schanz, L., Roberti, L., 1998: Correction of three-dimensional effects for passive microwave remote sensing of convective clouds, *J. Appl. Meteor.*, **37**, 1619-1632.
- Bauer, P., Marzano, F., A. Khain, I. Sednev, R. Meneghini, C. Kummerow, 1998: Combined cloud - radiative transfer modeling for improved retrievals of stratiform cloud parameters, *J. Atmos. Sci.*, submitted.
- Bauer, P., Poiares Baptista, J.P.V., and M. de Iulis, 1999: On the effect of the melting layer on the microwave emission of clouds over the ocean. *J. Atmos. Sci.*, **56**, 852-867.
- Bohren, C.F. and L.J. Battan, 1982: Radar backscattering of microwaves by spongy ice spheres. *J. Atmos. Sci.*, **39**, 2623-2629.
- Bohren, C.F. and D.R. Huffman, 1983: Absorption and scattering of light by small particles. Wiley Press, 530 pp.

- Bruggemann, D.A.G., 1935: Berechnung verschiedener physikalischer Konstanten von heterogenen Substanzen. I: Dielektrizitätskonstanten und Leitfähigkeiten der Mischkörper aus isotropen Substanzen. *Ann. Phys.*, 24, 636-679.
- Brussaard, G., 1985: Radiometry: a useful prediction tool?, European Space Agency Report SP-1071, Nordwijk (NL).
- Capsoni, C., Fedi, F., Paraboni, A., 1987: A comprehensive meteorologically oriented methodology for the prediction of wave propagation parameters in telecommunication applications beyond 10 GHz, *Rad. Sci.*, 22, 387-393.
- Choudhury, B.J., Schmugge, T.J., Chang, A., Newton, R.W., 1979: Effect of surface roughness on microwave emission from soils, *J. Geophys. Res.*, 84, 5699-5706.
- Chuang, C. and Beard, K. V., 1990: A numerical model for the equilibrium shape of electrified raindrop, *Journal of the Atmospheric Sciences*, 47, 1374–1389.
- Chylek, P., Damiano, P., Ngo, D., Pinnick, R.G., 1992: Polynomial approximation of the optical properties of water clouds in the 8-12 micron spectral region, *J. Appl. Meteor.*, 31, 1210-1218.
- Cunningham, R.M., 1978: Analysis of particle spectral data from optical array (PMS) 1D and 2D sensors, Preprint vol, IV Symp. Met. Obs. and Instr., Amer. Meteorol. Soc., Denver, Col. Apr 10-14, 345-349.
- Czekala, H., 1998: Effects of ice particle shape and orientation on polarized microwave radiation for off-nadir problems. *Geophysical Research Letters*, 25(10):1669–1672.
- Czekala, H., Stephan Havemann, Karsten Schmidt, Tom Rother, and C. Simmer., 1999: Comparison of microwave radiative transfer calculations obtained with three different approximations of hydrometeor shape *Journal of Quantitative Spectroscopy and Radiative Transfer*. (accepted).
- Czekala, H., and C. Simmer., 1998: Microwave radiative transfer effects by nonspherical hydrometeors. In Michael I. Mishchenko, editor, *Conference on Light Scattering by Nonspherical Particles: Theory, Measurements, and Applications*. NASA Goddard Institute for Space Studies, New York, September 29 - October 1, 1998.
- Czekala, H., and C. Simmer., 1998: Microwave radiative transfer with non-spherical precipitating hydrometeors. *Journal of Quantitative Spectroscopy and Radiative Transfer*, 60(3):365–374.
- Czekala, H., and C. Simmer., 1998: Mikrowellenstrahlungstransport mit asphärischen Regentropfen. In *Annalen der Meteorologie, Deutsche Meteorologen- Tagung 1998, 14. - 18. September 1998, Leipzig, Selbstverlag des Deutschen Wetterdienstes*.
- Czekala, H., C. Simmer, T. Rother, K. Schmidt, and S. Havemann., 1998: Microwave radiative transfer with nonspherical particles. In Joanna D. Haigh, editor, *Satellite Remote Sensing of Clouds and the Atmosphere II*, pages 174–185. Proceedings of SPIE Vol. 3220.

- Dobson, M.C., Ulaby, P.T., Hallikainen, M., El-Rayes, M., 1985: Microwave dielectric behaviour of wet soil. *IEEE TRans. Geosci. Remote Sens.*, 23, 35-46.
- Draine, B. T., and P. J. Flatau., 1994: Discrete dipol approximation for scattering calculations. *Journal of the Optical Society of America*, 11(4):1491–1499.
- English, S., Prigent, C., Guillou, C., Jones, D.C., 1994: Aircraft measurements of water vapour continuum absorption at millimetre wavelengths, *Quart. J. Royal Meteorol. Soc.*, 120, 603-624.
- Evans, K. F., and G. L. Stephens., 1995: Microwave radiative transfer through clouds composed of realistically shaped ice crystals. Part I: Single scattering properties. *Journal of the Atmospheric Sciences*, 52(11):2041–2057.
- Evans, K. F., S. J. Walter, A. J. Heymsfield, and M. N. Deeter., 1998: Modeling of submillimeter passive remote sensing of cirrus clouds. *Journal of Applied Meteorology*, 37:184–205.
- Fabry, F. and W. Szyrmer, 1998: Modeling of the melting layer. Part II: Electromagnetics. *J. Atmos. Sci.*, submitted.
- Ferrier, B.,S., 1994: A double moment multiple-phase four-class bulk ice scheme Part I: Description. *J. Atmos Sci.*, 51: 249-280.
- Gasiewski, A.J., 1993: Microwave radiative transfer in hydrometeors, in *Atmospheric remote sensing by microwave radiometry*, M.A. Jansen editor, Wiley & Sons, New York, 91-144.
- Guillou, A. Sobieski, P., Laloux, A., 1998: Radiative transfer equation with surface scattering for ocean and atmospheric parameters retrieval from radiometric measurements. *Int. J. Remote Sens.*, 15, 1743 - 1760.
- Guissard, A., Sobieski, P., Baufays, A., 1992: A unified approach to bistatic scattering for active and passive remote sensing of rough ocean surfaces. *Trends in Geophys. Res.*, 1, 43 - 68.
- Haferman, J.L., Krajewski, W.F., Smith, T.F., Sanche, A., 1993: Radiative transfer for a three-dimensional raining cloud. *Appl. Optics*, 32, 2795-2802.
- Haferman, J. L., T. F. Smith, and W. F. Krajewski., 1995: A multi-dimensional discrete-ordinates method for polarized radiative transfer. Part I: Validation for randomly oriented axisymmetric particles. *Journal of Quantitative Spectroscopy and Radiative Transfer*, 58(3):379–398.
- Haferman, J. L., 1999: Microwave scattering by precipitation (chapter 18), in *Light Scattering by Nonspherical Particles: Theory, Measurements, and Geophysical Applications*, edited by M. I. Mishchenko, J. W. Hovenier and L. D. Travis, Academic Press, 1999.
- Hornbostel, A., and A. Schroth., 1995: Determination of propagation parameters by Olympus beacon, rain rate, radiometer, and radar measurements. *Frequenz*, 49:224–231.
- Houze, R.A., 1982: Structures of atmospheric precipitation systems:] A global survey, *Rad. Sci.*, 17, 671-689.

- Hufford, G., 1991: A model for the complex permittivity of ice at frequencies below 1 THz, *Int. J. Infr. Mill. Waves*, 12, 677-682.
- Jones, D.C., 1995: Validation of scattering radiative transfer models using an aircraft radiometer and ground-based radar, Ph.D. Thesis, Reading UK, pp208.
- Jones, D.C., Thomason, J.W.G., 1995: Representation of mixed phase precipitating clouds in passive microwave radiative transfer models: Aircraft validation, SPIE Proceedings Series, 2584, 426-437.
- Kerr, Y.H., Njoku, E.G., 1990: A semiempirical model for interpreting microwave emission from semiarid land surfaces as seen from space. *IEEE Trans. Geosci. Remote Sens.*, 28, 384 - 393.
- Klaassen, W., 1988: Radar observations and simulation of the melting layer of precipitation. *J. Atmos. Sci.*, 45, No. 24, 3741-3753.
- Knollenberg, R.G., 1970: The optical array: An alternative to scattering or extinction for airborne particle size determination, *J. Appl. Meteorol.*, 9, 86-103.
- Kummerow, C. Weinman, J.A., 1988: Determining microwave brightness temperatures from precipitating horizontally finite and vertically structured clouds, *J. Geophys. Res.*, 93, 3720-3728.
- Kummerow, C., 1993: On the accuracy of the Eddington approximation for radiative transfer at microwave frequencies. *J. Geophys. Res.*, 98, 2757-2765.
- Lamkaouchi, K., Balana, A., Ellison, W.J., 1997: New permittivity data for sea water (30-100 GHz). Extension of ESA report 11197/94/NL/CN.
- Lemaire, D., Sobieski, P., Craeye, 1998: Rain generated ring-waves: Measurements and modelling for remote sensing. *IEEE Trans. Geosci. Remote Sens.*, submitted.
- Liebe, H.J., 1989: MPM - An atmospheric millimeter wave propagation model, *Int. J. Infr. Mill. Waves*, 10, 631-650.
- Liebe, H.J., Manabe, T., Hufford, G.A., 1989: Millimeter wave attenuation and delay rates due to fog and cloud conditions, *IEEE Trans. Antenn. Prop.*, 37, 1617-1623.
- Lipton et al., 1999: *IEEE Trans. Geosci. Rem. Sens.* Vol 27, No 1, p.620 (1999).
- Liu, Q., Simmer, C., Ruprecht, E., 1996: Three-dimensional radiative transfer effects on clouds in the microwave spectral range, *J. Geophys. Res.*, 101, 4289-4298.
- Marshall, J.S., Palmer, W.M.K., 1948: The distribution of raindrops with size, *J. Meteor.*, 5, 165-166.
- Marzano, F.S., Fionda, E., Ciotti, P., 1999: Simulation of radiometric and attenuation measurements along earth-satellite links in the 10-50 GHz band through horizontally-finite convective raincells, *Rad. Sci.*, 34, pp. 841-858.

- Marzano, F.S., Fionda, E., Ciotti, P., 1997: Simulating microwave radiometric observations of cylindrically-shaped precipitation along slant paths, Proc. of 10th ICAP, pp. 2.226-2.229, Edinburgh (UK), 14-17 April, 1997.
- Maxwell-Garnett, J.C., 1904: Colors in metal glasses and in metallic films. Philos. Trans. Roy. Soc. London Ser. A, 203, 385-420.
- Meneghini, R. and L. Liao, 1996: Comparisons of cross sections for melting hydrometeors as derived from dielectric mixing formulas and a numerical method. J. Appl. Meteor., 35, 1658-1670.
- Meneghini, R., Liao, L., Iguchi, T., 1998: Effective dielectric constants of melting hydrometeors and their use in radar bright-band models. Proc. IGARSS'98Seattle, WA, July 6-10, 147-149. Submitted to IEEE Trans. Geosci. Remote Sens., 1997.
- Mishchenko, M. I., L. D. Travis, and D. W. Mackowski., 1996: T-matrix computations of light scattering by nonspherical particles: a review. *Journal of Quantitative Spectroscopy and Radiative Transfer*, 55(5):535–575.
- Mitra, S.K., Vohl, O., Ahr, M. and H.R. Pruppacher, 1990: A wind tunnel and theoretical study of the melting behavior of atmospheric ice particle. IV: Experiment and theory for snow flakes. J. Atmos. Sci., 47, 584-591.
- Monahan, E.C., O'Muircheartaigh, I.G., 1986: Whitecaps and the passive remote sensing of the ocean surface, Int. J. Remote Sens., 7, 627-642.
- Monahan, E.C., Lu, M., 1990: Acoustically relevant bubble assemblages and their dependence on meteorological parameters. IEEE J. Ocean Eng., 15, 340 - 359.
- Moss, S.J., Johnson, D.W., 1994: Aircraft measurements to validate and improve numerical model parameterisations of ice to water ratios in clouds, Atmos. Res., 34, 1-25.
- Mugnai, A., Smith, E., Tripoli, G., 1993: Foundations for statistical-physical precipitation retrieval from passive microwave satellite measurements. Part II: Emission source and generalized weighting function properties of a time dependent cloud radiation model, J. Appl. Meteor., 32, 17-39.
- Panegrossi, G., S. Dietrich, F.S. Marzano, A. Mugnai, E.A. Smith, X. Xiang, G.J. Tripoli, P.K. Wang and J.P.V.P. Baptista, 1998: Use of cloud model microphysics for passive microwave-based precipitation retrieval: significance of consistency between model and measurement manifolds, J. Atmos. Sci, 55: 1644-1673.
- Petty, G.W., Mugnai, A., Smith, E. A., 1994: Reverse Monte Carlo simulations of microwave radiative transfer in realistic 3-d rain clouds. 7th AMS Conference on Satellite Meteorology and Oceanography, Monterey, CA, 185-188.
- Plass, , N.P., Kattawar, G.W., Catchings, F.E., 1973: Matrix operator theory of radiative transfer: Rayleigh scattering. Appl. Opt., 12, 314 - 329.
- Pruppacher, H. R. and Pitter, R. L., 1971: A semi-empirical determination of the shape of cloud and rain drops, *Journal of the Atmospheric Sciences*, **28**, 86–94.

- Roberti, L. Haferman, J., Kummerow, C., 1994: Microwave radiative transfer through horizontally inhomogeneous precipitating clouds, *J. Geophys. Res.*, 99, 16707-16718.
- Roberti, L., Kummerow, C., 1999: Monte Carlo calculations of polarized microwave radiation emerging from cloud structures, *J. Geophys. Res.*, 104, 2093-2104.
- Rother, T., 1998: Generalization of the separation of variables method for nonspherical scattering on dielectric objects. *J. Quant. Spectrosc. Radiat. Transfer*, 60:335–353.
- Rother, T., and K. Schmidt., 1996: The Discrete Mie-Formalism for plane-wave scattering on axisymmetric particles. *Journal of Electromagnetic Waves and Applications*, 10:273–297.
- Rutledge, S. A. and P.V. Hobbs, 1983: The mesoscale and microscale structure and organization of clouds and precipitation in midlatitude cyclones. VIII: A model for the ‘seeder-feeder’ process in warm-frontal rainbands. *J. Atmos. Sci.*, 40, 1185-1206.
- Sauvageot, H., Omar, J., 1987: Radar reflectivity of cumulus clouds, *J. Atmos. Oceanic Tech.*, 4, 264-272.
- Schols, J.L., Weinman, J.A., Stewart, R.E., and Lawson, R.P., 1995: The retrieval of dry and wet snow distributions from SSM/I measurements and MM5 forecast results. Proceedings of the 1995 International Geoscience and Remote Sensing Symposium, Firenze, Italy, 887-889.
- Schols, J.L., Weinman, J.A., Alexander, G.D., Stewart, R.E., Angus, L.J., and A.C.L. Lee, 1999: Microwave properties of frozen precipitation around a north Atlantic cyclone. *J. Appl. Meteor.*, 38, 29-43.
- Sekhon, R.S. and R.C. Srivastava, 1970: Snow size spectra and radar reflectivity, *J. Atmos. Sci.*, 27, 299-307.
- Shivola, A. and I.V. Lindell, 1989: Polarizability and effective permittivity of layered and continuously inhomogeneous dielectric spheres. *J. Electrom. Waves Appl.*, 3, 37-60.
- Simmer, C., 1994: *Satellitenfernerkundung hydrologischer Parameter der Atmosphäre mit Mikrowellen*. Verlag Dr. Kovac. 314p.
- Smith, E.A., Xiang, X., Mugnai, A., Tripoli, G.J., 1994: Design of an inversion-based precipitation profile retrieval algorithm using an explicit cloud model for initial guess micro-physics, *Meteorol. Atmos. Phys.*, 54, 53-78.
- Smith, E., Yang, S., Hollis, T., Lamm, J., Bauer, P., Evans, F., Haddad, Z., Kummerow, C., Marzano., F., Mugnai, A., Olson, W., Panegrossi, J., Turk, J., 1998: Performance of precipitation profile retrieval algorithms. Proc. IGARSS'98, Seattle, Washington.
- Stogryn, A., 1972: The emissivity of sea foam at microwave frequencies. *J. Geophys. Res.*, 77, 1658-1666.
- Stroud, D., Pan, F.P., 1978: Self - consistent approach to electromagnetic wave propagation in composite media: Application to model granular metals. *Phys. Rev. B*, 17, 1602 - 1610.
- Swann, H., 1998: Sensitivity to the representation of precipitating ice in CRM simulations of deep convection, *Atmos. Res.*, 47-48, 415-435.

- Szermrej, W. and I. Zawadski, 1999: Modeling of the melting layer. Part I: Dynamics and microphysics. *J. Atmos. Sci.*, in press.
- Tao, K., Simpson, J., Soong, S.-T., 1987: Statistical properties of a cloud ensemble: A numerical study, *J. Atmos. Sci.*, 44, 3175-3187.
- Tripoli, G.J., 1992: A non hydrostatic model designed to simulate scale interaction, *Mon. Weather Rev.*, 120, 1342-1359.
- Tsang, L., Kong, J.A., 1977: Theory of thermal microwave emission from a bounded medium containing spherical scatterers. *J. Appl. Phys.*, 48, 3593 - 3599.
- Tsang, L., Kong, J.A., Shin, R.T., 1985: Theory of microwave remote sensing, Wiley & Sons, New York.
- Ulaby, F.T., Moore, R.K., Fung, A.K., 1982: Microwave remote sensing, vol. I, Addison-Wesley, London (GB).
- Ulaby, F.T., Moore, R.K., Fung, A.K., 1982: Microwave remote sensing. Vol. III, Addison-Wesley, London (GB).
- Vivekanandan, J., Turk, J., Stephens, G.L., and V.N. Bringi, 1990: Microwave radiative transfer studies using combined multiparameter radar and radiometer measurements during COHMEC. *J. Appl. Meteor.*, 29, 561-585.
- Weinman, J.A., Davies, R., 1978: Thermal microwave radiances from horizontally finite clouds of hydrometeors. *J. Geophys. Res.*, 83, 3099 - 3107.
- Wilheit, T.T., 1979: A model for the microwave emissivity of the ocean's surface as a function of windspeed, *IEEE Trans. Geosci. Electron.*, GE-17, 244-249.
- Wilson, D.R. and Ballard, S.P., 1999: A microphysically based precipitation scheme for the UK Meteorological Office Unified Model, accepted by Quart. J. Royal Meteorol. Soc.
- Wiscombe, W.J., 1980: Improved Mie scattering algorithms, *Appl. Opt.*, 19, 1505-1515.

## A **Permittivity models**

### Maxwell-Garnett

Following Maxwell-Garnett (1904; MG), an inhomogeneous particle is considered as a matrix material with randomly distributed spherical inclusions whose contributions are weighted by the volume fractions of the inclusions,  $f_i$ :

$$\epsilon_{eff} = \epsilon_m \frac{(\epsilon_i + 2\epsilon_m) + 2f_i(\epsilon_i - \epsilon_m)}{(\epsilon_i + 2\epsilon_m) - f_i(\epsilon_i - \epsilon_m)} \quad (6)$$

For randomly oriented elliptical inclusions the notation of Bohren and Battan (1982) reads:

$$\begin{aligned}\epsilon_{eff} &= \frac{(1-f_i)\epsilon_m + f_i\beta\epsilon_i}{1-f_i+f_i\beta} \\ \beta &= \frac{2\epsilon_m}{\epsilon_i-\epsilon_m} \left[ \frac{\epsilon_i}{\epsilon_i-\epsilon_m} \log \left( \frac{\epsilon_i}{\epsilon_m} \right) - 1 \right]\end{aligned}\quad (7)$$

$\epsilon_{eff}$ ,  $\epsilon_m$ , and  $\epsilon_i$  denote the complex permittivities of the mixture, the matrix, and the inclusion, respectively. The component with the small volume fraction is usually considered geometrically disconnected so that the imaginary part of the effective permittivity is driven by that of the component with the large volume fraction.

### Bruggemann

Aggregates are treated as mixtures where the contributions of permittivities  $\epsilon_1$  and  $\epsilon_2$  to the effective permittivity are weighted by their volume fraction  $f_1$  and  $f_2$  (Bruggeman, 1935; BR), thus:

$$0 = f_1 \frac{(\epsilon_1 - \epsilon_{eff})}{(\epsilon_1 + 2\epsilon_{eff})} + f_2 \frac{(\epsilon_2 - \epsilon_{eff})}{(\epsilon_2 + 2\epsilon_{eff})} \quad (8)$$

### Meneghini and Liao

Meneghini and Liao (1996; ML) used an error function to interpolate between the permittivities of an air-ice matrix with water inclusions,  $\epsilon_{iaw}$ , and a water matrix with air-ice inclusions,  $\epsilon_{wia}$ , as a function of fractional volume of ice,  $f_i$ , respectively:

$$\begin{aligned}Re(\epsilon_{eff}) &= 0.5 \{ [1 - erf(x)] Re(\epsilon_{wia}) + [1 + erf(x)] Re(\epsilon_{iaw}) \} \\ Im(\epsilon_{eff}) &= 0.5 \{ [1 - erf(x)] Im(\epsilon_{wia}) + [1 + erf(x)] Im(\epsilon_{iaw}) \}\end{aligned}\quad (9)$$

with the error function,  $erf(x)$ , which defines the weight of each configuration as a function of the parameters  $t$  and  $q$ :

$$\begin{aligned}erf(x) &= \frac{2}{\sqrt{\pi}} \int_0^x \exp(-y^2) dy \\ x &= \frac{[f_i/(1-f_i) - t]}{2q}\end{aligned}\quad (10)$$

The tuning parameters,  $t = 0.2$  and  $q = 0.1$ , were adjusted for 7.7 GHz.

Meneghini et al. (1998) updated their technique assuming a linear superposition of the three components air, ice, and water according to the extended effective medium approach of Stroud and Pan (1978):

$$\epsilon_{eff} = \frac{\epsilon_w f_w \langle E_w \rangle + \epsilon_a f_a \langle E_a \rangle + \epsilon_i f_i \langle E_i \rangle}{f_w \langle E_w \rangle + f_a \langle E_a \rangle + f_i \langle E_i \rangle} \quad (11)$$

where  $\epsilon_w$ ,  $\epsilon_a$ , and  $\epsilon_i$  represent the permittivities of water, air and ice with volume fractions  $f_w$ ,  $f_a$ , and  $f_i$ , requiring  $f_w + f_a + f_i = 1$ . The terms in brackets denote the average internal

electric fields assuming that a particle can be decomposed into individual cells over which the fields are homogeneous so that the summation of all cell contributions to the total field is equivalent to the average field multiplied by the number of cells. The ratio of average electric field  $\langle E_a \rangle / \langle E_i \rangle$  in (11) is computed from the Debye-formula assuming a dry snow particle with  $f_i^* + f_a^* = 1$ , and densities of snow, air, and ice,  $\rho_s, \rho_a, \rho_i$ :

$$\begin{aligned}\frac{\langle E_a \rangle}{\langle E_i \rangle} &= \frac{f_i^*(\epsilon_s - \epsilon_i)}{f_a^*(\epsilon_a - \epsilon_s)} \\ \epsilon_s &= \frac{\rho_i + 2k_i\rho_s}{\rho_i - k_i\rho_s} \\ k_i &= \frac{\epsilon_s - 1}{\epsilon_s + 2}\end{aligned}\quad (12)$$

Finally, both real and imaginary parts of  $\langle E_w \rangle / \langle E_i \rangle$  were computed by the conjugate gradient numerical method and parameterized in wavelength (10 - 95 GHz) and fractional melt water.

## Fabry and Szyrmer

The model of Fabry and Szyrmer (1998; FS) stems from comprehensive comparisons with measurements of radar reflectivities at 9.4 GHz and 0.9 GHz and showed a superior performance to any other model treating the particle in the classical fashion as given by MG or BR for different configurations of matrix and inclusion materials. The observations of FS confirm that using MG with a water matrix produces an overexpression of the bright band of radar reflectivity. A concentric shell configuration is assumed including a melting-stage dependent calculation of density change and position of the boundary between inner and outer shell. The density of a melting particle,  $\rho_m$ , is calculated from:

$$\rho_m = \frac{\rho_s \rho_w}{f_w^m \rho_s + (1 - f_w^m) \rho_w} \quad (13)$$

where  $\rho_s$  and  $\rho_w$  denote the densities of snow and water while  $f_w^m$  denotes the meltwater mass fraction. For a two-shell snowflake with a density discontinuity at radius  $r = r_s \alpha$ , the resulting densities of the core,  $\rho_{s,core}$ , and coat,  $\rho_{s,coat}$ , are:

$$\rho_{s,core} = \frac{\rho_s}{\alpha^\beta}, \quad \beta = -1, \quad \rho_{s,coat} = \rho_s \frac{1 - \alpha^{3+\beta}}{1 - \alpha^3} \quad (14)$$

which implies the assumption that snow density is a function of particle diameter, i.e.,  $\rho_s \propto D_s^{-1}$ . Once melting is initiated these densities change according to (13) and (14):

$$\rho_{m,core} = \frac{\rho_{s,core} \rho_w}{f_w^m \rho_{s,core} + (1 - f_w^m) \rho_w} \quad (15)$$

$$\rho_{m,coat} = \frac{\rho_{s,coat} \rho_w}{f_w^m \rho_{s,coat} + (1 - f_w^m) \rho_w} \quad (16)$$

The position of the density discontinuity is also a function of melting stage. FS assumed that  $\alpha = 0.5$  right before melting onset and continuously approaches 1 during melting following:

$$\alpha_m = \left[ \frac{\rho_w r_s^3 - \rho_{m,coat} r_m^3}{r_m^3 (\rho_{m,core} - \rho_{m,coat})} \right]^{1/3} \quad (17)$$

where  $r_m$  denotes the radius of the discontinuity position during melting while  $r_w$  denotes the radius of the completely melted particle. The optical properties can then be calculated using a Mie-code for concentric shell - type spheres (e.g., Bohren and Huffman, 1983).

## B 3-D recursive solution for isotropically scattering media

It is convenient to define the angular average,  $U$ , of the brightness temperature,  $TB$ , and rewrite the radiative transfer equation, RTE, for  $U$  in a more compact form by using the convolution operator. The crucial step is to recognize that the Laplace transform of the last equation represents the summation of a geometrical series in which  $U$  can be expressed through (Brussaard, 1985). By anti-transforming, it follows that the pseudo-source function,  $J$ , is given by:

$$J(\tau) = (1 - \omega_o)B(T) + U(\tau) = \sum_n J_n(\tau) \quad (18)$$

where  $\tau$  is the optical thickness unit-vector,  $\omega_o$  is the single scattering albedo,  $B(T)$  the black-body radiance associated with volume temperature.  $J_o(\tau) = (1 - \omega_o)B(T)$  and the successive order  $J_n$  can be computed through appropriate integral expressions (Marzano et al., 1999).

Since the above iterative solution has been derived under the restrictive assumption of isotropic scattering, the scattering phase function is unitary, that is its volumetric asymmetry factor  $g$  is zero (Gasiewski, 1993). Thus, it is interesting to analyze the validity limits imposed by this condition for the considered ground-based radiometry application in the 10-50 GHz band. It has been shown that, for rainrates ( $R$ ) up to 75 mm/h, the single scattering albedo is always less than 0.5 and increases monotonically due to the increase of scattering. Correspondingly, the asymmetry factor remains around -0.10 at 13.0 GHz, meaning that the backward scattering is dominant, and amounts to 0.15 at 50.2 GHz, where the forward scattering is the prevailing effect. For the intermediate frequencies at 23.8 and 31.6 GHz it is between -0.05 and 0.05. Thus, we can conclude that for  $R$  less than 75 mm/h and in the 10-50 GHz frequency band the error due to the isotropic scattering assumption is in average less than 10% (Marzano et al., 1997).

In case of atmospheric precipitation, convective raincells can be idealized as finite volumes whose width and height may depend on the precipitation intensity itself (Capsoni et al., 1987; Kummerow and Weinman, 1988). The main features of convective precipitation are that the clouds are horizontally finite (some kilometers) and strongly vertically extended (up to the tropopause) (Houze, 1982; Smith et al., 1992). A cylindrical shape for convective rainfall is a common idealization and this is the reason why we have specialized our 3-D model for finite circular cylinders. To the purpose of computing the source function  $J$ , the cylindrical volume has been divided into sub-volumes, determined by the interception of concentric cylindrical surfaces with parallel planes. In particular, the diameter has been subdivided into 10 intervals and the height into 20 intervals. For media with  $\omega_o < 0.6$ , which is the raincell case, it has been verified that a cutoff number  $N$  of the series expansion of  $J$  equal to 4 is sufficient to ensure the series convergence. After computing  $J$  within each subvolume, the integral form of the RTE has been solved through a Gauss-Legendre quadrature by selecting the subvolumes intercepted by the propagation direction line.

## C Model descriptions

Table 1: Radiative transfer model summary.

Features	UKMO	DLR-1	DLR-2	UBonn
Applications:	model validation, data assimilation, instrument preprocessing testing	retrieval technique development	retrieval technique development	fundamental research, retrieval technique development, model validation
Targeted sensors:	SSM/I, TMI, AMSU, SSM/T2, aircraft	SSM/I, TMI, AMSU, SSM/T2, PR	SSM/I, TMI, AMSU, SSM/T2	ground based sensors, aircraft, SSM/I, TMI, AMSU, SSM/T2
Model dimensions:	1-D	1-D	1-D	1-D
Model type:	Eddington	Eddington	Matrix Operator	SOS and iterative solution
Polarization:	quasi	quasi	4 Stokes parameters, skalar coeffs.	4 Stokes parameters, angle dependent extinction matrix and absorption vector
Based on:	Kummerow (1993)	Weinman and Davies (1978)	Plass et al. (1973), Bauer and Schluesel (1993)	Simmer (1994), Czekala and Simmer (1998)
Contact:	dcjones@meto.gov.uk	peter.bauer@dlr.de	peter.bauer@dlr.de	hczechala@uni-bonn.de
Frequency range:	5-1000** GHz (200 GHz for sea surface)	1-1000** GHz	1-1000** GHz	1-1000** GHz
Zenith angles:	0-70°	any	any	any
Input parameters:	$z, p, T, f, q_c, q_r, q_i, T_o, u$	$z, p, T, q_w, q_c, q_r, q_s, q_g, q_h, q_i, T_o, u, C_v, C_w, \sigma, m_v, m_s$	as in DLR-1	atmospheric profiles (radiosondes, artificial, automatic generation from given key values)
Output parameters:	<b>TB</b> , <i>LWP</i> , <i>IWP</i> , <i>WVP</i>	<b>TB</b> , <b>Z</b> , <i>LWP</i> , <i>IWP</i> , <i>WVP</i> , <b>wf</b>	as in DLR-1	$\text{TB}(z, \theta)$ (Stokes vector in every altitude), <i>LWP</i> , <i>IWP</i> , <i>WVP</i> , <b>wf</b>

(\*\* = only for the atmosphere)

Table 2: Radiative transfer model summary (cont'd).

Features	UKMO	DLR-1	DLR-2	UBonn
Gas absorption:	MPM-89	MPM-92 (all MPMs)	MPM-92 (all MPM)	MPM-92 (all MPM)
Hydrometeor size distributions:		non-precip.: mod- $\gamma$ , precip.: exponential	non-precip.: mod- $\gamma$ , precip.: exponential	nearly arbitrary
Hydrometeor treatment:	Mie-calculations (Wiscombe, 1990)	Mie-calculations	Mie-calculations	T-Matrix, DMF and Mie
Special features:		melting hydrometeors, slant paths	melting hydrometeors	non-spherical particles with preferred orientation, scattering database
Ocean surfaces:				
Water permittivity:	Lamkaouchi (1997)	Guillou et al. (1998)	Guillou et al. (1998)	Ulaby et al. (1986)
Foam coverage / emissivity:	Monahan and O'Muircheartaigh (1986)	Monahan and Lu (1990), Stogryn (1972)	Monahan and Lu (1990), Stogryn (1972)	Wisler and Hollinger (1986), Monahan and O'Muircheartaigh (1986), Wilheit (1979), Stogryn (1972)
Scattering model:		Guissard et al. (1992)	Guissard et al. (1992)	
Wave model:	Wilheit (1979), Choudhury (1979)	Lemaire et al. (1998)	Lemaire et al. (1998)	3-scale facet model (Schrader, 1995), Cox and Munk (1954)
Land surfaces:				
soil emissivity:		Tsang and Kong (1977), Dobson et al. (1985)	Tsang and Kong (1977), Dobson et al. (1985)	Input data
vegetation transmissivity:		Ulaby et al. (1986)	Ulaby et al. (1986)	Input data
roughness parameterization:		Kerr and Njoku (1990)	Kerr and Njoku (1990)	Input data
Further development:	slant-paths, melting layer	improved melting physics, param. non-sphericity	improved melting physics, param. non-sphericity	3D, melting layer, different particle orientations

Table 3: List of Parameters.

$T$	= dry bulb temperature
$p$	= pressure
$z$	= altitude
$f$	= relative humidity
$q_w$	= specific humidity
$q_c$	= cloud liquid water content
$q_r$	= rain liquid water content
$q_s$	= snow water content
$q_g$	= graupel water content
$q_h$	= hail water content
$q_i$	= cloud ice water content
$T_o$	= surface temperature
$u$	= near-surface windspeed
$C_v$	= fract. vegetation coverage
$C_w$	= fract. water coverage
$\sigma$	= roughness parameter
$m_v$	= integrated vegetation water path
$m_s$	= volumetric soil moisture
<b>TB</b>	= brightness temperature vector
<b>Z</b>	= radar reflectivity vector
<i>LWP</i>	= liquid water path
<i>IWP</i>	= ice water path
<i>WVP</i>	= water vapor path
<b>w<sub>f</sub></b>	= weighting fct. matrix.

# Microwave emission from covered surfaces: zero-order versus multiple scattering

Christian Mätzler

## 1 Introduction

Much of the earth's surface is covered by canopies like vegetation or snow; therefore it is instructive to compare approaches to model microwave emission of such systems (Figure 1). For an observer from above, a growing cover is an increased screening of the underlying surface by scattering, absorption and self emission. Here the discussion is limited to soft covers by which is meant that the transition from the atmosphere to the canopy is gentle enough to avoid reflections. Reflection is accounted for at the bottom surface, and volume interactions are allowed inside the cover. Limited lateral inhomogeneity will be considered, but polarization effects are neglected. The models can be extended to include polarization, hard covers and multi-layer systems. It will be found that model errors can be corrected by redefining the model parameters in appropriate ways.

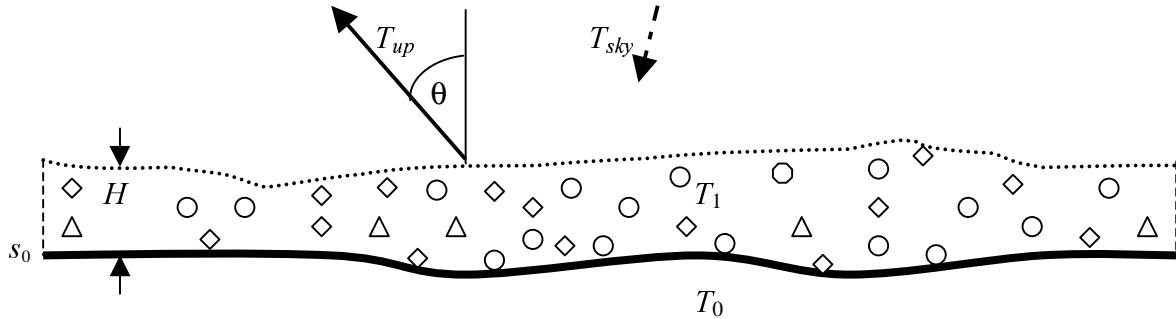


Figure 1: Geometry of thermal radiation from the earth's surface at temperature  $T_0$  covered by a soft canopy at temperature  $T_1$  of thickness  $H$ , being illuminated by  $T_{sky}$ .

## 2 Zero-order scattering model (Kirdiashev et al. 1979)

The zero-order scattering model of Kirdiashev et al. (1979) is often used in passive microwave radiative transfer. Zero order means that the scattering source function is neglected in the radiative transfer equation (s. Chanzy and Wigneron, 2000, this issue, Sect. 2.2, p. 90). This model gives a lower bound of the emissivity, but by using effective parameters, the model becomes quite realistic. Energy conservation is recovered by Equation (13) below. The upwelling brightness temperature  $T_{up}$  at an angle  $\theta$  from zenith, including single interactions between canopy and ground, is given by

$$T_{up} = (1 - s_0) L T_0 + (1 + L s_0)(1 - L)(1 - \omega^*) T_1 + [\omega^*(1 - L)(1 + s_0 L) + s_0 L^2] T_{sky} \quad (1)$$

where  $T_0$  and  $T_1$  are the soil and vegetation temperature, respectively,  $T_{sky}$  the downwelling sky brightness temperature,  $s_0$  is the soil reflectivity,  $\omega^*$  the effective single scattering albedo

$$1 - \omega^* = k_a / k_e^* \quad (2)$$

and  $L$  the cover attenuation, given by

$$L = \exp(-\tau^*/\mu); \mu = \cos(\theta); \tau^* = k_e^* H \quad (3)$$

where  $\tau^*$  is the effective vegetation opacity which depends on the effective extinction coefficient  $k_e^*$  and the cover height  $H$ . Equation (1) corresponds to Equation (3) of Chanzy and Wigneron, 2000, this issue, with the additional contribution by sky radiation, and using their Expressions (5) and (6) where the unwanted contributions from forward scattering are removed (Delta-Eddington approximation).

#### **Relationship to other models**

1) With regard to the HUT snow emission model (Pulliainen et al. 1999), it can be shown that for negligible reflection ( $s_1=0$ ) at the air-snow interface, this model is equivalent to the model of Kirdiashev et al. (1979) if the effective extinction coefficient  $k_e^*$  is represented by

$$k_e^* = k_e - q(k_e - k_a) ; \quad 0 < q < 1 \quad (4)$$

where  $q$  is the fraction of forward-scattered radiation (Ishimaru, 1978). In the HUT model  $q$  is regarded as a fitting parameter, often assumed to be close to 1. Basically,  $q$  is a function of frequency and snow grain size and can be estimated from theoretical considerations, e.g. by using the strong fluctuations approach. The definition of  $k_e^*$  given by (4) is equivalent to the one of Chanzy and Wigneron, 2000, this issue. Finally it is noted that the full HUT model includes polarization and non-zero values of  $s_1$ .

2) The emission model of Ulaby and Stiles (1980), see also (1)-(5) in Johnsen and Heygster, 2000, this issue, again for negligible reflection at the cover surface ( $s_1=0$ ), is similar to the model of Kirdiashev et al. (1979); however, the factors  $(1+s_0L)$  in Equation (1) are replaced by 1, and the term  $s_0L^2$  is ignored. Thus ground reflections of downwelling radiation are ignored.

### **3 Multiple-scattering model in two-stream approach (MEMLS\_simplified)**

The Delta-Eddington approximation is also applied in multiple scattering using the two-stream approach. Meador and Weaver (1980) showed that different formulations of this approach are equivalent. Let us therefore consider just one of them, the snow emission model MEMLS of Wiesmann and Mätzler (1999), see also Mätzler et al. (2000) in this issue. It can be adapted to Figure 1, by considering a single layer ( $n=1$ ) on top of a soil surface. For a canopy with low density, the effective refractive index can be approximated by 1; then there is no refraction and no reflection at the cover surface. Furthermore there is no trapped radiation within the cover because total reflection is absent. With these simplifications the observable brightness temperature  $T_{up}$  is given by

$$T_{up} = t_1 s_0 \frac{r_1(1-s_0)T_0 + t_1 T_{sky} + e_1 T_1}{1 - r_1 s_0} + t_1(1-s_0)T_0 + r_1 T_{sky} + e_1 T_1 \quad (5)$$

where the internal reflectivity  $r_1$  and transmissivity  $t_1$  of the scattering layer are

$$r_1 = r_0 \left(1 - t_0^2\right) \left(1 - r_0^2 t_0^2\right)^{-1} \quad (6)$$

$$t_1 = t_0 \left(1 - r_0^2\right) \left(1 - r_0^2 t_0^2\right)^{-1} \quad (7)$$

and for a layer of height  $H$  the one-way transmissivity  $t_0$  through the slab is

$$t_0 = \exp(-\gamma H / \cos \theta) \quad (8)$$

the reflectivity  $r_0$  at infinite thickness is

$$r_0 = \gamma_b (\gamma_a + \gamma_b + \gamma)^{-1} \quad (9)$$

and the effective attenuation coefficient  $\gamma$  (eigenvalue of the two-stream model) is

$$\gamma = \sqrt{\gamma_a(\gamma_a + 2\gamma_b)} \quad (10)$$

where  $\gamma_a$  is the absorption coefficient and  $\gamma_b$  the scattering coefficient (excluding forward scattering) of the cover. In case of a non-vanishing reflectivity at the cover surface, the appropriate formulae (7) and (10) of Wiesmann and Mätzler (1999) with  $s_1 > 0$  can be used instead of Equation (5) above, and in case of a multi-layer medium the model becomes the full MEMLS, including vertical and horizontal polarization.

## 4 Comparison

All models describe  $T_{up}$  as linear combinations of three temperatures  $T_0$ ,  $T_1$  and  $T_{sky}$

$$T_{up} = tT_0 + eT_1 + rT_{sky} = e_{sys}T + rT_{sky} \quad (11)$$

where  $t$  is the effective transmissivity for radiation from the underlying surface,  $e$  the layer emissivity,  $e_{sys} = e+t$  and  $r$  are the emissivity and reflectivity of the ground and cover system, and  $T$  is the effective temperature of this system, i.e. a weighted mean value:

$$T = \frac{tT_0 + eT_1}{e + t} \quad (12)$$

Often the temperature of the ground and of the layer are the same; then  $T=T_0=T_1$ . The parameters  $e$ ,  $r$ ,  $t$ , and  $e_{sys}$  are related by Kirchhoff's Law (Kirchhoff, 1860):

$$e + r + t = 1, \quad \text{or} \quad e_{sys} = e + t = 1 - r \quad (13)$$

Expressions for  $e$ ,  $r$  and  $t$  as predicted by the two models are shown in Table 1 together with the corresponding absorption and scattering coefficients.

*Table 1:* Parameters of the two models, describing the microwave radiation according to (11) from a single layer ( $n=1$ ) on top of a soil surface with reflectivity  $s_0$ .

Parameter	Zero-Order Scattering Model Kirdiashev et al., HUT( $s_1=0$ ), etc.	Multiple-Scattering Model MEMLS ( $n=1$ , $s_1=0$ )
absorption coefficient	$k_a$	$\gamma_a$
scattering coefficient	$k_s^* = k_e^* - k_a$	$\gamma_b$
$t$	$L(1-s_0)$	$t_1 \frac{1-s_0}{1-r_1 s_0}$
$e$	$(1-\omega^*)(1-L)(1+s_0L)$	$(1-r_1-t_1) \frac{1+s_0(t_1-r_1)}{1-r_1 s_0}$
$r$	$\omega^*(1-L)(1+s_0L) + s_0 L^2$	$\frac{r_1 + s_0(t_1^2 - r_1^2)}{1-r_1 s_0}$

There are three parameters in each model ( $\omega^*$ ,  $L$ ,  $s_0$  in Kirdiashev's model,  $r_1$ ,  $t_1$ ,  $s_0$  in MEMLS) derived from 4 physical parameters (absorption coefficient, scattering coefficient,  $H$  and  $s_0$ ). Of the 3 output parameters  $e$ ,  $r$ ,  $t$  only 2 are independent. Multiple interactions lead to products of  $s_0 r_1$  in Table 1 and to terms including  $r_0^2$  in (6) and (7). Now, all multiple interactions may be taken into account in Kirdiashev's model in such a way that  $e$ ,  $r$  and  $t$  agree with the multiple scattering model, namely by redefining the parameters  $L$  and  $\omega^*$  :

$$L = \frac{t_1}{1 - r_1 s_0} \quad \text{and} \quad \omega^* = r_1 \left( 1 + t_1 \frac{1 - s_0}{1 - r_1 s_0 - t_1} \right) \quad (14)$$

In these quantities the parameters of the cover and of the ground appear to be coupled. Thus in an extended interpretation, the model of Kirdiashev et al. (1979) is sufficient for describing all situations, including those where multiple scattering dominates. However, model parameters should be used carefully. As shown above they tend to be coupled. This became already apparent in Equations (5) and (6) of Chanzy and Wigneron (2000) where the classical  $\omega$ ,  $\tau$  radiative transfer parameters were transformed by the Delta-Eddington method to account for effective scattering and extinction applicable to the given geometry, i.e. the removal of forward scattering. In the examples to follow, we will return to the original definitions of  $L$  and  $\omega^*$ , concentrating on  $r = 1 - e_{\text{sys}}$ . This is the key parameter of interest here.

### **Optically thin cover**

Although it is not quite apparent, it can be shown that for an optically thin cover both models give identical results. Then  $L = t_1 \Rightarrow 1$ , and for  $s_0=0$ , we have  $r = k_s^* H = \gamma_b H \Rightarrow 0$ . The reflectivity increases linearly with layer thickness. This is shown in Figure 2 ( $s_0 = 0$ ,  $k_s^* = k_e^* - k_a = 1/\text{m}$ ) for small thickness ( $H \ll 1\text{m}$ ). With increasing thickness in Figure 2, the two models start to differ, giving smaller  $r$  for the multiple-scattering model. The screening of the soil reflectivity by the canopy is shown in the semi-log representation of Figure 3 for  $s_0 = 0.3$ . The values of  $r$  are quite similar in both models up to a thickness of 10 cm in the high absorption case and even up to 30 cm for low absorption.

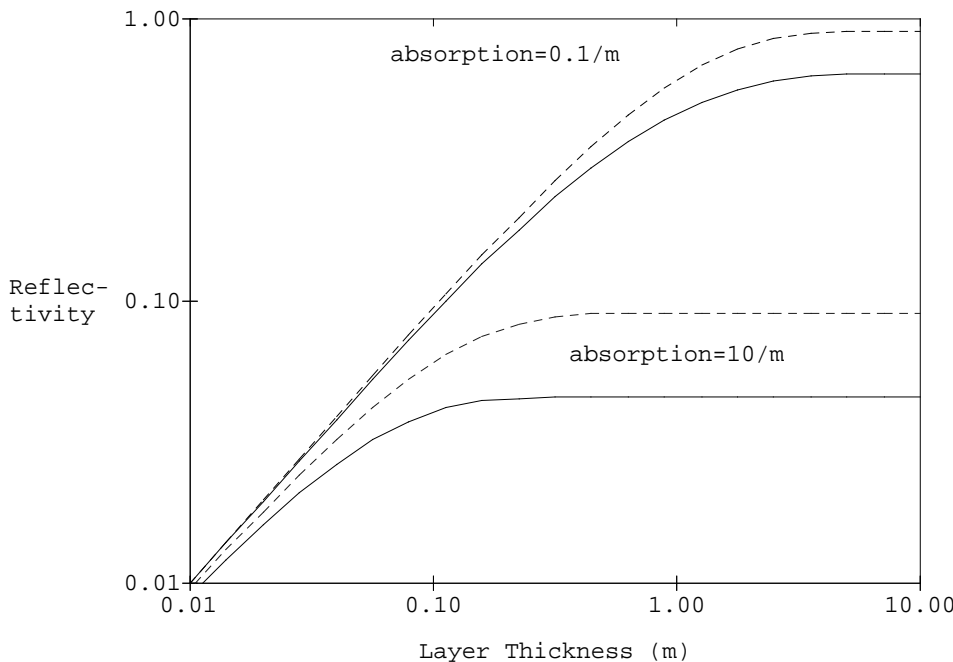
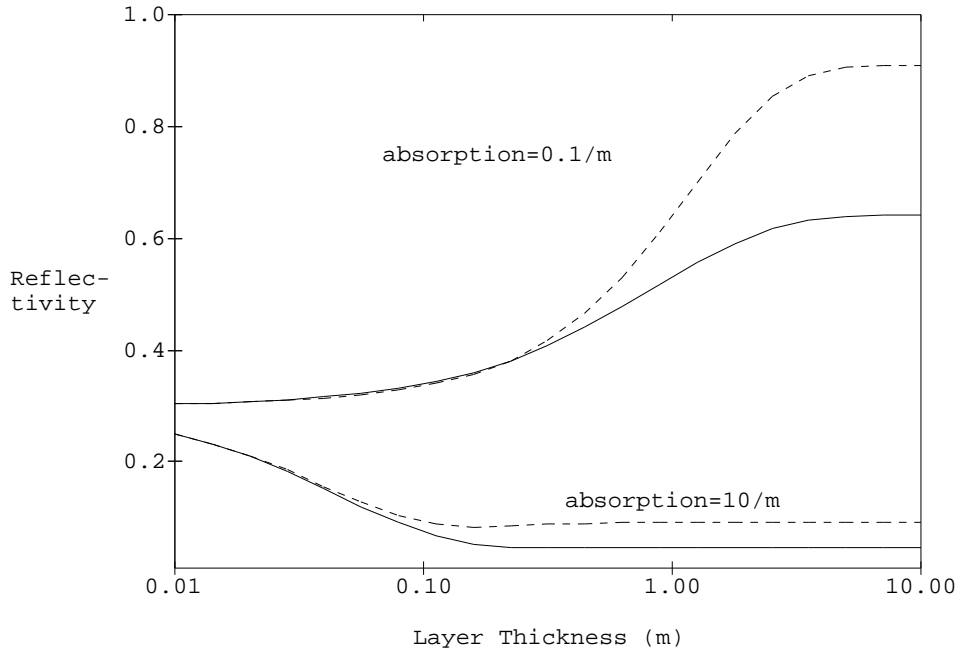


Figure 2: Reflectivity  $r$  for  $s_0 = 0$ , effective scattering coefficient  $k_s^* = \gamma_b = 1/\text{m}$  versus layer thickness for two different values of the absorption coefficient ( $k_a = 0.1/\text{m}$  and  $10/\text{m}$ , respectively) for the zero-order (dashed) and multiple-scattering (solid line) model.



*Figure 3:* Same as Figure 2, for  $s_0 = 0.3$ , with linear reflectivity scale .

### Optically thick cover

Differences between zero-order and multiple-scattering models are especially apparent if a deep cover is considered, i.e. if  $t = L = t_1 = 0$  and  $r_1 = r_0$ . In this situation  $e$  and  $r$  of Table 1 reduce to the ones of Table 2.

*Table 2:* Parameters  $e, r$  for vanishing transmissivity.

Parameter	Kirdiashov	MEMLS ( $n=1, s_1=0$ )
$e$	$1-\omega^*$	$1-r_0$
$r$	$\omega^*$	$r_0$

The reflectivity approaches  $\omega^*$  in the zero-order model and  $r_0$  in the multiple-scattering model. That there is a significant difference between  $\omega^*$  and  $r_0$  is apparent from Figure 4. For small ratios  $x = k_s^*/k_a$  the difference is a factor of 2 in  $r$ . In both models  $r \Rightarrow 1$  for  $x \Rightarrow \infty$ . However, the convergence is quite different. In the zero-order model we have

$$1-r = 1 - \omega^* = 1 - \frac{x}{x+1} \Rightarrow \frac{1}{x} ; \quad x \gg 1 \quad (15)$$

whereas in the multiple-scattering model the convergence is

$$1-r = 1 - r_0 = 1 - \frac{x}{x+1+\sqrt{1+2x}} \Rightarrow \sqrt{\frac{2}{x}} ; \quad x \gg 1 \quad (16)$$

Thus the convergence is much more rapid in Equation (15). The exact theory and observations show that (16) is more accurate than (15), see Chandrasekhar (1960), Bohren and Barkstrom (1974) and Bohren (1987).

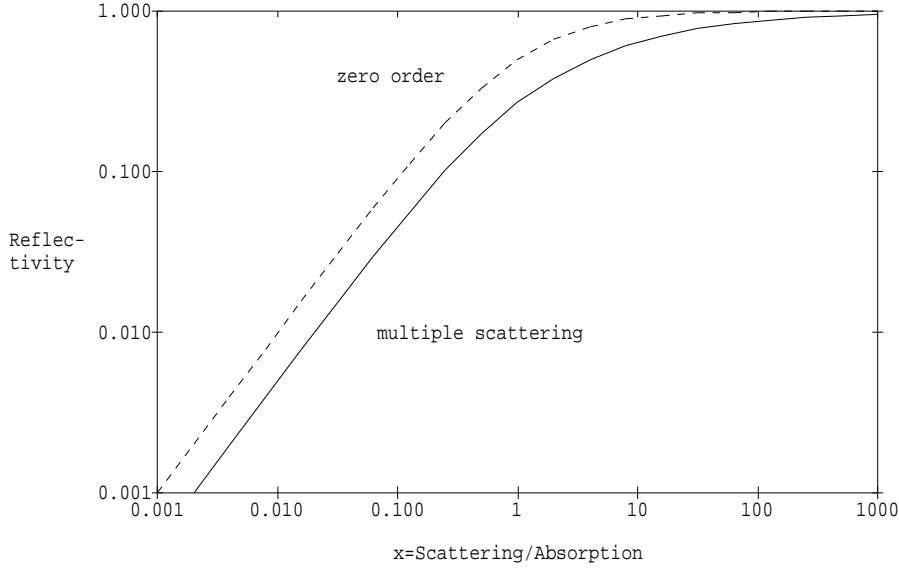


Figure 4: Reflectivity of a half space ( $t = 0$ ) versus ratio of scattering to absorption coefficient in zero-order ( $\omega^*$ , dashed) and multiple scattering ( $r_0$ , solid line) approximation.

## 5 Effects of lateral inhomogeneity

In order to expand the models to three-dimensional geometry, as indicated by the lateral thickness variation in Figure 1, a smoothness condition for the lateral inhomogeneity is needed to avoid large changes in the parameter vector  $\mathbf{P} = (H, k_e^*, k_a, \gamma_a, \gamma_b)$  over the lateral distance,  $H \tan \theta + \delta$ , over which a ray travels when traversing the layer. Here  $\delta$  is the lateral diffusion length due to scattering which is estimated from the scattering coefficient  $k_s$  (now including forward scattering) and the mean number  $k_s H$  of scattering events over  $H$

$$\delta \approx k_s H^2 \text{ for } k_s H < 1; \quad \delta \approx \sqrt{\frac{H}{k_s}} \text{ for } k_s H > 1; \quad (17)$$

From (17) we find that  $\delta < H$ . Now, the one-dimensional models can be applied to three-dimensional canopies if

$$\overline{(\delta + H \tan \theta) \left| \frac{\partial P_j}{\partial l} \right|} \ll \overline{P_j} \quad (18)$$

where  $l$  is a lateral displacement, and the averaging (indicated by overbars) is to be done over the pixel area. If Condition (18) is fulfilled, Equation (11) can be applied to every surface element, and by averaging the results  $T_{up}$  over a given footprint of size  $A$ , the pixel brightness temperature at the bottom of the atmosphere

$$\overline{T_{up}} = \frac{1}{A} \int_A T_{up} dA \quad (19)$$

is obtained. The exponential attenuation introduces a nonlinearity of  $T_{up}$  with regard to height, biomass, water content etc. Linearity results only for optically thin canopies.

An example of an inhomogeneous cover is the tundra snowcover of Figure 5. The emissivity  $e_{sys}$  of the ground-canopy system, consisting of 4 snow layers, was computed with MEMLS. The cover is optically thin at 35 GHz, thus the results are correlated with layer thickness, here dominated by the ground height, see Figure 6 (left). On the other hand the snow is optically

thick at 94 GHz, thus there is no correlation between emissivity and thickness; however a correlation with the height of the snow surface can be seen, see Figure 6 (right). This is due to a modulation by hoar layers present within the snowpack (Sturm and Holmgren, 1994).

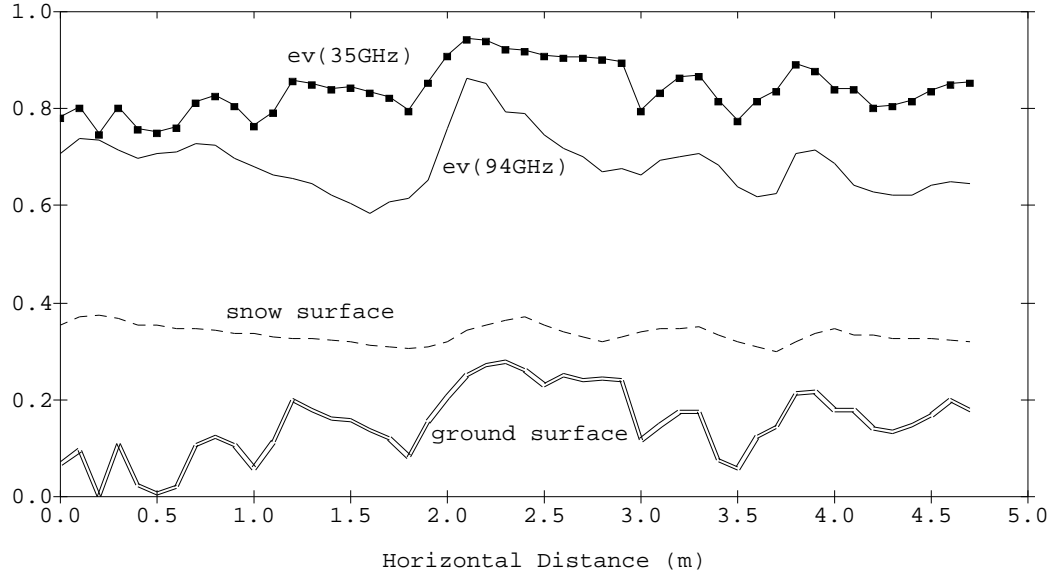


*Figure 5:* System emissivity at vertical polarization,  $\theta=50^\circ$ , 35 GHz (pointed solid line) and 94 GHz (solid line) along a horizontal distance of a 4-layer snowcover in the tundra of Alaska. The surface heights of ground (double) and snowpack (dashed line) are shown (in m). Snow data from Sturm and Holmgren (1994), microwave simulation with MEMLS.

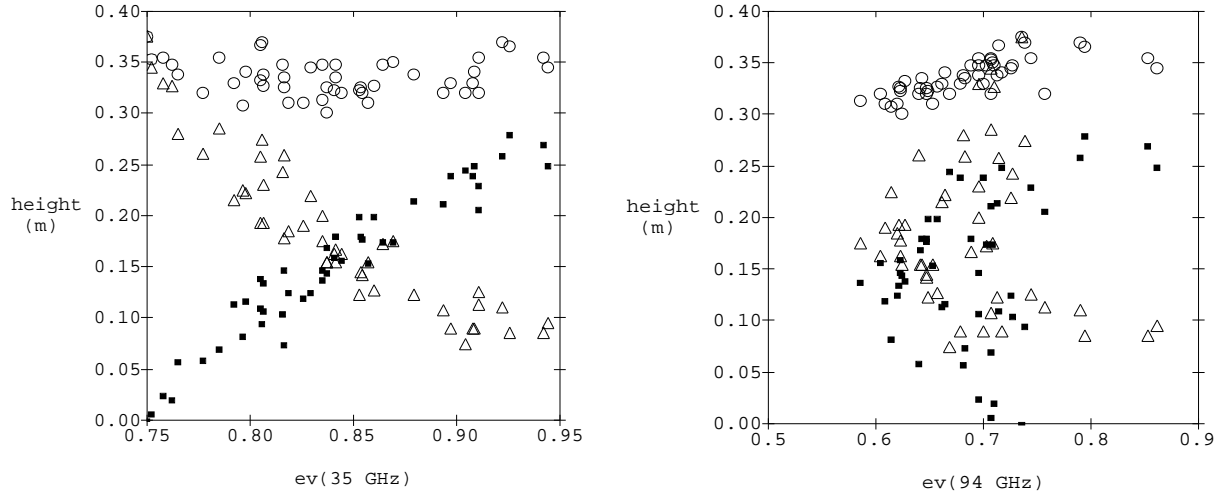


*Figure 6:* Correlations between system emissivity at vertical polarization,  $\theta=50^\circ$ , 35 GHz (left) and 94 GHz (right) and heights of ground surface (points) and snow surface (o) and snowpack thickness ( $\Delta$ ).

## 6 Conclusions

Zero-order and multiple-scattering models for microwave emission from covered surfaces were presented and compared. Apart from three temperatures, the system is characterized by three independent model parameters to be derived from four physical parameters (cover height, absorption coefficient, scattering coefficient and soil-surface reflectivity). Conclusions are:

- Both models consider the same situation, both cover the full range of  $e$ ,  $r$ ,  $t$  from 0 to 1, and both can be extended to three-dimensional situations for conditions limited by (18).
- Differences arise for appreciable attenuation and volume scattering. Therefore any physical interpretation in terms of scattering parameters should be done carefully. This is important if radiometric data are used to derive scattering and absorption coefficients, single-scattering albedo and optical depth.
- Multiple scattering models are physically more correct; they should be given preference in physical interpretation when the opacity is not small. Noticeable differences occur even for small values of the ratio, scattering to absorption coefficient. Furthermore, since small-angle forward scattering is ineffective in the situation described here, suitable modifications of the scattering and extinction coefficients (Equation (4), Delta-Eddington Approximation) are needed.
- Due to the neglect of the scattering source function, the zero-order model generally leads to a smaller emissivity, i.e. larger reflectivity than the multiple-scattering model, see Figs. 2 to 4. An exception is seen in Figure 3 for thickness values near 0.1 m where one dashed curve is slightly below the solid line. This is due to the neglect of multiple interactions between soil and cover in the zero-order model.

## References

- Bohren C.F. and B.R. Barkstrom, "Theory of the optical properties of snow", *J. Geophys. Res.*, Vol. 79, pp. 4527-4535 (1974).
- Bohren C.F., "Multiple scattering of light and some of its observable consequences", *Amer. J. Phys.* Vol. 55, pp. 524-533 (1987).
- Chandrasekhar, S. "Radiative Transfer", Dover Publication, New York (1960).
- Chanzy A. and J.P. Wigneron, "Microwave emission from soil and vegetation", this issue, pp. 89-103 (2000).
- Ishimaru A. "Wave propagation and scattering in random media", Vol. 2, Equation (14-73), Academic Press, New York (1978).
- Johnsen K.P. and G. Heygster, "Emissivity modelling of sea and lake ice", this issue, p. 149 (2000).
- Kirchhoff G. "Über das Verhältnis zwischen dem Emissionsvermögen und dem Absorptionsvermögen der Körper für Wärme und Licht", *Poggendorfs Annalen der Physik und Chemie*, Bd. 19, pp. 275-301 (1860).
- Kirdiashev K.P., A.A. Chucklantsev and A. Shutko, "Microwave radiation of the earth's surface in the presence of vegetation cover", *Radioteknica*, Vol. 24, pp. 256-264 (1979).
- Mätzler C., A. Wiesmann, J. Pulliainen and M. Hallikainen, "Development of microwave emission models of snowpacks", this issue, p. 105 (2000).
- Meador W.E. and W.R. Weaver, "Two-stream approximations to radiative transfer in planetary atmospheres: A unified description of existing methods and a new improvement", *J. Atmosph. Sci.* Vol. 37, pp. 630-643 (1980).
- Pulliainen J., Grandell J., Hallikainen M., "HUT snow emission model and its applicability to snow water equivalent retrieval," *IEEE Trans. Geosci. Remote Sensing*, Vol. 37, pp. 1378-1390 (1999).
- Sturm M., and J. Holmgren, "Effects of microtopography on texture, temperature and heat flow in Arctic and sub-Arctic snow", *Annals of Glaciol.*, Vol. 19, pp. 63 – 68 (1994).
- Ulaby F.T., and W.H. Stiles, "The active and passive microwave response to snow parameters", *J. Geophys. Res.* Vol. 85, pp. 1045-1049 (1980).
- Wiesmann, A. and C. Mätzler, "Microwave emission model of layered snowpacks", *Remote Sensing of Environment*, Vol. 70, pp. 307-316 (1999).

# Relief effects for passive microwave remote sensing<sup>1</sup>

Christian Mätzler and Andy Standley

## Abstract

The signal of a microwave radiometer observing a land surface from space is composed of surface and atmospheric contributions, both of which depend on the relief. For proper interpretation of the data these effects should be quantified and, if necessary, taken into account. Relief effects are twofold: First, the path through the atmosphere between the surface and the sensor depends on the altitude of the emitting surface, thus leading to a height-dependent atmospheric influence. The effect can be taken into account by standard atmospheric radiative transfer models if the elevation of the surface and the atmospheric state are known. Second, more relevant for the present discussion is the variable topography of land surfaces, consisting of slopes, ridges and valleys, sometimes with characteristic alignments, and surfaces surrounded by elevated terrain. These surfaces interact radiatively, not only with the atmosphere, but also with each other, leading to the tendency to enhance the effective emission. Under such circumstances, deviations occur from the standard hemispheric emission of a horizontal surface. The interactions do not only depend on topography and emissivity, but also on the bistatic scattering behavior. Special attention will be paid to the radiation enhancement in a landscape of lambertian surfaces with elevated horizons. As an example, simulated data for southern Norway are shown.

## 1 Introduction

Although relief effects can be quite significant for microwave radiometry on land, so far they have not received proper attention. Relief effects are twofold: First, the path between the radiation source at the surface and the sensor depends on the surface altitude, thus leading to relief-dependent atmospheric contributions. This effect is the topic of Section 2. Section 3 is devoted to a variable topography, consisting of valleys and ridges; characteristic effects due to tilted surfaces and elevated horizons will be described and illustrated in Section 4.

## 2 Flat horizon

The classical geometry of remote sensing of the terrestrial surface is a pair of half spaces separated by a horizontal surface, leading to a flat horizon. In this situation there is no shadow of any kind. The relief effects are determined by the dependence of the emitted radiation on surface altitude  $h$ . Blackbody radiation with a brightness temperature equal to the physical temperature  $T_0$  is produced in the lower half space, part of which is transmitted, and thus emitted ( $T_e$ ) into the upper half space where it is sensed by a radiometer. Radiation from the upper to the lower half space ( $T_{sky}$ ) is much smaller than  $T_0$ . The  $p$ -polarized emitted brightness temperature  $T_{ep}$  above a flat surface with reflectivity  $r_p$  (or emissivity  $e_p$ ) is given by

$$T_{ep} = e_p T_0 = (1-r_p) T_0 \quad (1)$$

The upwelling radiation  $T_{up}$  just above the surface is the sum of the radiation emitted by the lower half space and the reflected sky radiation  $T_{sky}$ :

---

<sup>1</sup> Paper submitted to Internat. J. Remote Sensing, Dec. 1998, revised and accepted, June 1999.

$$T_{up} = (1-r_p)T_0 + r_p T_{sky} \quad (2)$$

The brightness temperature  $T_{bp}$  at satellite level is the attenuated upwelling radiation plus the radiation emitted by the atmosphere (atmospheric scattering being neglected):

$$T_{bp}(\theta) = T_{up} t + T_a(1-t) \quad (3)$$

where  $t$  is the atmospheric transmissivity in the observation direction and  $T_a$  is the temperature of the atmosphere. The above equation applies to the polarization and direction corresponding to  $T_{up}$ . In case of an inhomogeneous atmosphere  $T_a$  has to be considered as an effective temperature  $T_{a,up}$  for upwelling radiation. For a plane-parallel atmosphere  $t$  is given by

$$t(h, \theta) = \exp(-\tau_h / \cos \theta) \quad (4)$$

where the zenith opacity  $\tau_h$  is the vertical path integral of the absorption coefficient  $\alpha(z)$  through the atmosphere, starting at the surface. The reflectivity  $r_p$  at polarization  $p = h, v$  in (2) may be composed of a specular, polarized component  $r_{s,p}$  and of a diffuse, unpolarized component  $r_d$ :

$$r_p = r_{s,p} + r_d \quad (5)$$

The following discussion is concentrated on the derivation of expressions for  $T_{up}$  depending on properties of the relief. It will be assumed that the total reflectivity  $r_p$  is given by (5), where  $r_{s,p}$  is a perfectly specular component and  $r_d$  is a lambertian component. In Ulaby et al. (1981, Sec. 4-16.2),  $r_{s,p}(\theta)$  and  $r_d$  are expressed by  $\Gamma(\theta, p)$  and  $0.25\sigma_0^0$ , respectively, where  $\theta$  is the observation angle with respect to the surface normal, and  $p$  is the state of polarization ( $p = v, h$ ). According to Ulaby et al. (1981),  $T_{up}$  can be written as

$$T_{up}(\theta, h) = e_p(\theta)T_0 + r_{s,p}(\theta, p)T_{sky}(\theta, h) + \frac{r_d}{\pi} \iint T_{sky}(\theta_s, \Phi_s, h) \cos \theta_s d\Omega_s \quad (6)$$

where  $h$  is the height of the surface above sea level. The last term in (6) is the diffusely scattered sky radiation, here to be called  $r_d \cdot T_d$ ; as a result of Lambert scattering  $T_d$  depends only on  $h$ . We assume that the incident sky radiation is unpolarized. For a plane-parallel atmosphere  $T_{sky}$  depends on  $\theta_s$  and  $h$  only, thus performing the integration in (6) over azimuth, using  $d\Omega_s = \sin \theta_s d\theta_s d\Phi_s$  leads to

$$T_d(h) = 2 \int_0^{\pi/2} T_{sky}(\theta_s, h) \cos \theta_s \sin \theta_s d\theta_s \quad (7)$$

For an isothermal atmosphere at temperature  $T_a$  with a cosmic background  $T_c$  we have

$$T_{sky}(\theta_s, h) = T_c e^{-\tau_h / \cos \theta_s} + (1 - e^{-\tau_h / \cos \theta_s}) T_a \quad (8)$$

Equation (8) can be used even for a non-isothermal atmosphere if  $T_a$  is an effective air temperature  $T_{a,down}$  for downwelling radiation (e.g. Mätzler, 1992; Ingold et al., 1998). Integration of (7), using (8) gives

$$T_d = T_a - (T_a - T_c) t_d \quad (9)$$

where

$$t_d = 2E_3(\tau_h) = \exp(-\tau_h / \cos \theta_d) \quad (10)$$

is the effective transmissivity of the diffuse sky radiation,  $E_3$  is the exponential integral of order  $n=3$  (Abramowitz & Stegun, 1974), and the last expression in (10) defines the effective

incidence angle  $\theta_d$ . For an optically thin atmosphere ( $\tau_h < 0.2$ ) we have  $\theta_d \approx 60^\circ$  (Mätzler, 1987). Following this representation, we get

$$T_{up} = T_0 e_p(\theta) + T_a r_p(\theta) - (T_a - T_c)[r_{sp}(\theta)t(\theta) + r_d t_d] \quad (11)$$

A simplification occurs if  $\theta = \theta_d$ ; then  $t = t_d$  and

$$T_{up} = T_0 e_p(\theta_d) + T_a r_p(\theta_d) - (T_a - T_c)r_p(\theta_d)t_d \quad (12)$$

Now, since  $\theta_d$  is often between  $50^\circ$  ( $\tau_h \approx 1$ ) and  $60^\circ$  ( $\tau_h = 0$ ), and since this is also the case for the incidence angle of sensors with conical scanning (SMMR, SSM/I, AMSR), this simplified formula has been used frequently. The difference between (11) and (12) is negligible if at least one of the following conditions is valid (plane-parallel atmosphere):

- the atmosphere is sufficiently transparent ( $t_d \approx 1$ ),
- $\theta \approx \theta_d$
- $r_d \approx 0$

After having found the expressions for  $T_{up}$  we can determine its value from surface and atmospheric properties. Inserting  $T_{up}$  in (3) leads to the relief-dependent radiation  $T_{bp}$  at satellite level, including its dependence of on  $h$ .

### 3 Terrain with tilted surfaces

In addition to the altitude effects on atmospheric radiation, there are effects due to tilted surfaces. On the one hand, the local incidence angle of a tilted surface depends on the orientation of the surface with respect to the view direction of the sensor, and on the other hand, the tilted surfaces imply a variable and elevated horizon, depending on azimuth, shadowing parts of the sky. In these directions the incident sky radiation is replaced by the radiation of the elevated landscape.

Because the scale of the relief is assumed to be large with respect to the sensing wavelength, both effects (at the large scale) can be described by geometrical optics. A facet model is indicated, see e.g. Schanda (1986, Section 4.3); such a model was used to describe the microwave emission of the rough sea surface at mm wavelengths by Prigent and Abba (1990) who assumed each facet to be a specularly reflecting surface element. In contrast to their model we allow, in accordance to Section 2, that the surface elements have a partly specular and a partly lambertian component.

#### 3.1 Emission from large-scale rough surfaces

Reflection on and emission from a local surface facet can be treated as in Section 2 with the exception that the surface normal  $\mathbf{n}$  used to define the plane of incidence deviates from the vertical  $\mathbf{z}$  direction by a tilt angle  $\alpha$ , oriented by an azimuth angle  $\phi$  with respect to the global plane of incidence (Figure 1). The transformation from the global to the local plane of incidence affects both the scattering geometry and the polarization. The local angle of incidence  $\theta_l$  is given by

$$\cos \theta_l = \sin \theta \sin \alpha \cos \phi + \cos \theta \cos \alpha \quad (13)$$

Furthermore the linear polarization is rotated by an angle  $\varphi$ , given by

$$\sin \varphi = \sin \phi \sin \alpha / \sin \theta_l \quad (14)$$

After the reflectivities  $r_{vl}(\theta_l)$  and  $r_{hl}(\theta_l)$  have been determined in the local reference frame, they can be represented in the global (satellite-earth surface) frame, taking into account the polarization rotation:

$$r_v(\theta) = r_{vl}(\theta_l) \cos^2 \phi + r_{hl}(\theta_l) \sin^2 \phi \quad (15)$$

$$r_h(\theta) = r_{vl}(\theta_l) \sin^2 \phi + r_{hl}(\theta_l) \cos^2 \phi \quad (16)$$

In our choice of the reflectivity, this transformation only acts on the specular components  $r_{s,p}$ , since  $r_d$  is independent of incidence angle and polarization.

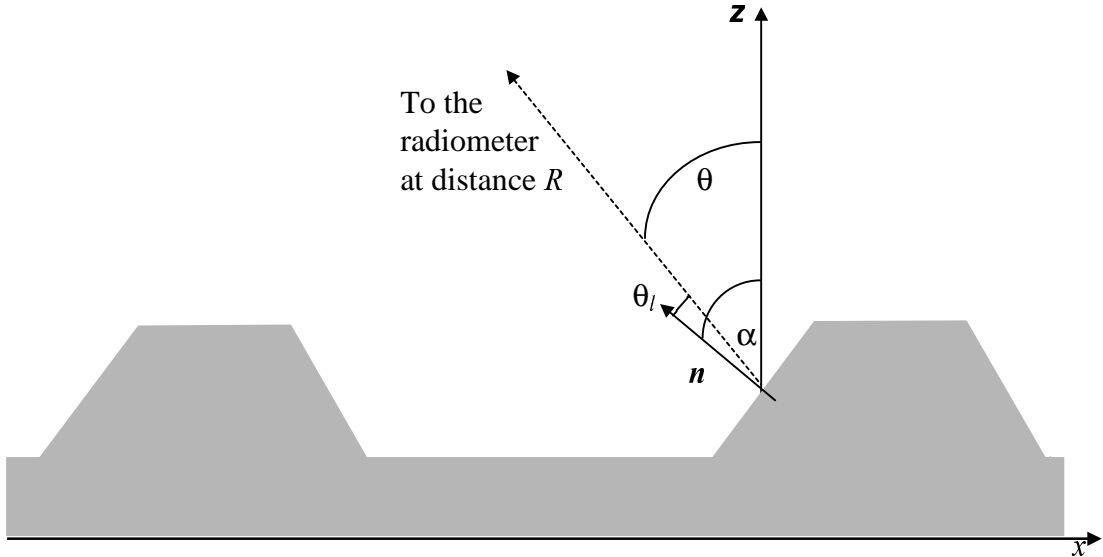


Figure 1: Local  $\theta_l$  and global  $\theta$  incidence angles on a surface tilted by angle  $\alpha$ .

### 3.2 Shadowing effects

The concept of shadows (and relief-related modulations of illumination) can be applied to passive radiation by Kirchhoff's law where emission corresponds to absorption in a reciprocal ray, i.e. one that is transmitted by the radiometer. By doing so, we find the following effects:

- The surface facet appears enhanced or reduced in size (i.e. view solid angle), or is even hidden from a given view direction, depending on incidence angle, slope and orientation of the facet.
- Shadowing effects include radiation reflected by the surface facet, i.e. radiation emitted by some elevated part of the relief which is incident on the facet. This shadow radiation replaces the radiation from the hidden sky. It means also that the incident radiation is composed of a sky term and of a terrestrial term.

Both effects are to be described here, starting with the former, see Figure 1. For a visible facet, the contribution to the received radiation depends on the solid angle  $\Omega = A \cos \theta_l / R^2$  under which the facet appears, where  $A$  is the true surface area of the facet and  $R$  is the distance to the radiometer antenna. A surface area is usually represented on a map by its projection  $A_h$  on a horizontal plane. If we use this projected area, then we get

$$\Omega = \frac{A_h \cos \theta_l}{R^2 \cos \alpha} \quad (17)$$

Now, the total signal at a given polarization collected by the radiometer antenna is a beam-weighted sum over the radiation from all visible facets (numbered from  $j=1$  to  $n$ ) within the antenna footprint:

$$T_{b,total} = \frac{1}{\Omega_{total}} \sum_{j=1}^n T_b(A_j) \cdot \Omega_j \quad (18)$$

The remainder of this section is devoted to the estimation of the latter effect, assuming that the surface is a Lambert scatterer ( $r_v = r_h = r_d$ ). Let us consider a horizontal profile in some direction  $x$  through a landscape as shown in Figure 2. The quantity of interest is the zenith angle  $\theta_H$  of the horizon to the right. At a given surface position the sky radiation is limited to incidence angles  $\theta$  smaller than  $\theta_H$ . For larger angles, enhanced incident radiation at brightness temperature  $T_h$  appears from the elevated landscape. Let us define the total upwelling brightness temperature by  $T_{up}$  (total) as the sum of the radiation from a flat horizon,  $T_{up}$  (Section 2), plus the increase  $\Delta T_{up}$ , i.e.

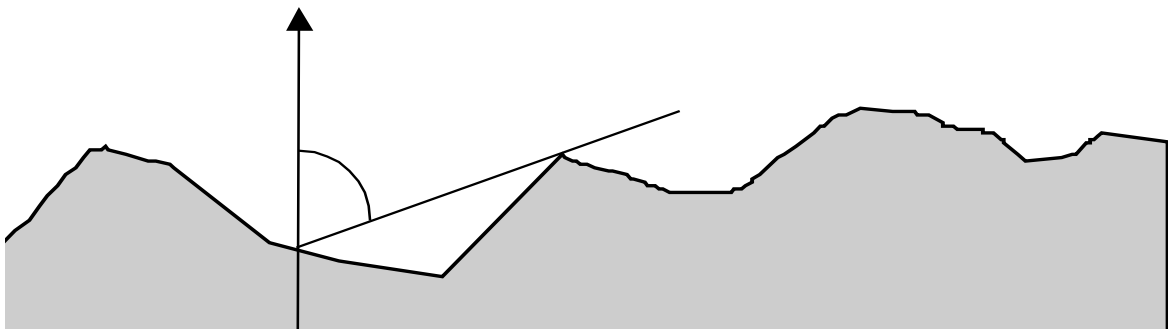


Figure 2: Profile through a simple landscape to illustrate the horizon at zenith angle  $\theta_H$ .

$$T_{up}(\text{total}) = T_{up}(\text{Section 2}) + \Delta T_{up}. \quad (19)$$

The increase describes the enhancement, resulting from  $T_h$  being larger than the hidden  $T_{sky}$ :

$$\Delta T_{up} = \frac{r_d}{\pi} \int_0^{2\pi} d\beta \left( \int_{\theta_H}^{\theta_{max}} T_h(x, \theta) \cos \theta \sin \theta d\theta - \int_{\theta_H}^{\pi/2} T_{sky}(\theta) \cos \theta \sin \theta d\theta \right) \quad (20)$$

The angle  $\beta$  is the azimuth angle of the surface-profile direction. The upper limit in the first  $\theta$  integral is denoted by  $\theta_{max}$ . This value is  $\pi/2$  for a horizontal facet, but for a tilted facet,  $\theta_{max}$  may be larger or smaller depending on the orientation of the facet (i.e. the integration has to include all incident directions of the local facet). Note that values of  $\theta_H$  and  $\theta_{max}$  depend on azimuth  $\beta$ .

Let us add a comment for the case of a partly specular facet: The above expression for  $\Delta T_{up}$  is still valid as long the specularly reflected ray emanates from the sky. The situation is especially simple for horizontal facets; then  $T_{up}$  is given again by (19). For tilted surfaces, the effects of Section 3.1 have to be applied. In situations with a heavy relief, ray-tracing techniques may be applied to include multiple specular reflections and emissions between facets.

Now we return to Equation (20) to estimate the increase  $\Delta T_{up}$  for a lambertian facet. In the simplified case of a horizontal facet at the lower altitude  $h_1$  where  $\theta_{max}=\pi/2$  we have

$$\Delta T_{up} = \frac{r_d}{\pi} \int_0^{2\pi} d\beta \int_{\theta_H}^{\pi/2} [T_h(x, \theta) - T_{sky}(\theta)] \cos \theta \sin \theta d\theta \quad (21)$$

In order to estimate an upper limit  $\Delta T_{up,max}$  of  $\Delta T_{up}$ , we assume that the elevated surface is a black body at constant temperature ( $T_h = T_0$ ). This situation is approximated, e.g. by a forest-covered hill. These simplifications lead to

$$\Delta T_{up,max} = \frac{r_d (T_0 - T_{sky})}{2\pi} \overline{\int_0^{2\pi} d\beta \cos^2 \theta_H} = r_d (T_0 - T_{sky}) \overline{\cos^2 \theta_H} \quad (22)$$

where the horizontal bar in the last expression means averaging over azimuth  $\beta$ . With this expression it is rather simple and straightforward to compute  $\Delta T_{up,max}$  using a Digital Elevation Model (DEM). The key quantity is  $\overline{\cos^2 \theta_H}$ . Let us assume a hilly relief with an effective angle  $\theta_H$  of  $70^\circ$ , thus  $\overline{\cos^2 \theta_H} \approx 0.12$ . In order to produce a noticeable increase  $\Delta T_{up}$ , the diffuse reflectivity  $r_d$  has to be large enough. For  $r_d = 0.2$  and for  $T_0 - T_{sky} = 260\text{K}$ , the correction term  $\Delta T_{up,max}$  is  $6\text{K}$ . The effect gets stronger as the ruggedness of the terrain increases. In an area dominated by steep slopes the azimuth average of  $\overline{\cos^2 \theta_H}$  within deep valleys may reach 0.5. Since such regions have limited lateral extent, their overall contribution to the radiometer pixel value may still not be very important. In a further situation we assume that besides a constant surface temperature  $T_0$ , the surface reflectivity  $r_p$  is everywhere the same and given by  $r_d$ . Then, under the assumption of single interactions between surface facets,  $\Delta T_{up}$  becomes

$$\Delta T_{up} = r_d (1 - r_d) (T_0 - T_{sky}) \overline{\cos^2 \theta_H} \quad (23)$$

The difference with respect to (22) is the additional factor  $(1 - r_d)$ . Including multiple bounces of radiation between surface elements leads to  $\Delta T_{up}$  values between (22) and (23). If the reflecting facet is a tilted surface, we can still use the above expressions for  $\Delta T_{up}$ , however, with  $\theta_H$  being the local incidence angle  $\theta_{lH}$  of the horizon.

At low elevation angles, atmospheric emission is often not negligible. Increasing atmospheric emission increases  $T_{sky}$  and thus reduces  $\Delta T_{up}$  to values closer and closer to zero. Simulations of  $\Delta T_{up}$  using DEM and realistic atmospheric data will quantify the actual behavior.

#### 4 The example of southern Norway

As an illustration of pure relief effects (i.e. of the geometrical factors), let us consider the rugged terrain of southern Norway. The relief is shown by the DEM in Figure 3, and Figure 4 shows the computed values of  $\overline{\cos^2 \theta_H}$  whose range extends from 0 to about 0.3 with extremes up to 0.4. Roughly speaking, Figure 4 looks like a negative of Figure 3. However, on a closer look, there are significant differences. The main valleys and Fiords clearly seen in Figure 3 almost disappear in Figure 4 where the brightest areas are found in small and narrow valleys, e.g. in the upper left part of the image. The extended mountain area in the southern part are practically unaffected. The other parameters of interest are the local incidence angle  $\theta_l$  and the polarization rotation angle  $\varphi$ . Instead of  $\theta_l$  its deviation from  $\theta$  is shown in Figure 5 for southern Norway, and Figure 6 shows  $\varphi$  of the same region.

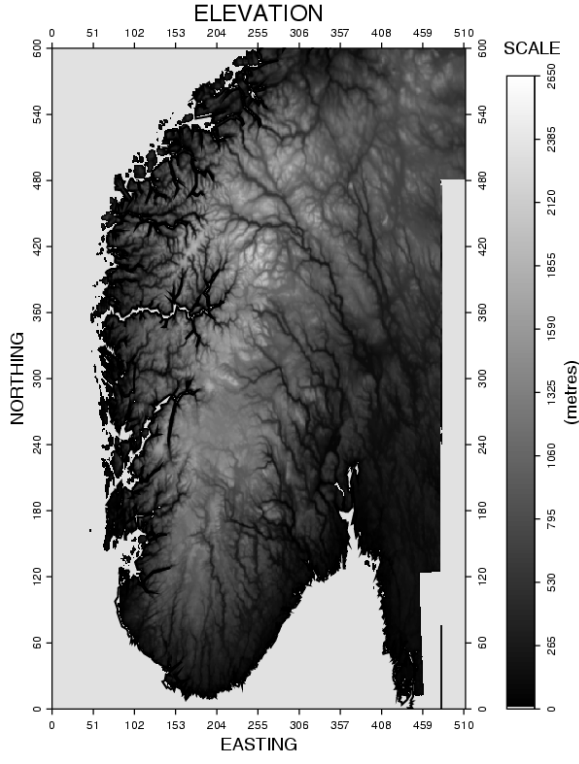


Figure 3: Digital elevation model of southern Norway, resolution 1km (horizontal), 100m (vertical)

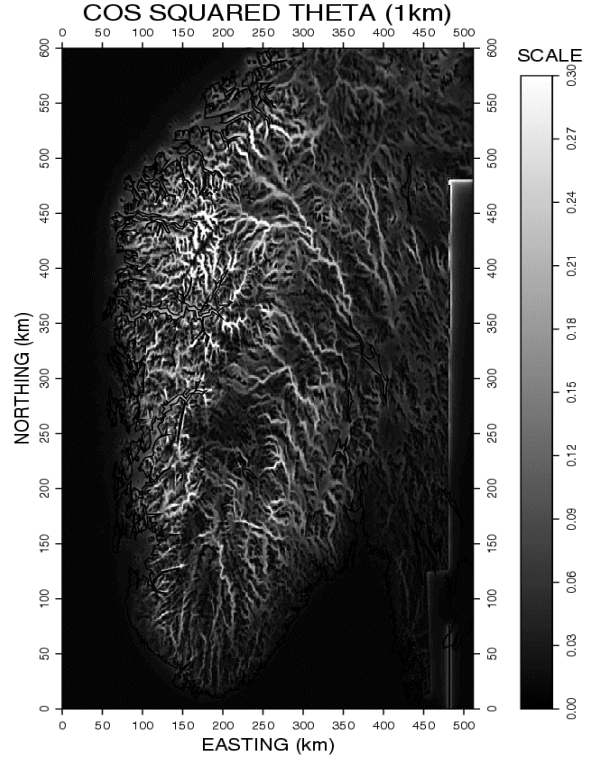


Figure 4: Values of  $(\cos \theta_H)^2$  in southern Norway.

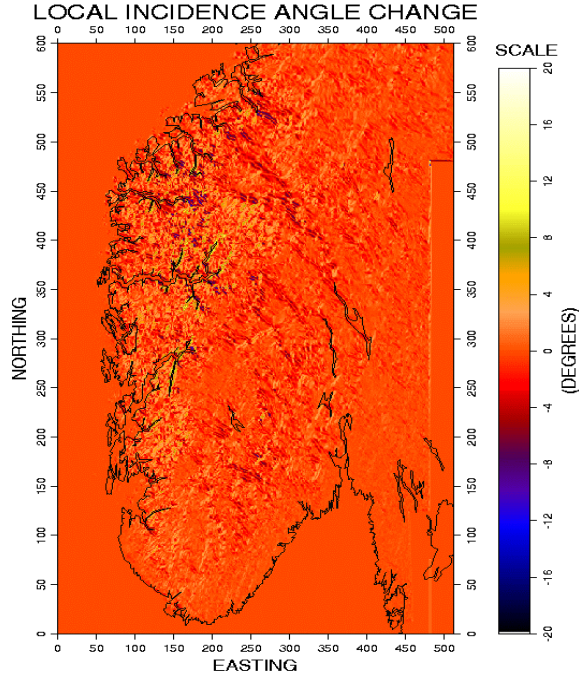


Figure 5: Change  $\theta_l - \theta$  of the local incidence angle for SSM/I by the relief in southern Norway.

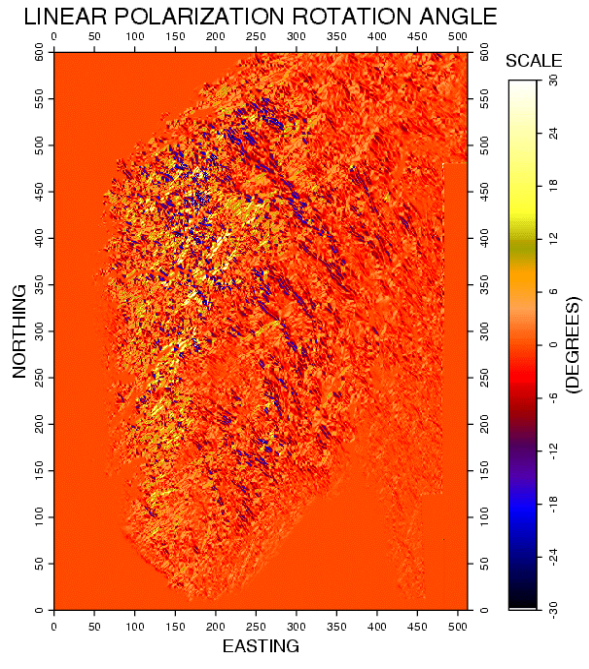


Figure 6: Rotation angle  $\varphi$  of linear polarization for SSM/I by the relief in southern Norway.

These data are of interest if the reflectivity depends on incidence angle and polarization, i.e. for the specular component  $r_{s,p}$ , but not for lambertian surfaces. The radiometer aspect direc-

tion was taken from an average descending SSM/I orbit. Figures 4 to 6 were created from Figure 3 with a software package of Frew and Dozier (1986).

## 5 Conclusions

We considered relief effects on the upwelling brightness temperature  $T_{up}$  at the surface and on the brightness temperature  $T_{bp}$  to be observed above the atmosphere. At frequencies of relevant atmospheric attenuation, major effects result from the variable atmospheric contributions due to their dependence on the altitude  $h$  of the emitting surface. Additional effects occur due to the shadowing of sky radiation by an elevated horizon. For lambertian surfaces this contribution can be estimated from  $\cos^2 \theta_H$ . The formulas were derived for surfaces whose reflectivity can be described by a partly specular and a partly lambertian scattering behavior. The shadowing effects of a hilly terrain with an elevated horizon were computed for lambertian surfaces, and as an example the situation of southern Norway was shown. The effect can be expressed by an increase  $\Delta T_{up}$  of  $T_{up}$ . The formulas for  $\Delta T_{up}$  are also valid if a specular component exists, as long as the specularly reflected rays do not lead to an additional increase of  $T_{up}$ . A ray-tracing method is required to model multiple specular reflections. In addition to shadowing effects, tilted surfaces lead to changes in incidence angle and to a rotation of the plane of linear polarization.

## Acknowledgment

This work was part of "Snowtools", a European Environment and Climate Project, supported by the Commission of the European Community, Contract No. NENV4-CT96-0304, and by the Swiss Federal Office of Education and Science, Contract No. BBW 95.0847.

## References

- Abramowitz M., and Stegun I., 1974: Handbook of Mathematical Functions, New York: Dover.
- Frew J., and J. Dozier, 1986: "The Image Processing Workbench, portable software for remote sensing instruction and research", Proc. Internat. Geoscience and Remote Sensing Symposium, ESA SP-254, pp. 271-276, European Space Agency, Paris, 1986.
- Ingold T., Peter R., Kämpfer N., 1998: Weighted Mean Tropospheric Temperature and Transmittance Determination at mm-Wave Frequencies for Ground-Based Applications. Radio Science, Vol. 33, pp. 905-818.
- Mätzler C., 1992: Ground-based measurements of atmospheric radiation at 5, 10, 21, 35 and 94 GHz. Radio Science 27, pp. 403-415.
- Mätzler C., 1987: Applications of the Interaction of Microwaves with the Seasonal Snow Cover. Remote Sensing Reviews, Vol. 2, pp. 259-387.
- Prigent, C. and P. Abba, 1990: Sea-surface equivalent brightness temperature at millimeter wavelengths, Annales Geophysicae, Vol. 8, pp. 627-634.
- Schanda E., 1985: Physical Fundamentals of Remote Sensing, Springer-Verlag, Berlin.
- Ulaby F.T., Moore R.K., Fung A.K., 1981: Microwave Remote Sensing, Active and Passive. Vol. I., Addison-Wesley Publ., Reading, Massachusetts, USA.

# Microwave emission from soil and vegetation

André Chanzy and Jean-Pierre Wigneron

## 1 Introduction

The emission of microwave radiation from soil and vegetation is localised in a layer the depth of which depends on both the radiation characteristics (frequency, polarization, propagation direction), and the soil and vegetation properties (dielectric permittivity, geometry). The layer is generally heterogeneous and contains elements with various geometries and dielectric properties. The size of the elements is often comparable to the wavelength and therefore, complex types of volume scattering can occur. Moreover, the vegetation canopy is a dynamic system with rapidly changing properties according to diurnal (soil moisture and temperature) and seasonal (vegetation, soil surface roughness, temperature) cycles as well as to soil wetting/drying sequences. So, the microwave emission models from soil and vegetation must account for the following time dependent characteristics:

- the soil surface dielectric constant or the surface soil moisture combined with a model of soil dielectric constant,
- the soil surface roughness,
- the vegetation biomass and geometry
- the vegetation dielectric constant,
- the soil and vegetation temperature profiles.

Microwave emission models from soil and vegetation were mainly developed at low frequencies, i.e. at frequencies lower than 20 GHz. Two types of model can be distinguished: the physical models to understand the emission processes in relation to the soil and vegetation geometry, and the semi-empirical models dedicated to inversion studies. At higher frequencies, most of the emission models are based on semi-empirical approaches.

The scope of the following section is to present the general modelling framework for soil and vegetation cases. Then we present a brief presentation of the selected models. Soil and vegetation are presented separately, since they are accounted through specific models. However, to represent a soil covered by vegetation, it is necessary to combine a soil and a vegetation model.

## 2 Microwave emission from vegetation

### 2.1 Physical models

#### *Coherent approach*

In the coherent approach, wave equations are used to derive the bistatic scattering coefficients, which are integrated to compute the total reflectivity. The emissivity  $e_p$  at polarization  $p$  (= h or v) is then obtained using the energy conservation law:

$$e_p(\theta_0, \phi_0) = 1 - 1/4\pi \int_{4\pi} [\gamma_{pp}(\theta_0, \phi_0, \theta_1, \phi_1) + \gamma_{pq}(\theta_0, \phi_0, \theta_1, \phi_1)] d\Omega_1 \quad (1)$$

where subscripts 0 and 1 stand for the incident and the reflected waves,  $\theta$  is the incidence angle and  $\phi$  the azimuth direction. Equation (1) is also referred to as the Peake Law. The bistatic scattering coefficients  $\gamma_{pq}$  and  $\gamma_{pp}$  can be computed with vegetation described either by a continuous medium (Stogryn, 1974, Fung and Fung, 1977, Fung and Ulaby, 1978, Tsang and Kong, 1981, Jin and Kong, 1984, Lee and Kong, 1985) or a discrete medium (Lang et al, 1983). The Peake law is interesting to bridge studies in the active and passive domains. However, it was developed to derive the surface emissivity. In case of vegetation, where transmission through the canopy may be important, the Peake Law must be used with care, since it does not account for the thermal structure of the medium.

### **Incoherent approach**

The incoherent approach is based on the radiation intensity. The radiative transfer equation can be written at v polarisation for the vegetation, which is divided into horizontal layers:

$$\mu \frac{dI_v(\mu, z)}{dz} = k_a \frac{2k_0 T(z)}{\lambda^2} - k_e I_v(\mu, z) + k_e \int_{-1}^{+1} P(\mu, \mu') I_v(\mu', z) d\mu' \quad (2)$$

where  $I_v$  is the specific intensity,  $\lambda$  the wavelength,  $k_a$  and  $k_e$  the absorption and the extinction coefficients,  $\mu = \cos(\theta)$  and  $P(\mu, \mu')$  is the phase function (In a fully polarimetric formulation, the phase function becomes a matrix, the specific intensity becomes the Stokes vector, and  $k_a$  and  $k_e$  become appropriate absorption and extinction vectors). The right side of Equation (2) is the sum of the emission term, the extinction and the scattering source. The phase function,  $k_a$  and  $k_e$  can be computed either for a continuous or discrete medium. When considering a continuous medium, the vegetation is described by statistical dielectric fluctuations. They are characterised by autocorrelation functions, usually parameterised by a horizontal and a vertical correlation length (Jin , 1989, Wigneron et al., 1993a).

With the discrete medium, the scatterers are determined by simple geometric elements (ellipsoid, cylinder, disc), which are characterized by their dimension and dielectric constant (Ferrazoli et al., 1992, Wigneron et al., 1993b, Ferrazoli and Guerriero, 1996). The different models using the discrete media approach differed by the resolution of the radiative transfer equation. Ferrazoli et al. 1992 computed the bistatic scattering coefficient using the matrix doubling method to combine the different layers in the vegetation canopy. Then they calculate the emissivity with the Peake law. Wigneron et al. 1993b numerically resolved the radiative transfer equation. The thermal emission of each layer is accounted for to allow the description of a given temperature profile on the microwave emission.

## **2.2 Simplified models**

When the scattering source term is negligible (Kirdashev et al., 1979), the solution of the radiative transfer equation (Equation 2) simplifies to:

$$T_{Bp} = (1 + L\Gamma_p)(1 - L)(1 - \omega)T_v + (1 - \Gamma_p)L T_s \quad (3)$$

where:

$T_v$  and  $T_s$  are the vegetation and soil effective temperature, respectively;

$\Gamma_p$  is the soil reflectivity

$\omega$  is the single scattering albedo ( $1 - \omega = k_a/k_e$ )

$L$  is the canopy attenuation, given by :

$$L = \exp(-\tau/\mu) \quad (4)$$

where  $\tau$  is the vegetation opacity, which depends on the extinction coefficient and the canopy height ( $\tau = k_e \cdot H$ ).

The simplified expression of  $T_B$  is widely used (Mo et al., 1982, Kerr and Njoku, 1990, Wegmüller et al. 1994, Van de Griend and Owe 1994, Wigneron et al. 1995a, Van Oevelen 1999) for the estimation of surface parameters (soil moisture and vegetation). The elimination of the scattering source term is a strong hypothesis for frequencies above ~5-10 GHz. When limiting the scattering term to the forward direction (Delta-Eddington approximation), the radiative transfer equation takes the simplified formulation given above, with  $\omega$  and  $\tau$  replaced by  $\omega^*$  and  $\tau^*$ , given by:

$$\omega^* = (1-\alpha)\omega/(1-\alpha\omega) \quad (5)$$

$$\tau^* = (1-\alpha\omega)\tau \quad (6)$$

where  $\alpha$  represents the fraction of the radiation intensity scattered along the incident direction.  $\omega^*$  and  $\tau^*$  are often estimated as  $\omega$  and  $\tau$  from experimental data (Pampaloni and Paloscia, 1986).

At low frequencies (<10 GHz), Jackson et al. (1982), Wang et al. (1990), Jackson and Schmugge (1991), Haboudane et al. (1996), and Chanzy et al. (1997a) further simplified the equation by assuming that  $\omega$  is equal to 0 and  $T_v=T_s$ . Such a simplification leads to the following equation:

$$T_{Bp} = (1-L^2\Gamma_p)T_v \quad (7)$$

### 2.3 Dielectric constant of vegetation elements

Two models are generally used :

- The Debye-Cole dual dispersion dielectric model is valid over the 0.1-20 GHz range (Ulaby and El-Rayes, 1987). It accounts for the relaxation frequency of the bound water, which was determined experimentally.
- The semi-empirical formula of Mätzler (1994a) is valid over the 1-100 GHz range.

## 3 Microwave emission from soil

### 3.1 Physical emission models

For rough surface, soil emission models are based on the Peake law (Equation 1). In the soil case, the bistatic scattering coefficients are computed using Kirchhoff's approximations or using the small perturbation approach (Mo et al., 1987, Schiffer, 1987, Saatchi et al. 1994, Fung 1994, Laguerre 1995). As an extreme case, the soil emissivity can be derived for smooth soil from the Fresnel reflectivity. With all these approaches, the radiation emission below the surface is neglected. A difficulty arises by surface models is then the determination of the soil dielectric constant and more specifically, the soil layer depth (hereafter referred to as sampling depth  $\delta$ ) over which the dielectric constant should be characterised.

The soil dielectric constant vertical profile can be accounted for in emission models from layered media. In such models, the soil is assumed to be smooth. Different approaches were

developed. With the coherent models, the radiation intensity is computed from the electric field determined at the boundary of each layer. In the Wilheit model (Wilheit, 1978), the electric field is computed at each layer interface for an electromagnetic wave propagating through the soil. The fractional energy absorption  $f_i$  in each layer, the thermal weighting function, is then derived from the electric fields. The radiant flux is obtained by multiplying the weighting function by the average temperature of each layer. Wilheit (1978) found two sampling depths, one for temperature  $\delta_T$  and one for the reflectivity  $\delta_r$ . An alternate model is that of Njoku and Kong (1977); this model is based on the fluctuation-dissipation theorem. Comparative studies (Schmugge and Choudhury, (1981); Costes et al. (1994)) have shown that both models provide almost identical results.

Burke et al., (1979) proposed a model based on an incoherent approach. However, in their model, the moisture and temperature profiles contribute to the effective temperature calculation only, whereas the soil emissivity is solely determined by the soil dielectric constant in the surface layer.

Coherent and incoherent models can be easily combined to a mechanistic model of soil heat and mass flows in order to provide temporal variation of the soil microwave emission. Suresh Raju et al., (1995) have shown the importance of the diurnal cycles. Moreover, they found that diurnal cycles have an impact on the effective value of the sampling depth of the soil emission models.

### 3.2 Semi empirical emission models

Choudhury et al. (1979) proposed a simple model based on the smooth soil reflectivity ( $R_p$ ) and the standard deviation of height ( $\sigma$ ) to characterize the roughness :

$$r_p(\theta) = R_p \cdot \exp(-4k^2\sigma^2 \cos^2 \theta) \quad (8)$$

where  $r_p$  is the reflectivity of the rough surface at  $p$  polarisation ( $h$  or  $v$ ). This formulation has a physical meaning since it represents the coherent reflectivity of the scattered radiation along the specular direction. Often the term  $h = k^2\sigma^2$  is treated as a free parameter fitted to the experimental data independently at each frequency, incidence angle and polarisation. Wang and Choudhury (1981) proposed another reflectivity formulation, which includes the depolarisation of the radiometric signal associated with the surface roughness :

$$r_p(\theta) = [(1-Q)R_p + QR_q] \cdot \exp(-h \cos^2 \theta) \quad (9)$$

Here  $h$  and  $Q$  are empirical parameters, and  $q$  is the polarization orthogonal to  $p$ . Wang and Choudhury (1981) showed that once  $h$  and  $Q$  are fitted, the model predicts properly the angular variations of the soil reflectivity. Wang et al. (1983) showed that for very rough soils the angular dependence in  $\cos^2(\theta)$  should be replaced by 1. This leads to another formulation with an additional parameter where the exponential factor in (9) is modified by  $\exp[-h \cdot \cos^n(\theta)]$  with  $n$  varying from 0 to 2.

We notice that this formulation is also applied to vegetated surfaces at high frequencies using appropriate parameters (Hewison and English, 2000, this issue). In their model, the spectral dependence of the reflectivity is represented by the Debye/Fresnel formulae.

Wegmüller and Mätzler (1999) proposed an empirical formula of the soil emissivity, derived from surface-based measurements at frequencies from 3 to 100 GHz. They related the emis-

sivity at  $h$  and  $v$  polarization at a given incidence angle  $\theta$  to the Fresnel reflectivity at  $\theta$  ( $h$  polarization only), to a an empirical function of  $\theta$ , polarization and surface roughness ( $\sigma$ ).

### 3.3 Soil dielectric constant

At low frequencies, several semi-empirical or empirical models are available (Wang and Schmugge, 1980, Hallikainen et al., 1985, Dobson et al., 1985). The soil composition is accounted for through the granulometric fractions of clay and sand. They are used in empirical relations to estimate the fraction of water bound to the soil constituents. The frequency and temperature dependences are governed by the Debye equation applied to saline water. The validity of such models is limited to 18 GHz since most of the observations, required to parameterise the fraction of bounded water, were limited to that frequency range.

At higher frequencies (>20 GHz) there are only a few soil dielectric properties data sets (Ulaby et al., 1986, Calvet et al. 1995a, Frasch et al., 1998). England et al. (1992) proposed a simple approximate expression at SSM/I frequencies. Calvet et al. (1995a) presented experimental measurements from 23 to 90 GHz.

## 4 Selection of emission models

To build a model of microwave emission from vegetated surfaces, we have to combine several sub-models to represent :

- the radiative transfer in the canopy,
- the dielectric constant of vegetation elements,
- the soil emissivity,
- the dielectric constant of the soil surface,
- the surface effective temperature.

In the following sections, we present one or two possibilities for each sub model. The selection is made to provide a model that is the closest as possible to the physics as a research tool and a simpler model dedicated to the inversion applications.

The model developed by Wigneron (Wigneron et al. 1993b, Wigneron et al. 1995b) is selected for the physical representation of the vegetation emission. An incoherent approach is preferred since it allows to account for the thermal structure of the canopy. A discrete description of the vegetation medium is chosen in order to have measurable inputs. At the present time, this is not possible with the continuous medium approach. Indeed, the correlation lengths of the dielectric constant in the vegetation are minimally related to the geometrical description of the vegetation elements (Wigneron et al. 1993, Wigneron et al. 1995b, Calvet et al. 1995b, Calvet et al. 1996). To go further with the continuous approach, new experiments should be designed to establish the explicit relationships between the geometric vegetation parameters and the parameters of the continuous model, such as the correlation lengths of the vegetation dielectric constant.

The semi-empirical model given in Equation (3), hereafter referred to as  $\omega-\tau$  model, is widely used and therefore is selected as the simple model dedicated to the inversion applications.

For the soil emissivity, the available physical models have a narrow field of validity regarding the surface roughness conditions. Consequently, we only selected the h-Q semi empirical model (Equation 9).

For the dielectric constant we selected the most common models.

Finally, we present different approaches to estimate the microwave effective temperature.

#### 4.1 Physical model of microwave emission from vegetation

The model of Wigneron ((Wigneron et al. 1993b, Wigneron et al. 1995b) solved the radiative transfer equation (2) in the vegetation canopy represented as a discrete medium.

Purpose of the model	To compute the brightness temperature ( $T_B$ ) of vegetated surface.
Applications	Research studies on the microwave emission
Model variables	frequency (1-25 GHz)
Input parameters	<ul style="list-style-type: none"> <li>- volume fraction of the vegetation (<math>m^3/m^3</math>)</li> <li>- canopy height (m)</li> <li>- dielectric constant of the vegetation</li> <li>- dimensions of the ellipsoids (m) (leaves)</li> <li>- probability density function of the leaf orientation (inclination, azimuth, rotation along foliar axis)</li> <li>- dimension of the cylinders (m) (stem, branches, trunk)</li> <li>- Probability density function of the cylinder orientation (inclination, azimuth)</li> <li>- Soil reflectivity</li> <li>- Soil effective Temperature (K)</li> <li>- Vegetation temperature (K)</li> <li>- Thermal gradient within the canopy (K/m)</li> <li>- Atmospheric downwelling radiation (K)</li> </ul>
Output parameters	$T_B$ at both polarizations (h and v) and at $\theta_i$ ( $0 < \theta_i < \pi/2$ )
Expected errors	$\approx 15$ K (Wigneron 1993, Wigneron et al. 1993b, 1995b).

#### 4.2 Semi-empirical model of microwave emission from vegetation

The  $\omega-\tau$  model (Equation 3) is based on a simplified resolution of the radiative transfer equation (Equation 2) primarily proposed by Kirdiashev et al. (1979).

Purpose of the model	To compute the brightness temperature ( $T_B$ ) of vegetated surfaces
Applications	Inversion for retrieving surface geophysical parameters: surface soil moisture, vegetation water content, surface temperature
Input parameters	<ul style="list-style-type: none"> <li>- single scattering albedo (<math>\omega</math>) at a given polarization and frequency</li> <li>- optical thickness (<math>\tau</math>) at a given polarization and frequency</li> <li>- Soil reflectivity</li> <li>- Soil effective Temperature (K)</li> <li>- Vegetation temperature (K)</li> <li>- Atmospheric downwelling radiation (K)</li> </ul>
Output parameters	$T_B$ at $\theta_i$ $0 < \theta_i < 60^\circ$
Expected errors	$\approx 5$ K over the range of soil moisture after fitting the vegetation parameters
Accuracy requirements	useful : $T_B = 5$ K Adequate : $T_B = 3$ K

The determination of  $\omega$  and  $\tau$  is the key step for implementing the model. Studies reported in the literature focussed on the low frequencies (below 15 GHz) since they are more suitable for inversion studies. We will first report studies dealing with  $\omega$  and  $\tau$  determination at these frequencies and then give some indications to tackle the microwave emission at higher frequencies. As  $\omega$  and  $\tau$  are generally fitted parameters, we do not make the distinction between  $\omega$ ,  $\tau$  and  $\omega^*$ ,  $\tau^*$  (Equations 5 and 6).

### **Characterisation of the single-scattering albedo**

In general  $\omega$  is estimated from brightness measurements by a fitting process;  $\omega$  is found to be small (<0.12) at low frequencies (<10 GHz) (Kerr and Wigneron, 1994, Van de Griend and Owe, 1994, Wigneron et al., 1995a, Wigneron et al., 1996). The spectral dependence of  $\omega$  is not always clear.  $\omega$  depends on the angle of incidence and polarization (Van de Griend and Owe, 1994, Wigneron et al., 1996) but such a dependence is often ignored (Kerr and Njoku, 1991, Wigneron et al. 1995a). Van de Griend and Owe, 1994 found that  $\omega_H/\omega_V = 0.83$  over savannah. Results of  $\omega$  are summarised in Table 1. The single-scattering albedo is also computed from  $k_a$  and  $k_e$ . Wigneron et al. (1995b) used a physical model (discrete model) to compute  $\omega$ . The physical model accounts for the scattering sources and therefore the apparent  $\omega$  in the  $\omega-\tau$  model can be different from  $\omega$  defined rigorously in the physical model.

### **Characterisation of the opacity**

The opacity  $\tau$  can be physically determined from the imaginary part of the dielectric constant of saline water in the vegetation ( $\epsilon''_{sw}$ ):

$$\tau = A \cdot f \cdot W_c \cdot \epsilon''_{sw} \quad (10)$$

Where  $A$  is coefficient related to the plant structure,  $f$  the frequency,  $W_c$  the vegetation water content. This formulation is valid at low frequencies (below 10 GHz). Since the  $A$  coefficient is not always a well-known term,  $\tau$  can be related to the canopy dielectric constant (Schmugge and Jackson, 1992).

$$\tau = 4 \pi (H/\lambda) \operatorname{Im}(\epsilon_{can}^{1/2}) \quad (11)$$

where

$$\epsilon_{can} = [1 + vegf(\epsilon_{veg}^\beta - 1)]^{1/\beta} \quad (12)$$

where  $vegf$  is the volume fraction of vegetation elements of the canopy. Best results are found for  $\beta=0.5$ , i.e. for the refractive mixing model. Another way to avoid the determination of  $A$  is followed by relating  $\tau$  to the  $W_c$  through an empirical relationship:

$$\tau = b \cdot W_c \quad (13)$$

where  $b$  is a coefficient which depends on plant structure; it is determined by experimental data sets. It appears to be strongly dependent on the frequency and in less extent on polarisation and angle of incidence. Furthermore  $b$  depends on temperature. At L band results converge within a rather small range of variation [0.1-0.15]. At higher frequencies,  $b$  values are variable, and there are no clear laws that help in sorting the results into vegetation classes. Therefore,  $b$  still needs to be estimated on a case by case basis. However, the  $\tau$  dependence on polarisation, which can be explained by the canopy structure and the leaf geometrical description, is addressed e.g. in Ulaby and Wilson (1985), Van de Griend and Owe (1994), and Wigneron et al. (1995a).

The opacity  $\tau$  can also be estimated by radiometric measurements. The idea is that the polarisation difference or the angular variations of  $T_B$  are linked to the amounts of vegetation. Thus,  $\tau$  is related to  $T_B$  indices, which needs to be insensitive to soil moisture (Haboudane et al. 1996, Chanzy et al. 1997a, Wigneron et al. 1999). Such an approach should be validated with different types of vegetation, see e.g. the following field experiments: Chukhlantsev et al. (1989) for tomato fields at L Band, Mätzler (1990) for oat, Mätzler (1994b) for beech trees, both at frequencies from 5 to 94 GHz, and van de Griend et al. (1996) for wheat at 1.4 and 5 GHz.

Table 1: Published values of the single-scattering albedo (WC: vegetation water content in kg/m<sup>2</sup>)

Source Vegetation type	Vegetation description	Frequency (GHz)	Polarisation	Incidence Angle (°)	$\omega^*, \omega$
Mo et al. 1982					
Soybean	WC=1.54	1.42	H and V	0-50	0.07
Soybean	WC=1.54	C Band	H and V	0-70	0.13
Corn	WC=0.66	1.42	H and V	0-50	0.04
Corn	WC=0.66	C Band	H and V	0-70	0.10
Grass	WC=1.34	1.42	H and V	0-50	0.04
Grass	WC=1.34	C Band	H and V	0-70	0.05
Ulaby et al. 1983					
Corn		1.4		0	0.04
Corn		1.4	H	40	0.13
Corn		5		0	0.05
Corn		5	H	40	0.05
Brunfeldt and Ulaby 1984					
Wheat	Mid season	2.7	H	>40	0.075
Wheat	Mid season	2.7	V	>40	0.118
Wheat	Mid season	5.1	H	>40	0.065
Wheat	Mid season	5.1	V	>40	0.081
Corn	Mid season	2.7	H	>40	0.049
Corn	Mid season	2.7	V	>40	0.082
Corn	Mid season	5.1	H	>40	0.092
Corn	Mid season	5.1	V	>40	0.085
Soybean	Mid season	2.7	H	>40	0.103
Soybean	Mid season	2.7	V	>40	0.124
Soybean	Mid season	5.1	H	>40	0.124
Soybean	Mid season	5.1	V	>40	0.127
Brunfeldt and Ulaby 1986					
Soybean	WC=2.3	2.7	H and V	0-50	0.05-0.1
Soybean	WC=2.3	5.1	H and V	0-50	<0.05
Pampaloni and Paloscia 1986					
Alfalfa	WC=1.6	9.7	H and V	0-50	0.05
Alfalfa	WC=1.6	37.5	H and V	0-50	0.05
Alfalfa	WC=0.5	9.7	H and V	0-50	0.04
Alfalfa	WC=0.5	37.5	H and V	0-50	0.03
Corn	WC=2.0	9.7	H and V	0-50	0.08
Corn	WC=2.0	37.5	H and V	0-50	0.03
Corn	WC=5.3	9.7	H and V	0-50	0.08
Corn	WC=5.3	37.5	H and V	0-50	0.06
Van de Griend and Owe 1994					
Shrub savannah		6.6	H	52	0.076
Shrub savannah		6.6	V	52	0.091
Wigneron et al. 1995a					
Wheat	WC=[0.5-2.5]	5	H and V	8-38	0.04
Soybean	WC=[0.2-1.5]	5	H and V	8-38	0.11
Wigneron et al. 1996					
Wheat	WC=[0.5-2.5]	5	H	8-58	0.065-0.05
Wheat	WC=[0.5-2.5]	5	V	8-58	0.07-0.115
Wheat	vegetative cycle	5	H	30-70	0.05-0.055
Wheat	vegetative cycle	5	V	30-70	0.07-0.09

### **Towards higher frequencies**

To tackle the vegetation emission at frequencies higher than 20 GHz, few modelling studies are available. To our knowledge, only the studies of Pampaloni and Paloscia (1986) and Wegmüller et al. (1994) use the  $\omega-\tau$  model. From an analysis based on a geometric optics, the latter proposed to extend the use of Equation (10) up to 40 GHz to compute  $\tau$  by multiplying the right term (Equation 10) by the leaf transmissivity. They also proposed a formulation for  $\omega$ , but their results were far larger than the fitted values proposed by Pampaloni and Paloscia (1986), an indication that there exists a significant difference between  $\omega$  and  $\omega^*$ , see (5)-(6).

Physical approaches were used in Isaac et al. (1989) and Choudhury et al. (1990) up to 40 GHz. However their models were not really validated against controlled data.

One can benefit from available data bases. In a recent study, Prigent et al. (1997) proposed a set of computed emissivities derived from SSM/I observations over different surfaces in Europe and Africa. Measurements were made 36.5 GHz at different dates over savannah using an airborne radiometer during the Hapex-Sahel experiment (Chanzy et al., 1997a). Ground-based multi-frequency measurements were collected over different crops (Chanzy et al. 1999, Mätzler and Wiesmann, 1999). Choudhury (1993) and Prigent et al. (1997) noticed that the emissivity slowly varies with frequency. This means that interpolation can be done from the existing data set to estimate an emissivity at a required frequency.

### **4.3 Soil emission model**

The selected model is the so-called h-Q model, the analytic form of which is given by Equation (9) (Wang and Choudhury, 1981).

Purpose of the model	To compute the soil reflectivity
Applications	Inversion for retrieving soil surface moisture offer the lower boundary condition in vegetation model
Input parameters	- surface roughness parameters h and Q - Soil dielectric constant within the sampling depth -exponent n
Output parameters	$T_B$ at $\theta_i$ ( $0 < \theta_i < 60^\circ$ )
Expected errors	$\approx 5K$ over the range of soil moisture after fitting roughness parameters
Accuracy requirements	useful : $T_B = 5K$ Adequate : $T_B = 3K$

To implement the model, one needs to determine the sampling depth and the surface roughness parameters.

#### **Sampling depth**

For the sampling depth there is an agreement for the following depths (Wang, 1987, Suresh Raju et al., 1995): 2-5 cm, 1 cm and 0.5 cm for the L, C and X bands, respectively. These values correspond to about 0.1 wavelength. For extreme aridity, such as dry desert sand, the penetration depth can be much larger (on the order of 1 m) than the above values. Dielectric properties and penetration depth of dry Sahara sand were published by Mätzler (1998).

#### **Surface roughness**

As far as the surface parameters are concerned, there is no clear relation between h and Q and the surface roughness description (Wang et al. 1983, Chanzy et al. 1994, Haboudane et al.

1996). This is likely a consequence of the error propagation in the fitting algorithm and/or of the existing correlation between  $h$  and  $Q$ . However, Kerr and Njoku, 1990 proposed a formulation for  $Q$  which depends on the frequency  $f$  (in GHz) and the standard deviation of the surface height  $\sigma$ :

$$Q=0.35(1-\exp(-0.6\sigma^2f)) \quad (14)$$

#### 4.4 Vegetation dielectric constant

Ulaby and El Rayes (1987) model:

Purpose of the model	To compute the dielectric constant of the vegetation elements within the 0.2-20 GHz range
Model variable	Frequency
Input parameters	- the gravimetric moisture of the vegetation (kg/kg) - the bulk density of the dry vegetation material (Kg/m <sup>3</sup> ) - the ionic conductivity of the free water solution - temperature
Output parameters	The dielectric constant (real and imaginary parts)
Expected errors	+/- 5% (Ulaby and el Rayes, 1987)

Mätzler (1994a) model:

Purpose of the model	To compute the dielectric constant of the leaves within the 1-100 GHz range. This model is the only one available at $f>20$ GHz
Model variable	Frequency
Input parameters	-the gravimetric moisture of the vegetation (kg/kg) -temperature
Output parameters	The dielectric constant (real and imaginary parts)

#### 4.5 Soil dielectric constant

The selected model is the Dobson et al. (1985) semi-empirical model:

Purpose of the model	To compute the dielectric constant of the soil in the 1.4-18 GHz range. This model accounts for bound and free water depending on soil type.
Model variable	Frequency
Input parameters	- Soil dry bulk density - Solid density - Soil salinity - sand fraction - clay fraction - Temperature
Output parameters	The soil dielectric constant (real and imaginary parts)
Expected error	$\approx 1$ for $\epsilon'$ $\approx 0.5$ for $\epsilon''$ (Dobson et al. 1985)

#### 4.6 Effective temperature

The effective emission temperature ( $T_e$ ) depends on the vertical temperature profiles of the soil and the canopy and a weighting function, which accounts for the contribution of each layer. To model the microwave emission,  $T_e$  is an important term to estimate since it can strongly vary (up to 50 K) during diurnal and/or annual climatic cycles.

The most common way is to use the skin temperature ( $T_s$ ) delivered by thermal infrared sensors. However, the major drawbacks from these approaches are the availability of  $T_s$  at the time of the microwave observation (requirement of cloud free condition), the significance of  $T_s$  in comparison to  $T_e$ . Choudhury et al., (1982) have shown that  $T_s$  is poorly related to  $T_e$  at frequencies lower than 10 GHz.

For well watered surface,  $T_e$  is close to the air temperature ( $T_a$ ) during the day and  $T_a$  is therefore a good estimator of  $T_e$  (Chanzy et al. 1997b). In dry condition,  $T_a$  remains a good estimator of  $T_e$  in the morning two hours after the beginning of the surface heating by solar radiation (Gaudin, 1994). In all cases  $T_a$  cannot be used to estimate  $T_e$  during the night period since the nocturnal surface cooling induces strong air temperature gradients near the surface which are also governed by the atmospheric conditions (humidity, cloudiness).

The major difficulties to estimate  $T_e$  come from the dry bare soils where the variations of  $T_e$  are the strongest. Choudhury et al., (1982) proposed a model based on  $T_s$  and a deep temperature  $T_d$ . Chanzy et al. (1997b) proposed a model to overcome the  $T_s$  availability problem by using either  $T_a$  or the microwave brightness temperature at X band and V polarisation, to estimate the near surface temperature.

$T_e$  can also be estimated using a combination of  $T_B$  measurements. McFarland et al. (1990), Hiltbrunner and Mätzler (1994), Njoku (1994) proposed empirical algorithms based on multi-channel measurements. Calvet et al. (1994), Calvet et al., (1996), Calvet and Jullien (1996) estimate  $T_e$  by an inversion of a microwave emission model using dual polarisation and multi-frequency measurements.

## 5 Conclusions and recommendations

The effort in physical modelling of the microwave emission should be pursued. We need theoretical tools to understand what the contributions of the different surface elements are to the total microwave emission. Moreover, the future inversion algorithms (i.e. the algorithms developed to derive surface geophysical parameters from passive microwave observations) will be based on a microwave multi-configuration approach. We need models that simulate consistent sets of brightness temperatures at the different configurations of measurements in order to optimise the inversion algorithms.

Most of the studies were done at low frequencies (<20 GHz) or at 37GHz. The continuity of the microwave emission signature should be further analysed to estimate the microwave emission at the other frequencies, especially at the frequencies of atmospheric sounders.

The discrepancies between model and experimental results, the variability in the fitted model parameters may be due to measurement errors or due to inadequacies in the selected models. Efforts in statistical analysis should be made to evaluate errors of measurements, models, parameter calibration and inversion algorithms. Measurements accuracy requirements should be established from such analysis.

We need reference sets of data that reach the above measurement accuracy requirements. The accuracy of the existing data should be evaluated. Measurement quality must be the priority for the future measurement campaigns.

Scaling issues need to be developed. Due to the pixel size, complex mixed pixels will be the common data delivered by microwave radiometers aboard satellites. An effort should be done to take benefit from the multi-configuration possibilities (polarisation difference, angular

variations, frequency signature) of the future microwave radiometers since the different radiometric measurements are delivered at the same scale and "orthogonal" information on the surface description may be retrieved from combination of measurements.

## References

- Brunfeldt D.R. and F.T. Ulaby, "Measured microwave emission and scattering in vegetation canopy", IEEE Trans. Geoscience and Remote Sensing, Vol. 22, pp. 520-524, (1984).
- Brunfeldt D.R. and F.T. Ulaby, "microwave emission from row crops", IEEE Trans. Geoscience and Remote Sensing, Vol. 24, pp. 353-359 (1986).
- Burke W.J., T.J. Schmugge and J.F Paris, "Comparison of 2.8 and 21 cm microwave radiometer observations over soils with emission model calculations", J. Geophys. Res., Vol. 84, pp. 287-294 (1979).
- Calvet J.-C, J.-P Wigneron, E. Mougin, Y.H. Kerr and J.L. Brito, "Plant water content and temperature of the Amazon forest from satellite microwave radiometry", IEEE Trans. Geoscience and Remote Sensing, Vol. 32, pp. 397-408 (1994).
- Calvet J.-C., J.-P. Wigneron, A. Chanzy, Suresh Raju and L. Laguerre, "Microwave dielectric properties of a silt loam at high frequencies", IEEE Trans. Geoscience and Remote Sensing, Vol. 33, pp. 634-642 (1995a).
- Calvet J.-C., J.-P. Wigneron, A. Chanzy and D. Haboudane, "Retrieval of surface parameters from microwave radiometry over open canopies at high frequencies", Remote Sens. Environ., Vol. 53, pp. 46-60 (1995b).
- Calvet J.-C. and J.-P. Jullien, "Land surface temperature retrieval in dry conditions from infrared and microwave satellite radiometry", Remote Sensing Reviews, Vol. 13, pp. 235-255 (1996).
- Calvet J.-C., A. Chanzy and J.-P. Wigneron, "Surface temperature and soil moisture retrieval in the Sahel from multifrequency microwave radiometry", IEEE Trans. Geoscience and Remote Sensing, Vol. 34, pp. 588-600 (1996).
- Chanzy A., D. Haboudane, J.-P. Wigneron, J.-C. Calvet and O. Grosjean, " Radiométrie micro-onde sur divers types de couverts végétaux : influence de l'humidité du sol." in : Colloque International ISPRS Mesures physiques et signatures en télédétection, Val d'Isère (FRA), 1994/01/17-21, pp 505-512, (1994).
- Chanzy A., T.J. Schmugge, J.-C. Calvet, Y. Kerr, P. Van Oevelen, O. Grosjean, J.R. Wang, "Airborne microwave radiometry on a semi arid area during HAPEX-Sahel, J. of Hydrology, Vol. 188-189, pp.285-309 (1997a).
- Chanzy A., Suresh Raju and J.-P. Wigneron, "Estimation of soil microwave effective temperature at L and C bands", IEEE Trans. Geoscience and Remote Sensing, Vol. 35, pp.570-580 (1997b).
- Chanzy A., J.-P. Wigneron, J.-C. Calvet, L. Laguerre and Suresh Raju, "Surface emissivity data from PORTOS-Avignon experiment", Appendix B, this issue, p. 171 (2000).
- Choudhury B.J., T.J. Schmugge, A. Chang and R.W. Newton, "Effect of surface roughness on the microwave emission from soils", J. Geophys. Res., Vol. 84, pp. 5699-5706 (1979).
- Choudhury B.J., T.J. Schmugge and T. Mo, "A parameterization of effective soil temperature for microwave emission", J. Geophysical Res., Vol. 87, pp. 1301-1304 (1982).
- Choudhury B.J., J.R. Wang, A.Y. Hsu and Y.L. Chien, "Simulated and observed 37 GHz emission over Africa" Int. J. Remote Sensing, Vol. 11, pp. 1837-1868 (1990).
- Choudhury B.J., "Reflectivity of selected land surface types at 19 and 37 GHz from SSM/I observations" Remote Sens. Environ., Vol. 46, pp. 1-17 (1993).
- Chukhlantsev A.A., S.P. Golovachev and A.M. Shutko, "Experimental study of vegetable canopy microwave emission", Adv. Space Res. Vol. 9, No. 1, pp. (1)317-(1)321 (1989).
- Costes F., Suresh Raju, A. Chanzy, I. Chênerie and J. Lemorton, "Microwave radiometry on bare soils: comparison of various emission models of layered media with measurements", in : Proceedings of the IGARSS'94 Symposium: Surface and atmospheric remote sensing: Technologies, Data Analysis and interpretation, Pasadena 1994/08/8-12, Volume III., pp. 1579-1581 (1994).

- Dobson M.C., F.T Ulaby, M.T. Hallikainen, and M.A. El Rayes, "Microwave dielectric behavior of wet soil-part II : dielectric mixing model", IEEE Trans. Geoscience and Remote Sensing, Vol. 23, pp. 35-46 (1985).
- England A.W., J.F. Galantowicz and M.S. Schretter, "The radiobrightness thermal inertia measure of soil moisture", IEEE Trans. Geoscience and Remote Sensing, Vol. 30, pp. 132-139 (1992).
- Ferrazoli P., L. Guerriero, S. Paloschia, P. Pampaloni and D. Solimini, " Modelling polarization properties of emission from soil covered with vegetation", IEEE Trans. Geoscience and Remote Sensing, Vol. 30, pp. 157-165 (1992).
- Ferrazoli P. and L. Guerriero, "Passive microwave remote sensing of forests : a model investigation", IEEE Trans. Geoscience Remote Sensing, Vol. 34, pp. 433-443 (1996).
- Fung A.K. and H.S. Fung, "Application of first order renormalization method to scattering from a vegetation-like half space", IEEE Trans. Geoscience Electron., Vol. 15, pp. 189-195, (1977).
- Fung A.K. and F.T. Ulaby, "A scatter model for leafy vegetation", IEEE Trans. Geoscience and Remote Electron., Vol. 16, pp. 281-285(1978).
- Fung A.K., "Microwave scattering and emission models and their applications", Artech house Remote Sensing library, Boston, USA, 573p (1994).
- Frash L.L., S.J. Mc Lean and R.G. Olsen, "Electromagnetic properties of dry and water saturated basalt rock, 1-110 GHz", IEEE Trans. Geoscience and Remote Sensing, Vol. 36, pp. 754-766 (1998).
- Gaudin T., "Estimation de l'évapotranspiration réelle d'un couvert de blé à partir de mesures radiométriques micro-onde", INRA, Unité de Science du sol d'Avignon, rapport interne, 75pp. (1994).
- Haboudane D., A. Chanzy, J.-C. Calvet, J.-P. Wigneron and F. Bonn, "Raiométrie micro-onde dans le cas des couverts végétaux partiels : estimation de la teneur en eau du sol", Canadian J. of Remote Sensing, Vol. 22, pp. 208-217 (1996).
- Hallikainen M.T., F.T. Ulaby, M.C. Dobson, M.A. El Rayes and L.K. Wu, "Microwave dielectric behavior of wet soils – Part I, empirical models and experimental observations", IEEE Trans. Geoscience and Remote Sensing, Vol. 23, pp. 25-34 (1985).
- Hewison T. and S. English, "Fast models for land surface emissivity", this issue, p. 117 (2000).
- Hiltbrunner D. and C. Mätzler, "Use of SSM/I passive microwave data for the study of the alpine regions", in : Colloque International ISPRS Mesures physiques et signatures en télédétection, Val d'Isère (FRA), 1994/01/17-21, pp 519-526 (1994).
- Isaacs, R.G., Y.Q. Jin, R.D. Worsham, G. Deblonde and V.J. Falcone, "The RADTRAN microwave surface emission models", IEEE Trans. Geoscience Remote Sensing, Vol. 27, pp. 422-440 (1989).
- Jackson T.J. , T.J. Schmugge and J.R. Wang, "Passive microwave sensing of soil moisture under vegetation canopy", Water Resour. Res., Vol. 18, pp. 1137-1142 (1982).
- Jackson T.J., and T.J. Schmugge, "Vegetation effects on the microwave emission of soils", Remote Sens. Environ., Vol. 36: 203-212 (1991).
- Jin Y.Q. and J.A. Kong, "Strong fluctuation theory for electromagnetic wave scattering by a layer of random discrete scatterers", J. Appl. Phys., Vol. 55, pp. 1364-1369 (1984).
- Jin Y.Q., "The radiative transfer equation for strongly-fluctuating continuous random media", J. Quant. Spectrosc. Radiat. Transfer., Vol. 42, pp. 529-537 (1989).
- Kerr Y.H. and E.G. Njoku, "A semi-empirical model for interpreting microwave emission from semi-arid land surfaces as seen from space", IEEE Trans. Geoscience and Remote Sensing, Vol. 28, pp. 384-393 (1990).
- Kerr Y.H. and J.-P. Wigneron, "Vegetation models and observations. A review", in: ESA/NASA International Workshop, B.J. Choudhury, Y.H. Kerr, E.G. Njoku and P. Pampaloni (Eds), VSP, Utrecht, pp. 317-344 (1994).
- Kirdiashev K.P., A.A. Chucklantsev and A. Shutko, "Microwave radiation of the earth's surface in the presence of vegetation cover", Radiotekhnika, Vol. 24, pp 256-264 (1979).
- Laguerre L., "Influence de la rugosité de surface en radiométrie micro-onde des sols nus: modélisation et expérimentation", Thèse de Doctorat de l'Institut National Polytechnique de Toulouse, France, 139p (1995).
- Lang R. and J.S. Sidhu, "Electromagnetic backscattering from a layer of vegetation : a discrete

- approach", IEEE Trans. Geoscience and Remote Sensing, Vol. 21, pp. 62-71 (1983).
- Lee J.K. and J.A. Kong, "Passive Microwave remote sensing of an anisotropic random-medium layer", IEEE Trans. Geoscience and Remote Sensing, Vol. 23, pp. 924-932 (1985).
- Mätzler C., "Seasonal evolution of microwave radiation from an oat field", Remote Sens. Env. Vol. 31, pp. 161-173 (1990).
- Mätzler C., "Microwave (1-100 GHz) dielectric model of leaves", IEEE Trans. Geoscience and Remote Sensing, Vol. 32, pp. 947-949 (1994a).
- Mätzler C., "Microwave transmissivity of a forest canopy: Experiments made with a beech", Remote Sensing of Environment, Vol. 48, pp. 172-180 (1994b).
- Mätzler C., "Microwave permittivity of dry sand", IEEE Trans. Geosci. Remote Sensing, Vol. 36, pp. 317-319 (1998).
- Mätzler C. and A. Wiesmann, "Surface emissivity data from microwave radiometer experiments of the University of Bern", Appendix A, this issue, p. 163 (2000).
- McFarland M.J., R.L. Miller and C.M.U. Neale, "Land surface temperature derived from the SSM/I passive microwave brightness temperatures", IEEE Trans. Geoscience and Remote Sensing, Vol. 28, pp. 839-845 (1990).
- Mo T., B.J. Choudhury, T.J. Schmugge, J.R. Wang and T.J. Jackson, "A model for microwave emission from vegetation-covered fields" J. of Geophysical Research, Vol. 87, pp. 11229-11237 (1982).
- Mo T., T.J Schmugge and J.R. Wang, "Calculation of the microwave brightness temperature of rough soil surface : bare fields", J. Geophys. Res., Vol. 87, pp. 11229-11237 (1987).
- Njoku E.G. and J.A. Kong, "Multifrequency microwave radiometer measurements of soil moisture", J. Geophys. Res., Vol. 82, pp. 3108-3118 (1977).
- Njoku E.G., "Surface temperature estimation over land using satellite microwave radiometry", in: ESA/NASA International Workshop, B.J. Choudhury, Y.H. Kerr, E.G. Njoku and P. Pampaloni (Eds), VSP, Utrecht, pp. 509-530 (1994).
- Pampaloni P. and S. Paloscia, "Microwave emission and plant water content: a comparison between field measurements and theory", IEEE Trans. Geoscience and Remote Sensing, Vol. 24, pp. 900-905 (1986).
- Prigent C., W.B. Rossow and E. Matthews, "Microwave land surface emissivities estimated from SSM/I observations", J. Geophys. Res., Vol. 102, pp. 21867-21890 (1997).
- Saatchi S.S., E.G. Njoku and U. Wegmüller, "Synergism of active and passive microwave data for estimating bare soil surface moisture", in: ESA/NASA International Workshop, B.J. Choudhury, Y.H. Kerr, E.G. Njoku and P. Pampaloni (Eds), VSP, Utrecht, pp. 205-224 (1994).
- Schiffer R., "Reflectivity of a slightly rough surface", Appl. Optics, Vol. 26, pp. 704-712 (1987).
- Schmugge T.J. and B.J. Choudhury, "Comparison of radiative transfer models for predicting the microwave emission from soils", Radio Science, Vol. 16, pp. 927-938 (1981).
- Schmugge T.J. and T.J Jackson, "A dielectric model of the vegetation effects on the microwave emission from soils", IEEE Trans. Geoscience and Remote Sensing, vol. 30, pp. 757-760 (1992).
- Stogryn A., "Electromagnetic scattering by random dielectric constant fluctuations in a bounded medium", Radio Science, Vol. 9 (5), pp. 509-518 (1974).
- Suresh Raju, A. Chanzy, J.-P. Wigneron, J.-C. Calvet, Y. Kerr and L. Laguerre, "Soil moisture and temperature profile effects on microwave emission at low frequencies", Remote Sens. Environ., Vol. 54, pp. 85-97 (1995).
- Tsang L. and J.A. Kong, "Scattering of electromagnetic waves from random media with strong permittivity fluctuations", Radio Science, 16: 321-329 (1981).
- Ulaby F.T., M. Razani and M.C. Dobson, "Effect of vegetation cover on the microwave radiometric sensitivity to soil moisture", IEEE Trans. Geoscience and Remote Sensing, Vol. 21, pp. 51-61 (1983).
- Ulaby F.T., R.K. Moore and A.K. Fung, "Microwave Remote sensing – Active and Passive, Vol. III : from theory to applications", Artech house, inc. Dedham (1986).
- Ulaby F.T. and M.A. El Rayes, "Microwave dielectric spectrum of vegetation- Part II: Dual-Dispersion model", IEEE Trans. Geoscience and Remote Sensing, Vol. 25, pp. 550-557 (1987).
- Ulaby F.T. and E.A. Wilson, "Microwave attenuation properties of vegetation canopies", IEEE Trans.

- Geoscience and Remote Sensing, Vol. 23, pp. 746-753.
- Van de Griend A. and M. Owe, "The influence of polarization on canopy transmission properties at 6.6 GHz and implications for large scale soil moisture monitoring in semi-arid environments", IEEE Trans. Geoscience and Remote Sensing, Vol. 32, pp. 409-415 (1994).
- Van de Griend A. M. Owe, J. de Ruiter and B. T. Gouweleeuw, "Measurement and behavior of dual-polarization vegetation optical depth and single-scattering albedo at 1.4 and 5 GHz", IEEE Trans. Geoscience and Remote Sensing, Vol. 34, pp. 957-965 (1996).
- Van Oevelen P., "Estimation of areal soil water content by means of microwave remote sensing", PhD dissertation, Wageningen Agricultural University, The Netherlands, in preparation (1999).
- Wang J.R. and T.J. Schmugge, " An empirical model for the complex dielectric permittivity of soils as a function of water content", IEEE Trans. Geoscience and Remote Sensing, Vol. 18, pp. 288-295 (1980).
- Wang J.R. and B.J. Choudhury, "Remote sensing of soil moisture content over bare field at 1.4 GHz frequency", J. Geophys. Res., Vol. 86, pp. 5277-5282 (1981).
- Wang J.R., P.E. O'Neill, T.J. Jackson and E.T. Engman, "Multifrequency measurements of the effects of soil moisture, soil texture and surface roughness", IEEE Trans. Geoscience Remote Sensing, Vol. 21, pp. 44-50 (1983).
- Wang J.R., "microwave emission from smooth bare fields and soil moisture sampling depth", IEEE Trans. Geosci. Remote Sensing, Vol. 25, pp 616-622 (1987).
- Wegmüller U., C. Mätzler and E. Njoku, "Canopy opacity model", in: ESA/NASA International Workshop, B.J. Choudhury, Y.H. Kerr, E.G. Njoku and P. Pampaloni (Eds.), VSP, Utrecht, pp. 375-387 (1994).
- Wegmüller U. and C. Mätzler, "Rough bare soil reflectivity model", IEEE Trans. Geosci. Remote Sensing, Vol. 37, pp. 1391-1395 (1999).
- Wigneron J.P., Y.H. Kerr, A. Chanzy and Y.Q. Jin, "Inversion of surface parameters from passive microwave measurements over a soybean field", Remote Sens. Env. Vol. 46, pp. 61-72 (1993).
- Wigneron J.-P., J.-C. Calvet, Y. Kerr, A. Chanzy and A. Lopes, "Microwave emission of vegetation: Sensitivity to leaf characteristics, IEEE Trans. Geoscience and Remote Sensing, Vol. 31, pp. 716-726 (1993b).
- Wigneron J.P., A. Chanzy, J.-C. Calvet and N. Bruguier, "A simple algorithm to retrieve soil moisture and vegetation biomass using passive microwave measurements over crop fields", Remote Sens. Environ., Vol. 51: 331-341 (1995a)
- Wigneron J.-P., J.-C. Calvet, A. Chanzy, O. Grosjean and L. Laguerre, "A composite discrete-Continuous approach to model microwave emission of vegetation, IEEE Trans. Geoscience and Remote Sensing, Vol. 31, pp. 201-211 (1995b)
- Wigneron J.-P. B. Combé, U. Wegmüller and C. Mätzler, "Estimation of microwave parameters of crops from radiometric measurements", Int. J. Remote Sensing, Vol. 17, pp. 2875-2880 (1996).
- Wigneron J.-P., P. Waldteufel, A. Chanzy, J.-C. Calvet and Y. Kerr, "Retrieval capabilities of the microwave interferometer MIRAS over the land surface (SMOS mission)", 6<sup>th</sup> Specialist meeting on microwave radiometry and remote sensing of the environment, Firenze 1999/03/16-18, 21p (1999).
- Wilheit T.T., "Radiative transfer in plane stratified dielectric", IEEE Trans. Geoscience. Electron., Vol. 16, pp 138-143 (1978).



# **Development of microwave emission models of snowpacks**

Christian Mätzler, Andreas Wiesmann, Jouni Pulliainen and Martti Hallikainen

## **1 Passive microwave remote sensing of snow**

### **Discovering microwave signatures of snowpacks and firn**

Passive microwave signatures of seasonal snowpacks are well known by their strong contrast between wet and dry snow, by the decreasing emissivity for dry snow with increasing frequency (10 to 100 GHz range) and by their potential to give snow-volume information in case of dry snow. Signatures have been observed for over 30 years mainly by ground-based studies (e.g. Kennedy and Sakomoto, 1966; Hofer and Schanda, 1978; Stiles and Ulaby, 1980; Ulaby and Stiles 1980; Mätzler 1987, 1994, Wiesmann et al. 1998), but also from aircraft and indirectly also from satellite observations (e.g. McFarland et al. 1987, Josberger et al. 1993), and an early review of the potential and limitations for remote sensing was published by Bernier (1987). A recent study, covering frequencies up to 220 GHz (Tait et al. 1999) showed that volume-scattering signatures of snowpacks continue throughout the mm wavelength range.

Different microwave signatures were observed for the perennial snow and firn on polar ice sheets (Gurvich et al. 1973, Gloersen et al. 1974, Zhang et al. 1989, Rott 1989, Rott et al. 1993). Lowest emissivities are often observed at low microwave frequencies around 10 GHz. This property is a consequence of the large depth of scattering layers coupled with the increase of grain size with increasing depth to which low-frequency radiation can better penetrate, typically from 10 m at 10 GHz to at most 1 m at 35 GHz (Rott 1989, Mätzler 1987).

### **Search for direct inversion algorithms and why physical modeling is better**

With variable success, different researchers developed algorithms, based on spectral features, to retrieve the water equivalent of snowpacks for radiometer data from satellites (e.g. Hallikainen and Jolma, 1986; Chang et al., 1987; Wang et al., 1992; Goodison and Walker, 1995; Tait and Armstrong, 1996; De Sève et al., 1997). Although high correlations were found by algorithms for snow depth under special conditions, the usefulness of these empirical models was limited to specific geographic regions and special snowpack histories (Rango et al., 1979; Foster et al., 1980; Künzi et al., 1982). Rott and Nagler (1995) showed that different snow types (wet snow, snow with crusts, dry snow) can well be delineated, but that a universal algorithm for snow water equivalent does not exist. Mätzler (1994) found from surface-based experiments that snow structure and layering of dry snow can dominate the signal. Tait and Armstrong (1996), being aware of special snowpack signatures, tried to optimize snow-depth algorithms by excluding certain data (types of snowpacks, special regions and weather conditions). These experiences tell us that a more physical approach including all snow parameters would be more adequate than empirical algorithms for single parameters. The information gain accompanied with a physical analysis is manifold because all snow properties can give valuable geophysical information, not only the water equivalent. Parameters to be derived from snow structure are the optical albedo and the diffusivity for mass and heat transfer within the snowpack. Furthermore, in a physical treatment it is possible to include the relief (Mätzler and Standley, 1999) and the background radiation. Recent experiments showed that even the background radiation can be measured through dry, alpine snowpacks, and that the data are useful for permafrost mapping by microwave radiometry at frequencies near 10 GHz (Gubler and Hauck, 1998).

## **2 Modeling efforts for seasonal snow and ice sheets**

In order to understand the influence of snowpack properties on the microwave signal and to explain snow signatures, theoretical investigations have been performed through both electromagnetic wave theory (Tsang, 1987; Stogryn, 1986; Surdyk and Fily, 1995) and radiative transfer (e.g. Chang et al. 1976; Tsang and Kong, 1977). So far it has been difficult to validate the results of modeling efforts mainly because the snow structure cannot be quantified easily. If it is described by grain size we need realistic size distributions. Such distributions are often hypothetical because of the required assumptions on grain shape (e.g. Jin, 1995). An alternative is to use the Born Approximation or the Strong Fluctuation Theory (SFT) where the structure can be quantified by the correlation length, a quantity measurable from snow sections (e.g. Reber et al. 1987). The SFT model of Stogryn (1986) was tested by Weise (1996a) in the implementation of Surdyk (1992), using Weise's own experimental data. The validation showed that the model is inaccurate, probably because multiple scattering is ignored in SFT. Indeed, West et al. (1993) showed, on the basis of the dense-medium radiative transfer theory applied to backscattering from snow, that multiple scattering by snow grains is important.

The development of snowpack emission models is further complicated by the fact that snow profiles show strong vertical inhomogeneity. Since the penetration depth of microwaves and the scattering coefficient depend on frequency and snow properties, a general model should account for realistic snow-profiles of all sensitive parameters. A successful model might then be used for the development of remote sensing tools for observing processes on and within the snowpack. An important internal process, modifying heat and vapor transfer and being responsible for the release of avalanches, is temperature-gradient metamorphism, often taking place near the bottom of the snowpack. This process is based on large water-vapor gradients; it leads to the formation of cohesionless depth hoar (Armstrong, 1977, 1985). Microwave emission of depth-hoar layers are very special due to the enhanced volume-scattering by the large crystals (Weise, 1996a,b). On the other hand, snowpack stratification has important implications for physical processes, such as avalanche formation by weak layers (Föhn et al. 1998; Fierz, 1998), reduced vertical diffusion of water vapor and heat transfer, and percolation of liquid water in case of wet snow (Arons and Colbeck, 1995, and references therein). Snow layers also mark meteorological events in the history of snowpacks, and thus they contain information about past weather conditions. Specific microwave signatures related to stratification are expressed, for instance, by polarization features of microwave emission, and sometimes by special spectral properties. Since the earliest radiometer observations, interest has been paid to layering of polar ice sheets (Gurvich et al. 1973; Rott et al. 1993; Surdyk and Fily, 1995; Steffen et al. 1999), and layer effects were also found in snow-covered sea ice (e.g. Mätzler et al. 1984). Microwave emission of layered media, such as firn, was computed in the past by several authors (e.g. Gurvich et al. 1973; Djermakoye and Kong 1979; West et al. 1996). Other models were related to volume scattering by the granular firn structure (e.g. Zwally, 1977).

Driven by the need for realistic microwave emission models, combining soil, vegetation, snowpacks and atmosphere, ESA launched a study to combine theoretical and experimental investigations in 1995. Two different snowpack emission models evolved from this initiative (Pulliainen et al. 1998): A single-layer model, developed at the Helsinki University of Technology, called "HUT Model", and the Microwave Emission Model of Layered Snowpacks (MEMLS), developed at the University of Bern. Whereas the first model is a semi-empirical, single-scattering model suitable for rapid emission computation, the second one is a

more sophisticated model suitable for simulations of all kinds of physical effects. A comparison of the two models with regard to the aspect of single-scattering versus multiple scattering is given in this report in the chapter "Microwave emission from covered surfaces: single versus multiple scattering". Both models are described below.

### The HUT Model

The HUT Model describes the snowpack as a single homogeneous layer and uses an empirical formulation for the snow extinction coefficient and an empirical forward scattering factor. It assumes that the scattering is mostly concentrated in the forward direction. The snow extinction coefficient is modeled as a function of snow grain size and frequency (Hallikainen et al. 1987), whereas the forward scattering factor is approximated to be a constant coefficient. The effects of forest canopy, soil surface roughness and atmosphere to the brightness temperature are considered by using empirical/semi-empirical formulas (Kurvonen and Hallikainen 1997, Kruopis et al. 1999, Wegmüller and Mätzler 1999, Pulliainen et al. 1993). A schematic presentation of the main emission contributions is shown in Figure 1.

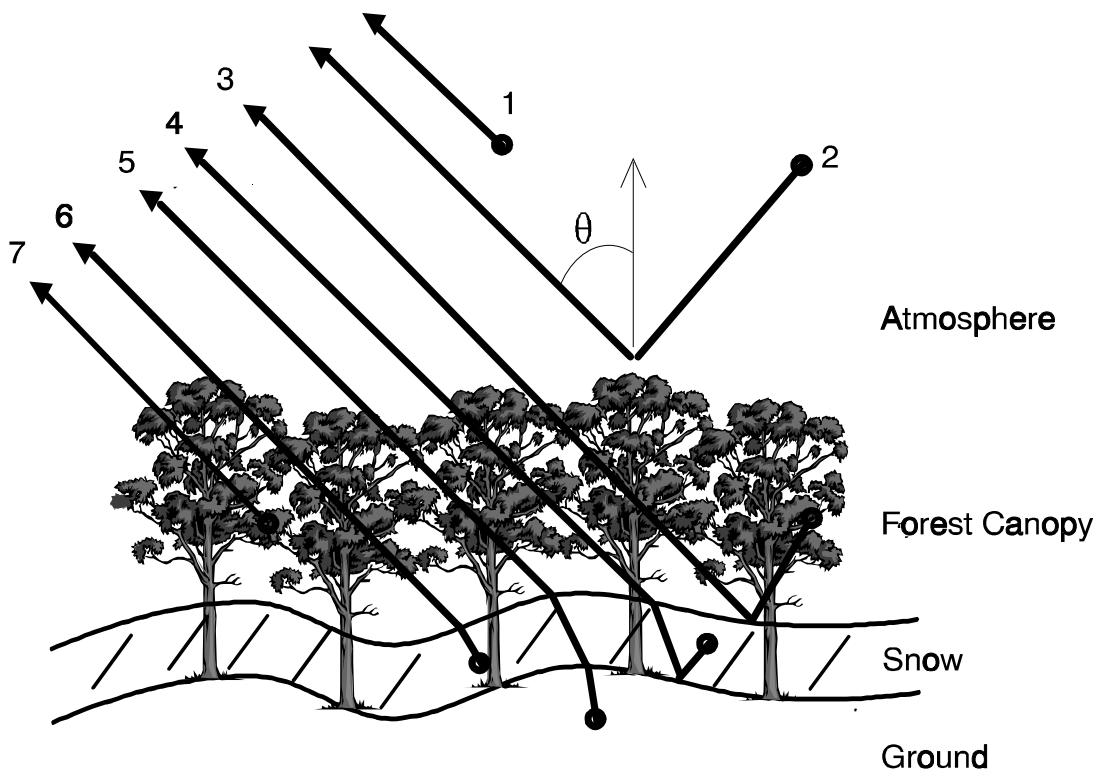


*Figure 1:* Schematic presentation of the main emission contributions included in the HUT snow emission model. The contributions are:

- 1: upward emitted atmospheric radiation
- 2: downward emitted reflected atmospheric contribution
- 3: downward emitted reflected forest canopy emission contribution
- 4: downward emitted reflected snowpack emission contribution
- 5: upward emitted soil emission contribution
- 6: upward emitted snowpack emission contribution
- 7: upward emitted forest canopy emission contribution.

The inclusion of vegetation and atmospheric emission contributions in modeling enables the use of the HUT model for interpreting space-borne radiometer observations. Comparisons of the HUT emission model predictions with independent experimental snowpack emission data and space-borne SSM/I observations show a good agreement in general (Pulliainen et al. 1999). An example of a comparison with space-borne SSM/I observations is shown in Figure 2. The HUT snow emission model is simple, and thus useful for direct retrievals of the water equivalent in snowpacks that are not strongly stratified. Care has to be taken at high frequencies (e.g. 90 GHz) where the penetration depth is often smaller than the snow depth. The single-layer model will then be unable to account for vertical gradients of snowpack properties.

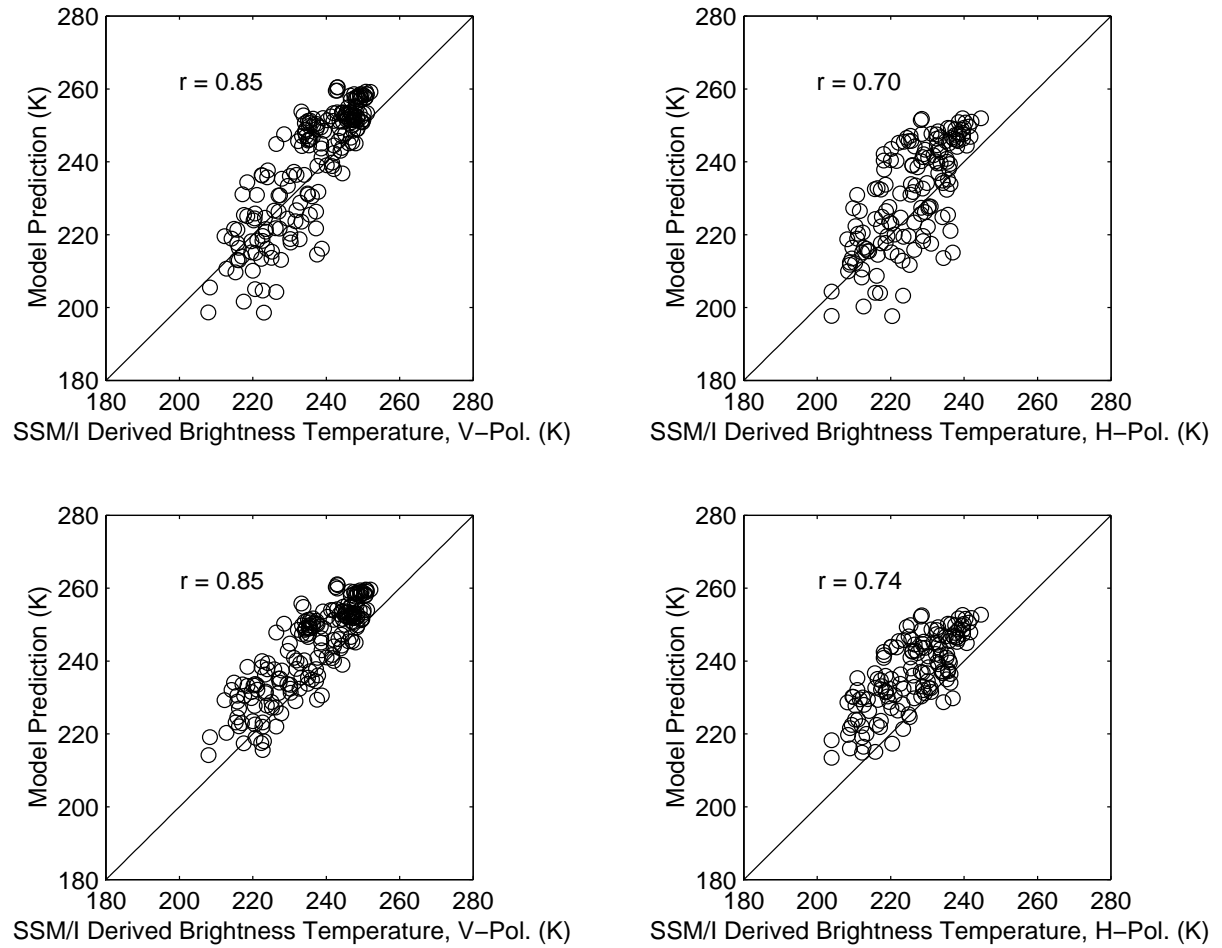


*Figure 2:* Comparison of SSM/I observations with the HUT snow emission model predictions. The observations and predictions for all SSM/I frequencies are combined. In-situ snow water equivalent, snow density, forest/land cover and air temperature information is used as model input. Snow grain size is treated with a fixed value of 1.1 mm.

Top: Comparison using balloon sounding-based in situ atmosphere profiles.

Bottom: Comparison using statistical atmosphere model (Pulliainen et al. 1993).

### The Microwave Emission Model of Layered Snowpacks (MEMLS)

MEMLS is based on radiative transfer, using a correlation-function approach to quantify snow structure, including multiple scattering both by stratification and by snow grains, refraction and radiation trapping by total internal reflection and a combination of coherent and incoherent superpositions of interface reflections (Wiesmann and Mätzler, 1999). The geometry of

the snowpack consisting of  $n$  ( $n \geq 1$ ) layers is illustrated in Figure 3. This model was achieved after detailed studies of single snow layers by Weise (1996a,b) and Wiesmann et al. (1998a). They found an empirical relationship between the scattering coefficient  $\gamma_s$ , frequency  $f$  and correlation length  $p_{ec}$ . The relationship was implemented in MEMLS; it is similar to Rayleigh scattering ( $\gamma_s \sim f^4 p_{ec}^3$ ) with regard to the correlation length, i.e. proportional to  $p_{ec}^{2.5}$ . The measured exponent of  $f$  is clearly below 4; it is also near 2.5. A limitation of the empirical fits for  $\gamma_s$  is in the applicable range of the observed frequencies (5 to 100 GHz), densities (0.1 to 0.4 g/cm<sup>3</sup>) and correlation lengths (0.05 to 0.3 mm), i.e. the situations found in dry winter snow. An example of emissivity simulations is shown in Figures 5 and 6 of the chapter "Microwave emission from covered surfaces: single versus multiple scattering" of this report.

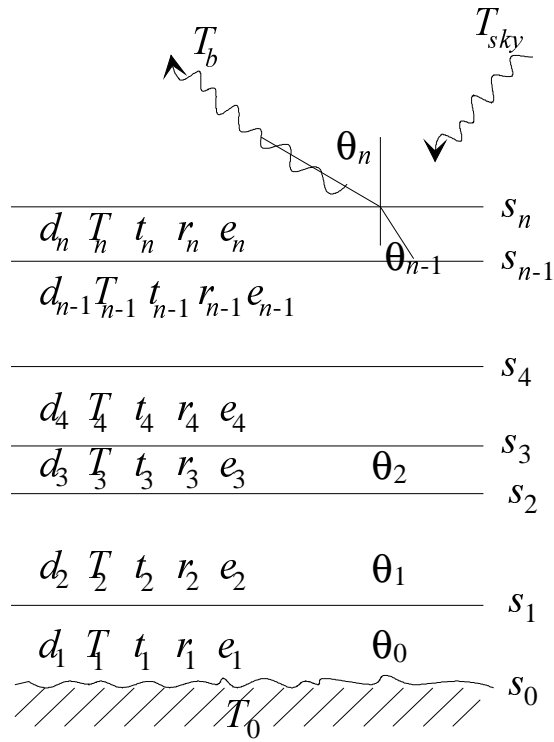


Figure 3: Geometry and parameters of the  $n$ -layer snowpack assumed in MEMLS;  $T_b$  is the scene brightness (model output) observed in direction  $\theta_n$ , and  $T_{sky}$  is the sky brightness.

In order to extend MEMLS, especially to coarse-grained snow, a physical model of volume scattering was developed by Mätzler and Wiesmann (1999), based on the improved Born Approximation (Mätzler, 1998). An exponential spatial autocorrelation function was selected and found to be reasonable. With this addition, MEMLS obtained a complete physical basis. The extended model is void of free parameters. Model validation included radiometric snow-samples of Wiesmann et al. (1998) on black-body and on metal plate, respectively, and coarse-grained crusts growing and decaying during melt-and-refreeze cycles. In all cases studied so far, i. e. for correlation lengths up to 0.7 mm, the model showed good agreement with the observations.

### Combination of microwave and physical snowcover models

A handicap of microwave emission models is the sometimes large number of input parameters. The overall quality of the simulations depends on the accuracy of these parameters, especially when the involved medium is complex. Up to now ground-truth measurements have

been used to provide the input. However, some parameters are difficult to collect. An alternative is to derive the snowpack data from physical snowcover models. They describe the properties of the snow cover from standard meteorological observations. These models have been developed to predict the mechanical, thermal, and optical snow properties for various applications, such as climate modeling, avalanche forecasting, and hydrology. The combination of such models with radiative-transfer models is a necessary step in the closure problem of surface effects in numerical weather prediction and data assimilation. In addition the combination is needed in the validation of both types of models. Furthermore, the detailed sets of required input parameters needed for realistic radiative-transfer computations can – in operational tasks – only be provided by such combinations. Several groups published recent research in this field: Shih et al. (1997) published a model to calculate backscattering from layered snowpacks, based on dense medium radiative transfer in combination with SNTHERM, a snow physical model to be explained below. Galantowicz and England (1997) presented a passive microwave model in combination with a soil-vegetation-atmosphere scheme based on the physical snow model of Anderson (1975). Wilson et al. (1999) combined a single-layer dry-snow emission model with a hydrological snowpack model derived from SNTHERM and applied it to an area in Colorado. Wiesmann et al. (1998b) developed and tested interfaces to combine MEMLS with two different models, CROCUS, and SNTHERM. SNTHERM is a one-dimensional mass and energy balance model, developed at the U.S. Army Cold Regions Research and Engineering Laboratory (CRREL) for predicting temperature profiles within the snow and frozen soil. The model is formulated to describe a snowcover over soil with high vertical and temporal resolution. CROCUS is a one-dimensional numerical energy and mass evolution model of snowcovers developed at Météo France. Its main objective is operational avalanche forecasting. Both models use meteorological data versus time as input. The output of both models can almost directly be used as input in MEMLS. Only the different descriptions of snow structure had to be adapted to the correlation length used in MEMLS. An example of a combined simulation at 35 GHz is shown in Figure 4. The strong emissivity fluctuations found early and late in the snow season are due to melt-refreeze cycles. During the dry snow phase an anticorrelation of the emissivity with snowheight can be recognized in the long-term behavior; the short-term variations, however, are uncorrelated.

The results obtained so far with both, CROCUS and SNTHERM, indicate reasonable agreement between the combined model and the observations. Discrepancies are observed in the polarization difference,  $T_v - T_h$ , which is often underestimated. This is due to the fact that the physical snowpack models cannot simulate the crusts (SNTHERM) or that their density is underestimated (CROCUS).

### **Outlook to applications and further improvements:**

The HUT Model can be used for snowpack emission modeling including contributions from snow, soil, forest canopies and atmosphere. It has potential to be applied for the retrieval of information concerning snow water equivalent (SWE) for dry snow, extent of dry snow cover, on-set of snow melt, and information on snow grain size and density.

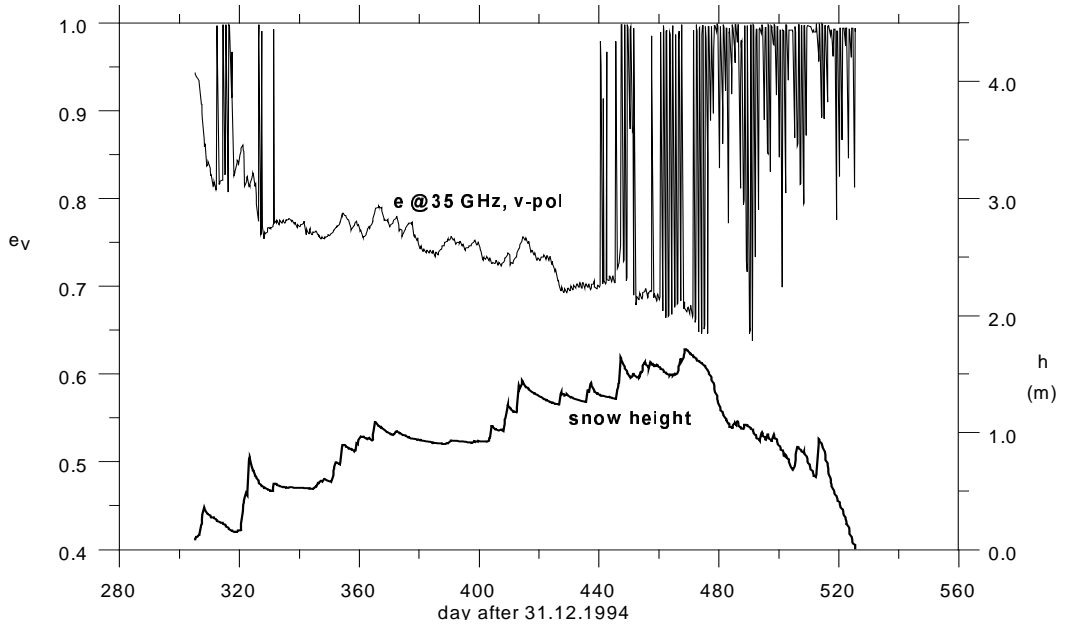


*Figure 4:* Variation of snow height  $h$  and snowpack emissivity  $e_v$  at 35 GHz, vertical polarization, during the snow season 1995/96 at the test site, Weissfluhjoch-Davos. The emissivity was simulated by the combined use of CROCUS and MEMLS from standard meteorological observations.

The investigations carried out up-to-date show promising SWE retrieval accuracies as HUT model is directly applied to SSM/I observations using a multi-parameter constrained iterative inversion procedure. For example, the areal SWE of the 50,000 km<sup>2</sup>-sized River Kemijoki drainage area was estimated with an overall RMSE of 24 mm for a single winter. The corresponding coefficient of determination ( $r^2$ ) was 0.92 (number of reference observations available for comparison was 30). These results were obtained under dry snow conditions (period from 1 Nov. 1993 to 31 March 1994) without using any training reference data.

MEMLS is useful to investigate the influence of snow parameters on the microwave signal and therefore is a tool to analyze microwave data of snow and to develop new snow characterization algorithms. It is also helpful for designing new radiometer systems. Furthermore MEMLS can become a key for new developments in snow physics. Some steps of future work are outlined here:

- To assess the sensitivity of MEMLS to special parameter variations, weighting functions, defined by  $w_{ij} = \partial e_p / \partial x_{ij}$ , where  $e_p$  is the emissivity at polarization  $p$  and  $x_{ij}$  is the  $i^{\text{th}}$  physical parameter of layer  $j$ , can be computed.
- The assumption of an isotropic and exponential correlation function is not valid in general, but so far, it has been a reasonable simplification of snow structure. By including the occasional snow-structure anisotropy (e.g. observed in new snow deposited under calm-wind condition, surface hoar, depth hoar) the model can be improved, especially its polarization behavior at frequencies above 30 GHz.
- Multiple versus single layer: It has been argued that single-layer snow emission models are more practical and thus more feasible than multi-layer models. This statement may be tested by simulations using MEMLS for different values of  $n$ . MEMLS is adaptive with

respect to  $n$ . Nevertheless it should be pointed out that layering is inherent to many snowpacks bearing signatures which may be revealed by microwave radiometry.

- A combination of SAFRAN/CROCUS (Durand et al., 1993) with MEMLS gives the possibility to simulate brightness temperature maps. SAFRAN (Système d'Analyse Fournissant des Renseignements Atmosphériques à la Neige) is a sophisticated meteorological model, calculating the input variables for snow cover simulations in a model topography over large areas (about 1000km<sup>2</sup>). Comparison of such maps with observed data makes it possible to validate forecasts on a large scale. On a local scale it may help to assess snowpack and background properties.
- Using past meteorological information, it is possible to simulate the emissivity of past conditions providing a tool for reanalyzing historical satellite data. This application is needed for model validation, and furthermore, opens the way to climate studies using different observational systems.
- With accurate knowledge of the surface emissivity, it is possible to determine atmospheric parameters from space-based observations.
- Due to the high sensitivity of microwave emission on internal snow-structure parameters, MEMLS can help to improve the snow physical models, especially the quantitative understanding of snow metamorphosis, and layer structure. As a feedback of such studies, also MEMLS will further be improved.

### **3 Recommended microwave emission models for snowpacks**

#### **Physical model: MEMLS**

Described by Wiesmann and Mätzler (1999), extended by Mätzler and Wiesmann (1999), Wiesmann et al. (1998b).

Purpose of the model	MEMLS computes transmissivity $t_p$ , emissivity $e_p$ and brightness temperature $T_p$ at polarization $p$ of a snow-covered surface under given illumination by $T_{sky}$ .
Applications, constraints	Seasonal and perennial snowpacks of any thickness with defined stratigraphy. Assimilation of $T_p$ for NWP, avalanche forecasts, hydrology, climatology, simulation of $T_p$ for sensitivity studies, as source for construction of simple models and inversion algorithms for snow parameters and ground temperature. Constraints to be assessed.
Model variables and ranges	Frequency range $f$ : 5 to 100 GHz, incidence angle $\theta$ : 0 to 60°, polarization: linear $h$ or $v$
Input parameters, including applicable ranges, options for selection and potential sources	Sky brightness temperature $T_{sky}$ (unlimited), ground temperature $T_0$ , ground-snow interface reflectivity $s_0$ (0 to 1), for each of the $n$ ( $\geq 1$ ) snow layers the following model parameters: Correlation length $p_{ec}$ : 0 to 0.7 mm, temperature $T$ : 100 to 273.15 K, snow density $\rho$ : 50 to 500 kg/m <sup>3</sup> , (possibly up to 900 kg/m <sup>3</sup> ) volumetric liquid-water content $W$ : 0 to about 0.15. Input parameters can be generated by physical snowpack models and meteorological information (Wiesmann et al. 1998b).
Output parameters	Standard: upwelling brightness temperature $T_p$ above the surface Optional: scene emissivity (0 to 1), snowpack transmissivity (0 to 1)
Expected errors	Validation made for various snow conditions (Wiesmann et al. 1998a; Wiesmann and Mätzler, 1999; Mätzler and Wiesmann, 1999) Present estimate: for $T_p$ : $\leq 10$ K, for $e_p$ : $\leq 0.03$ K
Accuracy requirements	Useful: for $T_p$ : 10 K, for $e_p$ : 0.03 K; further assessment needed Adequate: for $T_p$ : 3 K, for $e_p$ : 0.01 K

Further developments	<p>Weighting functions, <math>w_{ij} = \partial e_p / \partial x_{ij}</math>, where <math>x_{ij}</math> is the <math>i^{\text{th}}</math> physical parameter of layer <math>j</math>, can be computed in order to assess the sensitivity of the model to special parameter variations.</p> <p>Isotropic correlation functions other than exponential can easily be included. More work is needed to account for anisotropic snow structure.</p> <p>Presently the main uncertainty is due to errors of the input parameters. More accurate data on snow structure and better standards are needed.</p>
----------------------	---

### Semi-empirical model: HUT Model

Described by Pulliainen et al. (1999) and Pulliainen et al. (1998).

Purpose of the model	Computes brightness temperature and emissivity of snow-covered terrain, optionally including the effect of sparse coniferous forest canopy (under winter conditions) and atmosphere
Applications, constraints	Applicable for iterative inversion: snow water equivalent retrieval/monitoring in boreal forest zone (tested and demonstrated). Assimilation to hydrological models to be done. Potential areas of application: hydrology, meteorology, climatology, hydro-power production, flood prediction. Constraints to be assessed.
Model variables and ranges	Frequency: 5 to 100 GHz, nadir angle 20° to 70° (restricted by the soil emission model), polarization: linear h or v
Input parameters (including applicable ranges, options for selection and potential sources)	Sky brightness temperature (unlimited), ground temperature, snow temperature, ground-snow interface reflectivity, effective snow grain size (up to 1.6 mm), snow density (0.1-0.4 g/cm³). Optionally snow wetness (up to a few percentage units); calculation of ground-snow reflectivity e.g. using the model by Wegmüller and Mätzler (1999); calculation of atmospheric effects e.g. using the statistical model by Pulliainen et al. 1993.
Output parameters	Brightness temperature and emissivity of snow covered terrain (above the snow surface). Optionally: airborne or spaceborne observed scene brightness temperature or emissivity including the effect of forest canopy and atmosphere.
Expected errors, validation and quality checks	Validation performed against experimental controlled conditions measurements and SSM/I observations. Further error analysis to be done.
Accuracy ranges	To be assessed.
Scopes for further development	<p>Currently one empirical parameter (<math>q</math>) included. The behavior of <math>q</math> as function of frequency and snow grain size to be modeled using theoretical approaches.</p> <p>Development of operative snow parameter retrieval methods based on the HUT model.</p>

## References

- Anderson E.A., A Point energy and mass balance model of a snow cover, Ph.D. thesis, Dep. of Civ. Eng., Comm. on Grad. Stud. of Stanford University (1975).
- Armstrong R.L., "Continuous monitoring of metamorphic changes of the internal snow structure as a tool in avalanche studies", *J. Glaciol.*, Vol. 19, pp. 325-334 (1977).
- Armstrong R.L., "Metamorphism in subfreezing, seasonal snow cover: the role of thermal and vapor pressure conditions", PhD Thesis, University of Colorado, Fac. Graduate School, Dept. Geography (1985).
- Arons E.M and S.C. Colbeck, "Geometry of heat and mass transfer in dry snow: a review of theory and experiment", *Reviews of Geophys.* Vol. 33, pp. 463-493 (1995).
- Bernier P.Y. "Microwave Remote Sensing of Snowpack Properties: Potential and Limitations", *Nordic Hydrology*, Vol. 18, pp. 1-20 (1987).
- Chang A.T.C., P. Gloersen, T. Schmugge, Microwave emission from snow and glacier ice, *J. Glaciol.*, 16(1), pp. 23-39 (1976).
- Chang A.T.C., J.L. Foster, D.K. Hall, Nimbus-7 SMMR derived global snow cover parameters, *Ann. Glaciol.*, 9, pp. 39 - 44 (1987).
- De Sève D., M. Bernier, J.-P. Fortin, A. Walker, Preliminary analysis of snow microwave radiometry using the SSM/I passive-microwave data: the case of La Grande River watershed (Quebec), *Annals of Glaciology*, 25, pp. 353-361 (1997).
- Djermakoye B., and J.A. Kong, "Radiative-transfer theory for the remote sensing of layered random media", *J. Appl. Phys.* Vol. 50, pp. 6600-6604 (1979).
- Durand Y., E. Brun, L. Mérindol, G. Guyomarc'h, B. Lesaffre , E. Martin, A meteorological estimation of relevant parameters for snow models. *Ann. Glaciol.*, 18, pp. 65-71, 1993.
- Fierz C. "Field observations and modelling of weak-layer evolution", *Annals Glaciol.* 26, pp. 7-13 (1998).
- Föhn P.M., C. Camponovo and G. Krüsi, "Mechanical and structural properties of weak snow layers measured in situ", *Annals Glaciol.* Vol. 26, pp. 1-6 (1998).
- Foster J.L., A. Rango, D.K. Hall, A.T.C. Chang, L.J. Allison, B.C. Diesen, Snowpack monitoring in North America and Eurasia using passive microwave satellite data. *Rem. Sens. Environ.*, 10, pp 285-298 (1980).
- Galantowicz J.F., A.W. England: Seasonal snowpack radiobrightness interpretation using a SVAT-linked emission model, *JGR*, Vol. 102, No. D18, pp 21,933 - 21,946, Sept. 27, 1997.
- Gloersen, P., T.T. Wilheit, A.T.C. Chang, W. Nordberg and W.J. Campbell, "Microwave maps of the polar ice of the earth", *Bull. Amer. Meteo. Soc.*, Vol. 55, pp. 1442-1448 (1974).
- Goodison B.E., A.E. Walker, Canadian development and use of snow cover information from passive microwave satellite data, in *Passive Microwave Remote Sensing of Land-Atmosphere Interactions*, Editor B.J. Choudhury, Y.H. Kerr, E.G. Njoku, P. Pampaloni, pp. 245-262, VSP, Utrecht, The Netherlands (1995).
- Gubler H., Hauck C., Preliminary Measurements of BTS Using a Microwave Radiometer, *Permafrost and Climate in Europe (PACE)*, Project of the European Commission, ENV4-CT97-0492, WP 2, preprint (1998).
- Gurvich A.S., V.I. Kalinin, and D.T. Matveyev, "Influence of the internal structure of glaciers and their thermal radio emission", *ATM. Oceanic Phys.* Vol. 12, pp. 713-717 (1973).
- Hallikainen, M.T. and P.A. Jolma, "Retrieval of the water equivalent of snow cover in Finland by satellite microwave radiometry", *IEEE Trans. Geosci. and Remote Sensing*, Vol. GE-24, pp. 855-862 (1986).
- Hallikainen, M., F. Ulaby and T. Deventer, "Extinction behavior of dry snow in the 18- to 90-GHz range," *IEEE Trans. Geosci. Remote Sensing*, vol. GE-25, pp. 737-745 (1987).
- Hofer R., E. Schanda, Signatures of snow in the 5-94 GHz range. *Radio Science*, 13, pp. 365-369 (1978).
- Jin Y.Q. "Size parameters of snow grains in scattering and emission models", in B.J. Choudhury, Y.H. Kerr, E.G. Njoku, P. Pampaloni, (eds.) "Passive Microwave Remote Sensing of Land-Atmosphere

- Interactions", pp. 245-262, VSP, Utrecht, The Netherlands, pp. 273-283 (1995).
- Josberger, E.G., W.J. Campbell, P. Gloersen, A.T.C. Chang, and A. Rango, "Snow conditions and hydrology of the upper Colorado river basin from satellite passive microwave observations", *Annals Glaciol.*, Vol. 17, pp. 322-326 (1993).
- Kennedy J.M. and R.T. Sakamoto, "Passive microwave determination of snow wetness factors", Proc. 4<sup>th</sup> Internat. Symp. on Remote Sensing of Environment, pp. 161-171, Ann Arbor, Michigan (1966).
- Kruopis, N., J. Praks, A.N. Arslan, H. Alasalmi, J. Koskinen, and M. Hallikainen, "Passive microwave measurements of snow-covered forest areas in EMAC'95", Submitted for publication in IEEE Trans. Geosci. and Remote Sensing (1998).
- Künzi K.F., S. Patil, H. Rott, Snowcover parameters retrieved from Nimbus-7 Scanning Multichannel Microwave Radiometer (SMMR) data, *IEEE Trans. Geosci. Rem. Sens.*, GE-20, pp. 452-467 (1982).
- Kurronen, L. and M. Hallikainen, "Influence of land-cover category on brightness temperature of snow", *IEEE Trans. Geosci. Remote Sensing*, vol. GE-35, pp. 367-377 (1997).
- Mätzler C., R.O. Ramseier, and E. Svendsen, "Polarization effects in sea-ice signatures", *IEEE J. Oceanic Engin.*, Vol. OE-9, pp. 333-338 (1984).
- Mätzler C., "Applications of the Interaction of Microwaves with the Natural Snow Cover", *Remote Sensing Reviews*, Vol. 2, pp. 259-392 (1987).
- Mätzler C., Passive Microwave Signatures of Landscapes in Winter, *Meteorology and Atmospheric Physics*, Vol. 54, pp. 241 - 260 (1994).
- Mätzler C., "Improved Born Approximation for scattering in a granular medium", *J. Appl. Phys.*, Vol. 83, No. 11, pp. 6111-6117 (1998).
- Mätzler, C. and A. Wiesmann, "Extension of the Microwave Emission Model of Layered Snowpacks to Coarse-Grained Snow", *Remote Sensing of Environment*, 70, pp. 317-325 (1999).
- Mätzler C. and A. Standley, "Relief effects for passive microwave remote sensing", *Internat. J. of Remote Sensing*, in press (1999), see also this issue pp. 81-88 (2000).
- McFarland M.J., G.D. Wilke, and P.H. Harder, "Nimbus 7 SMMR investigation of snowpack properties in the Northern Great Plains for the Winter 1978-1979, *IEEE Trans. Geosci. Rem. Sens.* Vol. GE-25, pp. 35-45 (1987).
- Pulliainen, J., J-P. Kärnä and M. Hallikainen, "Development of geophysical retrieval algorithms for the MIMR", *IEEE Trans. Geosci. Remote Sensing*, Vol. GE-31, pp. 268-277 (1993).
- Pulliainen J., K. Tigerstedt, W. Huining, M. Hallikainen, C. Mätzler, A. Wiesmann, and C. Wegmüller, "Retrieval of geophysical parameters with integrated modeling of land surfaces and atmosphere (models/inversion algorithms)", Final Report, ESA/ESTEC, Noordwijk, Netherlands, Contract No. 11706/95/NL/NB(SC), Oct. (1998).
- Pulliainen J., Grandell J., Hallikainen M., "HUT snow emission model and its applicability to snow water equivalent retrieval," *IEEE Trans. Geoscience and Remote Sensing*, Vol. 37. pp. 1378-1390 (1999).
- Rango A., A.T.C. Chang, J.L. Foster, The utilization of spaceborne microwave radiometers for monitoring snowpack properties, *Nord. Hydrol.*, 10, pp. 25-40 (1979).
- Reber B., C. Mätzler, and E. Schanda, "Microwave Signatures of Snow Crusts: Modelling and Measurements", *Internat. J. Remote Sensing*, Vol. 8, pp. 1649-1665 (1987).
- Rott H. "Multispectral microwave signatures of the Antarctic Ice Sheet", in P. Pampaloni (Ed.), "Microwave Radiometry and Remote Sensing Applications", VSP, Utrecht, the Netherlands, pp. 89-101 (1989).
- Rott H., K. Sturm and H. Miller, "Active and passive microwave signatures of Antarctic firn by means of field measurements and satellite data", *Annals Glaciol.* Vol. 17, pp. 337-343 (1993).
- Rott H., T. Nagler, Intercomparison of snow retrieval algorithms by means of spaceborne microwave radiometry, in *Passive Microwave Remote Sensing of Land-Atmosphere Interactions*, Editor B.J. Choudhury, Y.H. Kerr, E.G. Njoku, P. Pampaloni, pp. 245-262, VSP, Utrecht, The Netherlands (1995).
- Shih S.-E., K.-H. Ding, J.A. Kong, Y.E. Yang: Modeling of millimeter wave backscatter of time-varying snowcover, *PIER*, Vol. 16, pp. 305 - 330 (1997).
- Steffen K., W. Abdalati and I. Sherjal, "Faceted crystal formation in the NE-Greenland low accumu-

- lation region", *J. Glaciol.*, Vol. 45, pp. 63-68 (1999).
- Stiles W.H. and F.T. Ulaby, "The active and passive microwave response to snow parameters, 1. wetness" *J. Geophys. Res.* Vol. 85, pp. 1037-1044 (1980).
- Stogryn, A., A study of the microwave brightness temperature of snow from the point of view of strong fluctuation theory, *IEEE Trans. Geosci. Rem. Sens.*, GE-24, No. 2, pp 220-231, 1986.
- Surdyk S. "Etudes des signatures spectrales micro-ondes obtenues par télédétection sur la calotte polaire Antarctique", Thèse de doctorat de l'institut national polytechnique de Grenoble (1992).
- Surdyk S., M. Fily, Results of a stratified emissivity model based on the wave approach: Application to the Antarctic Ice Sheet, *J. Geophys. Res.* Vol. 100, pp. 8837-8848 (1995).
- Tait A.B. and R.L. Armstrong, Validation of SMMR satellite-derived snow depth with ground-based measurements", *Internat. J. Remote Sensing*, Vol. 17, pp. 657-665 (1996).
- Tait A., D. Hall, J. Foster, A. Chang and A. Klein, "Detection of snow cover using millimeter-wave imaging radiometer (MIR) data", *Rem. Sens. Environment*, Vol. 68, pp. 53-60 (1999).
- Tsang L., J.A. Kong, Theory for thermal microwave emission from a bounded medium containing spherical scatterers, *J. Appl. Phys.*, 48(8), pp. 3593-3599 (1977).
- Tsang L., Passive remote sensing of dense nontenuous media, *J. Electrom. Waves Appl.*, 1(2), pp. 159-173 (1987).
- Ulaby F.T. and W.H. Stiles, "The active and passive microwave response to snow parameters, 2. The water equivalent of dry snow" *J. Geophys. Res.* Vol. 85, pp. 1045-1049 (1980).
- Wang J.R., A.T.C. Chang, A.K. Sharma, On the estimation of snow depth from Microwave radiometric instruments, *IEEE Trans. Geosci. Remote Sens.*, 30(4), pp 785-792 (1992).
- Wegmüller, U. and Mätzler, C., "Rough bare soil reflectivity model", *IEEE Trans. Geosci. Remote Sensing*, Vol. 37, pp. 1391-1395 (1999).
- Weise T., Radiometric and structural measurements of snow, Ph.D. Thesis, Inst. of Appl. Physics, University of Bern, Bern, Switzerland (1996a).
- Weise T, Radiometric data (11-94 GHz) and autocorrelation functions of dry snow samples, IAP-Report 96-2, Inst. of Applied Physics, Univ. of Bern (1996b).
- West R., L. Tsang and D.P. Winebrenner, "Dense medium radiative transfer theory for two scattering layers with a Rayleigh distribution of particle sizes", *IEEE Trans. Geosci. Remote Sensing*, Vol. 31, pp. 426-436 (1993).
- West R.D, D.P. Winebrenner, L. Tsang and H. Rott, "Microwave emission from density-stratified Antarctic firn at 6 cm wavelength", *J. Glaciol.*, Vol. 42, pp. 63-76 (1996).
- Wiesmann A. and C. Mätzler, Documentation for MEMLS 98.1, Microwave Emission Model of Layered Snowpacks, IAP-Report 98-2, Inst. of Applied Physics, Univ. of Bern, Remote Sensing of Environment, Vol. 70, pp. 307-316 (1999).
- Wiesmann A., C. Mätzler, T. Weise: Radiometric and Structural Measurements of Snow Samples, *Radio Science*, Vol. 33, No. 2, pp. 273 - 289 (1998a).
- Wiesmann A., C. Fierz and C. Mätzler, Simulation of microwave emission from physically modeled snowpacks, IAP-Report 98-8, Inst. of Applied Physics, Univ. of Bern (1998b). To be published in *Annals of Glaciology*, Vol. 31.
- Wilson L.T., L. Tsang, J.N. Hwang, and C.T. Chen, "Mapping snow water equivalent by combining a spatially distributed snow hydrology model with passive microwave remote-sensing data", *IEEE Trans. Geoscience and Remote Sensing*, Vol. 37, pp. 690-704 (1999).
- Zhang H., L. Toudal Pedersen and P. Gudmandsen, "Microwave brightness temperatures of the Greenland Ice Sheet", *Adv. Space Res.*, Vol. 9, pp. (1)277-(1)287 (1989).
- Zwally H.T. "Microwave emissivity and accumulation rate of polar firn", *J. Glaciol.*, Vol. 18, pp. 195-215 (1977).

# Fast models for land surface emissivity

Tim Hewison & Stephen English

## 1 Why develop a fast model?

Retrievals of atmospheric temperature and humidity profiles from satellite microwave radiometers require a background value of surface emission. Like models of sea surface emissivity, many radiative transfer models for land surfaces are computationally expensive, because they include scattering terms. Given the large amount of data and real-time operation, a fast emissivity model is required to represent the emissivity of both land and sea surfaces.

However, an additional problem needs to be addressed when deriving a fast model for land surfaces. Accurate radiative transfer modelling requires a large number of input parameters, which are not readily observable from space (e.g. spectral roughness or water content of vegetation).

For these reasons it is desirable to develop a simplified fast model, which can be empirically tuned to fit the observed data. Such a model should be capable of representing many land surfaces over a broad range of frequency and incidence angle.

## 2 Empirical models

In its simplest form, a fast model can represent the emissivity of all land surfaces at all frequencies by a constant value e.g.  $e=0.95$ . Although this is clearly a gross over-simplification, it was used for some time for MSU [English, 1998], which only has four channels between 50-60 GHz. This scheme will obviously produce large errors in retrievals where the emissivity is very different from this constant value (e.g. snow-covered land).

Therefore, we need to provide parameters for different surfaces. Also, in general, the frequency dependence of the various processes occurring at the surface needs to be represented, especially for surfaces with a large component of water, which has a high dielectric constant decreasing across the microwave band, or those where scattering is the dominant process, as this is also frequency dependent.

Grody (1988) proposed an empirical model to cover the emissivity as a function of frequency  $\nu$  of 7 surface types between 20-50 GHz, with the form:

$$e_n(\nu) = a_n + b_n \log(\nu),$$

where  $a_n$  and  $b_n$  are parameters fitted empirically for various surfaces identified by index  $n$ . Grody went on to extend the application of his model to frequencies between 10-90 GHz, by including two additional parameters, with the form:

$$e = \frac{e_0 + e_\infty (\nu / \nu_0)^k}{1 + (\nu / \nu_0)^k},$$

where  $e_0$ ,  $e_\infty$ ,  $\nu_0$ , and  $k$  are fitted to aircraft and ground-based observations. The parameters  $e_0$  and  $e_\infty$  represent the emissivity at zero and infinite frequency,  $\nu_0$  is the transition frequency and  $k$  is the "rate" of transition. However, non-monotonic emissivity spectra observed in dry

snow or fast ice cannot be represented without additional terms. Neither can it be applied to arbitrary view angles or polarisation.

### 3 A semi-empirical model

To address the shortcomings of earlier models, a new form has been proposed [Hewison and English, 1999]. This semi-empirical model uses Fresnel's formulae to calculate the specular reflectivity  $\Gamma_{sp}$  at polarisation  $p$  of a dielectric surface, whose permittivity can be described by a single Debye relaxation, neglecting the ionic conductivity term, as this is negligible for frequencies above 20 GHz.

$$\epsilon(v) = \frac{\epsilon_s - \epsilon_\infty}{1 - i \cdot (v/v_r)} + \epsilon_\infty,$$

where  $\epsilon(v)$  is the effective permittivity at frequency,  $v$ ,  $\epsilon_s$  is the static permittivity,  $\epsilon_\infty$  is the permittivity at infinite frequency, and  $v_r$  is the relaxation frequency.

Surface (Bragg) scattering by small-scale features is represented modifying the specular reflectivity by a roughness factor [Choudhury, 1979]:

$$\Gamma_p = \Gamma_{sp} \exp(-(4\pi v \sigma_s / c)^2 \cos^2 \theta),$$

where  $\sigma_s$  is the small-scale rms surface roughness, measured on a scale appropriate for the frequency;  $c$  is the speed of light and  $\theta$  is the view angle. In practice, the roughness must be fitted to the observed emissivity spectra; e.g. the value of  $\sigma \approx 0.2\text{mm}$  was found to fit the behaviour of frozen soil, which is clearly not a realistic rms roughness. This parameter does, however, allow the non-monotonic emissivity spectra of dry snow to be represented.

It was found necessary to include an additional parameter in the model to fit the airborne observations that the specular reflectivities calculated from Fresnel's formula considerably overestimate the difference between  $h$  and  $v$  polarisation. This parameter,  $Q$ , is simply fitted to the observed data and can take any value from 0.0 for a perfectly specular reflector to 0.5 for a perfectly rough surface.

$$e_p = (1 - \Gamma_p)(1 - Q) + (1 - \Gamma_q)Q,$$

where  $e_p$  is the emissivity in polarisation,  $p$ ,  $\Gamma_p$  is the reflectivity in polarisation  $p$ , and  $\Gamma_q$  is the reflectivity in the opposite polarisation.

Extinction by vegetation, volume scattering and surface scattering by large-scale features is not explicitly modelled. Because of this, the estimation of permittivity coefficients will not be equivalent to the actual permittivity of the surface materials.

### 4 Advantages and disadvantages

The Debye/Fresnel formulae provide a convenient mathematical framework, which allows us to create an often realistic and constrained functional form of the spectral dependence of emissivity, whilst its flexibility does not preclude the use of a physical formulation. It follows the same form as the fast emissivity model for the sea surface (English and Hewison, 1999), which greatly simplifies the representation of emissivity in retrieval and data assimilation

methods. However, this model is somewhat more computationally expensive, and requires more (5) parameters.

## 5 Fitting model parameters

All empirical or semi-empirical models require parameters to be fitted to match observations or the results of an accurate, physical model. In the absence of a comprehensive model including the physics of all processes affecting surface emissivity, the fast model's parameters can only be fitted to observed data. The model can also be used for interpolation of emissivity data.

### 5.1 Satellite data measured by Prigent et al. [1999]

Prigent *et al.* [1999] calculated emissivity for 9 different land-use classifications from data from the Special Sensor Microwave/Imager (SSM/I). They included a correction for atmospheric absorption, cloud masking and surface temperatures derived from infrared observations. Their 9 land-use classes are combinations of Matthews' [1983] database of 30 vegetation classes defined globally at a 1° resolution in latitude and longitude. The data used here is taken from Figure 2 of their paper, showing the average emissivity of each class calculated for October 1991 over the Meteosat area, covering Africa, Europe and western Asia.

Table 1 shows the average emissivity calculated from these channels for each vegetation class, with results of the least squares regression used to derive parameters for the FASTEM model. It also shows the rms error in the fit to FASTEM and a modified version, referred to as "Kerr", described later in this section. The results for all classifications show the emissivity decrease with frequency. This may be due to volume scattering by sand particles in the dry, underlying soils that dominate the study area.

Table 1: SSM/I emissivities calculated by Prigent *et al.* with fitted FASTEM parameters for  $\sigma_s=0$ .

Channel	19H	37H	85H	19V	37V	85V	$\epsilon_s$	$\epsilon_i$	$v_r$	Q	rms	Kerr rms
Desert	0.839	0.842	0.832	0.980	0.956	0.916	2.93	4.20	116	0.22	0.013	0.002
Shrubland	0.837	0.837	0.839	0.958	0.935	0.914	3.09	3.58	35.8	0.26	0.010	0.007
Tundra and mossy bog	0.853	0.844	0.824	0.920	0.905	0.896	3.19	4.33	51.3	0.35	0.002	0.016
Grassland	0.886	0.882	0.871	0.958	0.937	0.911	2.46	3.41	56.8	0.35	0.008	0.006
Sclerophyllous woodland	0.901	0.895	0.895	0.948	0.933	0.923	2.34	2.86	30.0	0.38	0.004	0.007
Deciduous woodland	0.915	0.904	0.896	0.954	0.931	0.921	1.88	2.89	30.0	0.40	0.004	0.006
Evergreen forest	0.937	0.915	0.905	0.955	0.928	0.919	1.33	2.79	30.0	0.45	0.002	0.004
Deciduous forest	0.931	0.922	0.917	0.960	0.945	0.937	1.75	2.46	26.5	0.41	0.003	0.005
Rain forest	0.947	0.924	0.921	0.960	0.929	0.927	1.24	2.58	30.0	0.47	0.004	0.004

Results for the most arid conditions (desert and shrubland) show FASTEM considerably overestimated the polarisation difference at high frequencies if a constant value for the polarisation mixing parameter, Q, is used, as illustrated in Fig 1a. This has been addressed by including an empirical frequency dependence in Q, modified somewhat from the form first proposed by Kerr and Njoku [1990]:

$$Q(v) = 0.50 \left[ 1 - \exp(-0.6 \cdot \sigma_l^2 \cdot v) \right]$$

where  $\sigma_l$  is the fitted parameter, originally intended to represent the large-scale roughness as a standard deviation of surface height in cm, and  $v$  is the frequency in GHz.

FASTEM was modified to include this, and fit  $\sigma_l$  instead of  $Q$ . The results are also shown as the solid lines in Fig 1b using a value of  $\sigma_l = 0.14$  cm. The residual errors, also shown in Table 1, indicate a much-improved ability to represent the observed decrease in polarisation difference with frequency over these arid surfaces. However, these results also show the residuals increase for more densely vegetated classes, suggesting such a model should not be used in these cases.

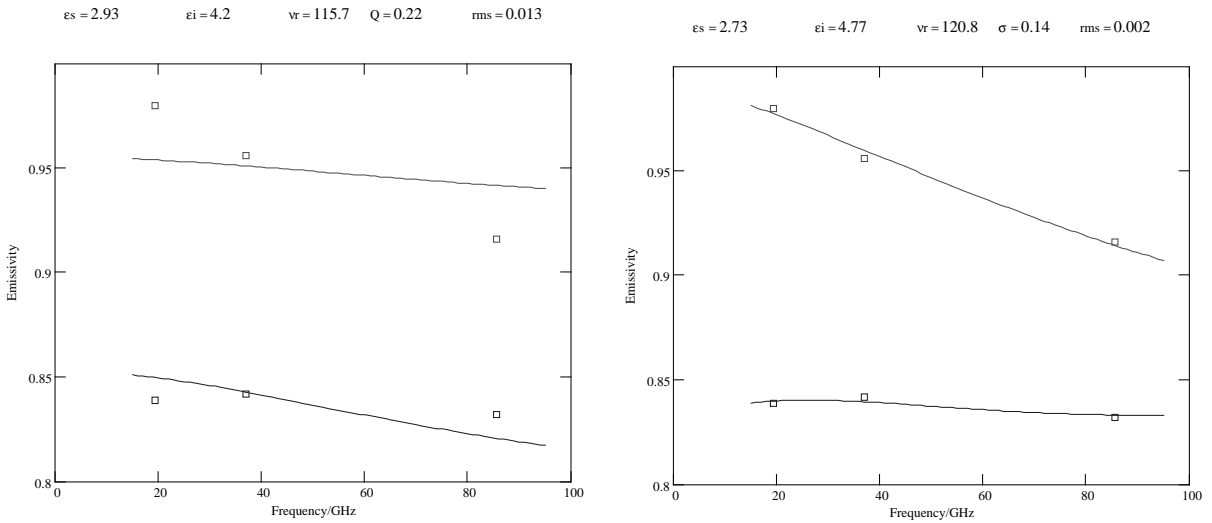


Fig 1: Desert emissivity calculated by Prigent *et al* (points) and modelled by FASTEM (lines) before (a) and after (b) modification to include frequency dependence in polarisation mixing parameter. Upper points/lines Vertical. Lower points/line Horizontal polarisation.

## 5.2 Satellite data measured by Morland [1999]

In her study of the influence of vegetation and precipitation semi-arid land surfaces, Morland [1999] calculated the emissivity of an area of Africa from SSM/I data. In this case, the study area was restricted to 0-5°E, 11-16°N, centred on the Hydrological and Atmospheric Pilot Experiment (HAPEX) site in the Sahel. Emissivities were calculated at 25-km resolution over this area on a daily basis from August to October 1992 during the transition from rainy to dry seasons. Her calculation included cloud masking and corrections for atmospheric absorption at the microwave frequencies of SSM/I and the infrared wavelengths of the Meteosat channel used to estimate the surface temperature. An empirical correction, based on the vegetation index, was also applied to the surface temperature to allow for its infrared emissivity being less than one.

In this case, data was analysed with respect to indices of vegetation and soil moisture. The Normalised Difference Vegetation Index (NDVI) was calculated on a weekly basis from short wave data from the Advanced Very High Resolution Radiometer (AVHRR) on the NOAA polar orbiting satellite. The Antecedent Precipitation Index (API) is intended to model the soil moisture available for evaporation in the uppermost 20 cm of the soil. It is calculated from kriged rainfall data and meteorological forcing.

**Dry Season:** Morland found a linear relationship between emissivity and NDVI during the dry season (October). The emissivity was calculated on a daily basis for 5 NDVI bins. The average was calculated of 5 days' data for the NDVI ranges 0.10-0.20 and 0.50-0.70. These values correspond to the north and south of the study area, which Matthews [1983] classifies as desert and tropical drought deciduous woodland, respectively and are referred to here as *bare soil* and *vegetation*. Only morning satellite overpasses were used, as there was less uncertainty in the surface temperature.

The average emissivity of these classifications is shown in Table 2. This shows that emissivity in both polarisations decreases with frequency for bare soil, and to a lesser extent, for dry vegetation. This suggests that, like Prigent's desert classification, volume scattering by dry, sandy soils reduces the emissivity at high frequencies.

Table 2 also shows the results of the least squares regression used to derive parameters for the FASTEM model, together with the rms error of the fitted model. Also shown are the residuals when fitting the observation to the modified form of FASTEM, which includes the Kerr formula to describe the increase in polarisation mixing with frequency. Again, this method is found to model the observed emissivity of bare soil more closely, but significantly worse for other surfaces.

Table 2: SSM/I emissivities calculated by Morland with fitted FASTEM parameters for  $\sigma_s=0$ .

Channel	19H	37H	85H	19V	37V	85V	$\epsilon_s$	$\epsilon_i$	$v_r$	Q	rms	Kerr rms
Water	0.315	0.346	0.518	0.602	0.638	0.781	71.5	4.30	13.1	0.09	0.016	0.024
Dry Soil	0.871	0.864	0.864	0.995	0.968	0.941	2.33	2.86	32.8	0.19	0.012	0.003
Dry Veg	0.946	0.934	0.933	0.968	0.951	0.950	1.35	2.19	23.4	0.41	0.003	0.004
Wet Soil	0.850	0.860	0.881	0.953	0.965	0.966	3.25	2.43	24.1	0.21	0.002	0.011
Wet Veg	0.930	0.917	0.943	0.958	0.942	0.959	2.16	2.07	0.1	0.40	0.008	0.009

**Rainy season:** Measurements during the rainy season (August and September) were also analysed by Morland to investigate the relationship between emissivity and soil moisture (as API). Although the emissivity was more variable during this period, its average value was found to be uncorrelated with API, even when the data was binned according to its vegetation index.

The average emissivity (19 GHz, horizontal polarisation) of the whole study area measured at around 5am was found to have a slight negative correlation with the precipitation from the previous day. However, data from the afternoon (5pm) overpass of the same satellite showed no such relationship. This is expected because evaporation during the day is very strong in this area, and most of the rain falls during the evening or night. These results support the theory that these channels are only sensitive to soil moisture very close to the surface, as the sensing depth is of the order of  $\lambda/10 \sim 1\text{mm}$  at 30GHz.

Average emissivities were calculated in the same way as for the dry season for 5 days when substantial rain had fallen overnight. Only using morning overpasses reduces the influence of evaporation. The results are also presented in Table 2. The emissivity is slightly lower at low frequency than during the dry season, but higher emissivity at high frequency for both soil and vegetation. The influence of volume scattering is now reduced due to the soil's higher absorption coefficient.

**Water:** Morland [1999] also calculated the sea-surface emissivity to validate her retrieval technique, using an equatorial region, where the sea surface temperature was  $+25^\circ\text{C}$ , and the wind-speed was  $<10\text{m/s}$ . These results highlighted a systematic bias with respect to modelled

sea surface emissivity at high frequencies, which Morland prescribed to inadequate correction for absorption by atmospheric water vapour. These results are also included in Table 2.

### 5.3 Airborne measurements by Hewison [1999]

Hewison [1999] measured the emissivity of forest and agricultural land using radiometers on a low altitude aircraft, over the same area of Sweden in summer (September 1995) and winter (March 1997). Microwave radiometers measured up-welling and down-welling brightness temperatures at 24, 50, 89 and 157 GHz. An infrared radiometer was also used to estimate surface temperature, assuming an infrared emissivity of 1. This calculation includes cloud masking and corrections for absorption in the atmosphere below the aircraft, in both up-welling and down-welling measurements of microwave and infrared brightness temperatures.

Two independent systems were used to classify land-use: analysis of video footage, and extraction from a high-resolution land-use map derived from LANDSAT imagery and data from the Swedish National Land Survey. The two methods produced consistent results. Some of the classifications with similar emissivity spectra have been combined here. **Bare soil** and **Frozen soil** are mainly silt loam, with high volumetric moisture content, which are differentiated by the surface temperature being greater than or less than 0°C. **Vegetation** is a combination of stubble and grass, covering at least 50% of the ground. **Forest** is a mixture of coniferous (85%) and deciduous (15%) trees measured in both summer and winter. Where the ground cover exceeded 70% coniferous trees, the emissivity approaches unity, and this is defined as **Dense Conifer**. Although data were measured at various incidence angles, the polarisation changes with scan angle. This complicated the analysis, so only the nadir observations are used to fit parameters for the FASTEM model. Values of the polarisation mixing parameter,  $Q$ , were estimated to optimise the model's representation of the variation of emissivity with view angle, by studying results from the 24 GHz channel. Table 3 summarises the average emissivity at nadir for these land-use classes, and the FASTEM model parameters fitted to these results.

Table 3: Nadir emissivities from airborne measurements by Hewison with fitted FASTEM parameters for  $\sigma_s=0$ .

Freq/GHz	24	50	89	157	$\epsilon_s$	$\epsilon_i$	$v_r$	$Q$	rms
Water 18C	0.443	0.513	0.573	0.668	55.2	6.41	27.4	0.00	0.003
Water 0C	0.491	0.588	0.657	0.733	49.1	7.13	18.0	0.00	0.003
Lake Ice	0.908	0.920	0.922	0.925	3.76	3.06	26.3	0.00	0.001
Bare Soil	0.955	0.967	0.962	0.966	2.55	2.10	22.0	0.50	0.001
Frozen Soil	0.962	0.982	0.979	0.980	3.08	1.70	11.9	0.35	0.002
Vegetation	0.959	0.966	0.962	0.973	2.37	2.01	37.3	0.42	0.001
Forest	0.985	0.987	0.987	0.992	1.64	1.25	120.	0.50	0.000
Dense Conifer	0.989	0.990	0.992	0.995	1.54	1.17	100.	0.50	0.000

The emissivity consistently increases with frequency and vegetation density. Frozen soil also shows a higher emissivity than areas where the surface temperature is above 0°C, due to change in permittivity of the water within the soil.

It is difficult to make conclusions about the ability of the model to reproduce the polarisation difference trend with frequency, and whether further refinement of the formulation of the polarisation mixing parameter is necessary.

#### 5.4 Ground-based measurements by Mätzler [1994]

Mätzler [1994] summarised the results of a series of experiments to measure the emissivity of various land surfaces with and without snow cover. These measurements were made with a ground-based radiometer, measuring 5 frequencies between 4.9 to 94GHz in horizontal and vertical polarisations at 50° incidence angle. Only the results from the 3 highest frequencies are considered here, as FASTEM is only intended to model emissivity at millimetre wavelengths. Mätzler confirmed that 4.9 GHz and 10.4 GHz can penetrate thin dry snow and vegetation and observed non-monotonic emissivity spectra in these cases, which cannot be represented by FASTEM without additional terms.

Mätzler reported results for a large number of object classes, many of which showed very similar emissivity spectra. For the purposes of this analysis, some of his classes have been combined by averaging to produce 8 groups. Results are shown in Table 4, with fitted FASTEM parameters.

**Water** is modelled data, based on specular reflection from a calm surface of water around +4°C, whose permittivity is represented by a single Debye relaxation. Results show very low emissivity, which increases with frequency and a strong polarisation difference, independent of frequency. As expected, FASTEM fitted these data very closely, with a low residual error.

**Bare soil** is sandy loam between 0 to 25°C, volumetric moisture 12% to 45% and an estimated rms roughness of 1cm. The emissivity was observed to increase with frequency, due to the permittivity of its liquid water content. The polarisation difference was small, and did not decrease with frequency significantly above 21GHz.

**Stony soil** has a high gravel content, and hence lower volumetric water than bare soil. The emissivity is corresponding higher and, again, increases with frequency.

**Frozen soil** is sandy loam between -6 to -1°C, volumetric moisture about 40%. This shows a much higher emissivity, as the permittivity of ice is much lower than water.

**Grass** includes unfrozen, short, medium and long grass between 8-44cm high. Results show a higher emissivity than bare soil, which decreases slightly with frequency, and very little polarisation difference. This suggests volume scattering by the grass is more effective at higher frequencies, and that this process dominates over absorption.

**Cereal** includes young barley and oat crops about 45cm high. Emissivities are again higher than bare soil, with a slight trend to increase with frequency. Unusually, the horizontal polarisation has a higher emissivity than the vertical, due to differential volume scattering within the vertically aligned canopy. The fitted FASTEM parameters reflect this, with a value of Q greater than 0.50.

**Wet snow** includes data from two sites when at least the surface layer was wet. This exhibits emissivities comparable with bare soil, which increase with frequency. Emission by the wet snow particles near the surface is the dominant process.

**Deep dry snow** is winter snow with a snow water equivalent between 25 to 63cm. The ice crystals within the snow-pack scatter out up-welling emission from the ground, causing the emissivity to decrease monotonically with frequency.

Table 4: Ground-based emissivities ( $50^\circ$ ) measured by Mätzler with fitted FASTEM parameters for  $\sigma_s=0$ .

Channel	21H	35H	94H	21V	35V	94V	$\epsilon_s$	$\epsilon_i$	$v_r$	Q	rms
Water	0.308	0.358	0.493	0.590	0.657	0.806	85.4	8.37	10.8	0.00	0.001
Bare soil	0.888	0.887	0.920	0.910	0.903	0.934	3.39	1.25	65.8	0.44	0.003
Stony soil	0.904	0.911	0.915	0.938	0.942	0.938	3.11	2.41	45.8	0.42	0.002
Frozen soil	0.951	0.951	0.938	0.958	0.952	0.950	1.96	2.30	60.0	0.46	0.002
Grass	0.945	0.941	0.939	0.944	0.940	0.946	1.19	2.27	7.7	0.49	0.002
Cereal	0.954	0.952	0.956	0.948	0.946	0.954	2.41	2.03	8.9	0.51	0.001
Wet snow	0.875	0.891	0.899	0.965	0.961	0.943	3.11	2.57	14.3	0.25	0.007
Deep dry snow	0.780	0.715	0.658	0.898	0.813	0.728	1.93	14.4	88.5	0.33	0.013

### 5.5 Comparison of emissivity measurements from different sources

FASTEM coefficients can be used to predict nadir emissivity spectra to allow ready inter-comparison of observations from various sources. Plots were produced for similar land-use classes from each source studied in this chapter. These are shown in Fig. 2.

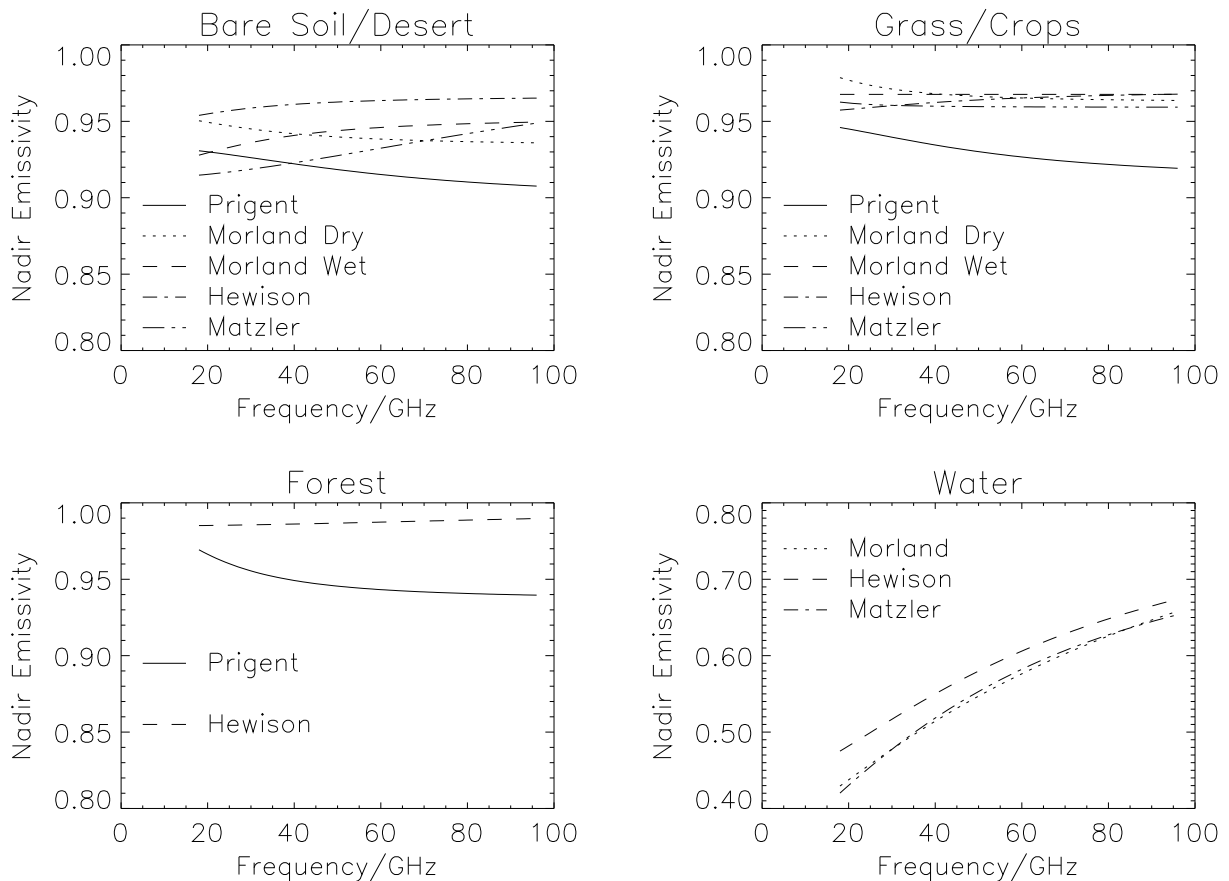


Fig 2: - Predicted nadir emissivity spectra for model fitted to observations

a) **Bare soil/desert.** This confirms that emissivity measured at low level tends to increase with frequency, while satellite derived observations show the opposite trend. However, both

sources of satellite observations concentrate on Africa, where many bare soil areas are very dry and sandy. The sand particles can volume scatter higher frequencies, causing a decrease in emissivity. Morland's results for wet soil indicate the opposite trend. The higher soil moisture increases its absorption coefficient, so the penetration depth decreases to the extent that volume scattering becomes negligible. Hewison's and Mätzler's observations are for loamy soils, where volume scattering is insignificant, so emissivity increases with frequency.

However, there remains a large difference in the absolute emissivity values calculated by Prigent *et al.* and Morland. Morland's classification method carefully selects areas of bare soil, whereas Prigent's values are averages for a land-use class, which would be expected to be less extreme. This difference is consistent with that observed for *grass/crops*, suggesting a systematic bias in one of the retrieval techniques. Morland validated her emissivity calculation against models of the sea surface emissivity, and found she underestimated reflectivity by a factor of up to 25% at 85GHz in humid conditions, which she attributed to inaccuracies in the correction for atmospheric absorption. This would be sufficient to explain the differences in observed emissivity spectra of *bare soil/desert* at high frequencies, but not at low frequencies, which are less affected by atmospheric absorption.

**b) Grass/crops** show broadly consistent results, with  $e \sim 0.97$ , except those of Prigent *et al.* Again, this may be due to the nature of the surface. Prigent's grassland class is dominated by African savannah, where a significant fraction of bare, sandy soil may be exposed. The other authors select this classification to include only dense vegetation. Morland's dry season results show higher emissivity at low frequencies, which may be due to this classification including some areas of drought-deciduous woodland. This is not the case in the wet season, as canopy absorption is higher.

**c) Forest** shows the largest difference between low and high altitude observations. Hewison's aircraft results indicate dense coniferous forestry acts as a blackbody across the millimetre-wave spectrum. Prigent's satellite measurements follow the same trend observed in all her land-use classes: that emissivity decreases with frequency, although the emissivity of forest is higher than other classes. However, even the large difference in its average value could be explained if Prigent's forest class contains only 50% ground cover and 50% bare soil as in **a)**.

**d) Water** is included for reference only, to show all schemes are capable of retrieving values of emissivity that increase with frequency. It is difficult to compare quantitatively the spectra from the different sources, as the emissivity is a strong function of sea surface temperature and windspeed. Warm water has a lower emissivity, but wind (especially foam) increases it. Hewison's and Mätzler's results are for cold, calm water surfaces while Morland's satellite measurements were in warm, windier conditions. Hewison's measurements were validated against what is currently believed to be the most accurate model of sea water permittivity at these frequencies [Lamkaouchi *et al.*, 1996]; whereas Mätzler's figures are just modelled data based on older values.

## 5.6 Conclusions from parameter fitting

This comparison has confirmed that satellite measurements generally show land surface emissivity decreases with frequency, whereas low altitude measurements show the opposite trend. A likely explanation is that they are not viewing comparable surface types. The satellite observations used in this study include large areas of dry, sandy soil, which volume scatter at higher frequencies, reducing the emissivity. This is illustrated by the different spectra observed by Morland for dry and wet soil.

The large differences between absolute values of emissivity calculated from SSM/I data by two authors could be partially explained by a bias introduced in the correction for atmospheric absorption. This highlights the sensitivity of satellite retrievals of emissivity to atmospheric water vapour and the need to validate these results. To confirm the surface emissivity is independent of scale, it should be measured at different altitudes. Airborne observations could accomplish this as they would allow atmospheric absorption to be measured explicitly.

This case study has also confirmed that measurements on large spatial scales (from satellite) show that the polarisation difference decreases with frequency, especially for bare soil and desert areas. This effect may be due to surface topography, whereby variations in surface height on the scale of a satellite field of view (tens of kilometres) depolarise emissions.

It should be emphasised that this comparison only included frequencies below 100GHz. Very few measurements have been made at higher frequencies. Hewison and English [1999] found non-monotonic emissivity spectra for dry snow, which could not be represented by FASTEM without additional terms.

Future refinements could extend FASTEM to a two-layer model. The lower layer could include frequency dependence in the polarisation mixing ratio for bare soil. The upper layer could represent absorption and scattering by a canopy of vegetation or snow, with a transmissivity based on a vegetation index or snow water equivalent depth.

## **6 Future refinements to the semi-empirical fast emissivity model**

Coefficients have been calculated from airborne observations of various forms of sea-ice and land surfaces in both snow-covered and snow-free conditions. With more extensive datasets, it should be possible to extend the model to better represent vegetated surfaces and the influence of variable soil moisture at the surface.

Soil may be modelled as a dielectric mix of soil particles, air and water. If the ratios and permittivity of each component are known, the combined effective permittivity may be calculated. It may also be possible to parameterise the static permittivity,  $\epsilon_s$ , in terms of the soil moisture, or some observable variable that depends on it.

Vegetation may be approximated as a fractional coverage of an optically thick medium over a bare soil surface. An extra parameter could be added to the model to represent vegetation, which could be estimated from an observable quantity, e.g. NDVI for satellite data.

## **References**

- Choudhury B.J., T.J.Schmugge, A.Chang and R.W.Newton, "Effect of surface roughness on the microwave emission from soils", *IEEE Trans. Geosci. Rem. Sensing*, **GE-21**, pp.465-472 (1979).
- English S.J., personal communication (1998).
- English S.J. and T.Hewison, "A fast ocean emissivity model", Section 4 in L.Eymard, S.English, P.Sobieski, D.Lemaire and E. Obligis, "Ocean surface emissivity modelling", this issue, p. 141 (2000).
- Grody N.C., "Surface identification using satellite microwave radiometers" *IEEE Trans. Geosci. Rem. Sensing*, **26(6)**, pp. 850-859 (1988).
- Hewison T.J. and S. English, "Airborne retrievals of snow and ice surface emissivity at millimeter wavelengths", *IEEE Trans. Geosci. Rem. Sensing*, **37**, pp. 1871-1879 (1999).
- Hewison T.J., "Airborne Measurements of Forest and Agricultural Land Surface Emissivity at Milli-

- metre Wavelengths," To be published in IEEE Geosci. Rem. Sensing, 1999.
- Kerr Y.H. and E.G.Njoku, "A semiempirical model for interpreting microwave emission from semiarid land surfaces as seen from space," IEEE Trans. Geoscience Rem. Sensing, Vol.26, No.3, 1990, pp.384-393.
- Lamkaouchi K., A.Balana and W.J.Ellison, "New permittivity data for Sea Water (30-100GHz)," Report on extension to ESTEC/ESA Contract No 11197/94/NL/CN, 1996
- Matthews E., "Global vegetation and land use: new high-resolution data bases for climate studies," J. Clim. Appl. Meteorol., **22**, pp. 474-486, 1983.
- Mätzler C., "Passive Microwave Signatures of Landscapes in Winter," Meteorol. Atmos. Phys., vol.54, 1994, pp.241-260.
- Morland J., "Satellite observations of the microwave emissivity of the land surface," Report on Met. Office Contract No. 1B/2778, 1999.
- Prigent C., J.P.Wigneron, W.B.Rossow and J.R.Pardo, "Frequency and angular variations of land surface emissivities: Can we estimate SSM/T and AMSU emissivities from SSM/I emissivities?" Submitted to IEEE Trans. Geosci. Rem. Sensing, 1999.



# Ocean surface emissivity modelling

L.Eymard, P.Sobieski, D. Lemaire, E. Obligis, S. English and T. Hewison

## 1 Short overview of the sea surface emissivity modelling

For a pure plane water surface, the emissivity of the sea surface could be simply derived from the Fresnel reflection coefficients. However, in natural sea conditions, the waves modify the surface emissivity, and the reflected sky emission and the contribution of the foam must be added. Sea surface emissivity models therefore include an electromagnetic model as well as a description of the waves, as a function of the near-surface wind, the foam fractional cover and the foam emissivity.

- Surface roughness is generally described as a combination of gravity waves and gravity-capillary waves. Figure 1 shows a typical radial spectrum. The gravity range corresponds to waves with a wavelength larger than several tens of centimetres, whose propagation is mainly influenced by gravity acceleration. The capillary waves have wavelengths of the order of one centimetre or less. Their dissipation is mainly due to viscosity. A directional spreading function is added to this radial spectrum.

Surface roughness models have been developed for many years based on laboratory measurements and in-situ observations. However, the ocean "case" cannot be directly derived from laboratory measurements, and the relevance of in-situ observations is difficult to assess in the full range of conditions (e.g. wave frequency range depending on the fetch, interaction with swell, non-stationary wind). Several authors have used radar data to help assessing or fitting surface models, but possible artefacts due to the radar itself or to the electromagnetic model cannot be totally eliminated.

Moreover, studies have often been made by separating gravity wave and the gravity-capillary wave spectra, inducing in some cases inconsistencies in their common frequency

i

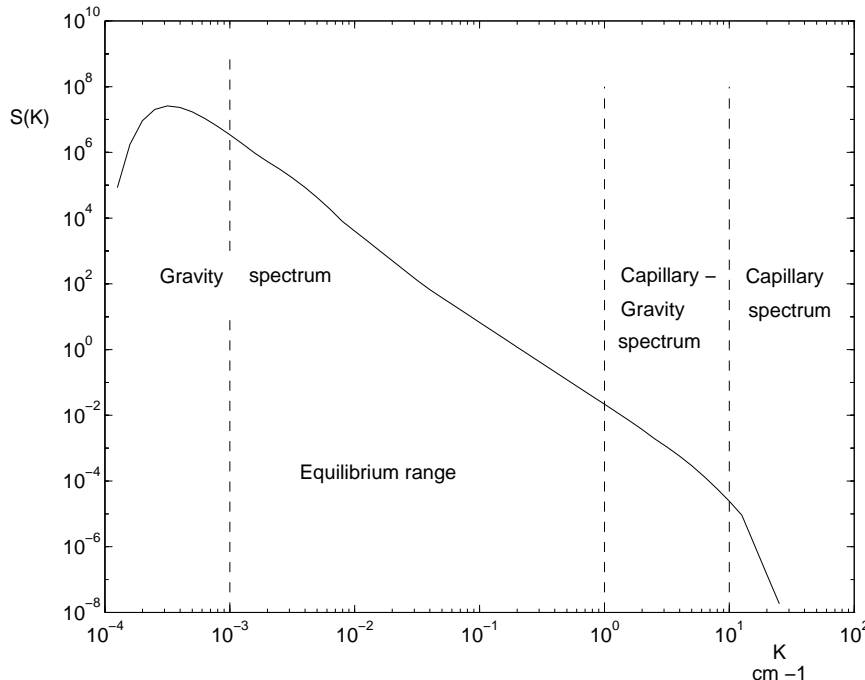


Figure 1 : Gross pattern of the sea-surface roughness spectrum.

The sea state is usually described in terms of the statistical properties of the sea surface, through the slope probability density function (pdf) and the wave spectrum. In case of fully developed seas, the wave spectrum is characterized by the surface wind speed only, or by the wind friction velocity, both being directly related under neutral stability conditions (Cardone, 1969). Different empirical sea spectra and slope descriptions have been proposed in the literature (Cox and Munk, 1954a,b; Pierson and Stacy, 1973; Bjerkaas and Riedel, 1979;...). The choice of an optimum description is not readily straightforward. For instance, the sea slope variance derived from Pierson and Stacy's spectrum is about twice the variance reported by Cox and Munk's optical measurements of sun glint over sea. The slope variance being roughly proportional to the wind speed, choosing Pierson and Stacy's variance rather than Cox and Munk's one yields the same effect as doubling the wind speed in the simulation. Recently, new models have been proposed, as those of Apel (1994), Elfouhaily et al (1997), and Lemaire et al (1999), mostly to simulate radar and radiometer measurements. Comparisons are on-going to establishing the most consistent models, as did recently Trokhimovsky et al (1999), Lemaire (1998), and also discussed in this report (section 3).

- Foam, spray and bubbles induce an additional signal which cannot be properly accounted for in roughness models. The foam fractional coverage is often expressed as a simple power-law function of the sea surface wind speed (Wu, 1979; Monahan and O'Muircheartaigh, 1986...). But other parameters like the thermal stability of the lower atmosphere and the viscosity of the sea water could have an impact on the whitecap coverage (Monahan and O'Muircheartaigh, 1986; Monahan and Lu, 1990). There are large discrepancies among these different schemes. The latter is the only one which makes the difference between the active and the passive effects of the foam and provides consistent results at all frequencies.

The foam emissivity within the microwave domain is very high, close to one. From radiometric measurements below 40 GHz, Stogryn (1972) proposed an empirical model, depending on incidence angle, frequency and polarization conditions. An alternative may be to use a physical approach (Droppleman, 1970; Rosenkranz and Staelin, 1972). But, in addition to the frequency, the incidence angle, the polarization and the SST, these theoretical models are sensitive to the depth of the foam and to its density. At high frequencies, given the uncertainty related to the foam depth and density, an emissivity of one seems to be an acceptable approximation for the foam (weak sensitivity to the SST, to the incidence angle (up to 45°) and to the polarization at 89 and 157 GHz).

- Dielectric properties of sea water : In 1977, Klein and Swift reexamined Stogryn's regression fit to take into account the new sets of measurements of Ho and Hall (1973) and Ho et al. (1974). The Klein and Swift model has been commonly used for a long time, although the authors recommended care using their model at frequencies above 10GHz. Klein and Swift (1977) and Stogryn (1972) both use a single Debye formula. Laboratory measurements made recently (Ellison et al, 1998) confirm that the single Debye model can be used at low frequency (under 30 GHz), and lead to new coefficients of the Debye model for sea water in natural conditions which was validated using both spaceborne and airborne radiometer data (Guillou et al, 1998). However, at higher frequency, this first set of measurements did not agree with the model extrapolation, and this departure could be explained using a double Debye model. This was also proposed by Manabe et al. (1987) and Liebe et al. (1991) for pure water. A second set of measurements has been performed between 30 and 100 GHz (Lamkaouchi et al, 1997), which has permitted to adjust the coefficients of the double Debye.

- Sea surface emissivity : Three main types of models are commonly used, as stressed by Guillou et al (1996) :
  1. *Simple models*: Most of the empirical models have been determined from Hollinger's measurements (1971) and from SMMR (Scanning Multichannel Microwave Radiometer) observations. All these measurements are limited to the low frequency range, up to 37GHz. They are highly dependent on the instrumental calibration and scanning geometry. The input parameters are usually limited to the sea surface wind speed, the frequency and angle of observation, and the sea surface temperature. To the flat sea surface specular emissivity, a corrected term is added to account for the surface roughness. A fractional foam coverage is often considered. Derived from low-frequency data, some of these models can potentially be used for other frequencies, at any sounding angle. This is the case of Francis et al.'s algorithm (1983) among other. More recently, Rosenkranz (1992) extrapolated the Wentz' semi-empirical emissivity model (1983) to the SSM/I channel characteristics.
  2. *Geometric optics approach*: The ocean surface is described by a series of reflecting plane facets characterized by an anisotropic slope distribution. Each individual facet is assumed to be infinite in front of the wavelength, and irregularities small or comparable to the wavelength are ignored. The elementary contribution of each facet to the upwelling brightness temperature is computed from the Fresnel reflection relations. One of the first calculations using this approach is due to Stogryn (1967). Wilheit's model (1979) is quite similar, although different in its formulation for the emissivity calculation. Prigent's model (Prigent and Abba, 1990), described in section 2.1, is derived from this one. Petty and Katsaros (1994) propose a parameterization of a geometric optics model for the specific SSM/I configuration too.
  3. *Two-scale models* : Attempts to enhance the agreement between theoretical predictions and low frequency observations led to the development of composite-surface models. Following previous work to interpret the mechanisms in the radar backscattering from the ocean at various incidence angles, Wu and Fung (1972), Wentz (1975), Guissard and Sobieski (1987), developed two-scale scattering models, by superimposing small structures (capillary waves, small gravity waves) on the large undulations (gravity waves). The scattering coefficients are expressed as the sum of two contributions. The first term concerns the large scale and is given by the geometric optics solution, slightly modified by the presence of the ripples, which impose a modification of the Fresnel reflection coefficients. The second term results from the average of the scattering coefficients due to the small irregularities over the large scale slope distribution, and these scattering coefficients are derived from the small perturbation theory. The two-scale model presented in section 2.2 is basically Sobieski and Guissard's one, improved by Lemaire (1998). At low frequency, the two-scale models have been shown to provide better overall agreement with Hollinger's observations, when fine tuning the input parameters (Wu and Fung, 1972; Wentz, 1975). The separation of the wave spectrum in two scales is based on a more or less arbitrary choice of the cutoff frequency or of the small-scale rms height as a function of the wind velocity and of the sounding wavelength.

At millimeter wave frequencies, the ocean becomes mostly "large scale". Thus the higher the frequency, the smaller the difference between two-scale models and simple models as Stogryn's one. Simulations of sea surface brightness temperatures, at 89 and 157 GHz, using both single scale (Stogryn, 1967) and two-scale (Wu and Fung, 1972; Wentz, 1975) confirm that the influence of the small irregularities decreases with increasing frequency.

## **2 The models to be proposed**

We propose three models for use in meteorology and ocean surface. The first one (Prigent's model) is based on the geometric optics approach and was developed initially by Prigent and Abba, (1990). The second is a two-scale model (UCL model), which is being used both in active and in passive microwaves, and was initially developed by Guissard and Sobieski, (1987). These two models will be compared in Section 3. A third model to be proposed will be described in Section 4; it is a simple and fast model useful for assimilation purposes which has been fitted to the first one (English and Hewison, 1998).

Although these models are quite different, they all use the same double Debye model of sea water permittivity, following the Lamkaouchi et al (1999) measurements. This model agrees with Ellison et al (1998) for frequencies lower than 30 GHz, but does not agree with Liebe et al (1991) model for pure water. A fit has therefore been introduced by English and Hewison (1998) to merge these two models at high frequency.

### **2.1 Prigent's geometric optics (GO) model**

This model was developed primarily by Prigent and Abba (1990), then it was improved and validated by Guillou et al (1996) and Boukabara (1997).

**2.1.1 The sea surface roughness :** In this model, two commonly adopted schemes can be used: the slope variances provided by Cox and Munk (1954a), and the Bjerkaas and Riedel (1979) wave spectrum.

**2.1.2 The foam contribution :** For the fractional foam coverage we selected Monahan and Lu's model which is the only one which makes the difference between the active foam (directly associated with breaking waves) and the passive foam (residual foam layer remaining after wave passing) and provides consistent results at all frequencies. The physical model of Droppleman (1970) was chosen to model the foam emissivity because it follows a physical approach and gives results consistent with the statistical measurements. Two parameters have to be defined in the model: the foam layer thickness and the ratio of the volume of air in the foam to the total volume of foam. They have been arbitrarily set to 1 cm and 0.95, respectively, to keep the emissivity high, but still lower than unity, in the usual frequency range (10 - 100 GHz).

**2.1.3 The sea surface model :** The sea surface description is derived from Wilheit (1979). The ocean surface is considered as a set of flat surfaces with an anisotropic slope distribution. Each facet is assumed infinite in size compared to the radiometer wavelength, and small-scale irregularities are neglected: the problem therefore reduces to geometric optics.

For each facet the downwelling radiation is specularly reflected by the facet, and the elementary contributions are computed using the Fresnel relationships. Shadowing and multiple reflection effects are taken into account, in the following manner: facets that are hidden from the receiver view are simply ignored in the calculation; for the facets oriented so steeply that the incident beam comes from below the horizon, the incident radiation temperature is taken to be the physical temperature of the sea. As the slope distribution is not identical in the alongwind and crosswind directions, the upwelling radiation coming from the facet in these two directions is transformed in horizontal and vertical polarization as defined relative to the global sea surface and the radiometer direction.

All the individual contributions are added up, after multiplying them by the cosine of the incidence angle on the facet, and they are weighted by the probability density of the surface slope distribution. The number of slopes to be simulated for a proper representation of the

density probability depends on the wind speed and the sounding direction. For most cases, 100 different slopes are enough.

The higher the frequency, the more valid the geometric optics approach. However, Wilheit (1979) showed that only a fraction of the slopes measured by Cox and Munk are active at lower frequency and the ripples responsible for the steepest slopes have a weak effect at low frequency (below 30 GHz). Confirming this, we used the model for simulating SSMI, ERS and TOPEX radiometer channels ranging between 18 and 37 GHz) and to provide inversion algorithms for ERS-2 (Eymard et al, 1996). Nevertheless, the model appears more efficient for retrieving atmospheric characteristics than the surface wind, and the most extensive validation of its performances was made at the MARSS airborne radiometer channels (89 and 157 GHz) by Guillou et al (1996).

*Table 2.1: Summary of Prigent's geometric optics model:*

Purpose of the model	computation of the apparent temperature of an ocean surface, given the downwelling radiation and the surface characteristics
Applications	simulation of brightness temperatures over ocean in the frequency range 20 - 200 GHz for retrieval of atmospheric parameters and surface wind estimate
Model variables	frequency, incidence angle, polarization
Input parameters	Tdown (K) at nadir, sea surface temperature (K), salinity ( $\hat{a}$ ), surface wind (m/s)
Output parameters	standard : apparent temperature in the satellite field of view; optional : surface emissivity
Expected errors	model validation made in the range 18 - 150 GHz using satellite and airborne radiometers lead to an error of a few K (less than 10K in any case)
Accuracy requirements	1 - 2K on apparent temperature for surface wind retrieval; 3 K acceptable for atmosphere retrievals
Further development	- update of the foam cover model after comparison between radiometer and optical measurements; - choice of the surface roughness model to replace the current one (Cox and Munk, 1954a,b)

## 2.2 The UCL two-scale model

The model was first developed by Guissard and Sobieski (1987), but recent improvements were brought. The version described hereafter accounts for results of Lemaire (1998) and Craeye (1998).

### 2.2.1 The sea surface roughness.

The new ocean surface spectrum proposed by Lemaire et al. (1999) is used. This model is also valid in non-fully developed state. In this spectrum, the large gravity waves are described in terms of geometrical parameters, while the spectrum of gravity-capillary waves is uniquely

determined to the local wind friction velocity. The geometrical parameters used to characterize the gravity waves are the spectral peak wave number and the significant slope. In particular, these two free parameters can be related to the wind speed using empirical expressions, to simulate mean ocean conditions. For the simulations performed and presented in section 3, the peak wave number has been computed using the Pierson and Moscowitz (1964) empirical formula valid for fully developed state, and a mean value for the significant slope representative of ocean conditions ( $\beta=0.70\%$ ). For the gravity-capillary waves, the spectral form used is based on recent wave-number spectra measurements in ocean conditions.

Besides the wind-induced waves, the surface model also takes into account the roughening in the presence of rain. For the rain drops impacts, laboratory results show that the ring waves that they generate are the main contribution to surface scattering (the stalks are less significant). The interactions between individual ring-waves are modeled through a full-rain surface spectrum determined experimentally at NASA/Wallops. A ring-wave spectrum has been proposed by Bliven et al (1997) and is used here. This spectrum has been determined for a single drop size (2.8 mm) and is a function of the rain rate only.

A combination of wind-wave and ring-wave spectra is obtained as the result of an equilibrium between the different generation and dissipation contributions. To some extent, the obtained combined spectrum reproduces the damping of short gravity waves often cited in the literature to explain some particular radar responses observed in case of rain.

#### 2.2.2 The foam contribution.

The foam is represented as a porous dielectric layer following Droppleman's (1970) model, and Monahan and Lu (1990) for the foam coverage, already mentioned in the previous sections. For use of this model, the foam layer thickness and the foam density have been arbitrarily set to 1 cm and 0.95, respectively.

#### 2.2.3 The seawater permittivity.

As for the other models, the seawater permittivity model used is the one developed by Ellison et al (1998) based on laboratory measurements of seawater samples up to 40GHz. The permittivity is related to the frequency, the water temperature and its salinity.

#### 2.2.4 The electromagnetic surface scattering model.

The electromagnetic model used allows the simulation of both radar and radiometer measurements. On the scattering point of view, active and passive measurements are not completely independent as explained hereafter. The radar response to the surface is determined by its backscattering coefficient or normalized radar cross section (NRCS). On the other hand, radiometric measurements are related to the emissivity  $e_p$  of the surface, since the noise power emitted by a surface at an absolute temperature  $T_0$  and measured by the radiometer, is proportional to  $e_p T_0$ . The emissivity has a value from zero to unity and is a function of surface roughness, polarization  $P$ , incidence angle  $\theta$ , complex dielectric constant, frequency and physical temperature (Peake 1959). In general, an object both emits and reflects thermal radiation, and under local thermodynamic equilibrium, the emissivity  $e_p$  and the reflectivity  $\Gamma_p$  of a target are related by :

$$e_p = 1 - \Gamma_p$$

The reflectivity of the surface in a direction of observation given by  $\vec{s}$ , is the sum of the contributions of the bistatic scattering coefficient from all incident directions  $\vec{i}$ . More formally, it can be expressed as:

$$\Gamma_p(-\vec{s}) = \frac{1}{4\pi \cos \theta_s} \iint \sigma_p^0(\vec{s}, \vec{i}) d\Omega_i$$

Since the backscattering coefficient is a particular case of the bistatic scattering coefficient where the incident and observation directions are opposite, i.e.  $\vec{s} = \vec{i}$ , this set of relations defines thus the link between radar and radiometer measurements at the surface level. It shows also that a key-element in a consistent computation of the scattering by the sea surface and of its emissivity, stands in the modeling of the bistatic scattering coefficient  $\sigma^o(\vec{s}, \vec{i})$ .

The electromagnetic model selected for the scattering by the ocean waves, follows a boundary perturbation approach. The model is presented by Guissard et al (1992). It is a two-scale method based on a decomposition of the sea surface in two distinct domains, representing the superposition of small waves on large ones. The terms *large* and *small* refer to the wavelength of the electromagnetic field. In this approach, the bistatic scattering coefficient is the sum of two terms :

$$\sigma^0 = \sigma_0^0 + \sigma_1^0$$

The first term is a zero-order term and corresponds to Kirchhoff's solution for the large-scale component. It is proportional to the large scale slope probability density function evaluated at the specular points, and to the square of the local effective Fresnel reflection coefficient. *Effective* stands for a correction applied to the local Fresnel reflection coefficient to take into account the loss in the reflected power due to the ripples on large waves. It is furthermore corrected by a shadowing function expressing the probability that a point of the surface is both illuminated from the incident direction and visible from the observation direction. The second term is a first-order term and appears as a Bragg scattering solution, where a whole range of surface wavelengths may be resonant with the incident field, because of the tilting of small waves by large ones. This tilting is represented through the large scale slope probability density function. The large scale slopes PDF used follows Cox and Munk formulation (1954), with the slope variances computed from the surface spectrum.

Three corrections are applied in the procedure for emissivity computations. First; as the slopes PDF is truncated above some slope value, a constant correction factor is applied to ensure the integral of the PDF to equal unity. Next, for emissivity computations, a correction is applied to the zero-order and the first-order terms. These corrections are based on evaluating the reflectivity  $\Gamma_p$  for a perfectly conducting surface (CEP) with the same geometry as the ocean surface. Since for a CEP one should have  $\Gamma_p = 1$ , we deduce a proportional correction factor which is applied on the real sea situation (dielectric surface). As the scattering calculations are limited to the first order and do not include multiple scattering effects, this correction actually accounts for these simplifications as well as for numerical inaccuracies.

A second aspect of the scattering model concerns the interaction between foam and electromagnetic waves. The foam has indeed a non-negligible impact on radiometric measurements. Its contribution is expressed by separating the sea surface into foam-free and foam-covered parts, proportionally to the foam coverage  $F$ . The covered part is assumed with a uniform distribution of foam and the scattering coefficient is then expressed as :

$$\sigma_p^o = \sigma_{p,waves}^o (1 - F) + \sigma_{p,foam}^o F$$

### **3 Model comparison**

*E. Obligis (CLS) D. Lemaire (UCL) and L. Eymard (CETP)*

We present results of a comparison between Prigent's geometric optics model and the UCL two-scale model, pointing out the importance of the sea-surface spectrum. We compared brightness temperatures and backscattering coefficients measured by 4 satellites with those simulated by 3 different surface models on coincident ECMWF fields. These comparisons were done for 3 satellites in 1997 (Topex-Poseidon/TMR, ERS2/MWR and SSM/I) and one more in 1998 (TRMM/TMI). This study allows us to test the different models at frequencies from 10 to 85 GHz, viewing angle from 0 to 53°, horizontal or vertical polarization.

#### **3.1 Tested models**

The comparisons have been performed using 3 different surface models, each associated to the same atmospheric model (Liebe et al. (1993) for absorption by water vapor and oxygen, Rayleigh approximation for absorption by cloud liquid water). The 3 surface models are : (1) Prigent's surface model (described in section 2.1), (2) the UCL electromagnetic model associated with the sea spectrum proposed by D. Lemaire (see section 2.2), and (3) the same electromagnetic model but associated this time with Elfouhaily (1998) spectrum.

#### **3.2 ECMWF extraction**

Twelve meteorological fields have been extracted from the European Center for Medium range Weather Forecast (ECMWF). The output grid has a resolution of 1.125°. They contain analysis and guesses of surface parameters and atmospheric profiles of pressure, temperature, humidity and cloud liquid water. The cloud cover and precipitation rate are also given. The satellite measurements are averaged in any grid mesh within an accuracy of +/- 2 hours in time, thus similar to the temporal window used for assimilation in the model.

#### **3.3 Filtering of cloudy pixels**

Before the comparisons were made we excluded some points in order to avoid contamination by clouds: a preliminary cloud liquid retrieval algorithm is applied to the measured brightness temperatures, and the pixels corresponding to an integrated liquid-water content of >200 g/m<sup>2</sup> are excluded. We also excluded meshes where the cloud liquid water predicted by the meteorological model is above the same threshold.

Figure 2 shows comparisons of simulated (UCLA 2 scale with Elfouhaily) versus measured (TRMM) brightness temperatures at 10, 19, 22, 37 and 85 GHz, and Tables 3.1, 3.2, 3.3 summarize the results obtained with each of the 3 models.

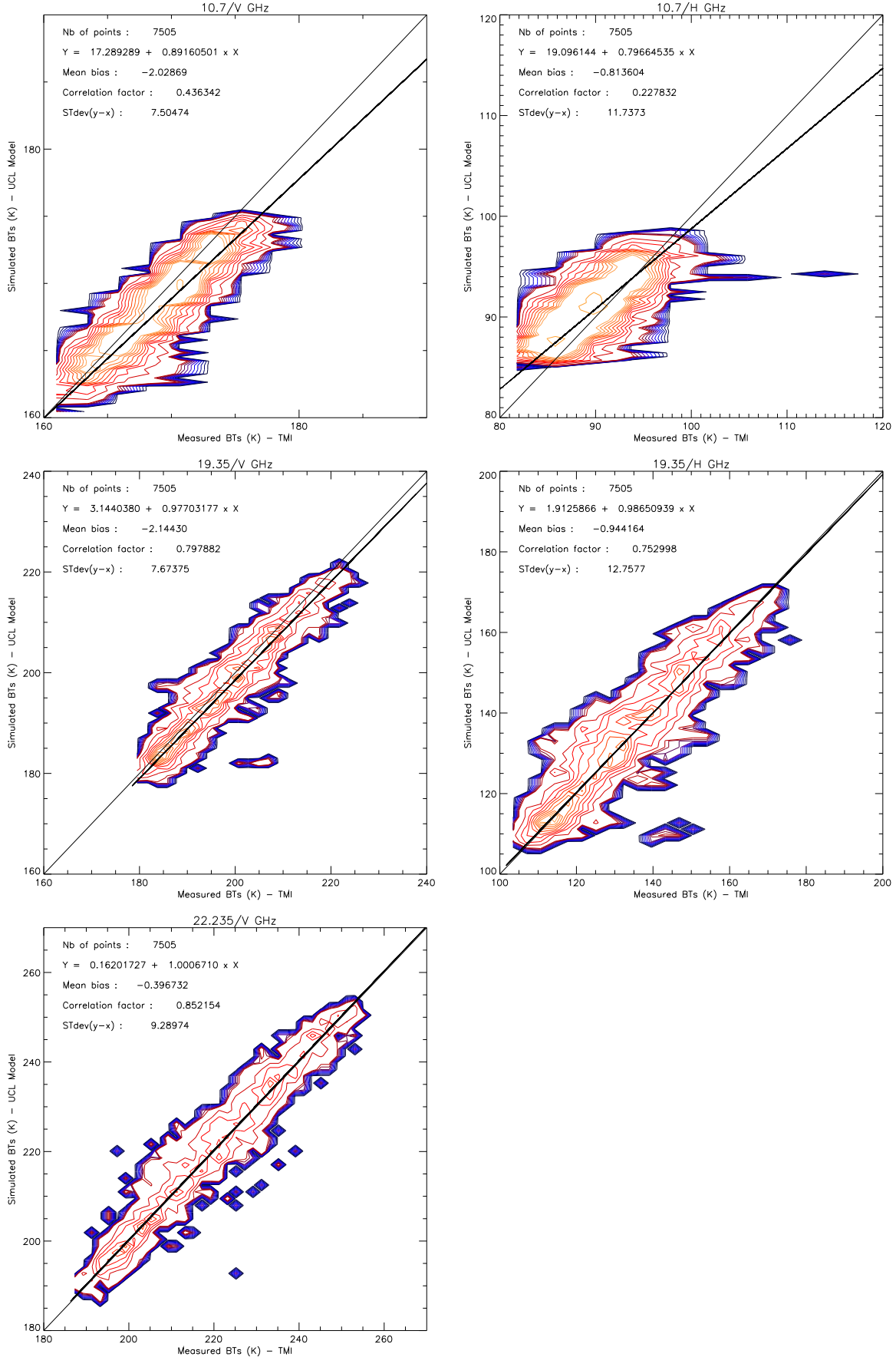


Figure 2: Simulated versus measured brightness temperatures, using the UCLA 2-scale emission model with the Elfouhaily surface model, and TRMM cloud-screened data from top to bottom at frequencies of 10, 19, 22 GHz, v polarization (left) and h polarization (right).

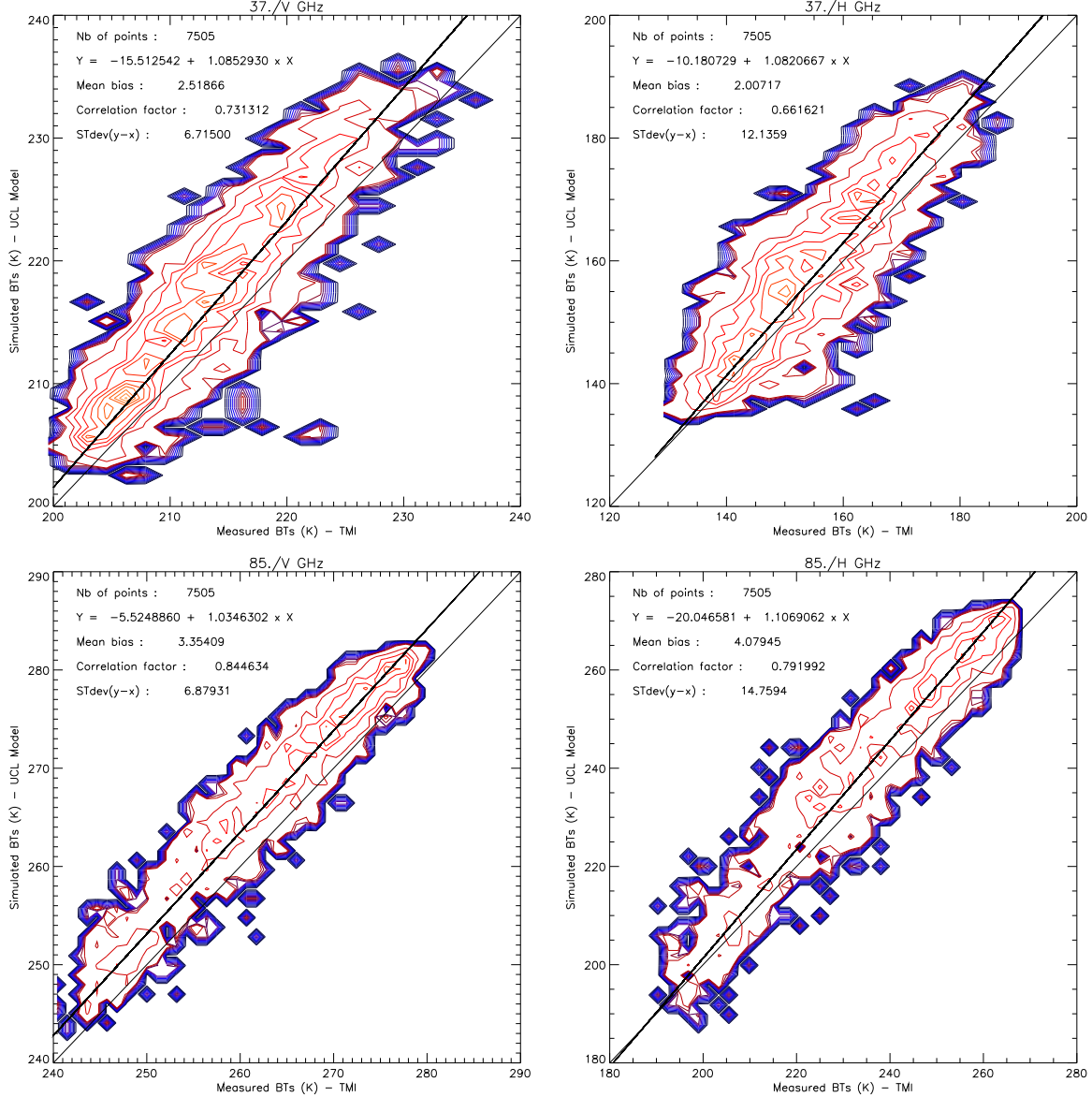


Figure 2: continued, here at 37 and 85 GHz

The comparisons are characterized by the number of coincident points, the bias (simulations-measurements), the standard deviation, the correlation coefficient, and also by the intercept and the slope of the regression straight line. As we do not know if the differences between measurements and simulations are due to the models (meteorological model or radiative transfer model) or to a possible calibration error, we preferred to compute an orthogonal regression.

### 3.4 Comparison of the brightness temperatures

The mean biases between measured and simulated brightness temperatures are weak, with values always lower than 5K, except in SSM/I configuration where they are strongly negative in case of the UCL model, especially at low frequencies. At oblique incidence, biases between measured and simulations by Prigent's model are almost always weaker than with UCL model. The standard deviations reach 14K and are systematically higher in horizontal polarization, where the sensitivity to oceanic surface is more important. Note that these deviations vary little from one model to another. The correlation coefficients are good, higher than 0.7, except for the 2 lower frequency channels of TMI (10.7 GHz). In this case, the low correlation can be

explained largely by the non-uniform beam filling (presence of rain cells, surface wind variability).

#### **Conclusions from this comparison :**

- 1) The results are satisfactory since biases are almost overall lower than 5 K and correlation coefficients higher than 0.7.
- 2) The results are consistent : biases vary regularly and always similarly for one model to another, for one channel to another, for one polarization to the other.
- 3) The agreement between measurements and simulations are higher in case of nadir viewing angle where the sea surface sensitivity is lower. It also indicates that the crucial problem is the surface geometry description (sea surface spectrum) and not the dielectric description of the sea.
- 4) An additional study (not shown) brought out the fact that differences between models are highly dependent on the surface wind speed and on polarization.

It appears from the 2 last points that it is necessary to further validate and improve the description of the surface, especially the sea-surface spectrum.

*Table 3.1:* Statistics of the comparisons between measurements and simulations by Prigent's GO model.

Radiometer	Channel	Bias (K)	Stdev. (K)	Corr. Coeff.	Regression Coeff. Slope, intercept (K)	
ERS2/MWR <i>1753 points</i>	23V	3.24	7.57	0.93	1.00	2.50
	36V	0.80	4.61	0.80	1.11	-17.89
TOPEX/TMR <i>2000 points</i>	18V	-0.94	4.32	0.82	1.19	-26.26
	21V	0.70	6.26	0.94	1.13	-19.33
	37V	1.04	5.30	0.72	1.37	-59.72
SSM/I <i>18224 points</i>	19V	-2.63	7.05	0.86	1.03	-8.05
	19H	-2.17	11.59	0.81	1.04	-7.18
	22V	-1.45	6.98	0.95	1.02	-6.01
	37V	1.45	5.65	0.79	1.09	-17.16
	37H	-1.34	10.82	0.70	1.20	-32.04
	85V	2.57	5.31	0.94	1.09	-21.53
	85H	-0.67	12.20	0.89	1.16	-37.05
	10V	-0.46	7.25	0.43	0.85	25.43
TRMM/TMI <i>7445 points</i>	10H	0.53	12.06	0.18	1.17	-13.00
	19V	-0.13	7.42	0.80	0.98	4.47
	19H	0.71	13.07	0.74	1.00	-1.65
	21V	0.96	9.32	0.85	0.99	3.61
	37V	4.14	7.47	0.73	1.08	-13.84
	37H	2.40	11.27	0.66	1.07	-8.32
	85V	4.33	7.34	0.84	1.02	-0.01
	85H	4.21	14.85	0.79	1.10	-19.07

*Table 3.2:* Statistics of the comparisons between measurements and simulations by the UCL two-scale model with Lemaire spectrum.

Radiometer	Channel	Bias (K)	Stdev. (K)	Corr. Coeff.	Regression Coeff. Slope, intercept (K)	
<b>ERS2/MWR</b> <i>1753 points</i>	23V	5.08	8.52	0.93	1.00	4.20
	36V	2.64	5.18	0.81	1.12	-17.25
<b>TOPEX/TMR</b> <i>2000 points</i>	18V	0.36	4.18	0.82	1.18	-23.99
	21V	2.42	6.72	0.94	1.14	-18.92
	37V	2.73	5.82	0.73	1.37	-57.93
<b>SSM/I</b> <i>18224 points</i>	19V	-7.97	10.28	0.86	1.01	-10.02
	19H	-6.41	12.72	0.82	0.96	-1.64
	22V	-4.99	8.57	0.95	0.95	-15.44
	37V	-1.87	6.04	0.79	1.25	-55.08
	37H	0.75	10.82	0.70	1.22	-34.91
	85V	0.08	5.08	0.94	1.17	-43.28
	85H	-0.03	12.06	0.89	1.16	-34.40
	10V	-2.94	7.80	0.44	0.90	15.21
<b>TRMM/TMI</b> <i>7445 points</i>	10H	0.62	11.73	0.23	0.81	19.18
	19V	-2.85	7.91	0.80	0.99	0.46
	19H	0.88	12.76	0.75	0.99	3.16
	21V	-0.96	9.35	0.85	1.01	-2.05
	37V	1.50	6.44	0.73	1.10	-19.64
	37H	3.91	12.57	0.66	1.08	-8.60
	85V	2.55	6.60	0.84	1.05	-10.66
	85H	5.13	14.90	0.79	1.09	-14.43

Table 3.3: Statistics of the comparisons between measurements and simulations by the UCL two-scale model with Elfouhaily spectrum.

Radiometer	Channel	Bias (K)	Stdev. (K)	Corr. Coeff.	Regression Coeff. Slope, intercept (K)	
ERS2/MWR <i>1753 points</i>	23V	4.22	8.02	0.94	1.00	4.61
	36V	1.70	4.77	0.81	1.11	-16.04
TOPEX/TM <i>R</i> <i>2000 points</i>	18V	-0.05	4.14	0.82	1.17	-22.56
	21V	1.70	6.42	0.94	1.13	-18.20
SSM/I <i>18224 points</i>	37V	1.75	5.46	0.73	1.36	-58.29
	19V	-7.10	9.61	0.86	1.0	-6.30
TRMM/TMI <i>7445 points</i>	19H	-8.17	13.70	0.82	0.96	-2.72
	22V	-4.29	8.13	0.95	1.04	-12.52
	37V	-0.69	5.68	0.79	1.22	-47.63
	37H	-2.70	11.17	0.70	1.22	-37.84
	85V	1.18	4.98	0.94	1.13	-33.31
	85H	-1.40	12.44	0.89	1.18	-41.21
	10V	-2.03	7.50	0.44	0.89	17.29
	10H	-0.81	11.74	0.23	0.80	19.09

## 4 A fast ocean emissivity model

S. J. English and T.J. Hewison

### 4.1 Application of fast model techniques to ocean emissivity

A fast radiative transfer calculation can be performed by either simplifying the physics to a problem which can be solved easily (e.g. a band model for gaseous absorption is a fast simplification to the line by line calculation) or by using regression (e.g. a neural network) to relate the results of the accurate but slow calculation to a set of predictors. The method of simplification should always produce a physically reasonable solution but many problems cannot easily be simplified without losing accuracy. The method of regression may only give a physically reasonable solution when the value of the predictors lies inside that used to generate the regression coefficients.

For the accurate calculation of ocean emissivity the estimation of specular reflectivity can easily be simplified and yet remain adequately fast whereas the treatment of roughness is usually slow because the contribution from every ocean wave slope needs to be calculated. Therefore a fast ocean emissivity model is best devised to first calculate the specular emissivity using a physical model and then adding a roughness correction which is calculated by regression using predictors which will have to include all parameters which could influence

the change in emissivity due to roughness. The two most obvious are windspeed and view angle.

## 4.2 Description of the model

Petty and Katsaros (1994) developed a parameterisation of the ocean emissivity assuming that the emissivity could be written as

$$\epsilon = \epsilon_s + \delta\epsilon$$

where  $\epsilon_s$  is the specular emissivity and  $\delta\epsilon$  is the contribution from roughness. The specular component is calculated using Fresnel theory using a Debye model of the permittivity based on laboratory measurements. The emissivity  $\epsilon$  is calculated using geometric optics based on the Cox and Munk (1954a) sea-slope variance model. The increase  $\delta\epsilon$  is then estimated by subtracting  $\epsilon_s$  from  $\epsilon$ . Regression coefficients for  $\delta\epsilon$  are calculated by linear regression against a set of predictors. The Petty and Katsaros model was developed for SSM/I which has a view angle which is almost fixed at around  $53^\circ$ . Their approach has been extended to generate coefficients for the Advanced Microwave Sounding Unit. It was found necessary to use more predictors to capture the variation with view angle. The predictors are: Windspeed and windspeed squared, secant of view angle and secant of view angle squared, and the product of windspeed and secant of view angle. It is devised to provide an estimate of emissivity for any channel between 10 and 200 GHz for any view geometry up to  $60^\circ$  at windspeeds from 0 to  $20 \text{ ms}^{-1}$ . A simple term has been added to account for enhancement of the emissivity by Bragg scattering following Choudhury et al. (1979) and the effect of foam has also been simply accounted for using the formula of Monahan and O'Muircheartaigh (1986). The recent dielectric model of Lamkaouchi et al. (1997), based on laboratory measurements up to 100 GHz, is used. The model is described in English and Hewison (1998).

## 4.3 Validation

### 4.3.1 Accuracy of fit to a geometric optics calculation

The fast model reproduces the geometric optics calculation which was used to estimate  $\delta\epsilon$  to within maximum departures of 0.005 at high angle and windspeed but generally differences are within 0.001. The geometric optics model is believed to have a random error of around 0.005 to 0.02. Generally the fast model differences are less than 10% of the expected geometric optics error. This is an acceptable error for a fast model.

### 4.3.2 Validation against airborne radiometers at 24, 50, 89 and 157 GHz

The model has been validated against airborne radiometers flown on the UK Met. Office C-130 aircraft (see Guillou et al. 1996). Figs. 3 and 4 show the difference between emissivities calculated using the fast model and emissivities estimated from the radiometer data plotted against view angle for two different windspeeds ( $0$  and  $12 \text{ ms}^{-1}$ ). These figures show a comparison for the complete model, for  $\epsilon_s$  with the Bragg term removed, for  $\epsilon_s$  with the roughness correction removed and finally for a specular calculation only ( $\epsilon_s$ ). Adding the roughness term reduces the standard deviation of the difference to around 0.01-0.015 which is comparable with our expected error in the geometric optics model.

#### 4.3.3 Validation against the Advanced Microwave Sounding Unit

The differences between observed brightness temperatures from the Advanced Microwave Sounding Unit (AMSU) on NOAA-15 and brightness temperatures calculated using a radiative transfer model using a background (forecast) profile are plotted against windspeed and skin temperature in Figs. 5 and 6. All the window channels on AMSU are shown except the 150 GHz channel which suffers RF interference and would give results which are difficult to interpret. No trend is seen with windspeed except for the highest view angles ( $>50^\circ$ ) where the calculation underestimates the observation at low windspeed. As there is no reason to expect the forecast model windspeed error to correlate with AMSU scan position, this is almost certainly a forward model error. Fig. 5 used twice the Cox and Munk roughness to generate the roughness correction,  $\delta\epsilon$ . At low windspeed the emissivity at high view angle is very sensitive in horizontal polarisation to the slope variance model. The slope variance could be tuned as a function of windspeed to remove the trend in Fig. 5. No trend of difference with skin temperature is found except at 89 GHz. This suggests that the model of Lamkaouchi et al. (1997) is giving very good results for the lower frequency channels, but is not reproducing the 89 GHz channel very well. Lamkaouchi's data are sufficient to suggest strongly that a second relaxation process is occurring around 160 GHz, but insufficient to fully characterise it. This matters at 89 GHz and the poorer agreement at 89 GHz supports future work to fully characterise the second relaxation process. This is required to make best use of the high frequency channels on AMSU (89, 150, 183 GHz).

#### 4.4 Summary

A fast model has been developed and is described in more detail in English and Hewison (1998). The model is based on Petty and Katsaros (1994). It proves to be a very accurate fit to a geometric optics solution and gives good validation against both airborne radiometer data and AMSU data. The only problems appear to be the high sensitivity of the high angle horizontal polarisation to windspeed, where further tuning of the slope variance model could reduce biases and the permittivity calculation at 89 GHz. However the airborne data did not suggest the trend of error with skin temperature seen in the AMSU data and it may therefore be an artefact of errors in the atmospheric modelling rather than the emissivity modelling. More laboratory measurements at higher frequency and airborne radiometer validation are required to properly characterise the behaviour at high frequency. An alternative set of coefficients for this model has been devised which use 2 times the Cox and Munk slope variance (as supported by a number of sea slope models - see Guillou 1994 and Apel 1994). These significantly reduce the bias at low windspeed at high view angle but slightly degrade the fit in other windspeed/view angle combinations. Therefore at present the recommended set of coefficients are those following Wilheit's geometric optics model.

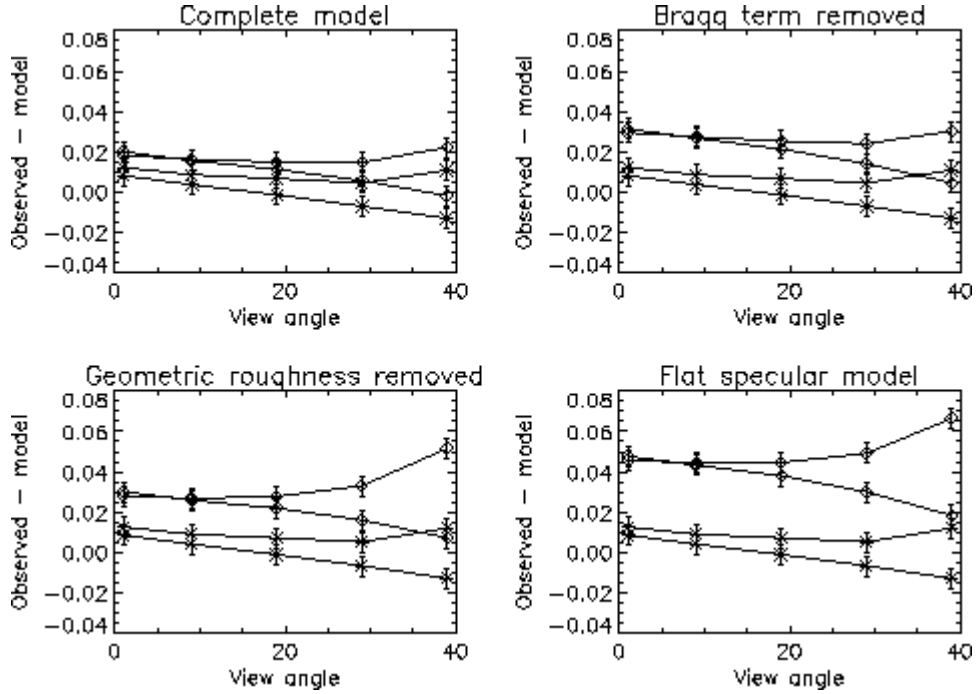


Figure 3: Difference between emissivities calculated using fast model and emissivities estimated from airborne measurements of 24 GHz zenith and nadir brightness temperature made at 30m altitude. Skin temperature was estimated from a broadband infra-red radiometer. The diamonds denote high wind-speed ( $12 \text{ ms}^{-1}$ ) and the stars low windspeed ( $0 \text{ ms}^{-1}$ ). In each case the upper curve is horizontal polarisation and the lower curve vertical polarisation. The comparison shows that  $12\text{ms}^{-1}$  wind gives rise to a 4-5% error in a purely specular calculation. The complete model fits the data to within 1-2%, errors being highest at high view angle.

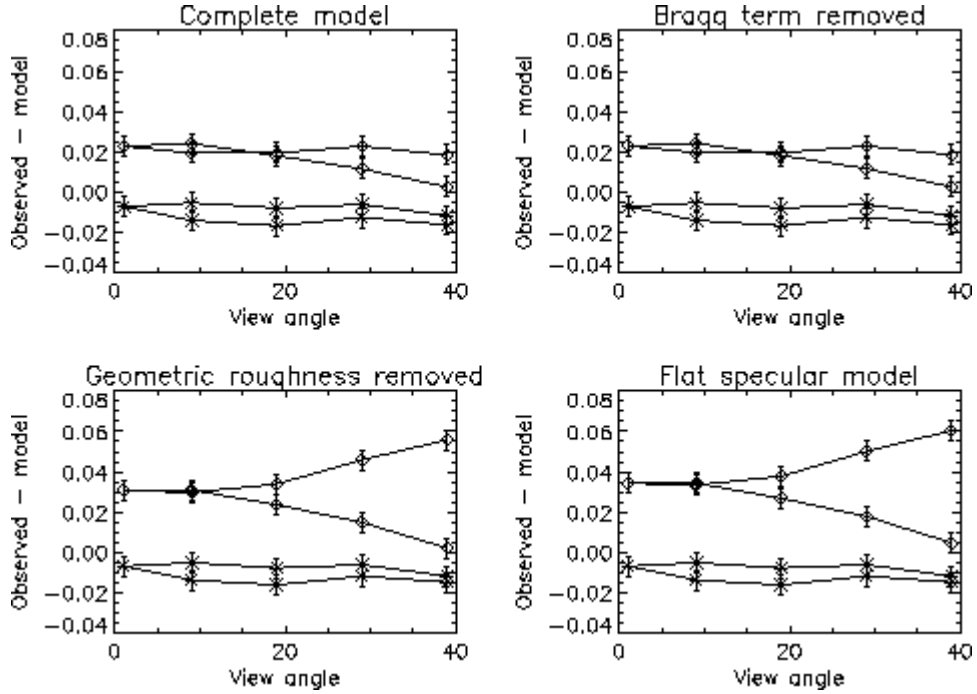
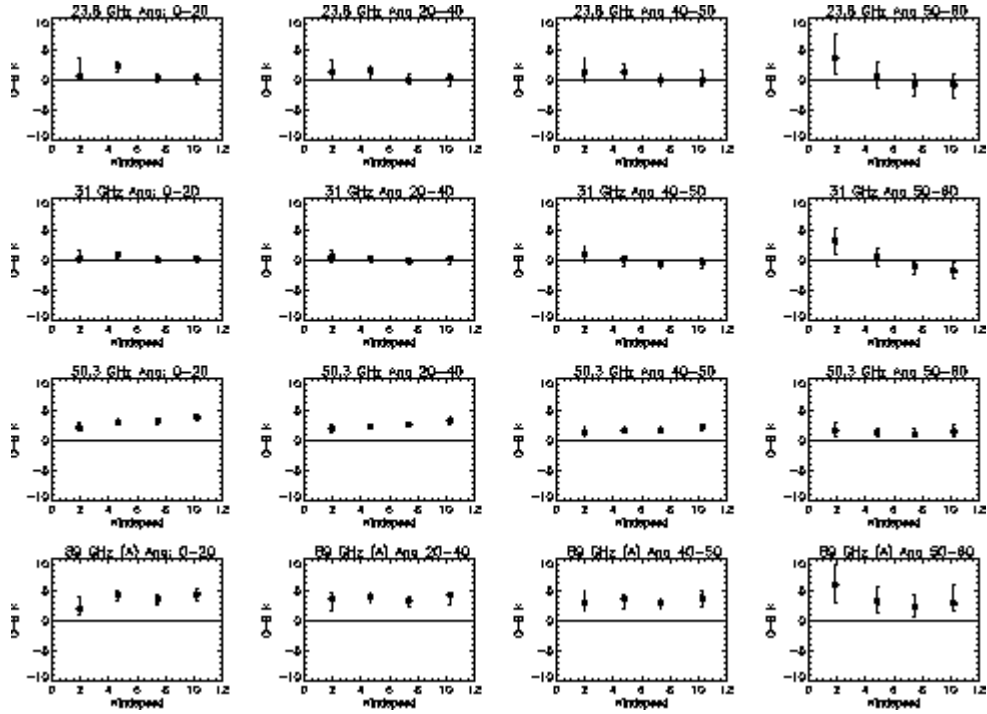
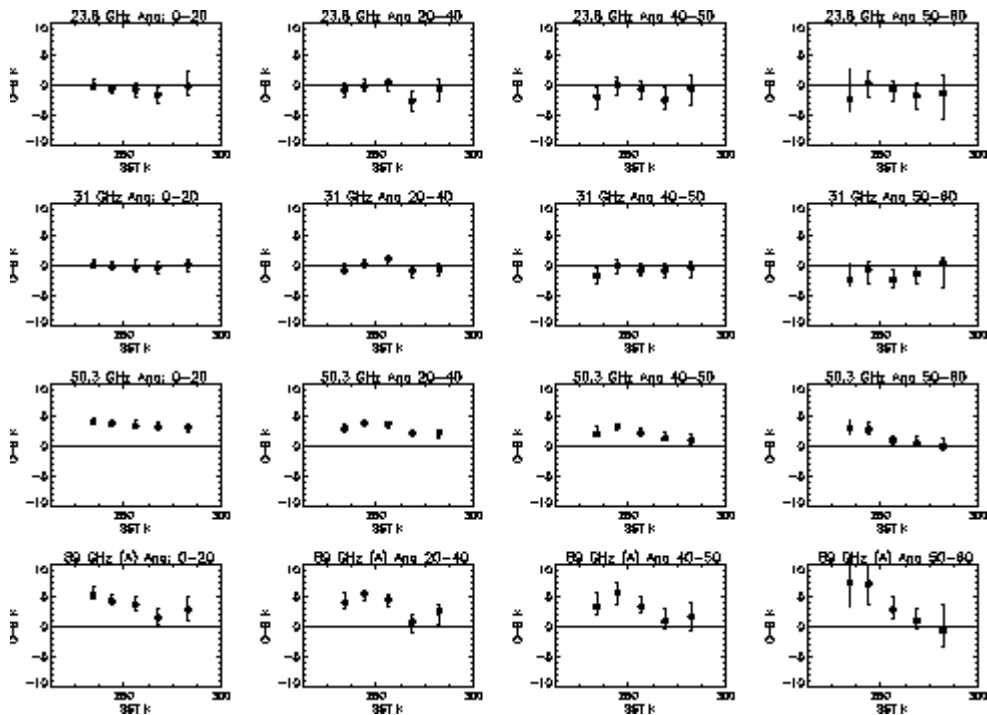


Figure 4: As Fig. 3, but for 157 GHz. Here the model gives a slight residual error correlation with windspeed. This may imply that the roughness at a given windspeed is too low.



*Figure 5:* Difference between brightness temperatures observed by the Advanced Microwave Sounding Unit at 24, 31, 50 and 89 GHz and brightness temperatures calculated using an NWP model to estimate surface windspeed, temperature and the atmospheric temperature and humidity profile. The comparison is plotted for different view angle ranges as a function of windspeed. A slight correlation of error with windspeed occurs at high view angle with the calculation underestimating the observed emissivity at low windspeed.



*Figure 6:* As Fig. 5 but plotted against skin temperature. No correlation of the difference is found except at 89 GHz..

## 5 Concluding remarks

Three surface emissivity models have been presented, among the models available in the literature. The first one (geometric optics), has been used for many purposes, and was found to work properly in most atmospheric applications. But the geometric optics approach is a better approximation at high frequency than in the low frequency range (below 15 - 12 GHz), for which a two-scale model should be preferred. The comparison between these two models, and using two sea surface spectra shows that the major uncertainty concerns the surface description, which is a function of the wind stress, possibly the swell and the foam cover. Much work remains to do on this question, by directly validating surface spectrum models, and to account for the complex interaction between the surface and the low atmosphere. The foam cover effect models, although small, has never been validated. A partial conclusion is that the difference obtained by using a model or another remains within a few Kelvin, making us confident for using them for atmospheric applications. The retrieval of surface properties might suffer from this lack of accuracy of the surface models.

Finally, the third model proposed has been optimized to get results similar to the geometric optics model, but using a fast code for operational meteorological applications.

## References

- Apel, J.R., 1994: An improved model for the ocean surface wave vector spectrum and its effects on radar backscatter, *J. Geophys. Res.*, **99**, 16269-16291.
- Bjerkas, A. W., and F. W. Riedel, Proposed model for the elevation spectrum of a wind-roughened sea surface, Tech. Memo. JHU/APL TG 1328, 31 pp., Appl. Phys. Lab., Johns Hopkins Univ., Laurel, Md., 1979.
- Bliven L., Sobieski P., Craeye C., "Rain generated ring-waves : measurements and modelling for remote sensing", *Int. J. of Remote Sensing*, Vol 18, Nr 1, pp. 221-228, 1997.
- Boukabara, S.A., Couplage des mesures hyperfréquences actives et passives. ThÈse de doctorat de l'Université Paris-VII, 1997.
- Cardone, J. J., Specifications of wind distribution in the marine boundary layer for wave forecasting, *Sci. Rep. GSL-TR69-1*, N. Y. Univ., University Heights, New-York, 1969.
- Choudhury, B.J., T.J. Schmugge, A. Chang and R.W. Newton, 1979: Effect of surface roughness on microwave emission from soils. *J. Geophys. Res.* **84**(C9), 5699-5706.
- Cox and Munk: Statistics of the sea surface derived from sun glitter., *J. Marine Res.*, **13**(2), 198-226, 1954a.
- Cox, C. and W. Munk, Measurements of the roughness of the sea surface from photographs of the sun's glitter, *J. Opt. Soc. of America*, **44**, 838-850, 1954b.
- Craeye, C., Radar signature of the sea surface perturbed by rain. Ph. D. Thesis, Université Catholique de Louvain, Faculté des Sciences Appliquées, 268 pp, 1998.
- Dropelman, J. D., Apparent microwave emissivity of sea foam, *J. Geophys. Res.*, **75**, 696-698, 1970.
- Elfouhaily, T., B. Chapron, K. Katsaros and D. Vandemark, A unified directional spectrum for long and short wind-driven waves. *J. Geophys. Res.*, **102**, 15781-15796, 1997.
- Ellison, W., A. Balana, G. Delbos, K. Lamkaouchi, L. Eymard, C. Guillou et C. Prigent, New permittivity measurements of sea water, *Radio Science*, **33**, 639-648, 1998.
- English S.J. and T.J. Hewison, 1998: A fast generic millimetre-wave emissivity model, *Proceedings of SPIE*, **3503**, 288-300.
- English, S. J., C. Guillou, C. Prigent, D. C. Jones, Aircraft measurements of water vapour continuum absorption at millimeter wavelengths, *Q. J. R. Meteorol. Soc.*, **120**, 603-625, 1994.
- Eymard, L., L. Tabary, E. Gérard, A. Le Correc and S.A. Boukabara, The microwave radiometer aboard ERS-1, Part 2 : Validation of the geophysical products, *IEEE Trans. Geosci. Remote*

- Sensing*, 34, 291-303, 1996.
- Francis, C. R., D. P. Thomas, E. P. L. Windsor, The evaluation of SMMR retrieval algorithms, in Satellite Microwave Remote Sensing, edited by T. D. Allen, 481-498, Ellis Horwood, Chichester, England, 1983.
- Guillou C., Etude du transfert radiatif dans l'atmosphère en microondes, a partir d'observations radiométriques aéroportées. PhD thesis, Univ. of Paris, 1994.
- Guillou C., English S.J., Prigent C., Jones D.C., Passive microwave airborne measurements of the sea surface reponse at 89 and 157 GHz, *J. Geophys. Res.*, 101(C5), 3775-3788, 1996.
- Guillou, C., W. Ellison, L. Eymard, K. Lamkaouchi, C. Prigent, G. Delbos, G. Balana, et S.A. Boukabara: Impact of new permittivity measurements on sea surface emissivity modelling in microwaves, *Radio Science*, 33, 649-667, 1998.
- Guissard, A. and P. Sobieski, An approximate model for the microwave brightness temperature of the sea, *Int. J. Remote Sens.*, 8, 1607-1627, 1987.
- Guissard A., Sobieski P., Baufays C., "A unified approach to bistatic scattering for active and passive remote sensing of rough ocean surfaces", *Trends in Geophys. Res.*, Vol. 1, pp 43-68, 1992.
- Ho, W. W., A. W. Love, M. J. Van Melle, Measurements of the dielectric properties of sea water at 1.43 GHz, *NASA Contractor Report CR-2458*, 1974.
- Ho, W. W., and W. F. Hall, Measurements of the dielectric properties of sea water and NaCl solution at 2.65 GHz, *J. Geophys. Res.*, 78, 6301-6315, 1973.
- Hollinger, J. P., Passive microwave measurements of sea surface roughness, *IEEE Trans. Geosci. Electron.*, GE-9, 165-169, 1971.
- Klein, L. A., and C. T. Swift, An improved model for the dielectric constant of sea water at microwave frequencies, *IEEE Trans. Antennas Propag.*, AP-25, 104-111, 1977.
- Lamkaouchi K., Balana A. and Ellison W.J., 1997: New permittivity data for sea water (30-100 GHz). Internal PIOM report, extension of ESA report 11197/94/NL/CN (available on request).
- Lemaire D., Non-fully developed sea state characteristics from real aperture radar remote sensing, Ph. D. Thesis, Université Catholique de Louvain, Faculté des Sciences Appliquées, 220 pp, 1998.
- Lemaire D., Sobieski P., Guissard A., "Full-range sea surface spectrum in non-fully developed state for scattering calculations", *IEEE Trans. GRS*, 37(2), 1038-1051, 1999.
- Liebe H. J., G. A. Hufford, T. Manabe, A model for the complex permittivity of water at frequencies below 1 THz, *Int. J. Infrared Millimeter Waves*, 12, 659-675, 1991.
- Liebe, H.J., G.A. Hufford, and M.G. Cotton, Propagation Modeling of Moist Air and Suspended Water/Ice Particles at Frequencies Below 1000 GHz. AGARD Conference Proc. 542, Atmospheric Propagation Effects through Natural and Man-Made Obscurants for Visible to MM-Wave Radiation, pp.3.1-3.10 (1993).
- Manabe, T., H. J. Liebe, G. A. Hufford, Complex permittivity of water between 0 and 30 THz, *IEEE Conf. Dig. 87CH1490-1*, 21-22, Orlando, FL, 1987.
- Monahan E.C. and O'Muircheartaigh I.G., 1986: Whitecaps and the passive remote sensing of the ocean surface., *Int. J. Remote Sensing*, 7(5), 627-642.
- Monahan, E. C., and I. G. O'Muircheartaigh, Whitecaps and the passive remote sensing of the ocean surface, Review article, *Int. Remote Sens.*, 7, 627-642, 1986.
- Monahan, E. C., and M. Lu, Acoustically relevant bubble assemblages and their dependence on meteorological parameters, *IEEE J. Ocean. Eng.*, 15, 340-349, 1990.
- Peake W.H., "Interaction of electromagnetic waves with some natural surfaces", *IRE Transactions on Antennas and Propagation*, pp 325-329, 1959.
- Petty G.W. and Katsaros K.B., The response of the SSM/I to the marine environment. Part II. A parameterization of the effect of the sea surface slope distribution on emission and reflection., *J. Atmos. and Oceanic Tech.*, 11(3), 617-628, 1994.
- Pierson W.J., Moskowitz L., A proposed spectral form for fully developed wind seas based on the similarity theory of Kitaigorodskii, *J. Geophys. Res.*, 69(24), 5181-5189, 1964.
- Pierson, W. J., and R. A. Stacy, The elevation, slope, and curvature spectra of a wind roughened sea, NASA Contract. Rep., CR-2247, 1973.
- Prigent, C., and P. Abba, Sea surface equivalent brightness temperature at millimeter wavelength,

- Annales Geophysicae*, 8, 627-634, 1990.
- Rosenkranz, P. W., and D. H. Staelin, Microwave emissivity of ocean foam and its effect on nadiral radiometric measurements, *J. Geophys. Res.*, 77, 6528-6538, 1972.
- Rosenkranz, P. W., Rough-sea microwave emissivities measured with the SSM/I, *IEEE Trans. Geosci. Remote Sens.*, 30, 1081-1085, 1992.
- Stogryn, A., The apparent temperature of the sea at microwave frequencies, *IEEE Trans. Antennas Propag.*, AP-15, 278-286, 1967.
- Stogryn, A., The emissivity of sea foam at microwave frequencies, *J. Geophys. Res.*, 77, 1658-1666, 1972.
- Trokhimovski, Y.G., Gravity-capillary curvature spectrum determined from the sea surface brightness temperature. Reprints of the IGARSS'99 conference (CDROM, 0-7803-5207-6/99), 1999.
- Wentz, F. J., A two-scale scattering model for foam-free sea microwave brightness temperatures, *J. Geophys. Res.*, 80, 3441-3446, 1975.
- Wilheit, T. T., A model for the microwave emissivity of the ocean's surface as a function of wind speed, *IEEE Trans. Geosci. Electron.*, GE-17, 244-249, 1979.
- Wu, S.T., Oceanic whitecaps and sea state. *J. Phys. Oceanogr.*, 9, 1064-1068, 1979.
- Wu, S. T., and A. K. Fung, A noncoherent model for microwave emissions and backscattering from the sea surface, *J. Geophys. Res.*, 77, 5917-5929, 1972.

# Emissivity Modelling of Sea Ice and Lake Ice

Klaus-Peter Johnsen and Georg Heygster

## Abstract

In order to better understand the radiometric signal of sea ice and lake ice between 1 and 100 GHz we present two different model approaches - the Strong Fluctuation Theory (SFT) and a Radiative Transfer Theory - and their combination (the Combined radiative transfer Strong Fluctuation Theory, CSFT). Due to the coherent Fresnel reflection coefficient, the SFT shows oscillations of the brightness temperature *e.g.* with frequency of observation and with ice thickness. These oscillations were observed within freshwater ice in a tank experiment. They are reduced in sea ice due to the large variations of the ice thickness within the footprint of groundbased radiometers or SSM/I (Special Sensor Microwave Imager). The CSFT calculates the non scattering contribution to the emissivity with a radiative transfer theory and shows no more the oscillations of the SFT and a good agreement with observed sea ice emissivities up to 40 GHz. Comparisons with radiometric *in-situ* measurements taken within the Arctic Ocean and from a tank experiment allow to obtain further knowledge about the parameters (snow and ice thickness, liquid water content within the snow) which govern the microwave signal of ice.

## 1 In-situ Measurements

### 1.1 Overview

Although there is a wide literature on *in-situ* observations of sea ice properties (*e.g.* Tucker et al., 1992, Hallikainen, 1996a) there are not yet distinct descriptions of different sea ice types in terms of those microphysical parameters which govern their emissivity properties. But the sensible parameters have been identified in a recent study (Fuhrhop et al., 1997), namely snow water content, snow density and grain size, and air bubble diameter and salinity. Our knowledge of these properties and especially their statistical variations on the scale of spaceborne passive microwave radiometers, *e.g.* several hundred of km<sup>2</sup>, is limited. Eicken et al. (1995) observed within one floe of level multiyear ice a variability as large as the one between floes of different origins and ages. They concluded that the regional differences in the microwave signature are due to other fractions of the ice such as melt ponds or pressure ridges.

Recently, the results of the Accelerated Research Initiative (ARI) on the Electromagnetic Properties of Sea Ice (EMPOSI) sponsored by the Office of Naval Research (ONR), Washington, DC, has been published in a special section of the IEEE Transactions of Geoscience and Remote Sensing.

Here we present radiometric *in-situ* measurements taken during ARK-XII/1 of the german R.V. Polarstern in the Kara and Laptev Sea from 12th of July to 23rd of September 1996 and thin lake ice measurements taken in a tank experiment at Lake Ladoga (Russia) and explain them with an incoherent radiative transfer model as well as with the coherent Strong Fluctuation Theory.

## *1.2 In-situ Measurements of Sea Ice Parameters*

During the cruise of R.V.Polarstern, a record of general ice conditions was kept based on observations from the ship's bridge (Lensu et al., 1996). The field program on the ice included taking of ice cores and thickness measurements as well as measurements of snow depth, temperature, density and microwave brightness temperatures (Augstein et al., 1997). During the entire expedition, the ice surface was found to be covered with snow either remaining from the previous winter, or new snow accumulating during the second half of the expedition. The microstructure of the snow (snow grain size, snow density), the distinct boundary between snow and ice as well as the low electric conductivity of the melted snow indicate this to be aged snow, rather than decomposed surface ice as commonly observed on summer Arctic sea ice (Grenfell, 1992, Eicken et al., 1995). The mean snow characteristic profiles distributed over 31 stations during the cruise are given in Table 1.

Table 1

Mean snow characteristics observed on horizontal profiles from 31 stations during the cruise of R.V.Polarstern.

Snow thickness:	
All profiles	$0.14 \pm 0.08$ m
Northern Kara Sea between Franz Josef Land and Severnaja Zemlja	$0.07 \pm 0.04$ m
Arctic Sector	$0.20 \pm 0.04$ m
Laptev Sea (south of 82°N)	$0.10 \pm 0.03$ m
Profile length	200 m
Snow density	$410 \pm 70$ kg/m <sup>3</sup>
Electric conductivity	$18 \pm 21$ $\mu$ S/cm

Generally, the snow showed fairly coarse grains; based on an analysis of 39 samples taken at these 31 stations with an image processing system, the mean major and minor axes of snow grains were found to be 2.3 and 1.1 mm, respectively. New snow also observed during the campaign from station 232 (19th of August 1996) onward had smaller grain size of around 0.5 mm. Furthermore temperatures at the interfaces of ice/snow and snow/air were recorded.

## *1.3 Radiometric Measurements of Sea Ice*

Surface based passive microwave sensors measure the brightness temperatures which depend on sea ice emissivity, physical temperature and the reflected sky radiation.

To obtain a better understanding of the corresponding microwave signatures with respect to the snow thickness we have performed groundbased passive microwave measurements during ARK-XII/1. Measurements collected during this expedition are particularly suitable for this kind of analysis because for the entire time the ice was snow covered, and only few melt ponds which could mimic fractions of open water in the spaceborne microwave data were observed until mid August.

The microwave instrumentation used during the ARCTIC 96 experiment consisted of three portable, linearly polarized Dicke radiometers operating at 11, 21, and 35 GHz.

To determine the microwave signatures of the snow covered ice the following procedure

was applied at the stations of ARK-XII/1: Measurements were performed along transects every 53 cm on level parts of ice floes to obtain clearly defined brightness temperatures. Thus, the error due to the incidence angle is below  $2^\circ$  which results in an error in the measured brightness temperature below 0.5 K. The incidence angle was set to  $50^\circ$  to match the SSM/I onboard the DMSP F13 spacecraft observing angle of  $51.7^\circ$ . Radiometric together with snow thickness measurements were taken along profiles of different lengths with 19 to 100 points. As an example, the emissivities as obtained from the observed brightness temperatures using the tipping curve method (Flückiger et al., 1994) at station 247 at 35 GHz (horizontal polarized) are shown in Figure 1. More details are given in (Johnsen, 1998).

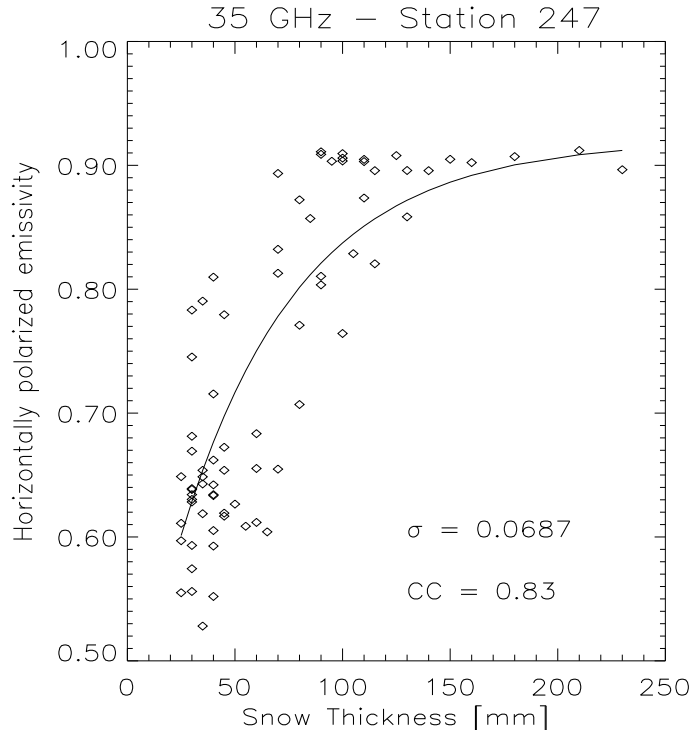
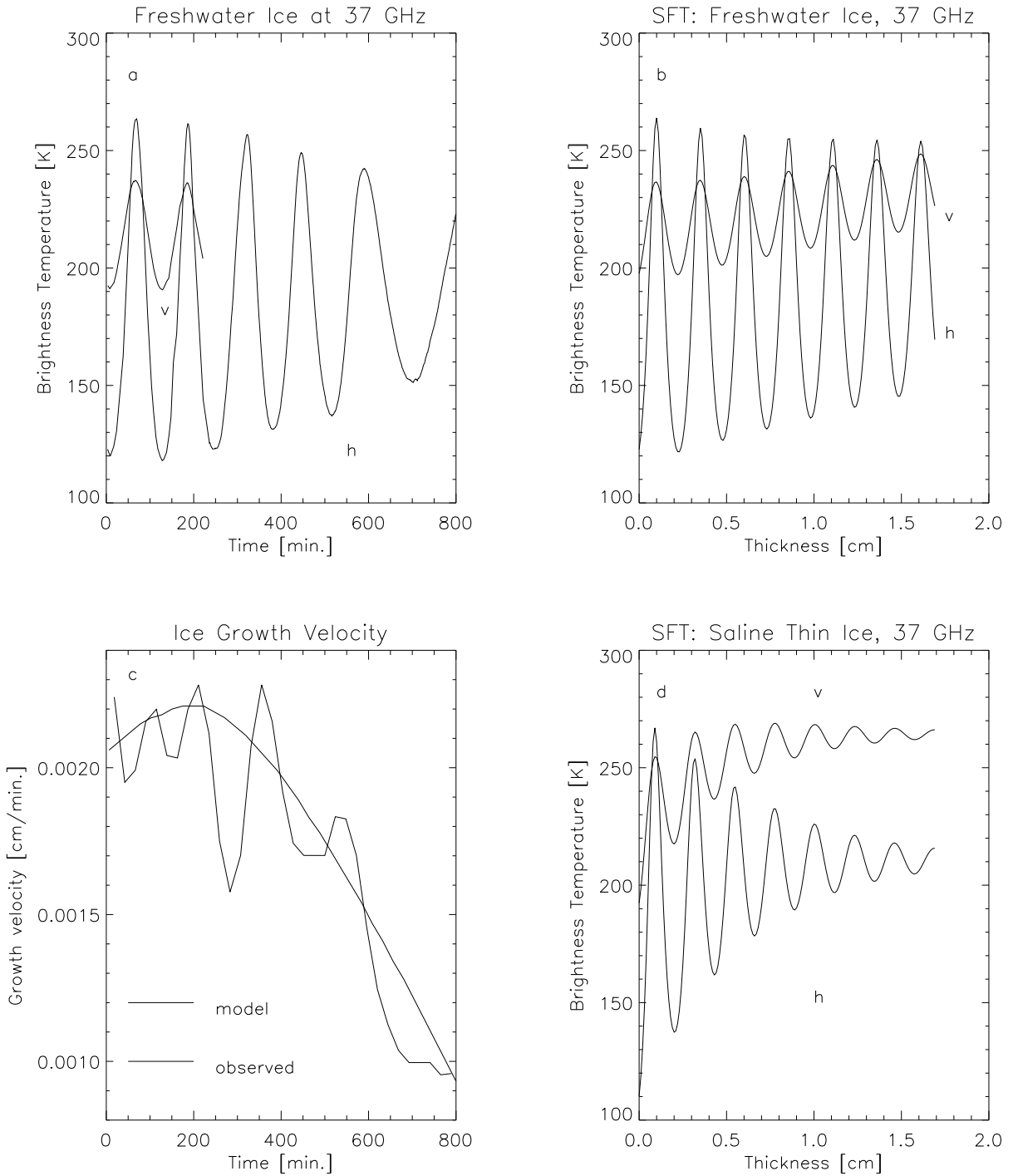


Figure 1. Radiometric measurements taken at 35 GHz at station 247 of ARK-XII/1. The line shows the model of Ulaby and Stiles.  $\sigma$  is the standard deviation and CC the correlation coefficient between the experimental and theoretical data. The physical temperature at the snow/air boundary was  $-1.0^\circ\text{C}$  and at the ice/snow boundary  $-2.6^\circ\text{C}$ .

#### 1.4 Radiometric Measurements of Thin Freshwater Ice

In Figure 2a radiometric measurements at 37 GHz taken over an open air tank filled with Lake Ladoga water are shown. The size of the tank was  $110 \times 300 \times 45 \text{ cm}^3$ . Before the onset of crystallization the water surface was cooled down to  $0^\circ\text{C}$  and was seeded by small snow crystals. During the experiment, air temperature dropped from  $-5.5^\circ\text{C}$  to  $-7.5^\circ\text{C}$  and then increased to  $-5.0^\circ\text{C}$ . The freezing ice was observed with a passive microwave radiometer at 37 GHz in both polarizations. The radiometer was mounted 1.5 m above the ice surface. The incidence angle was also set to  $50^\circ$ . The ice grew up to a thickness of about 1.7 cm. The brightness temperatures of the thin ice show strong oscillations with time.



**Figure 2.** Passive microwave measurements at 37 GHz of freshwater ice grown from Ladoga Lake water (a) and the modelling with the SFT (b). The maximum ice thickness was 1.7 cm. (c): Ice growth velocity as calculated from the microwave measurements of the freshwater ice and with a thermodynamical model of Maykut (Darovskikh et al., 1998). (d): Horizontally polarized brightness temperature of thin saline ice as calculated with the SFT. All parameter are identical to the thin lake ice except of the salinity, which is 5 ppt. v means the vertically polarized brightness temperature, h the horizontally polarized.

## 2 Microwave Emissivity Models of Lake and Sea Ice

### 2.1 Overview

Microwave sea ice signature models (Winebrenner et al., 1992) may be grouped by surface scattering models, mainly used to predict backscattering, and volume scattering models which are often solutions of the RT equations. But in sea ice the assumption of a non-dense medium where the scatterers are in the far field of each other is violated; Therefore several modifications have been developed which use the analytic wave theory based on Maxwells equations. They can be grouped into discrete scatterer approaches (e.g. Rother and Schmidt, 1996) and the random medium approaches (e.g. Stogryn, 1987). Here we use a radiative transfer as well as a random medium theory (Strong Fluctuation Theory, SFT) to explain the surface based radiometric measurements and a Combined radiative transfer-Strong Fluctuation Theory (CSFT) to explain the SSM/I data.

### 2.2 Radiative transfer model of Ulaby and Stiles

A model originally proposed by Ulaby and Stiles (1980) for snow over ground is used to interpret the calculated emissivities. The model assumes that the brightness temperature measured by the radiometer consists of two components, one due to the emission by the ice and the underlying water  $T_B^{ice}$ , and the other due to emission by the snow layer  $T_B^{snow}$ :

$$T_B = T_B^{ice} + T_B^{snow} \quad (1)$$

Ulaby and Stiles assumed plane-parallel snow and ice layers, neglected multiple scattering at the boundaries and derived for the emissivity

$$\epsilon = \frac{T_B}{T_0} = A + B \exp(-vd_s \alpha_e \sec \theta) \quad (2)$$

with  $T_0$  as the physical temperature of the sea ice and

$$A = Y_{as} \frac{\alpha_a}{\alpha_e} \quad (3)$$

$$B = Y_{as} Y_{si} - Y_{as} \frac{\alpha_a}{\alpha_e} \quad (4)$$

$$\alpha_e = \alpha_a + \alpha_s, \quad (5)$$

here  $Y_{as}$  and  $Y_{si}$  are the transmission coefficients at the interfaces from air to snow and from snow to ice, respectively,  $\alpha_a$  is the absorption coefficient,  $\alpha_s$  the scattering coefficient and  $\alpha_e$  the extinction coefficient of the snow layer in units of  $\text{cm}^{-1}$ . From equation 3 and  $\alpha_e \geq \alpha_a \geq 0$  follows that  $Y_{as} \geq A$ .  $v$  is the volume fraction and  $d_s$  is the snow thickness. In order to apply the model,  $A$ ,  $B$  and  $v\alpha_e \sec \theta$  have to be determined. The quantities  $Y_{as}$ ,  $Y_{si}$  and  $\alpha_a/\alpha_e$  cannot be determined directly but they are not necessary to use the model.

#### Applications

As an example in Table 2 the coefficients for the measurements at the stations 234, 246 and 247 generated by fitting the experimental values of  $\epsilon$  to (2) are given together with the standard deviation  $\sigma_\epsilon$ : one of all samples was removed and a best fit was derived from all other samples. Then the best fit was tested on the isolated sample. This process was repeated for all samples to derive the standard deviation with an independent test set.

The coefficients  $A$  at stations 246 and 247 are close to unity in all measurements, indicating that both the transmission  $Y_{as}$  at the snow to air interface and the quantity  $\frac{\alpha_a}{\alpha_e}$  are close

to 1; from the latter it follows that the scattering coefficient  $\alpha_s$  must be much smaller than the absorption  $\alpha_a$ . In contrast to this we found lower values for  $A$  at station 234 indicating stronger scattering. The coefficient  $A$  decreases with frequency due to increasing scattering with frequency.

The sum of the coefficients  $A + B = Y_{as}Y_{si}$  is larger at station 246 than at station 247. This shows that the transmission coefficient  $Y_{si}$  at station 246 (Table 2) is larger and hence also the influence of the underlying ice layer to the brightness temperature.

The vertically polarized emissivities have also been calculated and the standard deviations  $\sigma_\epsilon$  between the experimental and theoretical values are in the same range as the horizontally polarized emissivities. The best fit for the horizontal polarized 35-GHz-channel as obtained from (2) is also included in Figure 1.

Table 2

Coefficients generated by fitting the experimental values of  $\epsilon$  from station 234, 246 and 247 to equation (2).  $Y_{si}$  follows from (2) and  $A, Y_{as}, \frac{\alpha_a}{\alpha_e} \leq 1$ .  $\sigma_\epsilon$  is the standard deviation between the experimental and theoretical values of  $\epsilon$ . Freq. means frequency and Pol. polarization.  $\epsilon_m$  is the mean emissivity of the measurements and  $\sigma_m$  its standard deviation.

Freq. GHz	Pol.	$A$	$B$	$v\alpha_e \sec \theta$	$\sigma_\epsilon$	$Y_{si}$	$\epsilon_m$	$\sigma_m$
Station 234								
11	H	0.79	0.16	0.022	0.0232	0.95 ... 1.00	0.835	0.038
21	H	0.65	0.16	0.015	0.0342	0.81 ... 1.00	0.713	0.045
35	H	0.42	0.30	0.015	0.0381	0.72 ... 1.00	0.536	0.075
11	V	0.92	0.08	0.015	0.0086	1.00	0.953	0.019
21	V	0.72	0.24	0.015	0.0288	0.96 ... 1.00	0.812	0.060
35	V	0.46	0.42	0.017	0.0418	0.88 ... 1.00	0.611	0.099
Station 246								
11	H	0.98	-0.19	0.0026	0.0216	0.79 ... 0.81	0.839	0.025
21	H	0.96	-0.31	0.0030	0.0352	0.65 ... 0.68	0.747	0.049
35	H	0.87	-0.27	0.0031	0.0357	0.60 ... 0.69	0.681	0.049
11	V	1.00	-0.13	0.0032	0.0170	0.87	0.909	0.021
21	V	0.95	-0.22	0.0029	0.0380	0.73 ... 0.77	0.800	0.048
35	V	0.95	-0.30	0.0031	0.0356	0.65 ... 0.68	0.742	0.050
Station 247								
11	H	0.96	-0.40	0.028	0.0528	0.56 ... 0.58	0.864	0.067
21	H	0.94	-0.36	0.019	0.0575	0.58 ... 0.62	0.819	0.097
35	H	0.92	-0.51	0.018	0.0687	0.41 ... 0.45	0.737	0.125
11	V	0.99	-0.23	0.031	0.0295	0.76 ... 0.77	0.941	0.040
21	V	1.00	-0.34	0.018	0.0497	0.66	0.880	0.086
35	V	0.99	-0.47	0.018	0.0692	0.52 ... 0.53	0.825	0.121

## 2.3 Strong Fluctuation Theory

The Strong Fluctuation Theory (SFT) solves Maxwell's equations and accounts for the magnitude and the phase of the electromagnetic signal reflected within the layered structure of the ice and snow. With Kirchhoff's law the emissivity  $\epsilon_a$  at the polarization  $a$  ( $a = h$  or

$a = v$ ) can be written as (Winebrenner et al., 1992)

$$\epsilon_a = 1 - |R_a|^2 - \frac{1}{4\pi} \int (\gamma_{ah}(\vec{k}_0, \vec{k}) + \gamma_{av}(\vec{k}_0, \vec{k})) \sin \theta d\theta d\phi. \quad (6)$$

The SFT determines the bistatic scattering coefficients  $\gamma_{ah}$  and  $\gamma_{av}$  for a layered model. Each layer is described by the parameters temperature, thickness, density, salinity of the ice and water layers, the diameter of the air bubbles, ice and snow grains, the liquid water content of the snow, the angle of the brine pockets and the ratio of the length and diameter of the brine pockets. Details are given by Stogryn (1986, 1987).

### Applications

The SFT shows for thin ice an oscillatory behaviour of the brightness temperature with the ice thickness (Fig. 2b and (Darovskikh et al., 1998)). The amplitude, frequency and the phase of these oscillations depend on the microwave frequency and on the dielectric constant of the ice. This allows to determine the ice thickness (modulo the wavelength of the oscillations) and the ice growth velocity (Fig. 2c and (Darovskikh et al., 1998)). The decreasing growth velocity can be explained thermodynamically with a decreasing heat transport through the increasing ice cover (Maykut, 1978). For saline ice the amplitudes of the oscillations decrease with thickness (Fig. 2d).

### 2.3 Combined Radiative Transfer-Strong Fluctuation Theory (CSFT)

In contrast to these ground based measurements passive microwave signals observed from space do not show clear hints for an interference effect because they average over a large footprint. The footprint sizes of the SSM/I vary between  $15 \times 13 \text{ km}^2$  for the 85 GHz-channel and  $69 \times 43 \text{ km}^2$  for the 19 GHz-channel. If the variations of the horizontal ice structure within the footprint of the radiometer are so strong that interference effects are averaged out, an incoherent model, e.g. a radiative transfer technique would be more appropriate than a coherent one. But as the scatterers in the snow and ice are in the near field of each other, the postulations of the radiative transfer theory are violated. The inclusion of scattering is necessary because (1) it can contribute much to the emissivity of snow for frequencies above approximately 30 GHz and (2) the density of the uppermost layer of multiyear ice may be so small (Tucker et al., 1992) that its scattering contributes considerably to the total emissivity according to equation (6).

In order to model the emissivities we combine the SFT, which calculates the scattering part in the near field with a radiative transfer model:

The third term on the right hand side of equation (6) (integral over the bistatic scattering coefficients) is calculated with the fluctuating part of the electric field of the SFT (Stogryn, 1986). The oscillations of the SFT are caused by the Fresnel reflection coefficient  $R_a$ , the second term of equation (6). It is calculated in the SFT (Fuhrhop et al., 1997) with a Riccati differential equation from homogeneous layers with a mean dielectric constant.

Brekhovskikh (1973) has shown that  $R_a$  is the same as that from a layer model *without* scattering which uses a coherent radiative transfer approach. In the theory of radiative transfer it was shown (Ulaby et al., 1981) that the incoherent approach allows quite similar results like the coherent approach but without the oscillations. Here, we include scattering into the model formulated by Burke et al. (1979). They calculated the polarized brightness temperature  $T_{B,a}$  of a layered medium as

$$T_{B,a}(\theta_0) = \sum_{i=1}^N P T_i (1 - \exp(-\gamma_i(\theta_0) \Delta z_i)) \times \quad (7)$$

$$\times(1 + R_{a,i+1}(\theta_0) \exp(-\gamma_i(\theta_0)\Delta z_i))$$

with

$$P = \prod_{j=1}^i (1 - R_{a,j}(\theta_0)) \exp - (\sum_{j=2}^i \gamma_{j-1}(\theta_0) \Delta z_{j-1}).$$

In these equations  $N$  means the number of layers and  $\theta_0$  the incidence angle.  $\Delta z_i$  is the thickness of  $i$ -th layer of the sea ice. The absorption coefficient  $\gamma_i$  follows from the Poynting-Theorem (Burke et al., 1979) as  $\gamma_i = 2\omega k_{zi}^I/c$  with  $k_{zi}^I$  the imaginary part of the  $z$ -component of the wave number in the  $i$ -th layer,  $c$  the speed of light and  $\omega$  the angular frequency. From equation (7) we calculate the emissivity for the  $i$ -th isothermal layer as

$$\epsilon_{a,RAD} = \frac{T_{B,a}}{T} \quad (8)$$

with  $T = T_i$  as one constant physical temperature for all layers  $i = 1,..,N$ . This means that different physical temperatures of the layers are only considered in the calculation of the dielectric constants of the layers. But for the calculation of the brightness temperature a constant physical temperature is assumed. The thus induced error is small because the emitted radiation mainly emanates from the uppermost layers.

Because scattering of a dense medium is not implemented into the radiative transfer model, the reflectivity follows from the emissivity according to

$$|R_{a,RAD}|^2 = 1 - \epsilon_{a,RAD}. \quad (9)$$

Now, the idea of the CSFT is to replace the reflectivity  $|R_a|^2$  in equation (6) by  $|R_{a,RAD}|^2$  using (8) and (9):

$$\epsilon_{a,CSFT} = \frac{T_{B,a}}{T} - \frac{1}{4\pi} \int (\gamma_{ah}(\vec{k}_0, \vec{k}) + \gamma_{av}(\vec{k}_0, \vec{k})) \sin \theta d\theta d\phi. \quad (10)$$

The scattering term provides the description of dense media.

### *Applications*

Figure 3 compares the emissivities according to the SFT and the CSFT for the old ice (WMO, 1989) and Figure 4 for dark nilas without snow. For details about layers and their microphysical description see (Fuhrhop et al., 1997). For high frequencies (above approximately 40 GHz) the theories show similar values for the emissivities. For the lower SSM/I-frequencies the combined approach reproduces with good accuracy the mean value of the oscillatory emissivity of the SFT. The small oscillations of the CSFT emissivities result from the scattering contribution. An overview over the differences in the brightness temperatures between both theories for the SSM/I frequencies is given in Table 3. It shows that for multiyear ice the differences are below 7 K but for dark nilas the differences can increase up to 56 K. This can be explained by destructive interference in the 12 layers of the multiyear ice model.

In none of the investigated cases the CSFT produced horizontally polarized brightness temperatures greater than the vertically polarized ones.

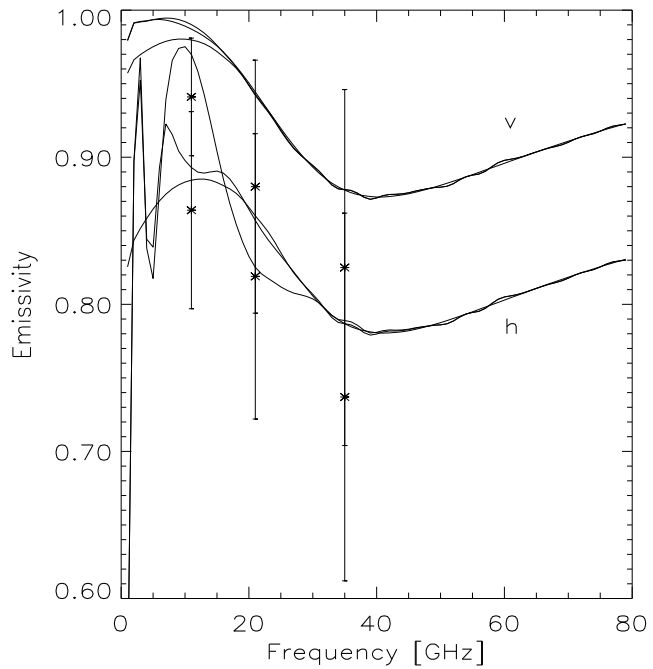


Figure 3. Comparison of SFT (solid line), CSFT (dotted line) and measurements taken at station 247 during ARK 12/I with R.V.Polarstern in the Laptev Sea. h: Horizontally polarized emissivity, v: vertically polarized emissivity. The dashed lines are the mean values of the emissivities over 15 different snow thicknesses with constant change of thickness, calculated with the SFT.

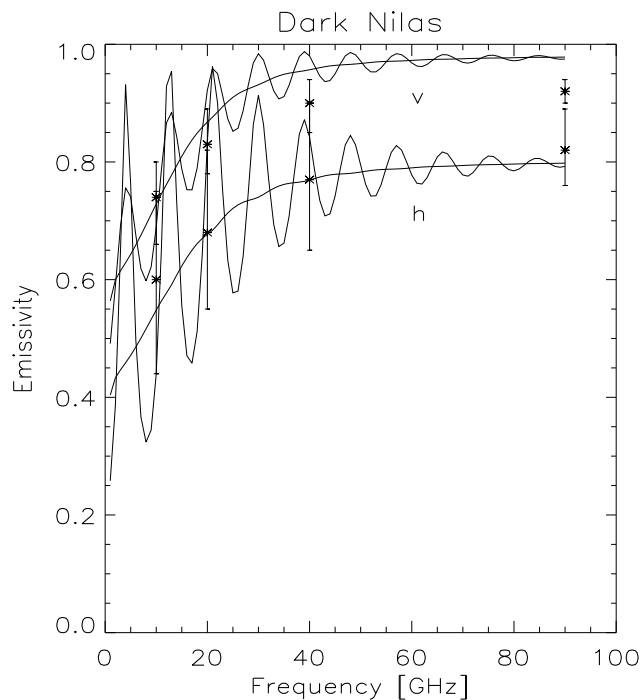


Figure 4. Comparison of the emissivities according to the SFT (oscillating), the CSFT (smooth) and radiometric measurements of dark nilas from Eppler et al.(1992). Parameters are given in (Fuhrhop et al., 1997).

Table 3

Differences of the Brightness Temperatures (in Kelvin) of the SFT and the CSFT for the frequencies of the SSM/I. For the parameters see (Fuhrhop et al., 1997).

Frequency	Dark Nilas		First-year Ice		Multiyear Ice	
No. of layers	3		8		12	
Polarization	H	V	H	V	H	V
19 GHz	7.4	1.2	-5.6	-0.5	-6.4	2.4
22 GHz	-55.9	-17.6	-0.3	0.0	-3.5	-0.8
37 GHz	-4.0	-1.2	-2.4	-0.1	-1.5	0.2
85 GHz	-2.3	-0.8	0.0	0.0	0.0	0.0

### *Application to SSM/I-data: Retrieval of the snow thickness over Arctic sea ice*

The CSFT can also be used under special conditions to derive the snow thickness over Arctic sea ice:

Neglecting the atmospheric influence the brightness temperature  $T_B^{SSM/I}$  as measured by the SSM/I can be described as the sum of the contributions from the open water  $T_B^{water}$  and the ice  $T_B^{ice}$ :

$$T_B^{SSM/I} = (1 - C)T_B^{water} + CT_B^{ice} \quad (11)$$

From this relation the vertically polarized brightness temperatures  $T_B^{ice}$  of the sea ice averaged over the considered sensor footprint were obtained from the assumed brightness temperature of the open water ( $T_B^{water} = 177.1$  K at 19 GHz and  $T_B^{water} = 201.7$  K at 37 GHz for the Arctic ocean), the brightness temperature  $T_B^{SSM/I}$  measured by the SSM/I and the ice concentration  $C$  as calculated by the NASA-Team-Algorithm (Cavalieri et al., 1992).

An algorithm was derived to retrieve the snow thickness from the gradient ratio

$$GR(37V, 19V) = \frac{T_B^{ice}(37V) - T_B^{ice}(19V)}{T_B^{ice}(37V) + T_B^{ice}(19V)}. \quad (12)$$

To reduce the influence of variations of the atmosphere weekly mean values of the SSM/I brightness temperatures were used. A comparison between the snow thickness measurements taken along the 31 profiles of ARK-XII/1 and the gradient ratio derived from daily mean brightness temperatures of the SSM/I (NSIDC, 1992) shows an exponential decrease with increasing snow thickness (Fig. 5). This behaviour is confirmed by consistent model calculations with the CSFT (Fig. 5). For these calculations the mean density and salinity profiles from all 11 ice cores and the mean snow grain sizes from the 31 snow profiles were taken. The model uses 3 snow layers and 8 ice layers. The snow liquid water content of 0.1 % in the lowest layer and 0 % in both others was derived from a best fit with a mean standard deviation of 6.3 cm for the snow thickness.

To derive the snow thickness (in cm) the regression to the CSFT model can be inverted and the inversion can be approximated by

$$d_s = 26.12 - \sqrt{707.4 + 6632.4GR(37V, 19V)}. \quad (13)$$

The difference between the SFT model and the inverted polynominal fit is below 1.8 cm in the range from 0 to 26.1 cm.

Some measurements of the SSM/I reveal large gradient ratios at large snow thicknesses. They are marked in Figure 5 with asterisks.

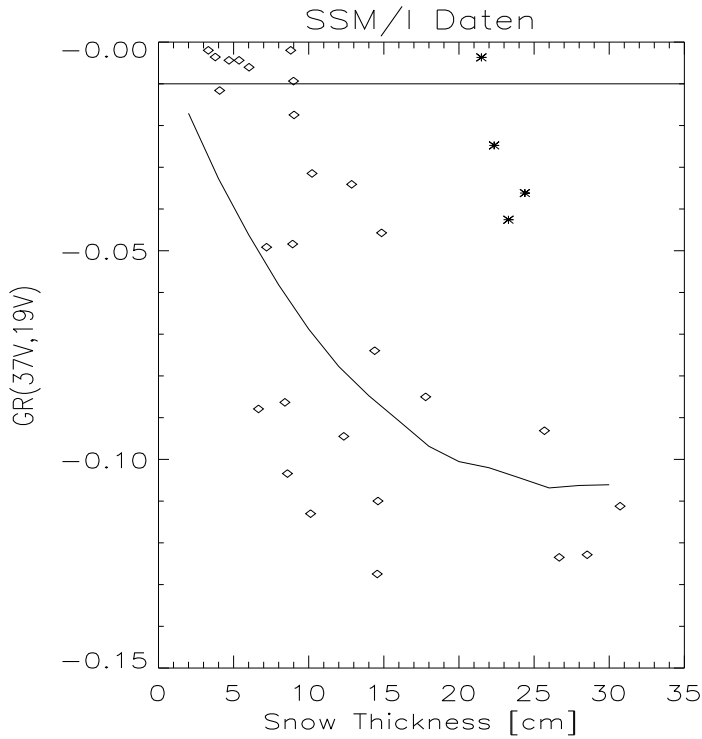


Figure 5. Mean snow thickness versus the SSM/I gradient ratio  $GR(37V,19V)$  for coincident snow thickness profiles and SSM/I pixels. The asterisks mark stations with air temperatures above  $-1.0^{\circ}\text{C}$  and strong melting. GR's above  $-0.01$  with high liquid water content due to air temperature above  $0^{\circ}\text{C}$  are also excluded. The line shows the best fit with the CSFT.

All of these SSM/I-measurements were taken at air temperatures above  $-1^{\circ}\text{C}$ . They have not been considered in the above algorithm because their gradient ratios are believed to be influenced by a high liquid water content in the snow due to elevated temperatures. These findings are supported by high temperatures at the snow/air boundary at stations 246 and 247 and corresponding large gradient ratios at these stations despite large snow thicknesses. Measurements with  $GR(37V,19V)$  larger than  $-0.01$  are also excluded because they could be influenced by high liquid water content of the snow due to temperatures above  $0^{\circ}\text{C}$ .

Performing a linear regression between the snow thickness  $d_s$  (in cm) of Antarctic first-year ice and the gradient ratio  $GR(37V,19V)$  derived from brightness temperatures of the ice at 19 and 37 GHz Markus and Cavalieri [16] obtained

$$d_s = -2.34 - 771 \cdot GR(37V, 19V). \quad (14)$$

The decrease of the gradient ratio  $GR(37V,19V)$  with increasing snow thickness is therefore smaller over Antarctic sea ice than over Arctic sea ice under the conditions observed during ARK XII/1.

An example of the snow thickness determined for the whole Arctic using the SFT is given in Figure 6. Measured gradient ratios below  $-0.106$  were set to  $-0.106$  because the SFT model does not show lower values. Because the algorithm was derived from SSM/I data with ice concentrations above 80%, we estimate it to be accurate down to  $\approx 60\%$  ice concentration. All pixels with ice concentration below 60% are not considered in Figure 6. The zonal means of the satellite data show an increase of the snow thickness with latitude (Fig. 7). A similar trend was obtained from mean values of snow thickness measurements

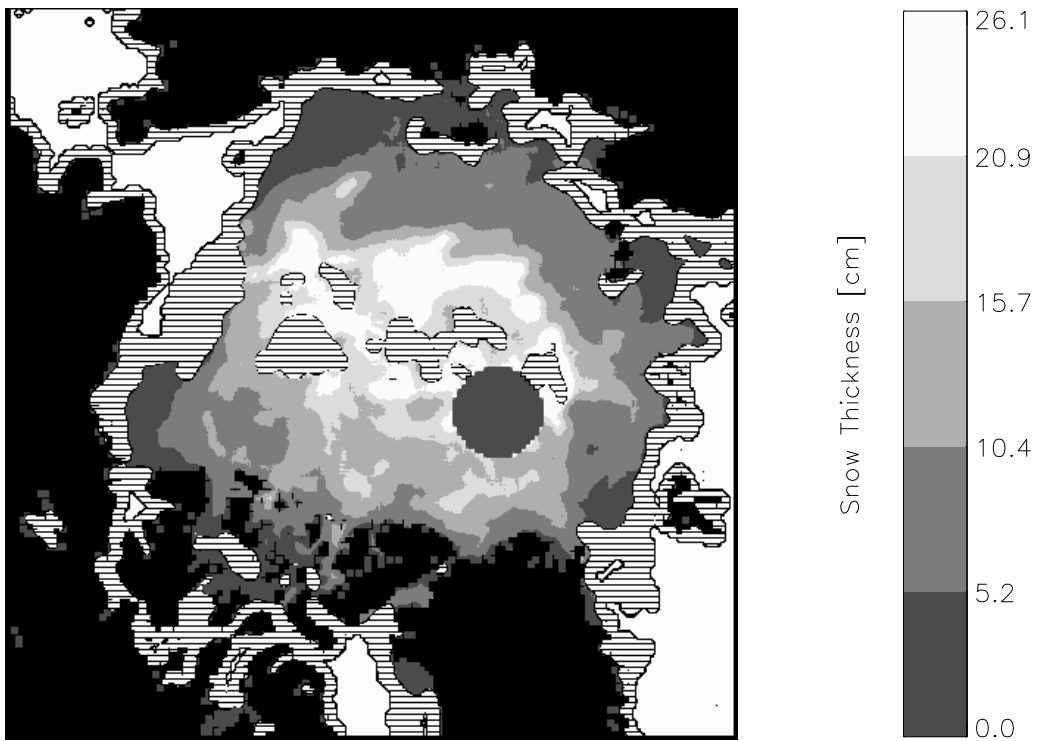


Figure 6. Mean snow thickness of Arctic sea ice between the 25th and the 30th of August 1996 derived from SSM/I data using the SFT regression according to Figure 5. Horizontal lines: ice concentration between 5 and 60%. White: ice concentration below 5%.

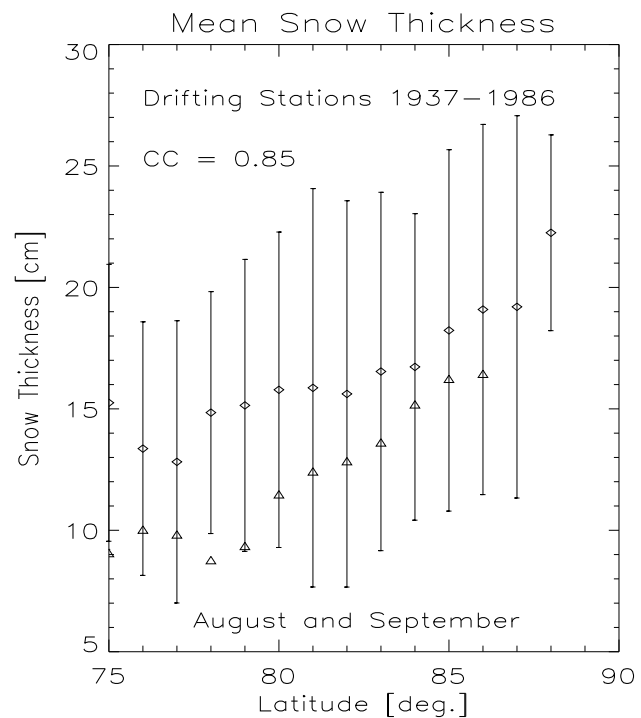


Figure 7. Mean snow thicknesses from russian drifting stations in August and September 1937-1986 (diamonds) and standard deviations versus latitude. The triangles mark the zonal mean snow thickness as derived from Figure 6. CC is the correlation coefficient between both values.

by the russian drifting stations between 1937 and 1986 in August and September (Fig. 7). Possibly the algorithm underestimates the snow thickness slightly, but the zonally averaged mean snow thicknesses determined with the SFT algorithm are with one exception within one standard deviation of the snow thickness measurements of the russian drifting stations.

### **3 Recommendations and further improvements**

- Radiometric *in-situ* observations of sea ice together with sea ice parameters in the Arctic and Antarctic are quite sparse. Nevertheless these combined measurements are necessary to derive physical models and to understand spaceborne radiometric data. Especially the snow thickness, liquid water content within the snow, the snow grain size and the ice density and salinity should be measured because of their strong influence on the microwave signal (Fuhrhop et al., 1997). Time series of all of these parameters together with the radiometric signal within different seasons would be quite helpful.
- Large lakes like Lake Ladoga are well performed research areas which allow to derive routinely many parameters of the ice and its snow cover together with SSM/I-measurements. These measurements would help to understand the time dependency of the radiometric signal of the SSM/I as resulting from the temporal evolution of the microphysical properties of the ice.
- The statistical variations of the sea ice parameters in the Arctic are so large that an incoherent approach to describe spaceborne passive microwave data is necessary. Due to the precise description of the scattering part within the strong fluctuation theory we presented a combined radiative transfer strong fluctuation theory. The coherence effect was analysed. It was shown that especially for thin ice this effect is important and can be used to derive the ice thickness under laboratory conditions.
- The models based on the strong fluctuation theory are currently restricted to frequencies below around 40 GHz. Above this frequency deviations could be obtained due to the use of the bilocal as well as the distorted Born approximation. To improve the accuracy, higher order terms of the Dyson equation are necessary to include in the models. This should be considered in greater detail in the future. This would also allow to include frequencies measured by humidity sounders like the SSM/T2 or the AMSU-B and calculate the unknown surface component of the microwave signal.
- A combined model for atmosphere, ocean and sea ice would allow to investigate joint sensitivities to microphysical parameters and the distribution of surface types within the footprint of the spaceborne sensors. A first version was presented by Fuhrhop et al. (1997) but more experimental data are necessary to validate it and thus allow to understand the radiometric signal of spaceborne passive microwave radiometers.

### **References**

- [1] E. Augstein and Cruise Participants. In *Die Expedition Arctic'96 des F.S. Polarstern, ARK XII mit der Arctic Climate System Study (ACSYS)*. Berichte zur Polarforschung, volume 234, Alfred-Wegener-Institut für Polar- und Meeresforschung, Bremerhaven, 1997.
- [2] A. E. Basharinov, L.T.Tuchkov, V.M.Polykov, and H.I.Ananov, editors. *Microwave measurements and plasma emission*. Sovetskoe Radio Publish House, 1968.
- [3] L. M. Brekhovskikh. *Waves in layered media*. Moskow, 1973.
- [4] W. J. Burke, T. Schmugge, and J. F. Paris. Comparison of 2.8- and 21-cm Microwave Radiometer Observations Over Soils with Emission Model Calculations. *Journal of Geophysical Research*, 84(C1):287–294, 1979.
- [5] A. Darovskikh, K.-P. Johnsen, V. Fedotov, K. Tyshko, H. Eicken, and G. Heygster. Growth velocity of freshwater ice and air bubble sizes linked to microwave radiometer measurements. In *The Proceedings of the 14th International Symposium on Ice, in press*. Editor: Hung Tao Shen, Vol.1, No.2, pages 391-395, Potsdam, New York, USA, 1998.

- [6] H. Eicken, M. Lensu, M. Leppaeranta, W.B. Tucker, A. J. Gow, and O. Salmela. Thickness, structure and properties of level summer multiyear ice in the Eurasian sector of the Arctic ocean. *Journal of Geophysical Research*, 100(C11):22697–22710, 1995.
- [7] D.T. Eppler et al. Passive Microwave Signatures of Sea Ice. In F. D. Carsey, editor, *Microwave Remote Sensing of Sea Ice*, Geophysical Monograph 68, chapter 4, pages 47–71. American Geophysical Union, 1992.
- [8] K. Flückiger, H. Gmünder, and C. Mätzler. Microwave Signatures of Sea Ice from ARKTIS 93 Experiment. *EARSEL Adv. Rem. Sens.*, 3:71–80, 1994.
- [9] R. Fuhrhop, G. Heygster, K.-P. Johnsen, P. Schluessel, M. Schrader, and C. Simmer. Study of Passive Remote Sensing of the Atmosphere and Surface Ice. *Final report for ESA Contract No.11198/94/NL/CN and Berichte aus dem Institut für Meereskunde, Kiel, Germany*, 297, 1997.
- [10] R. Fuhrhop, T. C. Grenfell, G. Heygster, K.-P. Johnsen, P. Schluessel, M. Schrader, and C. Simmer. A combined radiative transfer model for sea ice, open ocean, and atmosphere. *Radio Science*, 33(2):303–316, March–April 1998.
- [11] T. C. Grenfell. Surface-based passive microwave studies of multiyear sea ice. *Journal of Geophysical Research*, 97(C3):3485–3501, 1992.
- [12] M. Hallikainen. Physical basis for microwave remote sensing of sea ice and snow. *in:E.Raschke (ed.): Radiation and water in the climate system, NATO ASI Series, Series I: Global environment change*, 45:489–525, 1996.
- [13] M. Hallikainen. Retrieval of sea ice and snow parameters from microwave radiometer and radar data. *in:E.Raschke (ed.): Radiation and water in the climate system, NATO ASI Series, Series I: Global environment change*, 45:527–545, 1996.
- [14] K.-P. Johnsen. *Radiometric Measurements in the Arctic Ocean - Comparison between Theory and Experiment*. PhD thesis, University of Bremen, Germany, 1998.
- [15] M. Lensu, C. Haas, F. Cottier, C. Friedrich, J. Weissenberger, K. Abrahamsson, A. Ekdahl, A. Darovskikh, and K.-P. Johnsen. Arctic '96: Polarstern Ice Station Report. volume 214 of *M-series reports*. Helsinki University of Technology, 1996.
- [16] T. Markus and D. J. Cavalieri. Snow depth distribution over sea ice in the Southern Ocean from satellite passive microwave data. *Antarctic Sea Ice Physical Processes, Interactions and Variability*, AGU Antarctic Research Series, 74. American Geophysical Union, 1998.
- [17] G. A. Maykut. Energy Exchange Over Young Sea Ice in the Central Arctic. *Journal of Geophysical Research*, 83(C7):3646–3658, 1978.
- [18] W. Peake. Interaction of electromagnetic waves with some natural surfaces. *IRE Transactions on Antennas and Propagation*, AP-7:S324–S329, 1959.
- [19] V.F. Radionov, N.N.Bryazgin, and E.I.Aleksandrov, editors. *The Snow Cover of the Arctic Basin*. Hydrometeorological Publishing House, Saint Petersburg, Russia, 1997.
- [20] T. Rother and K. Schmidt. The discrete Mie-formalism for plane-wave scattering on axisymmetric particles. *Journal of Electromagnetic Waves and Applications*, 10:273–297, 1996.
- [21] A. Stogryn. A Study of the Microwave Brightness Temperature of Snow from the Point of View of Strong Fluctuation Theory. *IEEE Transactions on Geoscience and Remote Sensing*, GE-24(2):220–231, March 1986.
- [22] A. Stogryn. An Analysis of the Tensor Dielectric Constant of Sea Ice at Microwave Frequencies. *IEEE Transactions on Geoscience and Remote Sensing*, GE-25:147–158, 1987.
- [23] A. F. Treshnikov. *Atlas Arktiki (in Russian)*. Main Department of Geodesy and Cartography under the Council of Ministers of the USSR, Moscow, 1985.
- [24] W. B. Tucker, D. K. Perovich, A. J. Gow, W. F. Weeks, and M. R. Drinkwater. Physical properties of sea ice relevant to remote sensing. *Microwave Remote Sensing of Sea Ice*, AGU Geophysical Monograph, 68, pages 9–28. 1992.
- [25] F. T. Ulaby, R. K. Moore, and A. K. Fung. *Microwave remote sensing*, volume 1. Artech House, Norwood, MA02062, 1981.
- [26] F. T. Ulaby and W. H. Stiles. The Active and Passive Microwave Response to Snow Parameters - 2. Water Equivalent of Dry Snow. *Journal of Geophysical Research*, 85(C2):1045–1049, 1980.
- [27] D. P. Winebrenner et al. Microwave sea ice signature modeling. In F. D. Carsey, editor, *Microwave Remote Sensing of Sea Ice*, Geophysical Monograph 68, chapter 4, pages 47–71. American Geophysical Union, 1992.
- [28] World Meteorological Organization. WMO Sea-Ice Nomenclature. Technical Report WMO/OMM/BMO – No. 259 Supplement No. 5, World Meteorological Organization, Geneva, April 1989.

# **Appendix A: Surface emissivity data from microwave experiments of the University of Bern**

Christian Mätzler and Andreas Wiesmann

**Purpose:** Surface-based microwave signature studies from 2 to 100 GHz were carried out over years to provide empirical emissivity information for typical surface classes. The surface emissivity  $e_p$  (polarization  $p$ ) was determined from the effective object temperature  $T_{eff}$ , the brightness temperatures  $T_p$  of the object under investigation and of the downwelling sky radiation  $T_{sky}$  in the relevant direction, using the relationship:  $e_p = (T_p - T_{sky})/(T_{eff} - T_{sky})$ , ranging from 0 to 1. The data presented here are based on measurements made with the PAMIR system operating at 4.9, 10.4, 21, 35 and 94 GHz (Mätzler, 1987 to 1994) and with a set of newer portable radiometers at 11, 21, 35, 48 and 94 GHz (Weise, 1996; Wiesmann et al. 1996, Wiesmann et al. 1998, Mätzler et al. 1997). Additional experiments – not reported here – were made with the RASAM instrument, a combined radiometer and scatterometer, operating over the frequency range from 2 to 12 GHz. Data collected with this instrument are reported in a separate catalog (Wegmüller and Mätzler, 1993) which was described by Wegmüller et al. (1994).

**Applications:** To extract emissivity information, either directly from the data catalog or through a fast, empirical model, and to test microwave emissivity models.

## **References**

- Mätzler C. "Applications of the Interaction of Microwaves with the Natural Snow Cover", *Remote Sensing Reviews*, Vol. 2, pp. 259-392 (1987).
- Mätzler C. "Seasonal evolution of microwave radiation from an oat field", *Remote Sensing Environment* Vol. 31, pp. 161-173 (1990).
- Mätzler C. "Microwave transmissivity of a forest canopy: Experiments made with a beech", *Remote Sensing of Environment*, Vol. 48, pp. 172-180 (1994).
- Mätzler C. "Passive microwave signature catalog 1989-1992" (Vol.1), IAP-Report, Feb. (1993), Vol. 2. May 1994, Vol. 3, July (1994).
- Mätzler C. "Passive microwave signatures of landscapes in winter", *Meteorology and Atmospheric Physics*, Vol. 54, pp. 241-260 (1994).
- Mätzler C., T. Strozzi, T. Weise, D. Floricioiu and H. Rott, "Microwave snowpack studies made in the Austrian Alps during the SIR-C/X-SAR experiment", *Internat. J. Remote Sensing*, Vol. 18, pp. 2505-2530 (1997).
- Wegmüller U. and C. Mätzler, "Active and passive microwave signature catalogue (2-12 GHz)", IAP-Bericht, März (1993).
- Wegmüller U., C. Mätzler, R. Hüppi und E. Schanda, "Active and passive microwave signature catalogue on bare soil (2-12 GHz)", *IEEE Trans. Geoscience and Remote Sensing*, Vol. 32(3), pp. 698-702 (1994).
- Weise T. "Radiometric Data (11-94 GHz) and Autocorrelation functions of dry snow samples", Res. Report No. 96-2, Institute of Applied Physics, Univ. of Bern (1996).
- Wiesmann A., T. Strozzi and T. Weise, "Passive microwave signature catalogue of snowcovers at 11, 21, 35, 48 and 94 GHz", Res. Report No. 96-8, Institute of Applied Physics, Univ. of Bern (1996).
- Wiesmann A., C. Mätzler and T. Weise, "Radiometric and structural measurements of snow samples", *Radio Science*, Vol. 33, pp. 273-289 (1998).

## Instrument characteristics

PAMIR main system parameters, for more details, see Mätzler (1987); the portable radiometers have similar characteristics with an additional frequency at 48 GHz.

Variables: frequency: 5 selectable, any incidence angle selectable: 50° to 55°, full-beam width 9° to 10°, polarization: linear h,v, and intermediate values	4.9 GHz	10.4 GHz	21 GHz	35 GHz	94 GHz
Measurement precision, $\Delta T$ (K), at integration time of 1 s	0.1	0.1	0.1	0.1	0.2
Expected absolute error of brightness temperatures $T_v$ , $T_h$ (K)	1	1	1	1	2
Expected error of mean emissivity $e_p = (T_p - T_{sky})/(T_{eff} - T_{sky})$ , $p=h,v$	0.005	0.005	0.005	0.005	0.01
Expected error of polarization difference, $e_v - e_h$	0.003	0.002	0.002	0.002	0.005

## Standard ground-truth parameters

WE (mm)	Water Equivalent depth of snowpack (equivalent height of water column)
Hsnow (cm)	Snow height
dw (mm)	Equivalent depth of vegetation canopy water, also known as canopy water content
h (cm)	Height of vegetation canopy
mg	Gravimetric soil moisture (water mass/dry-soil mass)
$\epsilon'$	Real part of relative dielectric constant of the top 8 mm soil at about 1 GHz
$\rho$ (g/cm <sup>3</sup> )	Dry soil density
Teff (C)	Effective temperature of surface used to compute the emissivity
Tair, Tveg, Tsoil (C)	Air, vegetation and soil temperature, respectively

## Test sites, objects and data

### Object classes and test sites

Object Class	Test Site	Object-class description
YOUNG BARLEY	Tannacker, agricultural field in	7 situations of green winter barley crop in spring 1990, height from 15 to 100 cm, T>3°C
YOUNG OAT	Mosseedorf, near Bern, Switzerland Long.: 7.48° E	17 situations of green oat crop in spring 1989, height from 16 to 84 cm, T>7°C (Mätzler, 1990)
UNFROZEN GRASS		Combines the classes of unfrozen grass: SHORT, MEDIUM and HIGH
SHORT GRASS	Lat.: 47.0° N Altitude: 570 m a.s.l., sandy-loam soil, dry-soil density: 0.9 to 1.2 g/cm³	9 situations with grass cover, height 5 - 10 cm, volumetric soil moisture 13% to 60%, grass temperature above -1°C.
MEDIUM GRASS		4 situations of grass cover with height between 15 and 32 cm, T <sub>veg</sub> > 5°C.
HIGH GRASS		6 situations of grass cover with height between 32 and 55 cm, T <sub>veg</sub> > 10°C.
GRASS AFTER SNOW	pixel size: 1 m²	2 situations, just after snowmelt, when short grass was still pressed to the wet ground
FROST GRASS		3 situations of short grass with hoar frost at temperatures between -5°C and -2°C, frozen soil at -2 to -0.8°C.
FROZEN GRASS		4 situations of short, frozen grass without hoar frost at temperatures from -5 to -1.7°C, soil at -2 to 0°C (one situation with unfrozen soil).
FROZEN SOIL		2 situations of frozen, bare soil with surface temperatures of -6°C and -1°C, respectively, mostly frozen soil moisture of about 40% by volume, see low ε' at 1GHz.
BARE SOIL		9 situations of unfrozen, bare sandy-loam soil at temperatures between 0 and 25°C, volumetric soil moisture between 12% and 45%, roughness height about 1 cm.
POWDER SNOW		5 situations of 8 to 37 cm deep powder snow of Dec. 1990 and Nov. 1993 at T from -3 to -13°C, with WE up to 5 cm. The grass-covered soil was unfrozen, except for 1 case. Most of the dry snow was 1 to 7 days old.
THIN CRUST		5 situations in Nov. and Dec. 1990 of thin refrozen crusts on wet snow.
BOTTOM CRUST		2 situations of aged, refrozen snow (depths of 6 and 15 cm) on short grass and frozen ground.
WET SNOW		4 situations of wet snow on short grass and unfrozen ground
SLF_BARE	SLF: Acronym for alpine test site of Swiss Snow and Avalanche Research Institute, Weissfluhjoch Davos:	9 situations of the snow-free test site in wet and dry, unfrozen condition
SLF_BOTTOMCRUST	T	6 situations of a special snow situation observed in late 1984 and early 1985. An abundant snow fall in autumn 1984 metamorphosed to a 40 cm thick, hard crust and formed the bottom of the new winter snowcover. The crust was frozen to the ground, and subsequently covered by new snow.
SLF_DEEP	Lat. 48.83° N, Long. 9.81° E, Alt. 2560 m a.s.l., Ground: rocky serpentine soil.	50 situations of deep winter snow with WE between 25 and 63 cm
SLF_MEDIUM		12 situations of winter snow with WE between 10 and 25 cm
SLF_SHALLOW		11 situations of winter snow with water equivalents (WE) between 4 and 10 cm. Winter snow is dry, and it has not undergone melt metamorphism
SLF_THICKCRUST	pixel size: 10 m²	15 situations of wet snow covered by a 4 to 30 cm thick layer of refrozen snow
SLF_THINCRUST		20 situations of wet snow covered by a refrozen crust whose thickness is between 1 and 3 cm
SLF_WET		53 situations of wet snow, i.e. there was at least a wet surface layer

Mean values of ground-truth observed in each object class

Object Class	dw(mm)	h(cm)	Tveg(C)	mg(%)	$\rho$ (g/cm <sup>3</sup> )	Tsoil(C)	$\epsilon'$ soil	Tsnow(C)	Hsnow(cm)	WE(cm)	Tair(C)	Teff(C)
YOUNG BARLEY	1.94	47.2	11.3	30.6	1.22	11.3	22.9		0	0	11.4	11.1
YOUNG OAT	1.18	39.8	17.1	23.5	1.02	17.4	13.9		0	0	16.6	17.5
UNFROZEN GRASS	1.23	20.6	10.2	30.8	1.2	10.9	22.8		0	0	10.8	10.4
SHORT GRASS	0.71	8.9	5.9	36.1	1.21	6.6	29.4		0	0	6.1	6.2
MEDIUM GRASS	1.2	23.2	9.1	34.3	1.2	9.9	24.6		0	0	10.1	9.3
HIGH GRASS	2.23	44.1	18.1	16.8	1.18	18.7	5.4		0	0	19.9	18.3
GRASS AFTER SNOW	0.4	5	2.8	37.1	1.24	2.7	30.5		0	0	4.6	3.3
FROST GRASS	0.97	8.3	-3.7	37.8	1.23	-1.3	5.2		0.1	0.01	-2.5	-2.6
FROZEN GRASS	0.95	8.5	-3.2	44.3	1.22	-1.2	9.1		0	0	-2.7	-2.3
FROZEN SOIL	0.03	10	-4	33.3	1.15	-3.6	4.4		0.1	0.01	-5.1	-3.6
BARE SOIL	0.01	4.8	11.3	31.4	1.06	11.2	12.7		0	0	12	11.1
POWDER SNOW	0.48	7	-1.2	37.4	1.2	0	14.1	-8.4	24.1	3.65	-4.8	-1
THIN CRUST	0.4	5.8	-1.1	35	1.2	-0.2	5.2	-4.3	11	1.83	-2.4	-0.9
BOTTOM CRUST	0.75	6.5	-1.5	39.3	1.16	-0.7		-5.2	11	2.9	-1.3	-0.9
WET SNOW	0.4	8	0	35	1.2	0		0.0	14.3	3.06	2.3	0
SLF_BARE	0	0				8.4			0	0		8.4
SLF_BOTTOMCRUST	0	0						0		28.17		-3.9
SLF_DEEP	0	0						-6.6		44.94		-3.2
SLF_MEDIUM	0	0						-6		18.75		-3.2
SLF_SHALLOW	0	0						-4.1		7.32		-2
SLF_THICKCRUST	0	0						0		>10		-1.2
SLF_THINCRUST	0	0						-0.3		>10		-0.2
SLF_WET	0	0						-0.3		>10		-0.2

### Standard deviations of ground-truth observed in each object class

Object Class	Dw(mm)	h(cm)	Tveg(C)	mg(%)	p(g/ cm <sup>3</sup> )	Tsoil(C)	ε' soil	Tsnow(C)	Hsnow(cm)	WE(cm)	Tair(C)	Teff(C)
YOUNG BARLEY	1.5	33.7	3.7	4.7	0.04	3.5	2.2		0	0	4.8	3.8
YOUNG OAT	1.43	21.6	4.9	6.3	0.02	5.1	6.3		0	0	4.7	5.2
UNFROZEN GRASS	0.84	15.7	8.7	12	0.07	8.6	11.2		0	0	8.4	8.6
SHORT GRASS	0.26	2.2	8.1	9.1	0.09	7.9	3.6		0	0	6.2	7.9
MEDIUM GRASS	0.48	6.8	2.6	3.8	0.07	2.5			0	0	3.8	2.7
HIGH GRASS	0.98	7.7	6.4	9.3	0.04	6.1			0	0	6.9	6.3
GRASS AFTER SNOW	0.01	0	1.7	3.3	0.06	1	4.9		0	0	0.6	1.1
FROST GRASS	0.12	1.2	1.5	5.9	0.05	0.6			0	0	1.3	0.9
FROZEN GRASS	0.1	1	1.5	7.1	0.05	0.9	7.9		0	0	2.1	0.8
FROZEN SOIL	0	0	4.2	5.2	0.07	3.8	0.1		0.1	0.01	3.3	3.8
BARE SOIL	0.01	4.4	4.5	4.6	0.1	4.5	5.2		0	0	5.5	4.5
POWDER SNOW	0.18	4.5	0.5	5.4	0	0.3	9.8	4.7	10.3	1.94	2.7	0.2
THIN CRUST	0	1.1	0.4	0	0	0.3		2.2	6	1.22	1.3	0.4
BOTTOM CRUST	0.49	2.1	0.7		0.16	0.6		0.3	7.1	1.56	0.4	0.4
WET SNOW	0	4.8	0	0	0	0		0.0	8.2	1.59	2.2	0
SLF_BARE	0	0				4.2			0	0		4.2
SLF_BOTTOMCRUST	0	0								4.02		0.8
SLF_DEEP	0	0						5.6		11.95		1
SLF_MEDIUM	0	0						4.8		4.94		1
SLF_SHALLOW	0	0						2.6		2.44		1.1
SLF_THICKCRUST	0	0						0.2		>10		0
SLF_THINCRUST	0	0						0.9		>10		0
SLF_WET	0	0						0.9		>10		0

## Mean values of emissivities and of emissivity combinations of object classes based on PAMIR data, incidence angle 50°

Object class	4.9h	10.4h	21h	35h	94h	4.9v	10.4v	21v	35v	94v	4.9v-h	10v-h	21v-h	35v-h	94v-h	10v-5v	21v-10v	35v-21v	94v-35v	94v-21v	Comb*					
WATER-0-C	0.249	0.267	0.308	0.358	0.493	0.501	0.528	0.59	0.657	0.806	0.251	0.262	0.282	0.299	0.313	0.017	0.041	0.05	0.135	0.028	0.061	0.068	0.149	0.217	0.456	
YOUNG BARLEY	0.909	0.966	0.958	0.962	0.963	0.956	0.966	0.953	0.954	0.959	0.046	0	-0.005	-0.008	-0.004	0.057	-0.008	0.004	0.001	0.01	-0.012	0.001	0.005	0.006	0.022	
YOUNG OAT	0.904	0.936	0.95	0.941	0.949	0.952	0.948	0.943	0.937	0.949	0.046	0.012	-0.007	-0.005	0	0.027	0.014	-0.009	0.008	-0.005	-0.005	-0.006	0.012	0.006	0.036	
UNFROZEN GRASS	0.933	0.952	0.946	0.943	0.941	0.952	0.958	0.944	0.942	0.948	0.019	0.006	-0.001	-0.001	0.007	0.019	-0.006	-0.003	-0.002	0.006	-0.014	-0.002	0.006	0.004	0.053	
SHORT GRASS	0.912	0.947	0.944	0.946	0.946	0.939	0.956	0.943	0.943	0.951	0.027	0.009	-0.001	-0.002	0.005	0.035	-0.003	0.002	-0.001	0.017	-0.013	0	0.007	0.008	0.044	
MEDIUM GRASS	0.948	0.95	0.94	0.935	0.933	0.959	0.956	0.941	0.937	0.944	0.01	0.006	0.001	0.001	0.011	0.002	-0.01	-0.005	-0.003	-0.003	-0.015	-0.004	0.007	0.003	0.055	
HIGH GRASS	0.967	0.961	0.95	0.939	0.936	0.97	0.961	0.946	0.939	0.941	0.004	0	-0.004	0	0.006	-0.005	-0.011	-0.011	-0.003	-0.009	-0.015	-0.008	0.003	-0.005	0.084	
GRASSAFTER SNOW	0.902	0.91	0.901	0.902	0.905	0.912	0.925	0.905	0.91	0.92	0.01	0.014	0.004	0.008	0.015	0.009	-0.009	0	0.004	0.012	-0.02	0.005	0.01	0.015	0.071	
FROST GRASS	0.918	0.958	0.95	0.938	0.907	0.948	0.966	0.952	0.942	0.926	0.03	0.008	0.002	0.005	0.02	0.04	-0.008	-0.012	-0.012	-0.031	0.018	-0.014	-0.009	-0.016	-0.025	0.085
FROZEN GRASS	0.919	0.962	0.959	0.955	0.937	0.95	0.967	0.956	0.952	0.948	0.031	0.006	-0.003	-0.003	0.011	0.043	-0.003	-0.004	-0.018	0.018	-0.011	-0.004	-0.008	-0.005	0.045	
FROZEN SOIL	0.891	0.953	0.951	0.938	0.94	0.958	0.958	0.958	0.952	0.95	0.049	0.005	0.007	0.001	0.012	0.062	-0.002	0	-0.012	0.018	0	-0.006	-0.001	-0.008	0.031	
BARE SOIL	0.725	0.82	0.888	0.887	0.92	0.874	0.888	0.91	0.903	0.934	0.149	0.068	0.022	0.016	0.014	0.095	0.068	-0.002	0.033	0.014	0.022	-0.007	0.031	0.024	0.063	
POWDER SNOW	0.895	0.921	0.928	0.909	0.777	0.94	0.954	0.952	0.943	0.841	0.046	0.033	0.024	0.034	0.064	0.026	0.008	0.012	-0.161	0.013	-0.001	-0.008	-0.123	-0.112	0.126	
THIN CRUST	0.877	0.861	0.816	0.787	0.631	0.923	0.941	0.91	0.853	0.658	0.046	0.08	0.094	0.066	0.027	-0.016	-0.045	0.03	-0.156	0.018	-0.031	-0.057	-0.196	-0.252	0.503	
BOTTOM CRUST	0.882	0.919	0.85	0.708	0.443	0.945	0.954	0.898	0.753	0.466	0.063	0.034	0.048	0.046	0.023	0.037	-0.007	-0.142	-0.265	0.009	-0.056	-0.145	-0.287	-0.432	0.729	
WET SNOW	0.755	0.844	0.839	0.86	0.892	0.947	0.968	0.955	0.945	0.193	0.123	0.116	0.09	0.054	0.09	-0.005	0.021	0.031	0.021	-0.013	-0.004	-0.005	-0.009	0.381		
SLF_BARRE	0.778	0.855	0.904	0.911	0.915	0.89	0.92	0.938	0.942	0.938	0.112	0.065	0.033	0.031	0.023	0.077	0.049	0.007	0.01	0.03	0.017	0.004	0.003	0	0.035	
SLF_BOTTOMCRUST	0.822	0.767	0.705	0.615	0.648	0.939	0.922	0.829	0.699	0.733	0.117	0.155	0.123	0.083	0.085	-0.055	-0.062	-0.09	0.033	-0.017	-0.093	-0.13	0.034	-0.005	1.031	
SLF_DEEP	0.843	0.803	0.78	0.715	0.658	0.943	0.94	0.898	0.813	0.728	0.101	0.137	0.119	0.098	0.071	-0.04	-0.023	-0.065	-0.04	-0.004	-0.041	-0.086	-0.063	-0.158	0.734	
SLF_MEDIUM	0.85	0.831	0.771	0.682	0.612	0.937	0.938	0.893	0.785	0.669	0.086	0.107	0.122	0.103	0.057	-0.019	-0.06	-0.089	-0.073	0.001	-0.045	-0.108	-0.11	-0.22	0.79	
SLF_SHALLOW	0.865	0.847	0.833	0.768	0.672	0.934	0.938	0.921	0.848	0.638	0.069	0.092	0.088	0.08	0.016	-0.018	-0.014	-0.065	-0.104	0.004	-0.017	-0.073	-0.17	-0.231	0.53	
SLF_THICKCRUST	0.909	0.952	0.878	0.677	0.472	0.983	0.99	0.931	0.709	0.486	0.073	0.038	0.053	0.032	0.026	0.043	-0.074	-0.202	-0.206	0.007	-0.059	-0.222	-0.223	-0.445	0.965	
SLF_THINCRUST	0.901	0.938	0.942	0.9	0.707	0.967	0.984	0.976	0.938	0.744	0.066	0.046	0.034	0.038	0.036	0.037	0.004	-0.042	-0.195	0.017	-0.008	-0.037	-0.197	-0.233	0.255	
SLF_WET	0.812	0.871	0.91	0.921	0.906	0.954	0.975	0.971	0.941	0.143	0.104	0.066	0.05	0.035	0.059	0.039	0.012	-0.005	0.02	0	-0.004	-0.022	-0.03	-0.023		

\*: The parameter, COMB, is defined as an optimal linear combination of emissivities for snow discrimination (Mätzler, 1994):  

$$\text{COMB} = e_{\nu}(10.4) - e_h(10.4) + e_{\nu}(21) - e_h(21) + e_{\nu}(35) - e_h(35) + 3[e_{\nu}(10.4) - e_h(35)]$$

**Standard deviations of emissivities and of emissivity combinations of object classes based on PAMIR data, incidence angle 50°**

Object class	4.9h	10.4h	21h	35h	94h	4.9v	10.4v	21v	35v	94v	4.9v-h	10v-h	21v-h	35v-h	94v-h	10v-5v	21v-10v	35v-21v	94v-35v	94v-21v	Comb*	
WATER:0-8C	0.001	-0.007	-0.018	-0.028	-0.033	0.001	-0.01	-0.026	-0.035	-0.031	0	-0.004	-0.008	-0.003	0.002	-0.007	-0.012	-0.009	-0.006	-0.011	-0.016	
YOUNG BARLEY	0.059	0.036	0.032	0.024	0.018	0.026	0.014	0.013	0.012	0.066	0.022	0.02	0.011	0.007	0.055	0.005	0.009	0.007	0.013	0.003	0.005	
YOUNG OAT	0.057	0.029	0.015	0.015	0.018	0.013	0.011	0.01	0.012	0.039	0.018	0.005	0.006	0.004	0.028	0.02	0.006	0.007	0.008	0.006	0.006	
UNFROZEN GRASS	0.039	0.014	0.013	0.016	0.017	0.009	0.011	0.01	0.014	0.031	0.009	0.006	0.006	0.029	0.011	0.008	0.009	0.013	0.007	0.006	0.009	
SHORT GRASS	0.04	0.013	0.011	0.01	0.009	0.01	0.008	0.01	0.008	0.01	0.038	0.011	0.007	0.005	0.004	0.029	0.01	0.006	0.009	0.007	0.004	
MEDIUM GRASS	0.006	0.009	0.01	0.012	0.022	0.001	0.003	0.007	0.008	0.016	0.006	0.007	0.007	0.008	0.006	0.004	0.003	0.005	0.003	0.005	0.008	
HIGH GRASS	0.012	0.013	0.018	0.017	0.022	0.01	0.012	0.015	0.015	0.022	0.011	0.005	0.003	0.004	0.003	0.012	0.015	0.007	0.01	0.009	0.01	
GRASSAFTER SNOW	0.013	0.004	0.004	0.006	0.007	0.007	0.002	0.005	0.002	0.006	0.006	0.006	0.006	0.006	0.001	0	0.009	0.001	0.002	0	0.009	
FROST GRASS	0.007	0.006	0.004	0.004	0.008	0.005	0.004	0.001	0.006	0.009	0.002	0	0.005	0.001	0.004	0.003	0.003	0.005	0.004	0.003	0.003	0.003
FROZEN GRASS	0.022	0.008	0.004	0.006	0.009	0.012	0.006	0.004	0.004	0.008	0.015	0.004	0.002	0.004	0.004	0.015	0.007	0.007	0.004	0.006	0.003	0.002
FROZEN SOIL	0.002	0.004	0.009	0.001	0.001	0.005	0.002	0.01	0.001	0.001	0.007	0.002	0	0.001	0	0.001	0.006	0.009	0	0.007	0.008	0.001
BARE SOIL	0.07	0.052	0.036	0.039	0.031	0.033	0.03	0.022	0.026	0.021	0.039	0.023	0.015	0.014	0.011	0.031	0.024	0.016	0.019	0.011	0.012	0.012
POWDER SNOW	0.038	0.03	0.018	0.026	0.067	0.005	0.009	0.009	0.011	0.047	0.034	0.022	0.017	0.015	0.022	0.023	0.024	0.02	0.037	0.005	0.005	0.018
THIN CRUST	0.053	0.056	0.074	0.083	0.133	0.02	0.013	0.021	0.05	0.132	0.036	0.046	0.056	0.034	0.008	0.016	0.025	0.024	0.054	0.012	0.014	0.037
BOTTOM CRUST	0.01	0.018	0.08	0.097	0.015	0.004	0.002	0.042	0.088	0.002	0.006	0.016	0.038	0.009	0.013	0.008	0.062	0.017	0.112	0.003	0.04	0.046
WET SNOW	0.016	0.028	0.028	0.017	0.016	0.008	0.008	0.012	0.009	0.005	0.01	0.026	0.018	0.024	0.018	0.026	0.038	0.036	0.003	0.008	0.005	0.006
SLF_BARRE	0.025	0.023	0.016	0.021	0.038	0.018	0.02	0.017	0.019	0.039	0.011	0.01	0.013	0.008	0.002	0.02	0.011	0.014	0.008	0.012	0.008	0.009
SLF_BOTTOMCRUST	0.009	0.013	0.012	0.049	0.084	0.004	0.008	0.011	0.034	0.072	0.009	0.016	0.008	0.021	0.021	0.01	0.015	0.051	0.044	0.005	0.005	0.039
SLF_DEEP	0.026	0.041	0.048	0.064	0.104	0.011	0.012	0.005	0.064	0.111	0.021	0.033	0.022	0.02	0.029	0.033	0.034	0.037	0.12	0.011	0.026	0.037
SLF_MEDIUM	0.015	0.035	0.063	0.042	0.091	0.006	0.012	0.03	0.043	0.105	0.015	0.027	0.051	0.043	0.019	0.024	0.032	0.04	0.076	0.01	0.02	0.03
SLF_SHALLOW	0.02	0.022	0.031	0.053	0.141	0.007	0.005	0.014	0.048	0.148	0.016	0.018	0.021	0.015	0.028	0.021	0.029	0.039	0.141	0.007	0.013	0.041
SLF_THICKCRUST	0.032	0.022	0.055	0.102	0.047	0.006	0.005	0.037	0.104	0.069	0.031	0.022	0.029	0.011	0.028	0.042	0.045	0.059	0.109	0.005	0.036	0.07
SLF_THINCRUST	0.054	0.031	0.023	0.043	0.136	0.023	0.01	0.008	0.039	0.14	0.044	0.025	0.02	0.015	0.026	0.061	0.04	0.034	0.111	0.018	0.01	0.033
SLF_WET	0.072	0.07	0.053	0.042	0.042	0.021	0.018	0.016	0.015	0.036	0.059	0.06	0.041	0.035	0.021	0.062	0.045	0.03	0.062	0.015	0.009	0.012

### Example of data taken with the portable radiometers

Date: 17 January 1996, Test-Site: Weissfluhjoch (positions 1-7),

Object: dry winter snow, consisting of 3 layers

Frequency: 11, 21, 35, 94 GHz

Weather: Sunny

Air temperature (10:30): -2.1°C

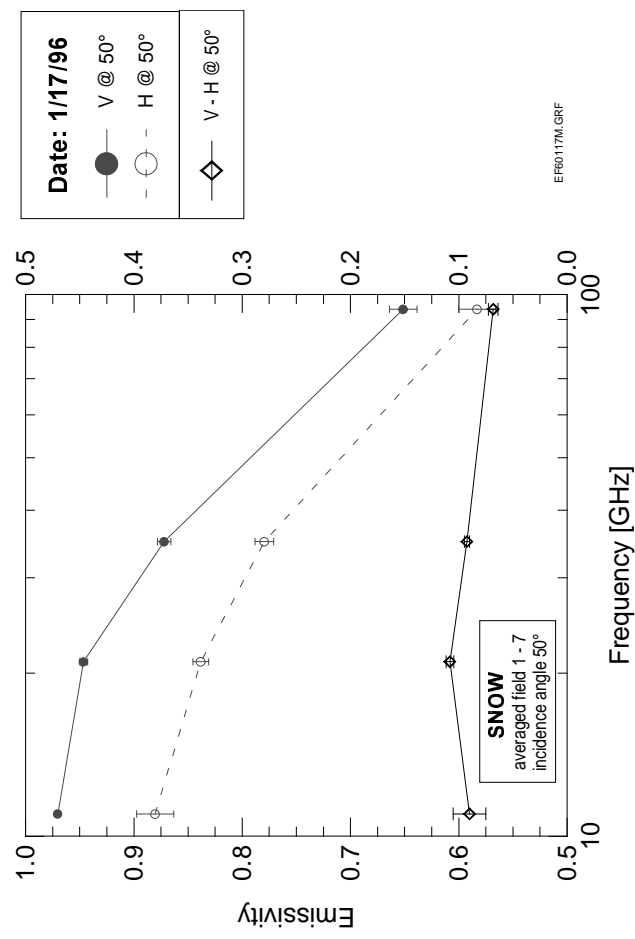
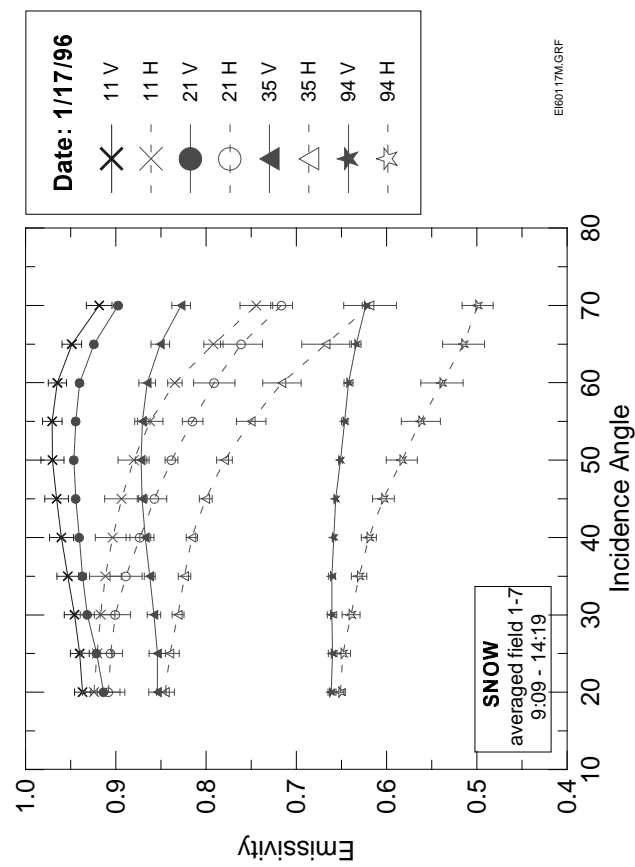
Surface roughness height < 1cm

Comments: plots of emissivity versus incidence angle (left) and versus frequency (right),  
 average values and std dev. from 7 scans at H and V polarization, frequency in GHz  
 according to key.

Snow vertical profile information:

	Height [m]	Grain Shape	Date	Dens.[kg/m <sup>3</sup> ]	$\epsilon'$	W [%]
0.50 - 0.68	/ \		15.01.96	244	1.43	0
0.25 - 0.50	● ●		15.01.96	335	1.59	0
0.00 - 0.25	Λ Λ		15.01.96	295	1.53	0

Hsnow (radiometer position): 63 cm, Hsnow (profile): 68 cm  
 Hsnow (radiometer position): 63 cm, Hsnow (profile): 68 cm  
 Temp. [°C] (Height [cm]) (14:30): -13.0° (68), -7.6° (60), -7.1° (50), -6.6° (40), -5.0°  
 (30), -3.4° (20), -2.2° (10), -1.6° (0)



## **Appendix B: Surface emissivity data from PORTOS-Avignon experiment**

André Chanzy, Jean-Pierre Wigneron, Jean -Christophe. Calvet, Laurent Laguerre and Suresh Raju

The data displayed in the following table were collected at the INRA research Centre near Avignon (43°55'N, 4°53'E, south of France) in 1993. Emissivity values were estimated from the measurements made by the PORTOS radiometer (Chanzy et al. 1994). The atmospheric and sky contributions were removed from the brightness temperature measured by PORTOS by an algorithm described in Calvet et al., 1995. Atmospheric and sky contributions were estimated using the outputs of the Météo-France 15 levels weather forecast model PERIDOT and the cloud observations made at the experimental site along with the radiometric acquisitions. The surface effective temperature was estimated by the skin temperature measured by a thermal infrared radiometer. The expected error in microwave emissivities is +/- 0.015.

All the measurements were made on a silty clay loam soil (27% of Clay, 11% of Sand). For each surface type, a set of three moisture conditions (wet, medium wet and dry) were gathered in the table in order to give the range of emissivity variations due to the soil moisture. Measurements of the surface characteristics (soil moisture, surface roughness and vegetation) are given in the table for each set of microwave measurements (one line in the table) since measurements at all radiometric configurations were collected together.

The whole Avignon 93 database is available on a CD (Chanzy et al., 1999), which can be obtained upon request (contact : [achanzy@avignon.inra.fr](mailto:achanzy@avignon.inra.fr)). The database includes a very large data set in terms of incidence, moisture, surface roughness, biomass and detailed ground truth data (detailed vegetation description, soil characteristics, water balance for the wheat surface, climatic measurements).

### **References**

- Calvet J.-C., J.-P. Wigneron, A. Chanzy, Suresh Raju and L. Laguerre, "Microwave dielectric properties of a silt loam at high frequencies", IEEE Trans. on Geoscience and Remote Sensing, Vol. 33, pp. 634-642 (1995a).
- Chanzy A., D. Haboudane, J.-P. Wigneron, J.-C. Calvet and O. Grosjean, " Radiométrie micro-onde sur divers types de couverts végétaux : influence de l'humidité du sol." in : Colloque International ISPRS Mesures physiques et signatures en télédétection, Val d'Isère (FRA), 1994/01/17-21, pp. 505-512, (1994).
- Chanzy A., J.-P. Wigneron, J.-C. Calvet, L. Laguerre and Suresh Raju, "Avignon 93 data base of passive microwave measurements collected from 1.4 to 90 GHz on various agricultural surfaces", letter submitted to International Journal of Remote Sensing (1999).

Emissivity measurements collected over agricultural surfaces with bare soil and vegetation covers at  $\theta = 40^\circ$

Veg. Type	Veg. water content ( $\text{kg/m}^2$ )	Surface observation	HRMS (mm)	Correl. length (mm)	Soil wat. content (0-5mm) ( $\text{m}^3/\text{m}^3$ )	Emiss. 1.4 GHz	Emiss. 5.05 GHz	Emiss. 10.65 GHz	Emiss. 23.8 GHz	Emiss. 36.5 GHz	Emiss. 90 GHz	Emiss. 90 V-pol
Bare	0	Very rough	60	72	0.247	0.83	0.91	0.80	0.84	0.84	0.87	0.89
Bare	0	Very rough	60	72	0.117	0.86	-	0.86	0.88	0.89	0.89	-
Bare	0	Very rough	60	72	0.011	0.91	0.95	0.90	0.92	0.93	0.94	0.95
Bare	0	Rough	19	66	0.311	0.75	0.88	0.79	0.86	0.82	0.85	0.83
Bare	0	Rough	19	66	0.132	0.82	0.93	0.83	0.90	0.86	0.89	0.87
Bare	0	Rough	19	66	0.014	0.90	0.95	0.93	0.90	0.94	0.93	0.94
Bare	0	Smooth	8	31	0.364	0.56	0.70	0.74	0.78	0.76	0.82	0.77
Bare	0	Smooth	8	31	0.189	0.75	-	-	0.85	-	0.86	-
Bare	0	Smooth	8	31	0.065	0.80	0.91	0.86	0.94	0.89	0.94	0.91
Bare	0	Very smooth	5	206	0.365	0.51	0.74	0.51	0.71	0.55	0.72	0.54
Bare	0	Very smooth	5	206	0.127	0.70	0.82	0.72	0.87	0.76	0.89	0.75
Bare	0	Very smooth	5	206	0.021	0.85	0.96	0.85	0.96	0.89	0.89	0.78
Wheat	1.9	green veg.	6	93	0.314	0.74	0.92	0.95	0.96	0.95	0.96	0.97
Wheat	2.6	green veg.	6	93	0.240	0.80	0.95	0.94	0.95	0.96	0.96	0.96
Wheat	2.6	green veg.	6	93	0.152	0.83	0.99	0.95	0.97	0.97	0.98	0.97
Wheat	1.2	Senescent	6	93	0.031	0.74	-	0.88	0.92	0.95	0.98	0.97
Wheat	1.1	Senescent	6	93	0.315	0.63	0.87	0.86	0.92	0.96	0.98	0.97
Wheat	1.1	Senescent	6	93	0.200	0.65	0.88	0.85	0.92	0.95	0.97	0.95
Sorgho	0.23	Sparse veg.	5	63	0.203	0.68	0.85	0.71	0.79	0.73	0.83	0.72
Sorgho	0.29	Sparse veg.	5	63	0.059	0.78	0.93	0.84	0.91	0.87	0.91	0.87
Sorgho	0.61	Sparse veg.	6	76	0.25	0.70	-	0.78	0.82	0.87	0.84	0.88
Sorgho	0.77	Sparse veg.	6	76	0.07	0.82	0.93	0.90	0.92	0.91	0.93	0.90

## **Appendix C: Members and Addresses**

### **COST 712, Project 1 Members**

#### **Subgroup: Spectroscopy, refraction and radiative transfer of the clear atmosphere**

Agnes Bauer, URA CNRS 249, Université Sciences et Tech. de Lille, F-59655 Villeneuve d'Ascq Cedex , Tel. +33 3 2043 4789; Fax: +33 3 2033 7020; email: bauer@lsh.univ-lille1.fr

Dietrich Feist, Institute of Applied Physics, University of Bern, Sidlerstr. 5, CH-3012 Bern, Tel. +41 31 631 86 78, Fax: +41 31 631 37 65, email: dietrich.feist@mw.iap.unibe.ch

Nicole Jacquinet-Husson, LMD/CNRS Ecole Polytechnique, F-91128 Palaiseau Cedex, Tel. + 33 1 69 33 48 02, Fax: + 33 1 69 33 30 05, E-Mail : husson@ara01.polytechnique.fr

Paul Ingmann, ESA - ESTEC, VRA, Postbus 299, NL 2200 AG Noordwijk zh  
Tel. +31 71 565 4459, Fax: +31 71 565 5675, email: pingmann@jw.estec.esa.nl

Peter Rayer, UK Meteorological Office, London Road, Bracknell RG12 2SZ, UK  
Tel: +44 1344 854106, Fax: + 44 1344 854026, Email: pjrayer@meto.gov.uk

Philip W. Rosenkranz, MIT, 77 Massachusetts Av., Rm. 26-343, Cambridge MA 02139 USA;  
Tel. +1 617 253 3073, Fax: +1 617 258 7864, email: pwr@mit.edu

#### **Subgroup: Clouds and precipitation**

Peter Bauer, Deutsches Zentrum für Luft und Raumfahrt, Linder Höhe, D-51170 Köln,  
Tel. +49 2203 601 2995; Fax: +49 2203 68309; email: peter.bauer@dlr.de

Harald Czekala, Meteorologisches Institut, Universität Bonn, Auf dem Huegel 20,  
D-53121 Bonn, Tel: +49 228 735194; Fax +49 228 735188; email: hczechala@uni-bonn.de

David C. Jones, UK Met.Office, Satellite Image Applic., R315, London Rd, Bracknell, RG12 2SZ,  
UK, Tel: +44 1344 854072, Fax: +44 1344 854412, email: dcjones@meto.gov.uk

Frank S. Marzano, University of Rome "La Sapienza", Dept. El. Eng., Via Eudossiana 18, I-00184 Roma, Tel:+39 6 44585408; Fax: +39 6 4742647; email: franko@ing.univaq.it

Alberto Mugnai, Istituto di Fisica dell' Atmosfera, P. Luigi Sturzo 31, I-00144 Roma  
Tel. +39 06591 5790, Fax: +39 06591 7625, email: mugnai@sung3.ifs.ri.cnr.it

Clemens Simmer, Meteorologisches Institut, Universität Bonn, Auf dem Huegel 20, D-53121 Bonn,  
Tel: +49 228 735190; Fax: +49 228 735188; email: csimmer@uni-bonn.de

Stephen English, Meteorological Office, London Road, Bracknell RG12 2SZ, UK  
Tel. +44 1344 854652 Fax:+ 44 1344 854026, email: senglish@meto.gov.uk

Pedro Baptista, ESA-ESTEC, PO Box 299, NL-2200 AG Noordwijk  
Tel. +31-71-5654319, Fax: +31-71 5654999, email: pedro@xe.estec.esa.nl

Alessandra Tassa, Istit. di Fisica dell'Atmosfera/CNR, Via Fosso del Cavaliere, I- 00133 Roma  
Tel. +39-06-4993 4333, Fax: +39-06-2066 0291, email: sandra@sunifa2.ifs.ri.cnr.it

### **Subgroup: Surface emissivity**

André Chanzy, INRA-Unité Sci. du Sol, Dom. Saint Paul, Site Agroparc, F-84914 Avignon Cedex 9  
Tel: +33 4 90 31 61 29, Fax: +33 4 90 31 62 44, email: achanzy@avignon.inra.fr

Laurence Eymard, CETP/IPSL/CNRS, U. St Quentin-Versailles, 10-12 ave de l'Europe, 78140 Velizy, France, Tel. +33 13925 4902, Fax: +33 13925 4922, email: laurence.eymard@cetp.ipsl.fr

Martti Hallikainen, Helsinki Univ. of Technol., Lab. Space Technol., Otakaari 5A, Fin-02150 Espoo, Tel. +358 9451 2371, Fax: 358 9451 2898, email: martti.hallikainen@hut.fi

Tim Hewison, Met O(RS), Y70, DRA, Farnborough GU14 6TD, UK  
Tel: +44 1252 395781, Fax: +44 1252 515523, email: tjhewison@meto.gov.uk

Georg Heygster, University of Bremen, PO Box 330440, D-28334 Bremen  
Tel. +49 421 218 3910, Fax: +49 421 218 4555, email: heygster@physik.uni-bremen.de

Klaus-Peter Johnsen, GKSS Forschungszentrum Geesthacht GmbH, D-21502 Geesthacht  
Tel. +49 4152 871560, email: johnsen@gkss.de

Piotr Sobieski, Universite Catholique de Louvain, Place du Levant 2, B-1348 Louvain-la-Neuve, Tel. +32 10 47 2303, Fax: +32 10 47 2089, email: Sobieski@tele.ucl.ac.be

Christian Mätzler (address, see below)

### **Coordinator of Project 1**

Christian Mätzler, Inst. Applied Physics, University of Bern, Sidlerstr 5, CH- 3012 Bern  
Tel. +41 31 631 4589, Fax: +41 31 631 3765, email: matzler@iap.unibe.ch

### **Other**

#### **Chairman of COST 712**

David Pick, Meteorological Office, Y70, DRA, Farnborough GU14 0LX UK  
Tele +44 1252 395718, Fax: +44 1252 515523, email: drpick@meteo.gov.uk  
After Oct. 31, 1999: Christian Mätzler

#### **COST Representative**

Zoltan Dunkel, COST Directorate General, Square de Meeus 8, B-1040 Brussels,  
Tel. +32 2 296 5169, Fax: +32 2 296 4289, email: zoltan.dunkel@dg12.cec.be